

**DEVELOPMENT OF MICROACTUATOR SYSTEMS BASED
ON THE PHOTOINDUCED MICROACTUATION EFFECT
FOUND IN FERROMAGNETIC SHAPE MEMORY ALLOYS**

Thesis submitted by

ABHISHEK BAGCHI

DOCTOR OF PHILOSOPHY (ENGINEERING)

**DEPARTMENT OF MECHANICAL ENGINEERING
FACULTY COUNCIL OF ENGINEERING & TECHNOLOGY
JADAVPUR UNIVERSITY
KOLKATA, INDIA**

2020

1. Title of the Thesis:

DEVELOPMENT OF MICROACTUATOR SYSTEMS BASED ON THE PHOTOINDUCED MICROACTUATION EFFECT FOUND IN FERROMAGNETIC SHAPE MEMORY ALLOYS

2. Name, Designation and Institution of the Supervisors:

DR. PRATIP KUMAR MUKHOPADHYAY

Senior Professor,
Department of Condensed Matter Physics & Material Sciences,
S. N. Bose National Centre for Basic Sciences,
Kolkata – 700106, India.

DR. SUSENJIT SARKAR

Professor,
Department of Mechanical Engineering,
Jadavpur University,
Kolkata – 700032, India.

3. List of Publications:

- I. A. Bagchi, S. Sarkar, P. K. Mukhopadhyay: “Investigations on colour dependent photo induced microactuation effect of FSMA and proposing suitable mechanisms to control the effect”, Indian J. Phys., 92 (2018) 883.
- II. Abhishek Bagchi, Suman Sarkar, Sandip Bysakh, Susenjit Sarkar, P. K. Mukhopadhyay: “Possible mechanisms for degradation of Photo Induced Micro Actuation effect in a Ferromagnetic Shape Memory Alloy at high temperatures”, J. Appl. Phys., 125 (2019) 144505.
- III. Abhishek Bagchi, Suman Sarkar, Sandip Bysakh, Susenjit Sarkar, P. K. Mukhopadhyay: “Studies on the effect of temperature on the Photo-Induced Microactuation effect of a Co-based FSMA system”, Shap. Mem. Superelasticity, (2020) <https://doi.org/10.1007/s40830-020-00270-6>.

- IV. Abhishek Bagchi, Suman Sarkar, Sandip Bysakh, Chandra Sekhar Tiwary, Susenjit Sarkar, P. K. Mukhopadhyay: “Effect of copper doping on the photo induced micro actuation property of Co-Ni-Al FSMA and its outcome on the structural and mechanical properties”, (Under review).

4. List of Patents:

Nil

5. List of Presentations in National / International / Conferences / Workshops:

- I. Abhishek Bagchi, B. Rajini Kanth, P. K. Mukhopadhyay: “Investigations on Photo Induced Microactuation of FSMA”, Poster Presentation at ICFSMA’16 organized by Tohoku University held in Sendai, Japan.
- II. Abhishek Bagchi, Susenjit Sarkar, P. K. Mukhopadhyay: “Photo Induced Control Mechanism of a proposed FSMA Microgripper System”, Oral Presentation at Bose Fest 2018 organized by S. N. Bose National Centre for Basic Sciences held in Kolkata, India.
- III. Abhishek Bagchi, Suman Sarkar, Susenjit Sarkar, P. K. Mukhopadhyay: “Effect of temperature on the photo induced microactuation property of FSMA”, Oral Presentation at Condensed Matter Days – 2018 organized by University of Burdwan held in Burdwan, India.
- IV. Abhishek Bagchi, Suman Sarkar, Sandip Bysakh, Susenjit Sarkar, P. K. Mukhopadhyay: “MICROSTRUCTURAL EVOLUTION AND FERROMAGNETIC SHAPE MEMORY RESPONSE IN RAPIDLY SOLIDIFIED Co-Ni-Al ALLOYS”, Poster Presentation at NMD – ATM 2018 organized by Indian Institute of Metals and Tata Steel Ltd. (Under the aegis of Ministry of Steel, Government of India) held in Kolkata, India.

STATEMENT OF ORIGINALITY

I **ABHISHEK BAGCHI** registered on **06/05/2016** do hereby declare that this thesis entitled “**DEVELOPMENT OF MICROACTUATOR SYSTEMS BASED ON THE PHOTOINDUCED MICROACTUATION EFFECT FOUND IN FERROMAGNETIC SHAPE MEMORY ALLOYS**” contains literature survey and original research work done by the undersigned candidate as part of Doctoral studies.

All information in this thesis have been obtained and presented in accordance with existing academic rules and ethical conduct. I declare that, as required by these rules and conduct, I have fully cited and referred all materials and results that are not original to this work.

I also declare that I have checked this thesis as per the “Policy on Anti Plagiarism, Jadavpur University, 2019”, and the level of similarity as checked by iThenticate software is 2%.

Signature of ABHISHEK BAGCHI:

Date:

Certified by Supervisors:

DR. PRATIP KUMAR MUKHOPADHYAY

Senior Professor,
Department of Condensed Matter Physics & Material Sciences,
S. N. Bose National Centre for Basic Sciences,
Kolkata – 700106, India.

DR. SUSENJIT SARKAR

Professor,
Department of Mechanical Engineering,
Jadavpur University,
Kolkata – 700032, India.

CERTIFICATE FROM THE SUPERVISORS

This is to certify that the thesis entitled “**DEVELOPMENT OF MICROACTUATOR SYSTEMS BASED ON THE PHOTOINDUCED MICROACTUATION EFFECT FOUND IN FERROMAGNETIC SHAPE MEMORY ALLOYS**” submitted by **Shri Abhishek Bagchi**, who got his name registered on **06/05/2016** for the award of Ph. D. (Engineering) degree of Jadavpur University is absolutely based upon his own work under the supervision of **Dr. Pratip Kumar Mukhopadhyay** and **Dr. Susenjit Sarkar** and that neither his thesis nor any part of the thesis has been submitted for any degree / diploma or any other academic award anywhere before.

THESIS SUPERVISORS

DR. PRATIP KUMAR MUKHOPADHYAY

Senior Professor,
Department of Condensed Matter Physics & Material Sciences,
S. N. Bose National Centre for Basic Sciences,
Kolkata – 700106, India.

DR. SUSENJIT SARKAR

Professor,
Department of Mechanical Engineering,
Jadavpur University,
Kolkata – 700032, India.

ACKNOWLEDGEMENTS

First and foremost, I would like to take this opportunity to express my sincere gratitude to my supervisors Dr. Pratip Kumar Mukhopadhyay and Dr. Susenjit Sarkar for their guidance, care and inspiration, which were indispensable in the course of completion of my research work. Their patient hearing, critical comments and intuitive approach towards the research problem helped me to learn a lot during the entire duration of my doctoral research career. Their stimulating suggestions, encouragement, detailed and constructive comments helped me in performing my research activities and writing the thesis. No word would be sufficient enough to express my lifelong gratitude towards my supervisors.

I would like to sincerely acknowledge the Council of Scientific & Industrial Research (CSIR), Government of India, for their financial support in the form of the grant of a direct Senior Research Fellowship to me for carrying out this thesis work. I would also like to express my deep sense of gratitude and thanks to S. N. Bose National Centre for Basic Sciences and Jadavpur University to allow me to carry out my research work throughout my doctoral program leading to this thesis.

I would like to thank all my past and present lab mates namely Dr. Sandeep Agarwal, Dr. Md. Injamamul Arief, Dr. Tanmoy Ghosh, Md. Sarowar Hossain, Dipanjan Samanta, Animesh Basak, Gurdeep Singh, Susmita Dey, Bishal Kumar Keshari and Indrajit Manna at S. N. Bose National Centre for Basic Sciences, who made my stay at the institute a very joyous, pleasant and memorable one. I would also like to thank all my past and present senior post-docs of the lab namely Dr. Rajini Kanth Bhogaju, Dr. Alo Dutta, Dr. Tapas Paramanik, Dr. Vinodh Kumar Shanmugam and Dr. Suman Sarkar for their constant help, suggestions and encouragements to carry out my research work and writing this thesis. I would also like to acknowledge all the faculty members, administrative staff and members of the technical cell of the institute for their constant support and cooperation during the entire duration of my stay at the institute. I would like to specially thank Mr. Amit Kumar Ghosh and Mr. Hrishikesh Nandi of the workshop of the institute for their constant help to me to carry out design and fabrication work of various microactuators and other equipment related to my research.

I gratefully acknowledge all the faculty members and administrative staff members of the Department of Mechanical Engineering at Jadavpur University as well as all administrative officials of the Office of the Faculty of Engineering & Technology at Jadavpur University for their kind support, guidance and constant cooperation towards me to carry out all my research activities as well as completing other official steps leading to this thesis.

I would like to acknowledge Dr. Sandip Bysakh of CSIR-Central Glass & Ceramic Research Institute, Kolkata for his help in carrying out and teaching me to analyze the Transmission Electron Microscopy (TEM) data of my samples. I am also sincerely grateful to Prof. Amalendu Biswas of Heritage Institute of Technology, Kolkata for his help and guidance to carry out the Finite Element Analysis (FEA) studies in suitable CAD software of various designs of microactuators related to my research activity.

It is very difficult to mention each and every one who has helped me to complete my research work successfully. I do recall with gratitude the assistance rendered by one and all.

Lastly and most importantly, I would like to offer my cordial homage to my parents. I like to pay my tribute to them for their blessings, encouragement and motivation throughout my academic career.

ABHISHEK BAGCHI

TABLE OF CONTENTS

Thesis Information	i
Statement of Originality	iii
Certificate from the Supervisors	iv
Acknowledgements	v
Table of Contents	vii
List of Abbreviations	xii
List of Figures	xiv
List of Tables	xxi
CHAPTER 1 INTRODUCTION	1
1.1 Introduction to smart materials	1
1.2 Ferromagnetic Shape Memory Alloys	6
1.3 Applications of Ferromagnetic Shape Memory Alloys	9
1.4 Choice of FSMA material for practical applications	11
1.4.1 Choice of Co-Ni-Al over Ni-Mn-Ga	11
1.4.2 Crystal structure of Co-Ni-Al alloys	15
1.5 Background and motivation of the present work	17
1.6 Scope of the present work	21
1.7 Organization of the thesis	24
CHAPTER 2 EXPERIMENTAL AND SIMULATION TECHNIQUES	27
2.1 Alloy preparation techniques	27

2.1.1	Arc melting	27
2.1.2	Melt spinning	29
2.1.3	Annealing	32
2.2	Compositional characterization	33
2.2.1	Scanning electron microscope with Energy dispersive X-ray analysis (SEM & EDAX)	33
2.3	Structural characterization	34
2.3.1	X-ray diffraction (XRD)	34
2.3.2	Transmission electron microscopy (TEM)	37
2.4	Magnetic characterization	39
2.4.1	Vibrating sample magnetometer (VSM)	39
2.5	Mechanical characterization	41
2.5.1	Tensile testing	41
2.6	Optical experimental setup	42
2.7	Simulation techniques	47
2.7.1	Analysis of Variance (ANOVA)	47
2.7.2	Finite Element Analysis (FEA)	48
CHAPTER 3	PHOTO INDUCED MICRO ACTUATION PROPERTY OF Co-Ni-Al FSMA	50
3.1	Introduction	50
3.2	Compositional dependence of Photo Induced Micro Actuation effect	51
3.3	Colour dependence of Photo Induced Micro Actuation effect	52
3.4	Control mechanisms of Photo Induced Micro Actuation effect	56
3.4.1	Laser power and wavelength dependent control mechanism	56

3.4.2	Laser polarization and wavelength dependent control mechanism	57
3.5	Response time of Photo Induced Micro Actuation effect	59
3.6	Statistical analysis of experimental data	61
3.6.1	Introduction to Design of Experiments	61
3.6.2	One way ANOVA studies on unpolarized laser data	61
3.6.3	Two way ANOVA studies on laser power data	66
3.6.4	Two way ANOVA studies on laser polarization data	69
3.6.5	Two way ANOVA studies on sample response time data	72
3.7	Structural characterization of $\text{Co}_{34}\text{Ni}_{35}\text{Al}_{31}$ FSMA	73
3.8	Conclusions	79
CHAPTER 4	THERMAL EFFECTS ON THE PROPERTIES OF PIMA OPERATION	81
4.1	Introduction	81
4.2	Gradual degradation of photo induced micro actuation effect	82
4.2.1	Heat treatment procedure of Co-Ni-Al FSMA	82
4.2.2	Gradual degradation of laser power dependent actuation	82
4.2.3	Gradual degradation of laser polarization dependent actuation	89
4.3	Microstructural evolution during heat treatment	94
4.4	Oxidation studies	100
4.4.1	Oxidation kinetics study	100
4.4.2	Microstructural features of oxidized $\text{Co}_{34}\text{Ni}_{35}\text{Al}_{31}$ FSMA	103
4.5	Magnetic characterization of oxidized sample	107
4.6	Conclusions	111

CHAPTER 5	INVESTIGATION OF COPPER DOPING ON PIMA EFFECT IN Co-Ni-Al ALLOYS	114
5.1	Introduction	114
5.2	Effect of copper doping on PIMA property	115
5.2.1	Effect of copper doping on laser power dependent actuation	115
5.2.2	Effect of copper doping on laser polarization dependent actuation	119
5.3	Improvement in mechanical properties of copper doped Co-Ni-Al	121
5.4	Microstructural evolution of copper doped samples	123
5.4.1	Microstructural evolution of $\text{Co}_{24}\text{Cu}_{10}\text{Ni}_{35}\text{Al}_{31}$	124
5.4.2	Microstructural evolution of $\text{Co}_{34}\text{Ni}_{35}\text{Al}_{21}\text{Cu}_{10}$	130
5.4.3	XRD analysis of the samples	134
5.5	Magnetic characterization of all samples	135
5.6	Conclusions	137
CHAPTER 6	DEVELOPMENT OF FSMA MICROACTUATORS	138
6.1	Introduction	138
6.2	PIMA operated FSMA microgripper system	140
6.2.1	Design of the microgripper system	140
6.2.2	Working principle of the microgripper system	144
6.2.3	Finite element analysis of simulated microgripper	145
6.2.4	Assembly of FSMA microgripper on robotic arm	153
6.3	PIMA operated FSMA relay system	155
6.3.1	Design of the relay system	155
6.3.2	Working principle of the relay system	158

6.3.3	Electrical specifications of prototype relay system	161
6.4	Conclusions	163
CHAPTER 7	CONCLUSIONS AND FUTURE OUTLOOK	164
7.1	Conclusions	164
7.2	Future outlook	167
	REFERENCES	168

LIST OF ABBREVIATIONS

SMA	Shape Memory Alloy
SME	Shape Memory Effect
M_s, M_f, A_s, A_f	Martensite Start Temperature, Martensite Finish Temperature, Austenite Start Temperature, Austenite Finish Temperature
FSMA	Ferromagnetic Shape Memory Alloy
MFIS	Magnetic Field Induced Strain
FSME	Ferromagnetic Shape Memory Effect
5M, 7M, NM	Five-Layered Tetragonal Martensite, Seven-Layered Near-Orthorhombic Martensite, Non-Modulated Tetragonal Martensite
T_c	Curie Temperature
BCC	Body-Centred-Cubic
FCC	Face-Centred-Cubic
SAED	Selected Area Electron Diffraction
XRD	X-Ray Diffraction
MEMS	Micro Electro-Mechanical Systems
PIMA	Photo Induced Micro Actuation
DOE	Design of Experiments
ANOVA	Analysis of Variance
TEM	Transmission Electron Microscopy
FEA	Finite Element Analysis
EDAX	Energy Dispersive X-Ray Analysis
SEM	Scanning Electron Microscope
EDS	Energy Dispersive Spectrometer

h k l	Miller Indices
BF	Bright Field
DF	Dark Field
PIPS	Precision Ion Polishing System
HRTEM	High-Resolution Transmission Electron Microscopy
STEM – HAADF	Scanning Transmission Electron Microscopy – High Angle Annular Dark Field
STEM – EDS	Scanning Transmission Electron Microscopy – Energy Dispersive Spectroscopy
VSM	Vibrating Sample Magnetometer
λ	Wavelength
FEM	Finite Element Modelling
M_s	Saturation Magnetization
H_c	Coercivity
μ_B	Magnetic Moment (Bohr Magneton)
M – H	Magnetization Hysteresis
SPDT	Single Pole Double Throw
NC	Normally Closed
NO	Normally Open

LIST OF FIGURES

Figure No.	Description
1.1	Temperature induced phase transformation of an SMA
1.2	Schematic diagram of Ferromagnetic Shape Memory Effect
1.3	Magnetic Field induced motion of martensitic twins in FSMAs
1.4	Magnetic Field induced phase transformation in FSMAs
1.5	Strain vs bandwidth chart for selection of smart materials
1.6	Crystal structure of full and semi Heusler alloys
1.7	(a) Sample at rest position (b) Sample at deformed position when excited by focused laser beam
1.8	(a) Laser power dependence of PIMA effect (b) Frequency response of the Co-Ni-Al sample (c) Laser polarization dependence of PIMA effect (d) Influence of temperature on PIMA effect
2.1	(a) Tri-arc furnace (b) Rotary vacuum pump
2.2	Schematic representation of melt spinning process
2.3	(a) Setup of the r. f. induction furnace (b) Main chamber of the furnace (c) Melt spun FSMA ribbons
2.4	Box type furnace for annealing
2.5	Energy dispersive X-ray analysis (EDAX) instrument
2.6	Schematic representation of X-ray diffraction process
2.7	RIGAKU MiniFlex II diffractometer (XRD) unit
2.8	Schematic representation of transmission electron microscopy
2.9	FEI Tecnai G2 30ST TEM
2.10	Schematic diagram of vibrating sample magnetometer
2.11	Lake Shore Cryotronics 7400 VSM unit

- 2.12 INSTRON Model 3365 universal testing system
- 2.13 Experimental setup to demonstrate PIMA effect
- 2.14 Nikon Eclipse Ti-U inverted research microscope
- 2.15 Schematic representation of dual deck microscope operation
- 2.16 SHODENSHA USB Microscope setup
- 3.1 XRD analysis of $\text{Co}_{34}\text{Ni}_{35}\text{Al}_{31}$ ribbon sample
- 3.2 (a) PIMA effect of FSMA sample in presence of blue laser (b) green laser (c) red laser
- 3.3 Microactuation of sample against unpolarized lasers
- 3.4 Laser power and colour dependence of PIMA effect
- 3.5 Laser polarization and colour dependence of PIMA effect
- 3.6 Vibration amplitude of the $\text{Co}_{34}\text{Ni}_{35}\text{Al}_{31}$ FSMA sample at different chopping frequencies
- 3.7 Total micro actuation of the $\text{Co}_{34}\text{Ni}_{35}\text{Al}_{31}$ FSMA sample at different chopping frequencies
- 3.8 Boxplot of displacement for unpolarized laser data
- 3.9 Normplot of Residuals for displacement for unpolarized laser data
- 3.10 Residuals vs Fits for displacement for unpolarized laser data
- 3.11 Residuals vs Order for displacement for unpolarized laser data
- 3.12 Main Effects plot for laser power data
- 3.13 Normplot of Residuals for displacement for laser power data
- 3.14 Residuals vs Fits for displacement for laser power data
- 3.15 Residuals vs Order for displacement for laser power data
- 3.16 Main Effects plot for laser polarization data
- 3.17 Normplot of Residuals for displacement for laser polarization data

- 3.18 Residuals vs Fits for displacement for laser polarization data
- 3.19 Residuals vs Order for displacement for laser polarization data
- 3.20 Bright field TEM image showing the existence of B2 ordered grain and L1₂ ordered matrix channel in the Co₃₄Ni₃₅Al₃₁ sample
- 3.21 (a – b) Selected area diffraction patterns taken along the [01 $\bar{1}$] and [001] zone axis of the BCC grain
- 3.22 (a) Selected area diffraction pattern taken along the [100] zone axis of FCC matrix channel (b) Dark field image of the red dotted box marked area of Figure 3.20
- 3.23 STEM – HAADF of Co₃₄Ni₃₅Al₃₁ FSMA
- 3.24 (a – c) Elemental mappings of the sample using STEM – EDS nano probe
- 3.25 STEM – EDS line composition profile across the grain and matrix channel using STEM nano probe along red line ‘AB’ of Figure 3.24(a)
- 4.1 Power dependent PIMA effect at room temperature and 50 °C
- 4.2 Power dependent PIMA effect at room temperature and 100 °C
- 4.3 Power dependent PIMA effect at 100 °C and 150 °C
- 4.4 Power dependent PIMA effect at 250 °C
- 4.5 (a) Power dependent PIMA effect at 300 °C (b) Power dependent PIMA effect at 350 °C
- 4.6 Colour dependent PIMA effect at various annealing temperatures
- 4.7 Polarization dependent PIMA effect at room temperature and 50 °C
- 4.8 Polarization dependent PIMA effect at 50 °C and 100 °C
- 4.9 Polarization dependent PIMA effect at 100 °C and 150 °C
- 4.10 Polarization dependent PIMA effect at 250 °C
- 4.11 (a) Bright field TEM image of the heat treated Co-Ni-Al sample (b) Blow up version of Figure 4.11(a) showing fine fault morphology
- 4.12 (a) High magnification bright field TEM image (b) Dark field TEM

image

- 4.13 (a) Diffraction pattern taken inside B2 grain of annealed sample (b) Diffraction pattern taken along [011] zone axis of L1₂ matrix
- 4.14 STEM-HAADF image of the same region shown in Figure 4.11(a)
- 4.15 (a-d) Elemental mappings using STEM – EDS nano probe, showing the cobalt rich nano sized precipitates along with the existence of oxygen inside the B2 ordered grain, evolved during annealing of the Co-Ni-Al alloy at 400 °C
- 4.16 (a) XRD pattern of the as spun and oxidized Co-Ni-Al samples (b) Expanded view of the XRD pattern of the as spun and oxidized
- 4.17 Square of mass gain versus oxidation time for the selected Co-Ni-Al FSMA at 400 °C
- 4.18 (a) TEM bright field image showing the formation of irregular and composite surface oxide layer along with the base alloy of the Co-Ni-Al sample oxidized at 400 °C for 35 hrs. (b) Corresponding HAADF image showing the atomic contrast of the composite oxide layer
- 4.19 (a – d) Spatial elemental mappings using STEM – EDS nano probe, showing the distribution of Co, Ni, Al, O in the composite oxide surface layer
- 4.20 (a – b) Selected area diffraction pattern taken from top and under hill oxide layer showing the formation of different types of oxide layer
- 4.21 STEM – EDS line composition profile across the top hill layer and base alloy using a STEM nano probe along red line 'AB' of Figure 4.19(d)
- 4.22 (a) Magnetization hysteresis (M – H) curve of as spun Co₃₄Ni₃₅Al₃₁ (b) (M – H) curve of the alloy oxidized at 400 °C for 35 hrs. (c) (M – H) curve of the alloy oxidized at 400 °C for 48 hrs.
- 4.23 Initial rise of (M – H) for as spun and oxidized samples with their difference
- 5.1 Comparison between laser power dependent PIMA effect of Sample A (Co₃₄Ni₃₅Al₃₁) and Sample B (Co₃₂Cu₂Ni₃₅Al₃₁)

- 5.2 Comparison between laser power dependent PIMA effect of Sample A ($\text{Co}_{34}\text{Ni}_{35}\text{Al}_{31}$) and Sample C ($\text{Co}_{24}\text{Cu}_{10}\text{Ni}_{35}\text{Al}_{31}$)
- 5.3 Comparison between maximum displacement of all the samples at room temperature
- 5.4 Comparison between laser polarization dependent PIMA effect of Sample A ($\text{Co}_{34}\text{Ni}_{35}\text{Al}_{31}$) and Sample B ($\text{Co}_{32}\text{Cu}_2\text{Ni}_{35}\text{Al}_{31}$)
- 5.5 Comparison between laser polarization dependent PIMA effect of Sample A ($\text{Co}_{34}\text{Ni}_{35}\text{Al}_{31}$) and Sample C ($\text{Co}_{24}\text{Cu}_{10}\text{Ni}_{35}\text{Al}_{31}$)
- 5.6 Engineering Stress vs Engineering Strain plot under tension at room temperature for $\text{Co}_{34}\text{Ni}_{35}\text{Al}_{31}$ and $\text{Co}_{24}\text{Cu}_{10}\text{Ni}_{35}\text{Al}_{31}$ alloys
- 5.7 Bright field TEM image showing the existence of B2 ordered grain having two different kinds of phase transformational morphology and L1₂ ordered matrix channel in the as spun $\text{Co}_{24}\text{Cu}_{10}\text{Ni}_{35}\text{Al}_{31}$ alloy sample
- 5.8 (a) Selected area diffraction pattern taken along [001] zone axis of the BCC grain marked as 'A' in Figure 5.7 (b) Selected area diffraction pattern taken along the [011] zone axis of FCC matrix channel marked as 'B' in Figure 5.7
- 5.9 (a) Bright field image of orange box marked area of Figure 5.7 showing the compositionally modulated and spinodally decomposed morphology of the B2 ordered grain (b) Bright field image of blue dotted box marked area of Figure 5.7 showing the existence of martensitic plates inside the B2 ordered grain
- 5.10 STEM – HAADF image of the STEM – EDS mapping region
- 5.11 (a – d) Elemental mappings using STEM – EDS nano probe, showing B2 ordered grains are rich in nickel and aluminium whereas matrix channel is rich in cobalt and copper in $\text{Co}_{24}\text{Cu}_{10}\text{Ni}_{35}\text{Al}_{31}$ alloy
- 5.12 STEM – EDS line composition profile across the grain and matrix channel using an STEM nano probe along orange line 'AB' of Figure 5.10
- 5.13 Bright field TEM image showing the existence of L1₂ ordered grain and martensitic plates inside the matrix channel of the $\text{Co}_{34}\text{Ni}_{35}\text{Al}_{21}\text{Cu}_{10}$ alloy

- 5.14 (a) Selected area diffraction pattern taken along the [100] zone axis of the grain confirming the $L1_2$ ordering (b) Selected area diffraction pattern taken along the [011] zone axis of the FCC matrix channel showing the splitting of (111), (022) and (200) types of planes
- 5.15 (a – b) Dark field image of the blue dotted box marked area of the matrix channel of Figure 5.13 formed by two split (111) type planes, showing the existence of alternating variants of the martensitic plates
- 5.16 An STEM – HAADF image of the same region shown in Figure 5.13
- 5.17 (a – d) Spatial elemental mappings using STEM – EDS nano probe, qualitatively showing the equal partitioning of cobalt, nickel, aluminium and copper in the entire microstructure of the $Co_{34}Ni_{35}Al_{21}Cu_{10}$ alloy
- 5.18 Rietveld refinement plots of XRD data of all the samples
- 5.19 Comparison among M-H curves of $Co_{34}Ni_{35}Al_{31}$, $Co_{32}Cu_2Ni_{35}Al_{31}$, $Co_{24}Cu_{10}Ni_{35}Al_{31}$ and $Co_{34}Ni_{35}Al_{21}Cu_{10}$ samples
- 6.1 Design of the FSMA microgripper system
- 6.2 (a) Actuating part of FSMA microgripper system (b) Gripping arm of FSMA microgripper system (c) Prototype FSMA microgripper system assembly
- 6.3 (a) Microgripper assembly in open position (b) Microgripper assembly in closed position when excited by focused laser beam
- 6.4 Solid modelling of microgripper assembly
- 6.5 Static structural analysis of microgripper system
- 6.6 Actuation of microgripper on application of mechanical force
- 6.7 Force applied by focused laser beams
- 6.8 Solid modelling of microgripper assembly with object
- 6.9 Static structural analysis of gripping mechanism
- 6.10 Gripping of object on application of mechanical force

- 6.11 Static structural analysis of contact region
- 6.12 Gripping force generated by focused laser beams
- 6.13 Robotic assembly with FSMA microgripper
- 6.14 Components of Part A of the SPDT relay system
- 6.15 Components of Part B of the SPDT relay system
- 6.16 Schematic diagram of the SPDT relay assembly
- 6.17 Schematic circuit diagram of the working mechanism of the SPDT relay system
- 6.18 Prototype FSMA SPDT relay system

LIST OF TABLES

Table No.	Description
1.1	Classification of different classes of smart materials
1.2	General characteristics of various FSMA systems
3.1	One way ANOVA analysis of unpolarized laser data
3.2	Grouping analysis of unpolarized laser data using Tukey method
3.3	Two way ANOVA analysis of laser power data
3.4	Two way ANOVA analysis of laser polarization data
3.5	Two way ANOVA analysis of chopper total actuation data
3.6	Two way ANOVA analysis of chopper vibration data
3.7	Composition of the melt spun alloy and various microstructural features determined by TEM – EDS analysis
4.1	Composition analysis of different composite oxide layers determined by STEM – EDS analysis for the Co-Ni-Al sample oxidized at 400 °C for 35 hrs.
4.2	Magnetic properties of as spun and oxidized $\text{Co}_{34}\text{Ni}_{35}\text{Al}_{31}$ FSMA
5.1	Rietveld refinement analysis of XRD data of all the samples
5.2	Magnetic properties of all the samples

CHAPTER 1: INTRODUCTION

1.1 Introduction to smart materials

While the stages of human civilization were previously associated with the material of construction (like copper, bronze, iron etc.), the current century is known as the silicon age, where digital logic is basically the driving force in day to day life. Ahead of this is the new-age materials which can work in response to external stimuli in a predictable and enhanced manner, where the material properties are utilized in various applications. Nowadays the goal is to look for smart materials, where the material is characterized by not the material of construction, but by the action it can or is expected to take. Smart materials are generally defined as a special class of materials that have been designed to have either one or many of its properties to be significantly altered in a controlled and repeatable fashion by application of any specific external stimuli and in some cases can be trained to react to the external stimuli [1.1, 1.2]. The change in property is reversible in nature and is inherent to the material. Examples of such materials are not too small either; they are generally classified based on the stimulant they are expected to react on. The reaction shown by the material may be in the form of changes in its volume, shape, colour, viscosity, etc. and these reactions may be exhibited as responses against changes in the external stimuli like temperature, magnetic field, electrical current, stress, etc. [1.1, 1.2]. A small but nevertheless instructive list of the classification of smart materials is shown in Table 1.1. The degree of smartness of these smart materials can be measured by their “responsiveness” to the controlling stimuli as well as their “agility”. Responsiveness of a smart material implies the amplitude of change in its properties whereas its agility implies the time taken to respond to the controlling stimuli [1.3]. The current interest in these smart materials arises due the further possibility that they can act as both sensors as well as actuators simultaneously.

Category	Controlling Factor	Smart Material
Colour changing	Light	Photochromic
	Temperature	Thermochromic
Actuating	Electric Field	Piezo-electric
	Temperature	Shape Memory Alloy
	Magnetic Field	Ferromagnetic Shape Memory Alloy
Thickness changing fluid	Electric Field	Electro-rheological Fluid
	Magnetic Field	Magneto-rheological Fluid
Self diagnosing materials	Light	Optical Fibre Composite

Table 1.1 Classification of different classes of smart materials

All smart materials are self sensing i.e. they can sense the change in the specific factors or stimuli to which they are expected to react to. They can also achieve precise actuation and control over the changes they are expected to take in response to their specific controlling factors. While traditional materials of construction are still suitable for most applications due to their specific properties, their main disadvantage is their inability to modify or adapt its properties or specifications when a change in the environment of operation arises. Smart materials are more capable than conventional materials to overcome or to adapt to these changes in environment as required. The most important and unique features common to almost all smart materials are as follows. They show real time response in changing their properties when they are subjected to a change in their controlling factors or stimuli. The smartness or responsiveness of smart materials is very reliable due to its reversible and repeatable nature. Due to these unique properties and other advantages over conventional materials, smart materials are gradually becoming the materials of choice for use in various engineering applications and discoveries of newer technologies [1.1, 1.2, 1.4]. Smart materials are suitable to be embedded in specific systems to carry out specific functions. Due to these factors, systems employing smart materials over other traditional materials

have the additional advantages of reduction in weight of the systems as well as less power consumption.

Among the smart materials indicated in Table 1.1, shape memory alloys (SMA) are extensively used in various engineering applications as they can generate mechanical work when subjected to thermal cycling. The property of SMAs by virtue of which the shape change phenomenon occurs is known as Shape Memory Effect (SME). The SME is defined as the process by virtue of which an SMA changes its shape or remembers a particular shape above a specific temperature which is called the transformation temperature of that particular SMA. SMAs which can remember its shape only above its transformation temperature are known as one way SMAs. However, some SMAs can be trained to remember two shapes, one below and the other above its transformation temperature. This feature is called two way shape memory effect. This is a hallmark property shown by SMAs where training can be imparted on an inanimate material proving that SMAs are in fact smart. All SMAs operate within a certain temperature range depending upon the composition of the alloy. Within this temperature range the SMAs have two phases. These two phases depend upon the transformation temperature for the selected alloy system. The phase of an SMA above its transformation temperature is known as the austenite phase whereas the phase below the transformation temperature is known as the martensite phase. Each of these two phases have different crystal structures [1.5]. Austenite phases have generally a cubic crystal structure while the crystal structure of martensite phases can be tetragonal, orthorhombic or monoclinic in nature. Austenite phase is much stronger than martensite phase because its crystal structure cannot be deformed by application of mechanical stress. Martensite phase can be again classified into two categories namely twinned martensite and deformed martensite. Twinned martensite structure is formed when an SMA is cooled down from its austenite phase below its transformation temperature. This twinned martensite phase is relatively soft and can be easily deformed by applying mechanical stress which results in the detwinning of the structure.

The transformation between the martensite and austenite phases is diffusionless and it occurs by solid state phase transformation i.e. there is a change

in the shape or volume of the structure and this transformation is known as martensitic phase transformation. This reversible phase transformation occurring between the martensite and the austenite phases and vice versa forms the basis of operation of this unique feature of the shape memory alloys [1.5]. The phase transformation process between the crystal structures of the martensite and austenite phases is shown schematically in Figure 1.1. From Figure 1.1 it can be seen that there are four characteristic temperatures which are associated with the phase transformation process. These four temperatures are martensite start temperature (M_s), martensite finish temperature (M_f), austenite start temperature (A_s) and austenite finish temperature (A_f) respectively. During the cooling cycle, the austenite phase starts to transform to the martensite phase at the martensitic start temperature and it finishes the phase transformation at the martensitic finish temperature. During the reverse process i.e. the heating cycle, the SMA starts transforming from the martensite phase at the austenitic start temperature and finishes its transformation into the austenite phase at the austenitic finish temperature.

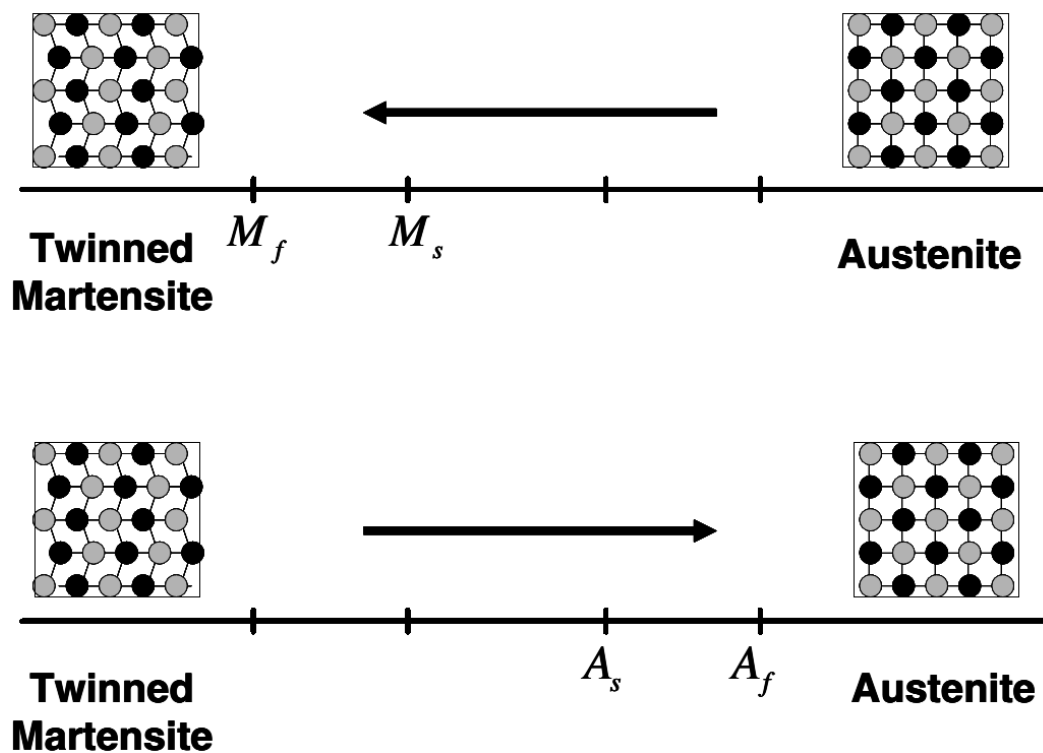


Figure 1.1 Temperature induced phase transformation of an SMA [1.5]

As stated earlier the property by virtue of which SMAs can remember their shapes only above their transformation temperature is called one way shape memory effect. In this phenomenon when an SMA in its martensite phase is deformed by the application of mechanical stress, it will hold onto its deformed shape even after the removal of the mechanical stress. To revert to its original shape by itself, the SMA has to be heated above its transformation temperature. By performing this heating operation, the SMA changes its crystal structure into the austenite phase and regains its original shape. Now if the same SMA is again cooled down below its transformation temperature it will hold onto its original shape that was achieved in the high temperature or austenite phase. So, in this case, the austenite to the martensite phase transformation does not cause any physical change in the shape of the SMA. The shape of the one way SMA in its martensite phase can only be deformed by the application of mechanical stress [1.5, 1.6]. In the case of one way SME, the SMA can remember the shape of only the austenite phase. However, under certain conditions an SMA can also remember the shape of its martensite phase. In those cases an SMA can exhibit reversible shape changes under the effect of thermal cycling on both sides of its transformation temperature. Again, as stated earlier this phenomenon is called two way shape memory effect. This two way SME is the resultant of continuous thermomechanical cycling which is also called training of the SMA. This training is achieved by applying a very large amount of mechanical stress to the SMA in its martensite phase. This large mechanical stress causes irreversible dislocations in the crystal structures of the SMA in order to stabilize the configuration of the martensite phase. Thus, the SMA can remember its shape in the martensite phase also resulting in two way SME upon thermal cycling. The SMA loses its two way SME if it is aged above a certain temperature [1.5, 1.6].

Shape memory alloys also possess pseudoelastic properties in its high temperature or austenite phase. This behaviour of SMAs is associated with stress induced martensitic transformation at temperatures above A_f . It results in strain generation during the loading cycle and subsequently recovery of that strain during the unloading cycle. If sufficient mechanical load is applied to an SMA in its stable austenite phase, the SMA transforms into a state containing stable detwinned martensite phase. When the mechanical loading is removed completely, the SMA

reverts back to its original austenite state. The detwinned martensite that is formed due to the application of mechanical stress is a form of stress induced martensite. The pseudoelasticity shown by the SMA material is due to the superelastic behaviour of the material [1.5, 1.6].

1.2 Ferromagnetic Shape Memory Alloys

In conventional SMAs, the shape change phenomenon of the alloy samples occurs by thermal cycling only around the martensitic transformation temperature. Ferromagnetic Shape Memory Alloys (FSMA) are a special class of SMAs where the shape memory effect (SME) of the alloys can be controlled by the application of a magnetic field too below its Curie temperature (T_C) above which the sample becomes paramagnetic in nature. Application of magnetic field also causes the rearrangement of the crystal microstructure of the FSMA resulting in large Magnetic Field Induced Strains (MFIS) in the materials [1.7, 1.8]. This Ferromagnetic Shape Memory Effect (FSME) was first observed in a Ni_2MnGa alloy system having a X_2YZ type Heusler crystal structure [1.9]. The large MFIS observed in FSMAs is due to the magnetic field induced realignment of the martensitic twins. Below the T_C point, the twin variants of FSMAs have preferred directions of magnetization. The application of magnetic field causes the motion of the martensitic twins with a favourable axis of orientation along the direction of the applied field, resulting in change in relative volume fraction of those favourable twins at the expense of other twins, leading to an external deformation in shape of the alloys [1.10 – 1.14]. The Ferromagnetic Shape Memory Effect is shown schematically in Figure 1.2. When the temperature of the FSMA is lowered below M_f , its crystal structure changes from the austenite phase to the twinned martensite phase. Now if a magnetic field is applied to the FSMA, detwinning of the martensitic structure occurs resulting in deformation of the alloy which is evident by the increase in length of the alloy from 'l' to 'l'' as shown in Figure 1.2. If the direction of the applied magnetic field is reversed, the FSMA sample regains its original shape of the twinned martensitic phase. This phenomenon is known as Ferromagnetic Shape Memory Effect. If the FSMA sample in its detwinned martensitic phase is heated above A_f , the sample regains its original shape of the austenitic phase by reverse martensitic transformation process [1.15].

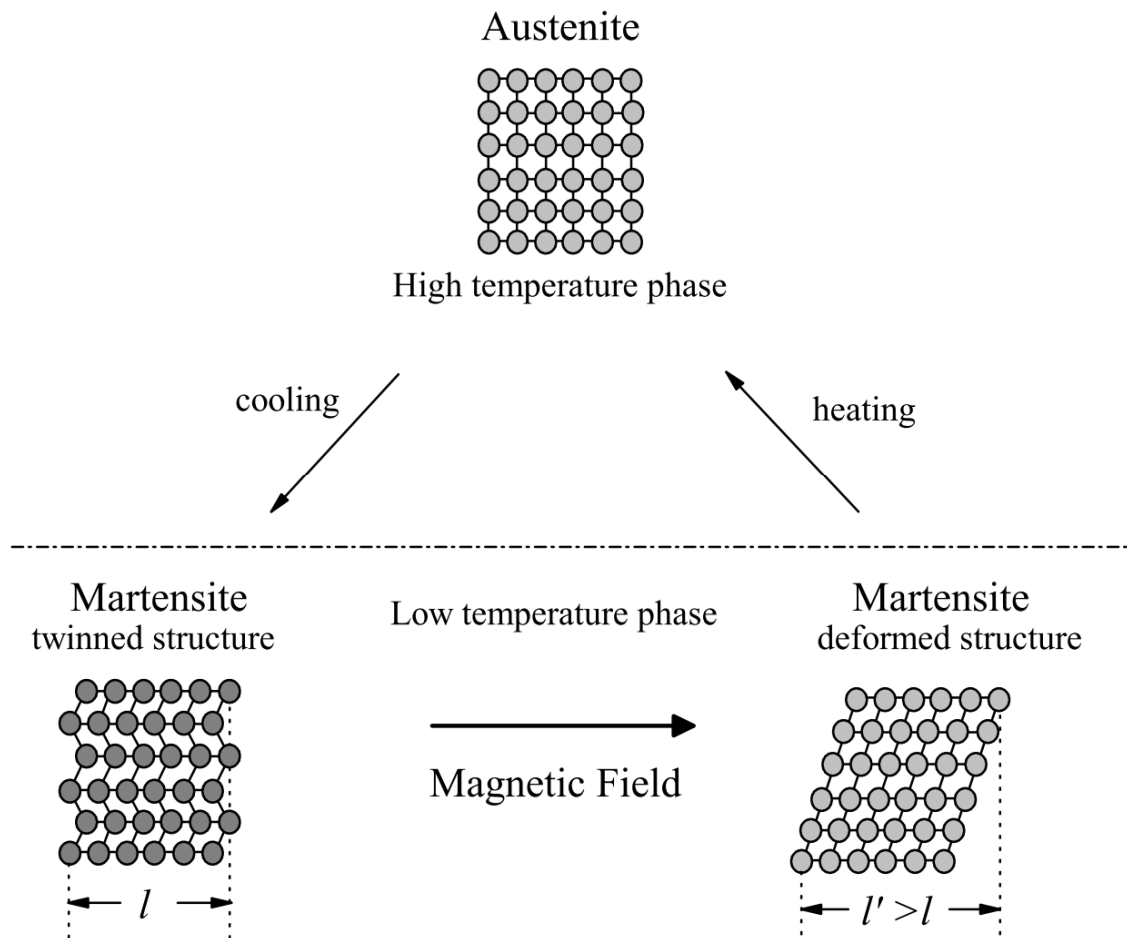


Figure 1.2 Schematic diagram of Ferromagnetic Shape Memory Effect [1.15]

In order to achieve reversible shape change in the FSMAs by this mechanism, the applied magnetic field must be accompanied by a simultaneous application of suitable external stresses. The magnetic field induced motion of the martensitic twins occurs in FSMAs with high magnetocrystalline anisotropy energy and low martensitic twin boundary motion energy [1.10, 1.11]. The effect of the applied magnetic field 'H' on the motion of the martensitic twins of the FSMAs is schematically shown in Figure 1.3. FSMAs generally show quicker response time as compared to SMAs, as the actuation of FSMAs is governed by applied magnetic field rather than the slow heating and cooling process controlling the actuation phenomenon of conventional SMAs. The response time of most FSMAs is in the range of milliseconds.

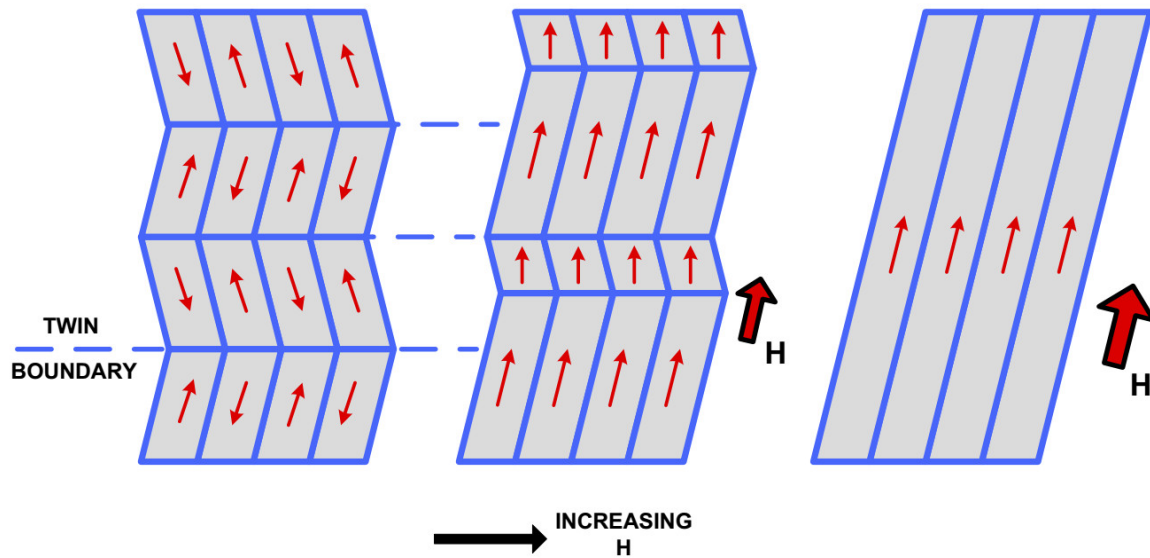


Figure 1.3 Magnetic Field induced motion of martensitic twins in FSMAs
[1.11]

Another property of FSMAs in addition to magnetic field induced motion of martensitic twins is the occurrence of magnetic field induced phase transformation in them. To achieve phase transformation in FSMAs by the application of magnetic field, the force of the magnetic field must be large enough to induce motion of the phase front of the FSMAs [1.11]. The effect of the applied magnetic field 'H' on the phase transformation of the FSMAs is schematically shown in Figure 1.4. This magnetic field induced phase transformation can also cause MFIS in FSMAs resulting in actuation mechanisms in some FSMAs [1.16]. The disadvantage of this phase transformation method is the requirement of application of extremely high magnitude of magnetic field to induce the phase transformation [1.17 – 1.19]. Thus, this method is not suitable for use in practical applications. The application of magnetic field also causes changes in the martensitic transformation temperature of FSMAs. Generally, there is a rise in the martensitic transformation temperatures in FSMAs on application of magnetic fields [1.20 – 1.22]. This property can also induce MFIS by inducing martensitic phase transformations in the FSMAs. The MFIS generated in FSMAs by this method is irreversible in nature. However reversible phase transformation by application of magnetic fields is also possible [1.23].

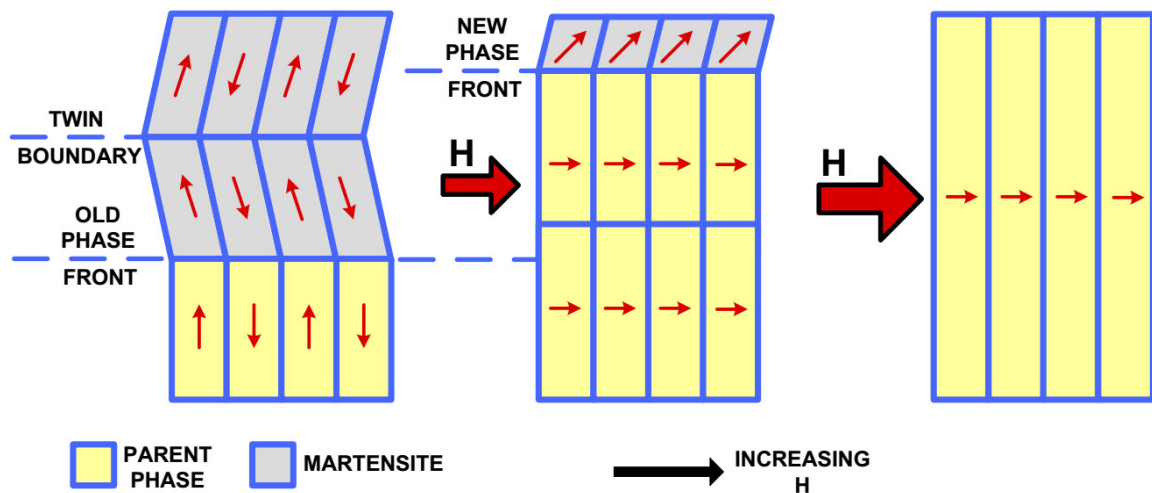


Figure 1.4 Magnetic Field induced phase transformation in FSMAs [1.11]

1.3 Applications of Ferromagnetic Shape Memory Alloys

One of the newest as well as most advanced fields of engineering where smart materials are gradually gaining popularity and are being extensively used is the field of micro electro-mechanical systems or MEMS technology [1.24, 1.25]. The most commonly used smart materials that are used in practical applications are the shape memory alloys (SMA) and the piezoelectric materials. SMAs like Nitinol has a maximum achievable strain of 10% but its response time is very slow with a frequency range of below 10 Hz [1.6]. This slow response time of conventional SMAs make them unsuitable for use in actuator applications. On the other hand, piezoelectric materials like Lead (Pb) Zirconate Titanate also known as PZT are very quick to respond to the stimuli with an operating frequency in the range of 100 kHz. But the maximum achievable strain in PZT is only of the order of 0.2%. As a result, it is also not suitable for use in many engineering applications. Due to these disadvantages of conventional SMAs and piezoelectric materials, the search began for a new class of smart materials for various engineering applications. Ferromagnetic shape memory alloys were found suitable for use as sensors and actuators due to the fact that they can produce sufficient amount of strain and they are also very quick to respond to the external stimuli i.e. the applied magnetic field in this case. FSMAs like Ni-Mn-Ga can produce maximum strains of

the order of 12% and their frequency response is in the range of 1 kHz [1.26, 1.27]. The main advantage of FSMAs over traditional SMAs is that it would overcome the slow response time and still produce sufficient amount of strain in the presence of applied magnetic field. Thus, FSMAs are becoming more popular than SMAs, piezoelectric materials as well as other classes of smart materials for use in practical applications because they can produce large magnetic field induced strains (MFIS) with quick response time [1.28 – 1.30]. A comparative study of the maximum strain and the response time required to achieve that strain for different classes of smart materials is shown schematically in Figure 1.5. From the schematic representation it can be inferred that the applicability of the smart material increases as its position is towards the upper right corner of the diagram.

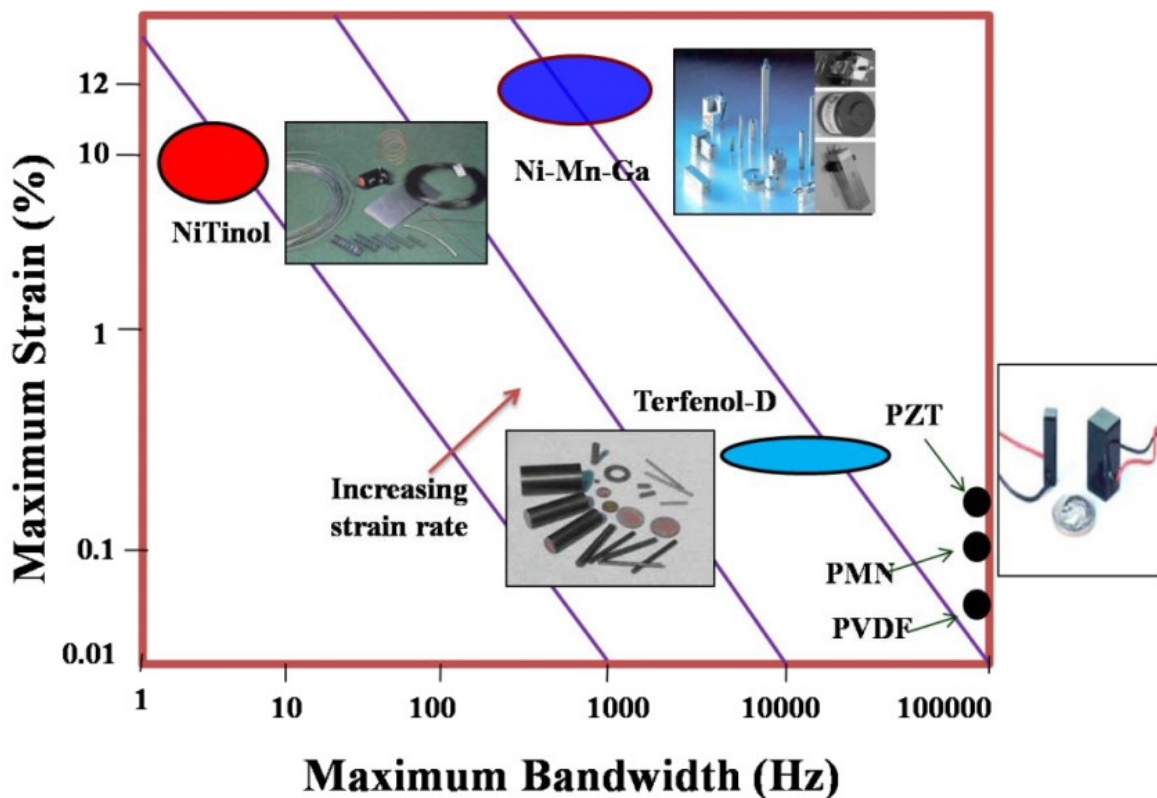


Figure 1.5 Strain vs bandwidth chart for selection of smart materials [1.15]

In addition to the properties stated above an ideal ferromagnetic shape memory alloy must have a high operating temperature range i.e. a high value of T_c as well as it must respond to lower values of applied magnetic field in order to be considered suitable for use as sensors and actuators in various engineering applications. Various practical applications of FSMAs like microsensors, microactuators, microgrippers, microvalves, microcouplers etc. have been perceived and built over time [1.31 – 1.36]. Since FSMAs produce actuation by themselves without the requirement of additional drivers, in many cases they themselves serve the function of the entire machine [1.37]. This reduces the size and weight of the machine and makes the system reliable and efficient. The main applications of FSMAs are in the field of sensors and actuators especially actuators [1.38]. The other important factor that has to be considered while choosing an FSMA for use in practical applications is its mechanical property. The FSMAs must be strong and ductile enough for practical application purposes.

1.4 Choice of FSMA material for practical applications

1.4.1 Choice of Co-Ni-Al over Ni-Mn-Ga

The most widely tried FSMAs in various types of practical applications are Ni₂-Mn-Ga which falls under the group of Ni₂-Mn-Z type of FSMAs (where Z can be any one of the following elements like Al, Ga, In, Sn and Sb). This is because Ni₂-Mn-Ga produces the highest amount of MFIS than any other FSMA. Moreover, the high frequency response of Ni-Mn-Ga results in faster response time which in turn results in faster, more accurate and better controlled switching mechanism in them than other FSMA systems. Other properties which make Ni-Mn-Ga suitable for practical applications are the presence of pre-martensitic phase transformation [1.39] and magnetocaloric effect [1.40]. As a result, Ni-Mn-Ga alloys have been extensively tried to be used as sensors, actuators and other potential application areas.

However, there are some serious disadvantages of using Ni-Mn-Ga FSMA systems in various forms of practical or industrial applications. Ni-Mn-Ga FSMAs have the X₂YZ type Heusler alloy structure. The crystal structures of the Ni-Mn-Ga

are very much dependent on the stoichiometric chemical composition as well as the heat treatment of the specific alloys. Thus, depending on the chemical composition and annealing temperatures of the alloys there can be different types of modulation in the crystal structures of Ni-Mn-Ga FSMAs in its martensite phase like the Five-Layered tetragonal martensite (5M), the Seven-Layered near-orthorhombic martensite (7M) and the Non-Modulated tetragonal martensite (NM) [1.41, 1.42]. As a result, the MFIS curves of different Ni-Mn-Ga FSMA systems vary considerably from one modulated crystal structure to another. This results in difficulty in controlling the fabricated actuators in bulk productions [1.43]. Another major disadvantage of Ni-Mn-Ga alloys is its Curie point (T_C) which is below 100 °C for most systems [1.44]. This low value of T_C is not suitable for many practical applications. The worst drawback of Ni-Mn-Ga FSMAs which render them unsuitable for actual application purposes is their high fragility. These alloys consist of only the β phase which has a body-centred-cubic (BCC) or B2 structure which causes the conventional as well as the magnetic shape memory effect. This β phase undergoes martensitic transformation in the ferromagnetic state. This β phase is responsible for the high fragility of the Ni-Mn-Ga FSMA systems. Due to this fragile nature of the materials, Ni-Mn-Ga FSMAs cannot be machined into the required designs of various perceived actuators which limit their usability in practical applications.

These major disadvantages of Ni-Mn-Ga FSMAs resulted in the search for other suitable FSMA systems which would overcome the problems faced with Ni-Mn-Ga alloys and be suitable for actual practical and industrial applications [1.43]. There are various FSMA systems that have been developed over time [1.45, 1.46] as possible alternatives to Ni-Mn-Ga systems. But most of these alloys are too costly to produce as well as they are too brittle for practical applications. Nevertheless, an informative list of such FSMA systems along with some general characteristics of such systems like its approximate maximum achievable MFIS, structure of the austenitic and martensitic phases, their approximate martensitic transformation temperature range as well as the relative ductility of the new systems as compared to Ni-Mn-Ga is demonstrated in Table 1.2.

FSMA System	Reported MFIS	Austenitic / Martensitic Structure	Transformation Temperature	Relative Ductility
Ni-Mn-Ga	6 – 12% in single crystals	L2 ₁ /10M or 14M, L2 ₁ /2M	around RT or below, well above RT	Fragile
Ni-Mn-Ga-Fe	1 – 5.5% in single crystals	L2 ₁ /10M or 14M	around RT or below	Better
Ni-Mn-Al	0.17% in single crystals, 0.01% in poly crystals	L2 ₁ /10M or 12M or 14 M, L2 ₁ /14M or 2M	around RT or below, well above RT	Improved by γ phase
Ni-Fe-Ga	0.02% in single crystals	L2 ₁ /10M or 6M or 14M	around RT	Improved by γ phase
Co-Ni-Al	0.06% in single crystals, 0.013% in poly crystals	B2/L1 ₀	below, above and well above RT	Improved by γ phase
Co-Ni-Ga	0.011% in melt spun ribbons	B2/L1 ₀	below, above and well above RT	Improved by γ phase
Fe ₃ Pt	0.6% in single crystals	Ordered fcc/fct	around 100 K	Intrinsically better
Fe-Pd	3.1% in single crystals, 0.01 – 0.05% in poly crystals, 0.06–0.07% in melt spun ribbons	Disordered fcc/fct	around RT or below	Intrinsically better

Table 1.2 General characteristics of various FSMA systems [1.43]

One of the FSMA systems which is being thoroughly investigated over the last few years as a potential alternative to Ni-Mn-Ga alloys in practical applications is the Co-Ni-Al FSMA system. The first reason behind the interest in Co-Ni-Al systems as potential FSMAs is the relatively cheaper cost of the constituent elements. Co-Ni-Al systems were first developed as Ni-Co-Al alloys with Ni as the majority element. Its origin is based on Ni-Mn-Z type of FSMAs where Mn was replaced by Co and Al acted as the ternary element. The Ni-Al β phase consists of the B2 structure. This is the cause of the SME. It was found that the addition of Co to the Ni-Al system caused the martensitic transformation of the β phase having a B2 structure into the β' phase having a $L1_0$ structure [1.47]. The presence of a face-centred-cubic (FCC) or $L1_2$ structured γ phase solid solution matrix engulfing the B2 grains were also observed. The γ phase can be introduced in the Co-Ni-Al systems by proper choice of the atomic weight percentage composition of each constituent elements. It can also be done by the process of controlled heat treatment. The presence of this second phase improved the hot workability of the alloys and also made the overall alloy system much more ductile at room temperature than the more commonly used Ni-Mn-Z FSMA systems [1.48]. This increase in ductility and improvement of mechanical properties in the $\beta+\gamma$ two phase alloys is due the decrease in the grain size of the β phase suspended in the γ matrix. One disadvantage of increasing the volume fraction of γ phase is the decrease in the magnitude of shape recovery of the FSMA, but this drawback can be overcome by proper training of the specific alloys [1.49].

As stated earlier, the low T_C of Ni-Mn-Ga systems greatly diminishes its operational range in practical applications. It was observed that in Ni-Co-Al systems, where Ni was the majority element, the T_C was considerably higher but the martensitic transformation temperature was also placed above the Curie point. It was then found out that increasing the Co content in the Ni-Co-Al systems making Co the majority element increases the T_C while also decreasing the martensitic transformation temperature [1.50]. In order to achieve higher martensitic transformation temperature, the Al content of the alloys were considerably decreased while Co content was simultaneously increased [1.49]. Thus Co-Ni-Al systems were developed and its applications as FSMAs were first considered. These FSMAs were characterized by their improved ductility over

conventional Ni-Mn-Ga systems and had a wider range of martensitic transformation temperatures than conventional FSMAs. The Curie point or T_c of these alloys were also found to be suitable for practical use. Other properties of Co-Ni-Al FSMAs which make these systems interesting for further investigations are their easy and hard axes of magnetization as well as their higher values of magnetocrystalline anisotropy energy. These magnetic properties displayed by the Co-Ni-Al systems is comparable to or in certain cases even better than the Ni-Mn-Ga systems [1.51]. However, the main disadvantage of Co-Ni-Al alloys is its very low value of MFIS [1.52, 1.53]. The cause of this low value of MFIS in Co-Ni-Al FSMAs may be the high critical stress required to achieve the variant reorientation of the $L1_0$ structure of the martensite phase [1.43]. It can also be stated that Co-Ni-Al FSMAs show excellent shape memory as well as superelasticity effects and two way shape memory effect can also be induced in these alloys by proper training [1.54 – 1.58]. All these factors combined make Co-Ni-Al FSMA systems highly suitable for use in various practical applications.

1.4.2 Crystal structure of Co-Ni-Al alloys

The crystal structures of FSMAs can be accurately determined by Electron Diffraction, Selected Area Electron Diffraction (SAED) and X-ray Diffraction (XRD) patterns while its magnetic structures can be determined by Neutron Diffraction patterns. Heusler alloys were first discovered when it was reported that the addition of a sp valence element to a Cu-Mn alloy made the resultant alloy ferromagnetic in nature though none of the constituent elements of the resultant alloy showed any ferromagnetism by themselves [1.59]. The structure of Heusler alloys can be of two types based on their stoichiometric compositions. They are full Heusler alloys having a X_2YZ type composition and half or semi Heusler alloys having a XYZ stoichiometric composition. These Heusler alloys are ternary intermetallic alloys comprising of two different transition metals in the X and Y positions respectively while the Z position is occupied by a sp valence element. While full Heusler alloys have a $L2_1$ type crystal structure consisting of four interpenetrating FCC sublattices, the semi Heusler alloys generally have a $C1_b$ structure consisting of three filled and one vacant interpenetrating FCC sublattices [1.60, 1.61]. Tetragonal and ordered $L1_0$ crystal structures which are also FCC in nature are

formed by stretching the parent structure along the z-axis. The crystal structure of both full and semi Heusler alloys is shown schematically in Figure 1.6. From the figure it can be seen that, in each unit cell of the crystal structure of the full Heusler alloys, the positions $(0,0,0)$ and $(\frac{1}{2}, \frac{1}{2}, \frac{1}{2})$ are occupied by the X atom, the position $(\frac{1}{4}, \frac{1}{4}, \frac{1}{4})$ is occupied by the Y atom and the position $(\frac{3}{4}, \frac{3}{4}, \frac{3}{4})$ is occupied by the Z atom respectively. In case of the semi Heusler alloys the $(\frac{1}{2}, \frac{1}{2}, \frac{1}{2})$ position of the unit cell remains vacant [1.62, 1.63]. Thus, the $C1_b$ type crystal structure can be derived from the $L2_1$ type crystal structure by vacating half of the X atom containing positions in an orderly manner [1.63]. As a consequence of this ordered vacating of positions, the structure no longer remains symmetrical around the centre.

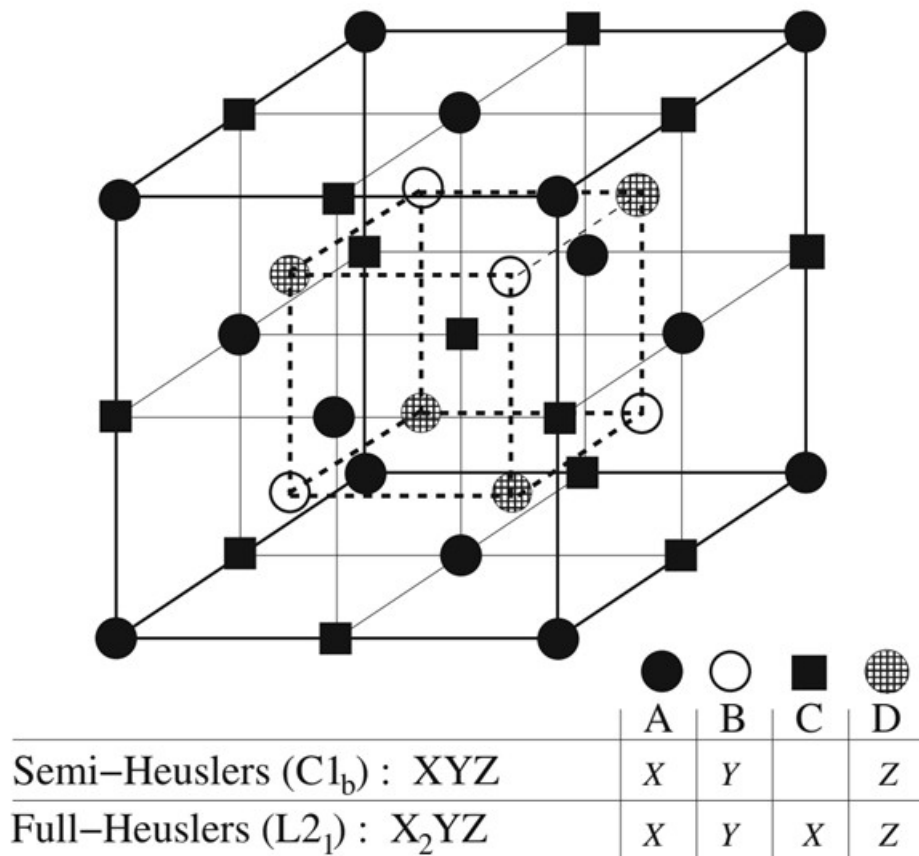


Figure 1.6 Crystal structure of full and semi Heusler alloys [1.62]

While it has been stated earlier that Ni-Mn-Ga possess a X_2YZ type full Heusler structure, the Co-Ni-Al FSMA systems which are more suitable for practical applications possess a XYZ type half Heusler or semi Heusler structure. In the case of Co-Ni-Al systems two transition metals Co and Ni occupy the X and Y positions of the structure, while the Z position of the crystal is occupied by Al. The parent or austenite phase of the Co-Ni-Al FSMA systems is highly symmetric and cubic in nature. As stated earlier, at the martensitic transformation temperature, Co-Ni-Al systems undergo martensitic transformation into a low symmetry martensite phase which is caused by a diffusionless distortion of the atoms of the parent crystal structure. Unlike Ni-Mn-Ga systems which can transform into different types of martensite structures viz. tetragonal, orthorhombic or monoclinic depending upon composition and heat treatment of the alloys, Co-Ni-Al systems show only $L1_0$ structure which is equivalent to the non-layered tetragonal martensite phase structures. Co-Ni-Al FSMA systems show the Ferromagnetic Shape Memory Effect (FSME) because the martensite phase of these alloys is ferromagnetic in nature.

1.5 Background and motivation of the present work

Ferromagnetic shape memory alloys (FSMAs) have been extensively used in micro electro-mechanical systems (MEMS) technology as microactuators due to their ability to generate mechanical work by virtue of its shape recovery property when they are subjected to thermal or magnetic cycling. FSMAs can be easily incorporated in appropriate MEMS as the sensing and actuating components of the devices. The main reason behind choosing FSMAs in various microactuator devices is its ability to achieve simple and effective control mechanisms of the actuating components including the possibility to achieve remote controllability. Besides this fact, the ability of FSMAs to achieve clean and silent actuation mechanism also makes them suitable for practical applications. The thermal energy required for operation and control of these FSMA microactuators is generally provided by conversion of electrical energy. Similarly, the magnetic force required for the magnetic cycling of the FSMAs is also provided by electromagnets. Thus, the presence of these electrical and magnetic equipment as the controllers make the overall MEMS devices bulky and heavy. In order to overcome this

disadvantage, newer controlling mechanisms were studied and developed to achieve remote operation of the FSMA microactuators making the micro electro-mechanical devices much more compact. One such method was to supply the thermal cycling energy by light instead of electrical energy. In order to achieve this, high powered laser beams were used as the heat source to provide the thermal cycling energy of the smart material [1.64 – 1.67].

Recently a novel and interesting observation was made where FSMA were found to demonstrate localized Photo Induced Micro Actuation (PIMA) effect when they were excited by a low powered focused laser beam [1.68]. From the initial studies it was observed that when a low powered focused laser beam was incident on the surface of the tiny microstructures of the FSMA sample, the microstructure immediately moved away from its rest position and remained in its newly deformed position for as long as the laser beam remained incident on the surface of the FSMA sample. As soon as the laser source was switched off, the microstructure of the FSMA sample immediately reverted back to its original rest position. The FSMA sample used to conduct the experiment for demonstrating the PIMA effect was a ribbon of composition $\text{Co}_{36}\text{Ni}_{36}\text{Al}_{28}$ produced by melt spinning the bulk sample in an r. f. induction furnace. The actual pictorial representation of the PIMA effect as obtained from the initial observations is shown in Figure 1.7. From the figures it can be seen that the alloy sample immediately deformed from its initial rest position as soon as it was excited by the focused laser beam. The insets of the figures show the side view of the microactuation phenomenon. Video recording of this unique and unprecedented property shown by the selected Co-Ni-Al FSMA system was also captured during the initial experimental studies conducted [1.69].

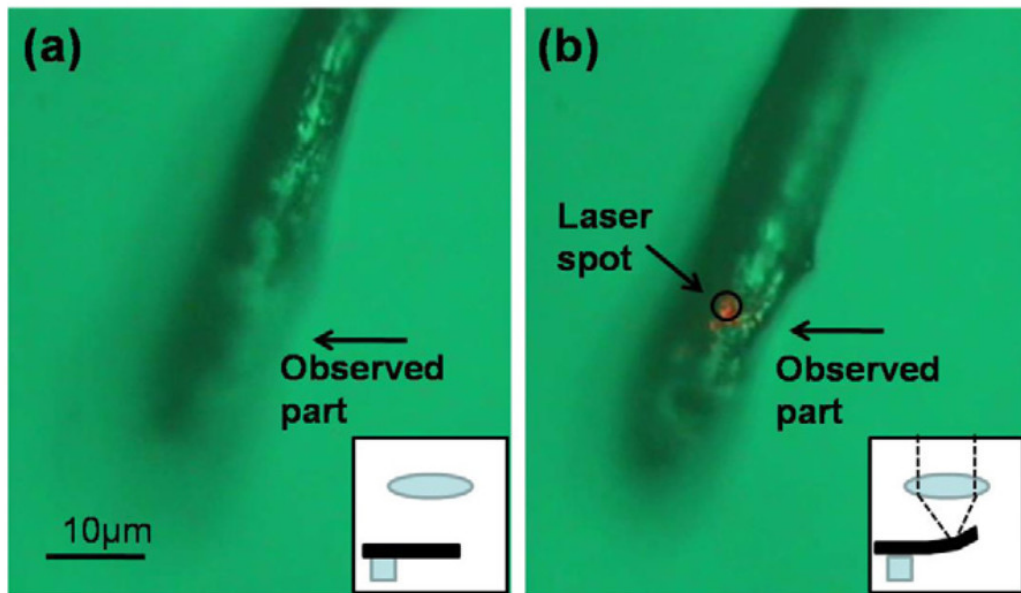


Figure 1.7 (a) Sample at rest position (b) Sample at deformed position when excited by focused laser beam [1.68]

The PIMA effect was studied systematically to better understand its nature in order to implement this property in actual practical applications [1.68]. Firstly, the laser power dependence of the PIMA effect was studied at room temperature. The study showed the linear nature of the amplitude of microactuation with respect to the variation in the power output of the incident laser beam. The results obtained are shown graphically in Figure 1.8(a). The response time required by the Co-Ni-Al sample to achieve its total actuation was then studied with the help of an optical chopper. The optical chopper was placed in the path of the laser beam falling on the surface of the sample and the chopping frequency was gradually varied. The actuation showed by the alloy for each chopping frequency is shown graphically in Figure 1.8(b). The study inferred that the Co-Ni-Al sample required approximately 1 sec. to achieve its total deformation regardless the power of the incident laser beam. This actuation phenomenon was also found to be fatigue resistant and robust over millions of oscillatory cycles. Further investigations were conducted to determine other factors affecting the PIMA effect. Thus, the dependence of the microactuation amplitude of the sample on the polarization of the incident laser beam was studied by placing a half-wave plate in the path of the incident laser beam. From the data shown graphically in Figure 1.8(c), it can be inferred that the

PIMA effect can be controlled periodically by controlling the polarization of the laser beam. All the above investigations were conducted at room temperature. In order to find out the operational limit of the PIMA effect, investigations were conducted at different temperatures for a particular laser power. The data obtained for various heating and cooling cycles is plotted in Figure 1.8(d) and it showed that the total achievable deformation of the sample decreased with rise in temperature and there was considerable loss in the microactuation amplitude after the sample reverted back to room temperature.

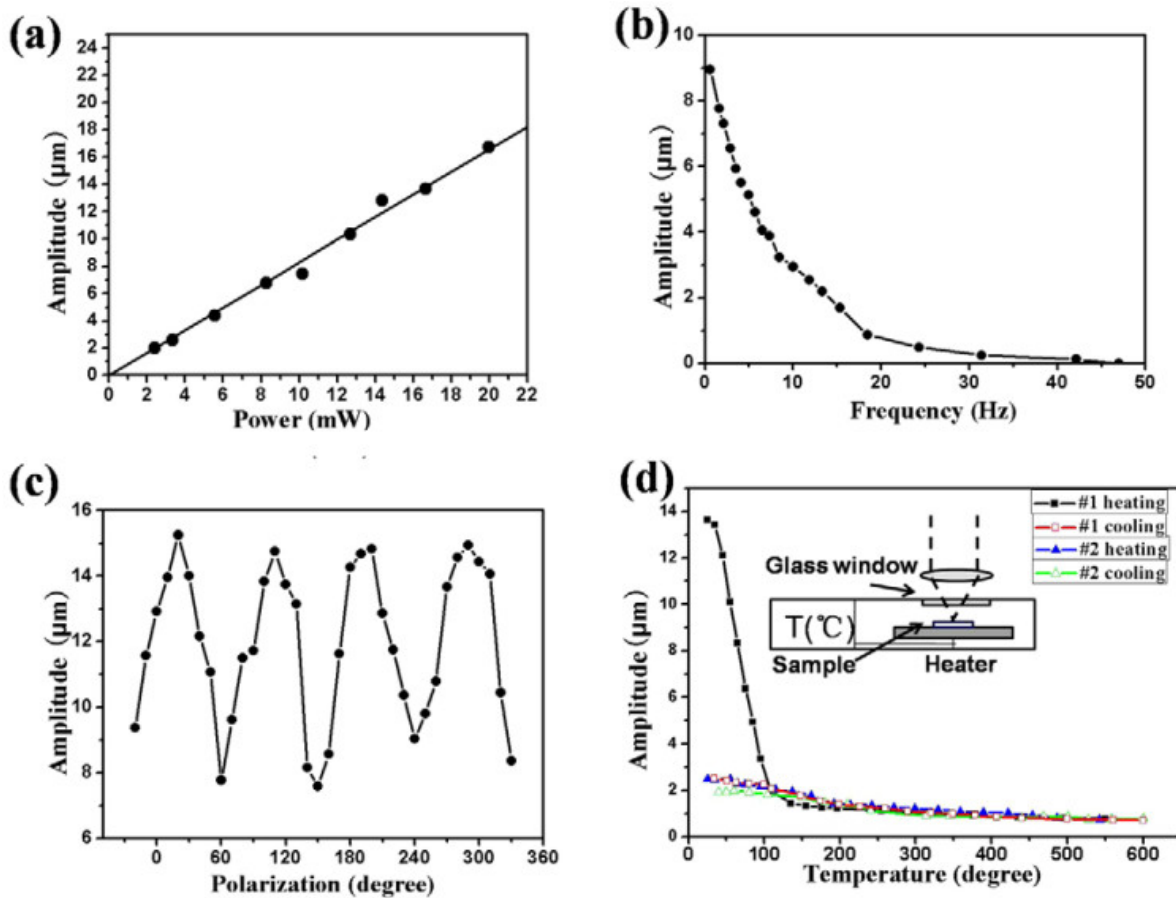


Figure 1.8 (a) Laser power dependence of PIMA effect (b) Frequency response of the Co-Ni-Al sample (c) Laser polarization dependence of PIMA effect (d) Influence of temperature on PIMA effect [1.68]

This unique property of FSMAs cannot be explained by thermal effect only. Efforts were made to explain the cause of this phenomenon. But the cause of this effect is still not understood properly. It was assumed that the ferromagnetic nature of the sample along with the SME of the β phase played an important role in the reversible and fatigue resistant PIMA effect. The composition dependence of the FSMAs could be attributed to the optimal combination of both β and γ phases in the Co-Ni-Al FSMA systems [1.68]. The above-mentioned study was the first such observation of this hitherto unknown phenomenon where laser power and polarization dependent, fatigue resistant and fast local microactuation of FSMAs were reported. PIMA effect was also found to be present in other FSMA systems like Ni-Mn-Ga. Though the exact reason behind this newly discovered PIMA effect is still unexplained, the PIMA property by itself is useful enough to be implemented for practical applications in various remote controlled, low powered and compact microactuator systems.

1.6 Scope of the present work

A lot of effort has been given to fully understand the cause of this photo induced micro actuation (PIMA) phenomenon. But till now it is not clear what causes this effect. Investigations were then carried out to find out whether any other material would show this unique PIMA effect. Experiments were carried out with different classes of materials but this property was not found in any class of materials other than FSMAs. For proper harnessing the property, the PIMA effect needed to be fully characterized. Towards this, the present study was devoted. With the discovery of the PIMA effect a new method to extend the control on the actuation mechanism of the microactuator systems can be proposed. In order to understand this effect in detail, systematic investigations were carried out using three different coloured diode lasers viz. red, blue and green. With this study on the PIMA phenomenon an effective, new and unique controlling mechanism for the fabrication and operation of various microactuator systems was proposed. The photo induced micro actuation effect of the FSMA sample was successfully demonstrated in detail and it was possible to control the phenomenon. Before actual implementation of the PIMA effect in practical use, analysis of the experimental data needed to be done in detail. Thus, Design of Experiments (DOE)

analysis was performed on the experimental data to find out the relations between response i.e. actuation of the sample with respect to various controlling factors. Analysis of Variance (ANOVA) studies was chosen to be implemented on the experimental data to conclusively provide evidence in support of the relationship between the actuation of the sample and the various controlling factors. Structural characterization of the Co-Ni-Al sample was done using Transmission Electron Microscopy (TEM) to correlate between the ferromagnetic shape memory effect (FSME) and the photo induced micro actuation (PIMA) effect shown by the ribbon sample.

It was conclusively proved that the amplitude of actuation of the Co-Ni-Al ribbons could be effectively controlled by various factors like colour, output power and polarization of the incident laser beams. This study paved the way for successful implementation of a new class of laser controlled remotely operated microactuator systems in the near future. Before actual implementation of this unique phenomenon in fabricating suitable microactuator systems is done, studies have been carried out to determine the workability of the Co-Ni-Al FSMA system in various environmental conditions where temperature plays an important role and it is subjected to different levels of oxidation. The variation in actuation of the alloy sample with different heat-treated condition has been determined in details in the present study. Transmission Electron Microscopy (TEM) was used to characterize the evolved microstructure for both the as-spun and heat-treated alloy samples. Thus, the correlation between microstructure and the photo induced micro actuation (PIMA) properties of the selected alloy have also been addressed in this work. Magnetic and thermal properties of the system were also studied systematically to adjudge the feasibility of implementing the PIMA effect for operation and control of suitable microactuator systems in varying environments in the near future.

One of the most important factors behind choosing Co-Ni-Al as the preferred FSMA system for practical applications is their better mechanical properties as compared to more widely studied FSMA's like Ni-Mn-Ga. Co-Ni-Al systems have better hot workability as well as better ductility near room temperature as compared to conventional FSMA's which makes them suitable for use as microactuators.

Efforts were made to further improve the ductility and other mechanical properties of the Co-Ni-Al FSMA system. In order to achieve this, appropriate proportions of copper were added to the Co-Ni-Al alloy. Studies were then conducted to determine the effect of different proportions of copper doping on the PIMA effect of the as-spun Co-Ni-Al alloy. Simultaneous studies were also carried out to determine the improvement in the desired mechanical properties of the newly developed copper doped Co-Ni-Al FSMA. Thus, comparing both the actuation data as well as the mechanical properties of the as-spun and the different copper doped alloys, an optimal FSMA system was chosen which can be suitably used for various microactuator applications in the near future. Transmission Electron Microscopy (TEM) was also used to characterize the evolved microstructure for both the as-spun and the newly developed copper doped FSMA samples. Magnetic and thermal properties of the new alloy systems were also studied systematically to adjudge the feasibility of implementing the PIMA effect of the newly developed copper doped Co-Ni-Al alloys for operation and control of suitable microactuator systems.

Once it had been definitely established that the Co-Ni-Al FSMA systems were suitable for the fabrication and operation of various laser controlled microactuators based on the PIMA effect, efforts were carried out to successfully implement this newly discovered phenomenon in actual practical applications. Before actual fabrication and operation of different FSMA microactuators were done by implementing the PIMA property shown by the alloys, simulation studies were done in suitable software to successfully simulate the actual microactuation process. In order to achieve this, various designs of suitable FSMA microactuator systems were developed using standard solid modelling software. After the solid modelling render was successful, the operation of the newly modelled microactuators were thoroughly characterized and studied in detail using standard Finite Element Analysis (FEA) software. On completion of successful finite element analysis of the simulated microactuator models, efforts were made to actually fabricate the modelled microactuator designs using the selected Co-Ni-Al FSMA systems. The fabricated microactuators were then operated and controlled by employing the unique PIMA effect shown by the Co-Ni-Al alloys. The data obtained by the actual fabricated FSMA microactuators were compared with the results of

the finite element analysis of the corresponding software model. As a result, the force exerted by the low powered focused laser beams on the FSMA microactuators as well as the work done by the laser induced FSMA microactuators operated by the principle of the PIMA effect can be successfully calculated. Thus, the present study paved the way for actual fabrication and operation of various suitably designed FSMA microactuators based on the newly developed and unique PIMA property shown by FSMAs.

1.7 Organization of the thesis

Chapter 1 of the thesis covers the introduction and overview of the work done and presented in the current thesis. It contains detailed literature review of previous works done related to and leading to the present work. The background and scope of the work done covered in this thesis are also discussed in details in this chapter.

Chapter 2 of the thesis covers the experimental and theoretical methods followed to carry out the research work presented in the current thesis. This chapter contains the procedure for the sample preparation as well the characterization techniques followed to determine the various useful properties of the samples related to the present work. Experimental procedures followed to fully characterize the photo induced micro actuation (PIMA) effect is also covered in this chapter. Finally, the theoretical methods followed like the design of experiments (DOE) studies as well as the finite element analysis (FEA) studies done related to the present work is covered in this chapter.

Chapter 3 of the thesis covers the experimental studies conducted to fully characterize the photo induced micro actuation (PIMA) effect shown by the Co-Ni-Al FSMA samples. This chapter deals with the discovery of the new and unique laser colour dependent PIMA property and its implementation in the operation and control of different perceived FSMA microactuator systems to carry out various useful engineering applications. This chapter also contains the basic design of experiments (DOE) analysis conducted on the experimental data obtained to conclusively provide evidence in support of the claim that the PIMA property can be

implemented as a new method to actually operate and control suitably designed FSMA microactuators in the near future. Investigations on the microstructure of the selected FSMA samples are also covered in this chapter.

Chapter 4 of the thesis covers the experimental studies conducted to find out the operational limit of the PIMA property of the Co-Ni-Al FSMA system in various environmental conditions where temperature plays an important role and it is subjected to different levels of oxidation. Relation between the actuation of the alloy sample with different heat-treated condition has been covered in detail in this chapter. Structural, magnetic and thermal studies conducted on the FSMA system to determine the correlation between microstructure and the photo induced micro actuation (PIMA) properties of the selected alloy have also been addressed in this chapter. Thus, this chapter systematically covers the feasibility of implementing the PIMA effect for operation and control of suitable microactuator systems in varying environments in the near future.

Chapter 5 of the thesis describes the detailed studies conducted to improve the ductility as well as other desired mechanical properties of the Co-Ni-Al system by addition of suitable proportions of ductile element copper to the original alloy composition. Optical, structural, magnetic and thermal studies conducted on the newly developed copper doped samples to characterize the correlation between the effect of copper doping and the PIMA property shown by the samples are also covered in detail in this chapter. Thus, this chapter deals with the feasibility of implementing the PIMA effect of the newly developed copper doped Co-Ni-Al alloys for operation and control of suitable microactuator systems.

Chapter 6 of the thesis describes the actual implementation of the PIMA property of the selected FSMA systems in the design, fabrication, operation and control of various suitable FSMA microactuator systems employing the PIMA property shown by the Co-Ni-Al FSMA systems. This chapter contains detailed simulation studies done on the perceived microactuators to determine various physical attributes of the perceived systems and the feasibility of their actual implementation in real life. Finally, this chapter consists of the actual development and operation of the FSMA

microactuators by using the PIMA effect to perform the desired engineering applications.

Chapter 7 of the thesis covers the findings and conclusions drawn from the present studies as well as the possible areas of interest for future studies.

CHAPTER 2: EXPERIMENTAL AND SIMULATION TECHNIQUES

2.1 Alloy preparation techniques

2.1.1 Arc melting

Bulk polycrystalline samples of the desired compositions of the Ferromagnetic Shape Memory Alloys (FSMA) were prepared by melting appropriate amounts of high purity ($\geq 99.9\%$) constituent elements in an inert argon gas atmosphere inside an arc melting furnace. A Centorr made (model no. 5TA) tri-arc furnace was used to prepare the FSMA samples. The arc furnace setup is shown in Figure 2.1. The furnace is capable of reaching temperatures greater than $3500\text{ }^{\circ}\text{C}$ and the maximum current that can pass through the three phases of the system is 400 A. This furnace has two main sections: (i) the lower section contains a copper hearth, and (ii) the upper section comprises three copper rods which hold three tungsten electrodes. The electrodes are insulated from both the upper and lower sections of the furnace. These two sections are separated from each other by a cylindrical Pyrex glass section which acts as a window to view the melting process as well as acts as an insulating stage between the upper and lower copper sections. Both the upper and lower sections are cooled by running chilled water. The copper hearth carries the metallic elements to be melted. The copper rods in the upper section of the furnace are placed through electrically insulated swivel balls which allow vertical as well as angular movements of the rods holding the electrodes.

To use this furnace, the hearth containing the materials to be melted is inserted into the tapered hole in the bottom of the furnace and clamped into position. The air inside the chamber was first evacuated by a rotary vacuum pump made by Vacuum Techniques (P) Ltd. The model can also be used as a diffusion pump. However, only the rotary pump option was used to achieve a chamber vacuum of the order of 10^{-3} mbar. This was sufficient to expel all the air inside the vacuum chamber. This was followed by backflushing the chamber with inert argon gas. This process was repeated 3 to 4 times to ensure oxygen free environment

inside the furnace chamber. During the melting process also, argon gas was flowed in continuously through the chamber to ensure an oxygen free environment of the chamber and prevent oxidation of the prepared alloys. The most important function of argon gas in the formation of the arc where argon plasma acts as the medium for arc formation. High current was generated by a 3-phase transformer. Arcing was initiated by momentarily touching the tungsten tips to the copper hearth. Heat generated by the electric arc struck between the tungsten electrode and the metals serves to melt the metals placed in the crucible to form an alloy. The electrodes are moved around and over the material in order to obtain a uniform and homogeneous melt. The specimen was turned over and melted several times to ensure the homogeneity of the sample. The chamber was allowed to cool down to room temperature before each melting. Then the arc is turned off by gradually decreasing the current from the power supply. The alloy formed is in the shape of spherical ingots.

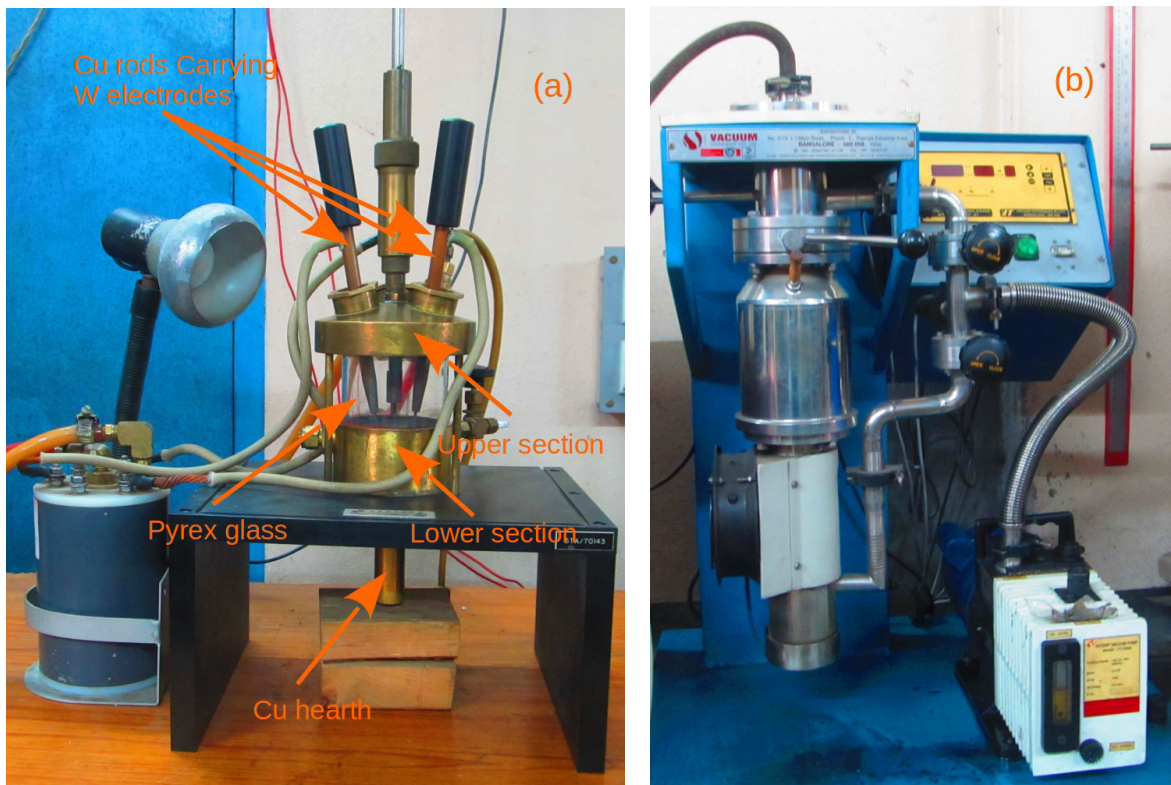


Figure 2.1 (a) Tri-arc furnace (b) Rotary vacuum pump [2.1]

2.1.2 Melt spinning

The PIMA effect was first observed in microstructures of amorphous ribbons of Co-Ni-Al FSMAs prepared by melt spinning bulk alloy ingots of the desired composition [2.2]. Melt spun FSMA ribbons are also more suitable for use as microactuators in practical applications than bulk ingots of the same composition because they can be easily formed in the desired shape of any perceived microactuators. Thus, in order to carry out the present work, ribbons of the desired composition of the FSMAs were prepared by melt spinning the arc melted bulk samples in an r. f. induction furnace. When an electrically conducting material is placed inside an alternating magnetic field producing coil, magnetic coupling occurs between the coil and the material placed inside the coil. Due to this magnetic coupling, eddy current opposing the magnetic field is induced in the material which results in very high resistive loss. As a result, the electrically conducting material gets heated up due to this resistive loss. If the material is ferromagnetic in nature, there will be additional hysteresis loss. This method of heating of the materials is known as induction heating. If sufficiently high magnetic field is produced in the coil, the high eddy current induced in the material can cause the material to melt due its own electrical resistance. Once the material gets melted, the magnetic coupling produces constant magnetic stirring in the melt material [2.3]. In case of ferromagnetic alloy samples like FSMAs, this constant stirring improves the homogeneity of the alloy samples.

The schematic representation of producing ribbons of desired compositions of the FSMA materials by rapid solidification technique is shown below in Figure 2.2. The r. f. induction melt spinning furnace used to prepare the ribbons of the desired compositions of the FSMAs was manufactured by Vacuum Techniques (P) Ltd. The melt spinning furnace setup used in the present study is shown below in Figure 2.3. The arc melted FSMA ingot was put inside a specially designed quartz crucible with a thin slot cut at the bottom of the crucible for the ejection of the molten alloy by application of argon gas pressure. The quartz crucible containing the alloy ingot was then placed in the coils of the induction furnace. The whole chamber was then vacuumed down to a pressure of 10^{-6} mbar using a combination of rotary and turbo pumping system. The chamber was then backfilled with inert

argon gas to prevent oxidation of the melted sample. The induction power supply was then switched on to melt the alloy ingot inside the quartz crucible. As high current flows through the induction coils, the sample melts inside the quartz crucible following the principle stated above. The induction coils are also cooled by the flowing chilled water to prevent its melting. The water chilled copper wheel is then rotated at a constant speed for obtaining the ribbons of desired thickness. The molten metal is then forced onto the rotating copper wheel through the slot at the bottom of the crucible by the application of argon gas pressure. The molten metal upon contact with the cold copper wheel solidifies rapidly into the form of ribbons due to the rotation of the copper wheel.

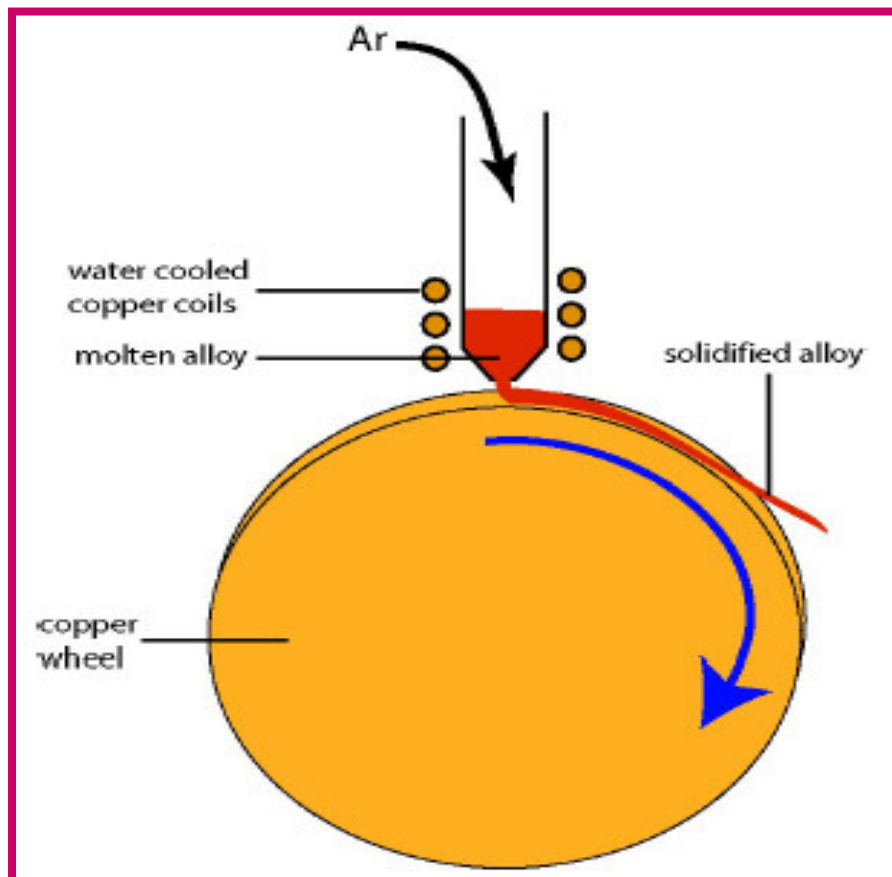


Figure 2.2 Schematic representation of melt spinning process

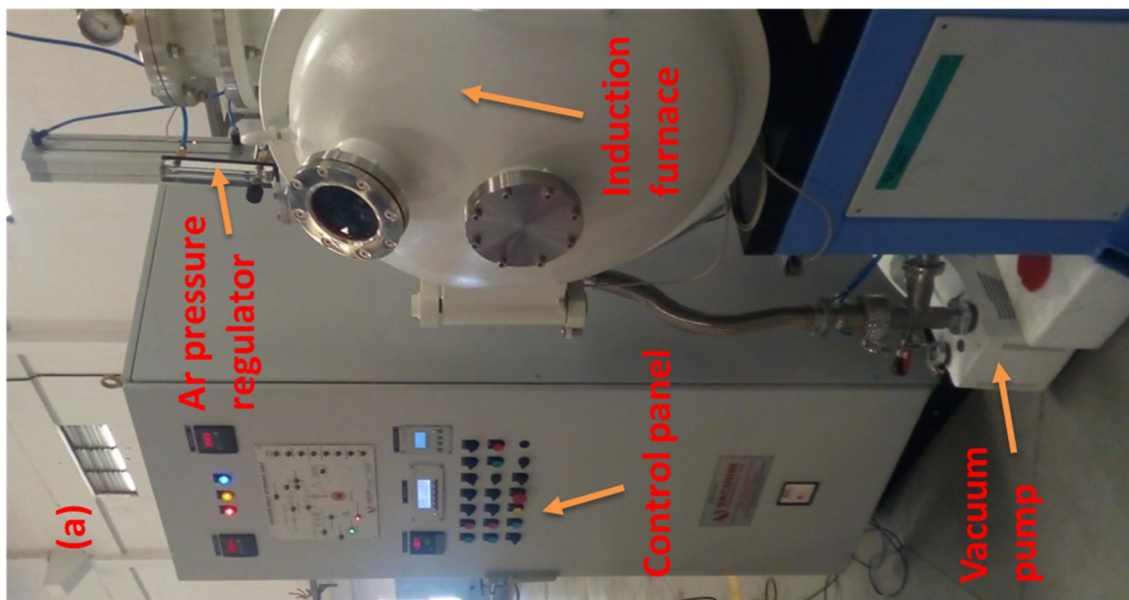
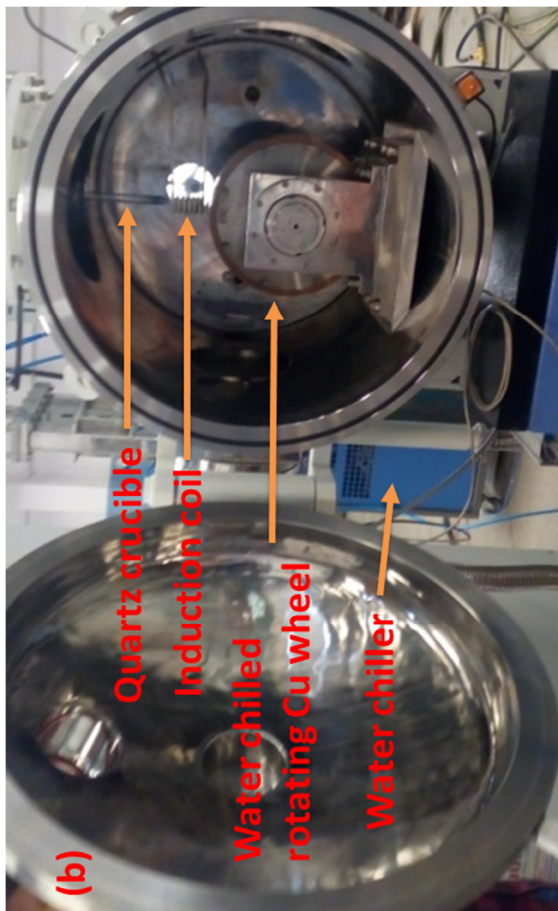


Figure 2.3 (a) Setup of the r. f. induction furnace (b) Main chamber of the furnace (c) Melt spun FSMA ribbons

2.1.3 Annealing

One of the studies carried out in the present work is the effect of temperature and oxidation on the Photo Induced Micro Actuation (PIMA) property shown by the Co-Ni-Al FSMA ribbons. Thus, to carry out these studies, the FSMA ribbons were placed freely on a quartz plate. The quartz plate containing the sample was then placed inside a box type furnace manufactured by Naskar & Co. as shown in Figure 2.4. The box type furnace has MoSi₂ heating elements and the system can achieve any temperature ranging from room temperature up to 1600 °C. The furnace has programmable temperature controllers for controlling the temperature holding time as well as the heating and cooling rates. After the program was executed i.e. the sample was heat treated and got oxidized for the desired temperature and time, the furnace was switched off to cool down the sample back to room temperature inside the furnace itself.

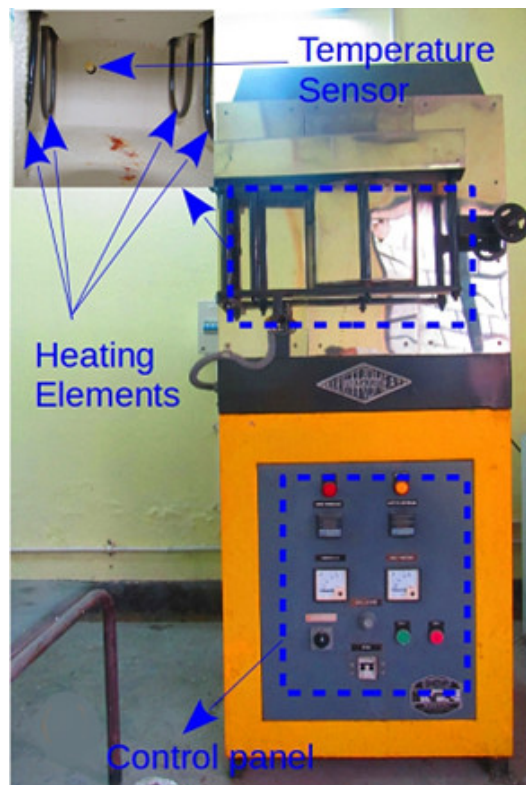


Figure 2.4 Box type furnace for annealing [2.1]

2.2 Compositional characterization

2.2.1 Scanning electron microscope with Energy dispersive X-ray analysis (SEM & EDAX)

The compositional analysis of the prepared Co-Ni-Al FSMA samples were carried out by a FEI™ made QUANTA FEG 250 model scanning electron microscope (SEM) instrument with an energy dispersive X-ray analysis (EDAX) attachment as shown in Figure 2.5. This method is a non-destructive analytical technique to analyse the chemical composition as well as the extent of homogeneity of the composition of the prepared alloys. The working principle of the EDAX instrument follows the basic theory that when high energy electrons interact with different materials, unique characteristic X-rays are generated for each element in the periodic table [2.4]. When a high energy electron beam of the order of 20 – 30 keV is incident on the sample surface, the electron beam penetrates the alloy surface upto a depth of a few microns. The energy of this incident beam excites the electrons of the inner orbital of the atoms of the constituent elements of the alloy. As a result of this excitation, the electrons get ejected from the atoms of the sample which are known as secondary electrons. In order to fill the gaps created by the ejection of the secondary electrons, the electrons from the outer orbital of the atoms jumps to the inner orbital. The difference in energy created due to the displacement of electrons from the outer to the inner orbital of the atoms is released in the form of X-rays. Due to the unique electronic structure of each element of the periodic table, the generated X-ray spectrum is also different for each element. The emitted X-rays are detected and analysed by the energy dispersive spectrometer (EDS) to identify the chemical composition of the prepared alloys. Along with the secondary electrons and the generated X-ray, backscattered electrons are also generated in the process mentioned above [2.4]. These secondary electrons as well as the backscattered electrons are used for capturing images of the sample surface. The SEM imaging technique utilizing the secondary electrons is also employed to study the morphology and topology of the prepared samples. The backscattered electrons are used for phase identification of multiphase samples by demonstrating contrasts in the compositions of the samples. The main advantage of SEM imaging technique is that, it combines high

magnification with large depth of field which results in a large surface area of the sample to be focused by the instrument. The compositional analysis of the prepared alloy samples was carried out on several spots at regular intervals covering the entire surface of the selected samples in order to check for the compositional homogeneity of the prepared samples.



Figure 2.5 Energy dispersive X-ray analysis (EDAX) instrument [2.5]

2.3 Structural characterization

2.3.1 X-ray diffraction (XRD)

X-ray diffraction (XRD) analysis is the most commonly used technique to characterize the crystal structure of materials so as to identify the phase of the materials. The lattice points of all crystalline materials are arranged periodically which can be described by the Bravais lattice system. The atoms of the constituent elements of the crystalline materials are placed on these lattice points in predetermined atomic arrangements. These periodic atomic arrangements of each

unique crystalline material are described by the lattice planes and indicated by the Miller indices (h k l). When an X-ray beam of suitable wavelength is incident on the alloy sample, the interactions of the X-ray with the atoms of the crystal results in both elastic as well as inelastic scattering of the radiation by the electrons present at the lattice points of the constituent atoms. The periodic arrangement of the atoms in the lattice planes of the crystal structure results in definite phase relationship between the incident and the elastically scattered waves having the same wavelength giving rise to diffraction patterns. The elastic scattering of the X-ray occurs in all directions. Most of the scattered waves from parallel lattice planes get cancelled out due to the destructive interferences. Constructive interferences only take place in directions which follow Bragg's law given by the relation $2d \sin\theta = n\lambda$, where d is the spacing between the diffracting lattice planes, θ is the angle between the incident wave and lattice plane, λ is the wavelength of the incident X-ray and n is an integer [2.6]. Thus, by using Bragg's law on the diffraction pattern of a crystal sample, the distance between the lattice planes as well as the lattice parameters of the crystal can be obtained. Further information about the atoms residing at a particular lattice point can also be obtained from the intensity of the peaks of the diffraction data [2.7]. The schematic representation of the X-ray diffraction process following Bragg's law is shown in Figure 2.6.

The XRD measurements were performed using a RIGAKU MiniFlex II diffractometer shown in Figure 2.7. The instrument uses an X-ray tube with copper target producing Cu K α of wavelength 1.54 Å for the XRD characterization. Nickel filters are used the instrument to remove the K β lines. The alloy samples were placed in specially designed glass sample holders and positioned inside the instrument. The X-ray source of the diffractometer was fixed while the sample stage and the detector rotated. The diffraction pattern was obtained by scanning the 2 θ angles ranging from 10° upto 120° at a rate of 1°/min with a step size of 0.02°. The obtained diffraction data were analysed using FullProf software to perform profile fitting on each XRD pattern. Thus, by analysing the diffraction pattern and indexing the XRD peaks, the structural properties of the FSMA samples can be characterized properly.

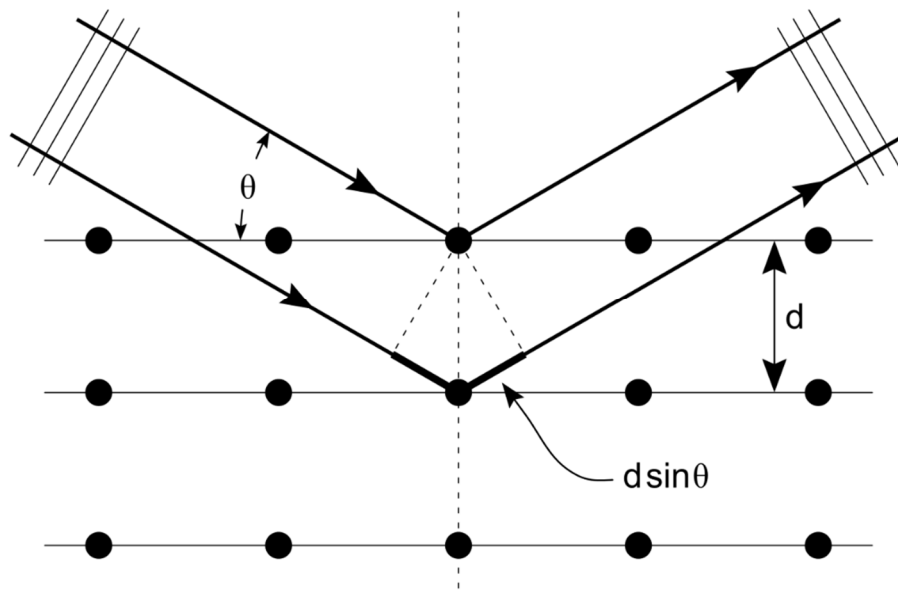


Figure 2.6 Schematic representation of X-ray diffraction process [2.8]



Figure 2.7 RIGAKU MiniFlex II diffractometer (XRD) unit [2.9]

2.3.2 Transmission electron microscopy (TEM)

Transmission electron microscope (TEM) is a very advanced and widely used instrument to study the detailed microstructure of materials. The detailed crystal microstructure of the FSMA samples were investigated by carrying out systematic TEM studies. TEM differs from an optical microscope where electrons of much smaller wavelength are used in place of light [2.10, 2.11]. The fundamental components of the TEM instrument is shown schematically in Figure 2.8. The electron beams from the electron gun are accelerated upto a high energy voltage of range 100 kV to 200 kV and then passed through the condenser lens onto the specifically prepared sample. The transmitted beams passing through the sample are then focused by an objective lens and then amplified by a projector lens to produce the desired image which is then captured. The lenses used in TEM are electromagnetic converging lenses. The transmitted electrons that pass through the sample are used to form the image by subtracting those electrons that get blocked or diffracted by the dense atoms of the sample. These black and white images thus obtained are called bright field (BF) images. The images that are produced by the diffracted electron beams are called dark field (DF) images [2.10, 2.11]. The dark field images can be further projected to produce selected area electron diffraction (SAED) patterns providing valuable information about the inter atomic spacing of the microstructure of the sample.

The detailed microstructural features of the FSMAs were investigated by using a FEI company TEM of model Tecnai G2 30ST operating at an accelerating voltage of 300 kV shown in Figure 2.9. The final TEM samples were prepared by argon ion milling process on a Gatan precision ion polishing system (PIPS) operating at an accelerating voltage of 5 kV and $5^\circ - 2^\circ$ incidence angle of the ion gun to obtain the desired sample thickness for carrying out TEM studies. Experiments were carried out to obtain the bright field and dark field TEM images along with the diffraction patterns as well the high-resolution transmission electron microscopy (HRTEM) images. The diffraction patterns of different zone axis were obtained by tilting the sample stage over a unit stereographic triangle to confirm the crystal structure of the phases involved and their orientation relations [2.10]. HRTEM images provide information about the distribution of equivalent atomic

column in the concerned phase. They are formed due to the interaction between the main electron beam and the diffracted electron beam in a certain zone axis [2.12, 2.13]. Scanning transmission electron microscopy – high angle annular dark field (STEM – HAADF) images along with scanning transmission electron microscopy – energy dispersive spectroscopy (STEM – EDS) technique were used to determine the compositional information of the samples from spot analysis, line scanning and elemental mapping of the particles using a STEM nano probe of the order of 1 nm in diameter [2.14 – 2.16].

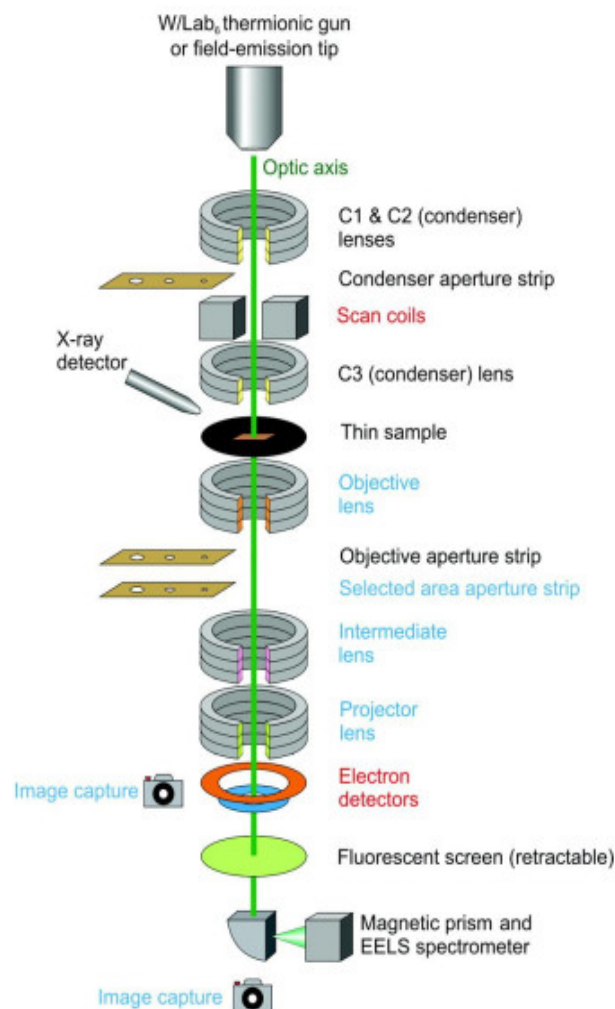


Figure 2.8 Schematic representation of transmission electron microscopy [2.10]



Figure 2.9 FEI Tecnai G2 30ST TEM [2.17]

2.4 Magnetic characterization

2.4.1 Vibrating sample magnetometer (VSM)

The magnetic characterization of the FSMA samples helps in the study of the magnetic and electronic behaviour of the alloys along with the transition behaviour of the FSMAs. In the present work, a vibrating sample magnetometer (VSM) instrument was used to measure the magnetization characteristics of the FSMAs. The VSM instrument was used to study the magnetization of the alloy samples as a function of magnetic field and temperature [2.18]. The schematic representation of the basic working principle of the VSM system along with the Lake Shore Cryotronics made model 7400 series commercial VSM instrument used for the present magnetization studies are shown in Figure 2.10 and Figure 2.11 respectively. The maximum magnetic field generated in the system is 1.67 T with a field homogeneity of $\pm 0.1\%$ over a 5 cm diameter circle. For low temperature magnetic characterization, a Model 74018 variable temperature

cryostat having a temperature range of 80 K to 400 K was used. For high temperature measurements, a Model 74034 high temperature oven having a temperature range of 300 K to 1273 K was used. The working principle of the VSM instrument is based upon the Faraday's law of induction according to which a change in magnetic flux induces a voltage. Under an applied magnetic field 'H', a magnetic moment 'm' is induced in the sample. The FSMA sample is fixed to a sample holder which is then positioned between suitably placed pickup coils under an applied magnetic field as shown in Figure 2.10 to magnetize the sample. A vertical sinusoidal mechanical oscillation with a fixed frequency is then applied to the sample. Due to this, magnetic flux enclosed by the pickup coils varies as a function of time. By varying the magnetic flux, an electric field is generated governed by the Faraday's law of induction thus inducing a voltage in the pickup coils which is proportional to the magnetic moment of the sample. The induced voltage 'V' in the pickup coil is denoted by the equation $V = \frac{d\phi}{dt} = \frac{d\phi}{dz} \frac{dz}{dt}$ where 'φ' is the magnetic flux in the pickup coils and 'z' is the vertical position of the sample with respect to the coils. For a sinusoidal mechanical oscillation, 'V' is proportional to the magnetic moment induced in the sample and is denoted by the equation $V = KmA\omega \sin(\omega t)$ where 'K' is the coupling constant, 'm' is the magnetic moment induced in the sample, $\omega = 2\pi f$ where 'f' is the frequency of oscillation of the sample and 'A' is the amplitude of oscillation of the sample [2.19].

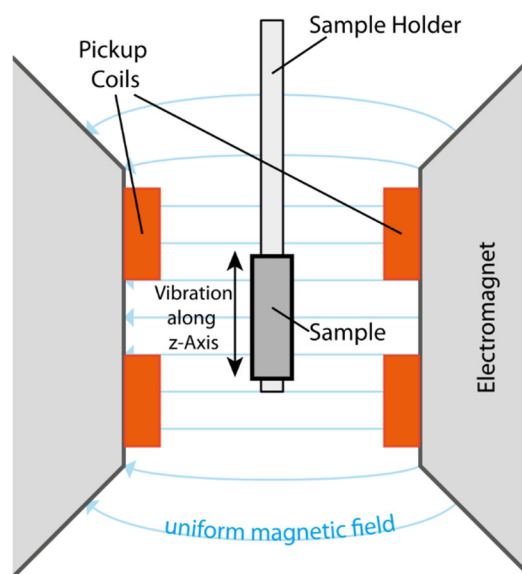


Figure 2.10 Schematic diagram of vibrating sample magnetometer [2.20]



Figure 2.11 Lake Shore Cryotronics 7400 VSM unit [2.21]

2.5 Mechanical characterization

2.5.1 Tensile testing

The tensile testing of the FSMA ribbons were carried out to study the yield strength and the ultimate tensile strength of the samples to determine the usability of the FSMAs in practical applications. The required parameters were calculated from the stress vs strain curve under tension obtained from the tensile tests undertaken. Other mechanical parameters like elastic modulus and Poisson's ratio of the materials can also be determined from the tests. The tensile tests were performed using an INSTRON Model 3365 electromechanical universal testing system attached with a wedge type gripper to hold the samples along with its associated Bluehill universal software as shown in Figure 2.12. The force capacity of this instrument ranges from 0.02 N to 5 kN. Generally, the test specimens required for the tensile tests in the universal testing system are prepared according to the ASTM standards. In the present work, ribbons of the selected FSMAs were studied for various practical applications whose mechanical properties are dramatically different than the bulk samples of the same composition [2.22]. The as-spun ribbons were used in the tensile tests to evaluate a qualitative trend to access the mechanical performance of the alloys.



Figure 2.12 INSTRON Model 3365 universal testing system

2.6 Optical experimental setup

The optical experimental setup used for the initial demonstration of the photo induced micro actuation (PIMA) effect is shown schematically in Figure 2.13. From the figure it can be seen that, the sample was mounted on a translation stage and placed directly below the objective lens of a microscope system. A red coloured laser beam of wavelength (λ) 660 nm and having power output of 80 mW was used to stimulate the sample. The laser beam was then focused onto the surface of the FSMA sample through the objective lens of the microscope system with the help of other optical components [2.2]. The real time actuation achieved by the microstructure of the sample was captured using a camera and its related software attached with the microscope system. The optical experimental setup used for the PIMA characterization reported in this thesis was based on this setup.

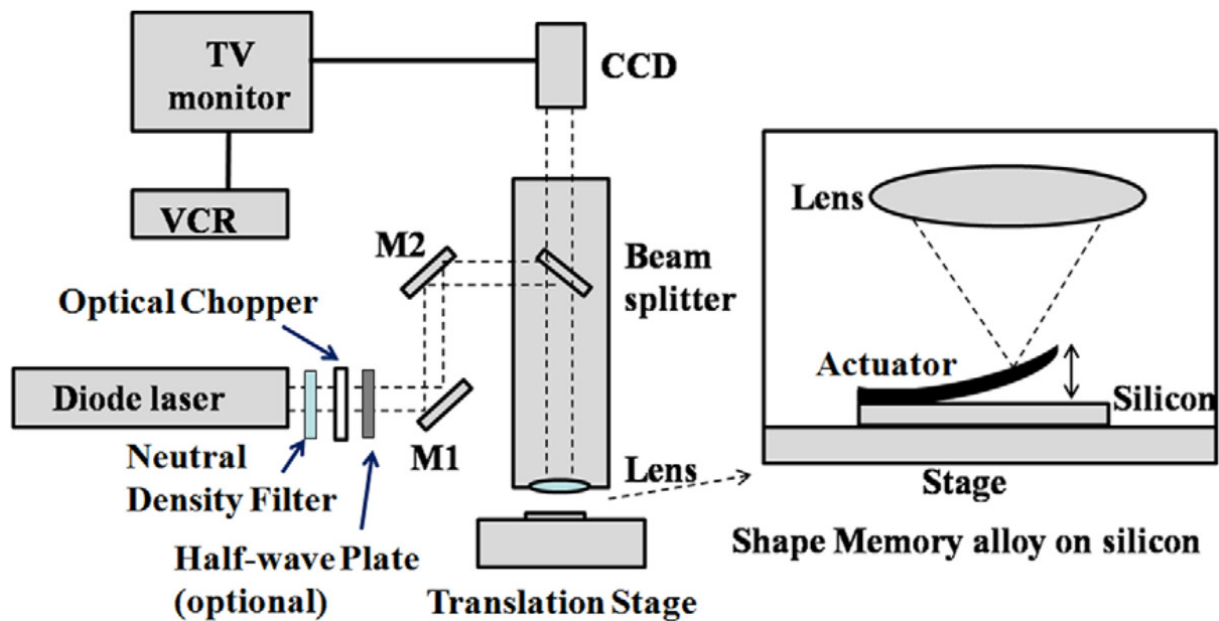


Figure 2.13 Experimental setup to demonstrate PIMA effect [2.2]

In order to study the PIMA effect in detail, thorough optical characterization of the FSMA samples were carried out using an elaborate experimental setup comprising of sophisticated microscope systems, different coloured diode lasers and other optical components. The main instrument used for the PIMA characterization of the samples was the optical microscope system. A Nikon made Eclipse Ti-U model dual deck inverted research microscope shown in Figure 2.14 along with its associated software was used for the PIMA measurements. The main microscope body was equipped with both left and right ports along with a bottom port for image acquisition purposes. The microscope system consists of a sextuple nosepiece for holding the objective lenses. The system has four objective lenses for different magnification levels. The first objective was a Plan Achromatic 4X lens with a working distance of 30 mm. The second one was a Plan Achromatic 10X lens with a working distance of 10.5 mm. The third objective was a Super Plan Fluor 40X lens with a working distance of 3.6 – 2.8 mm. The final objective used in the microscope system was a Super Plan Fluor 60X lens with a working distance of 2.61 – 1.79 mm. The system came with a 10X eyepiece having dioptr adjustment of FOV 22 mm as well as a 1.5X intermediate magnification changer. The microscope body consisted of both coarse and fine focus adjustment with focus

lock. The microscope system consisted of an x-y translating mechanical stage with an universal holder to accept all types of sample holders.

The main characteristic of the microscope system was its dual deck construction. Both the tiers of the microscope contained blank filter turrets for attaching mirrors or filters according to the requirements. Both the decks were equipped with stage height adjustment kit and back port unit having double lamp house adapter. One of the decks was used to attach the halogen lamp housing for illuminating the sample through the objective lenses. A 12 V, 100 W halogen lamp was used for the illumination purpose. The second deck of the microscope was used to simultaneously focus the laser beam onto the sample through the objective lenses along with the light source. Half mirrors were used in both the tiers of the dual deck structure for passing of light as well as laser in both directions to stimulate the sample as well as capture the image in the camera attached with the microscope for imaging purposes. The basic working principle of the dual deck microscope system is shown schematically in Figure 2.15. A 5 mega pixel high resolution CCD camera module was used for the image acquisition. The camera module had a sensitivity of ISO64 standard with a gain of 1 – 24X. It had binning modes of 2X2 and 4X4 with exposure control of 1/1000-60 sec and dynamic range of more than 60 db (1000:1). The camera module was capable of capturing 8/16 Bit images upto 37 FPS. The camera comprised of a C-mount 0.7X relay lens. The associated software used with the microscope system came with features like live image capture, video recording as well as auto measurement features of data like length, area, angle etc. of the captured images along with report generation facilities.



Figure 2.14 Nikon Eclipse Ti-U inverted research microscope

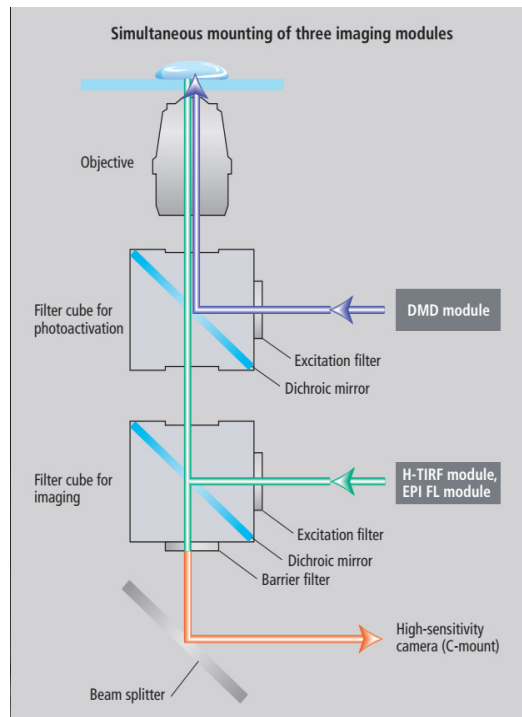


Figure 2.15 Working principle of dual deck microscope operation [2.23]

The PIMA properties of the FSMA samples were also characterized by another much simpler optical setup. This was done to compare and confirm the amplitude of actuation data obtained from the Nikon microscope system. Only then, this effect can be successfully implemented to effectively control any proposed microactuator system. Furthermore, the PIMA control mechanism should be operable even without an elaborate optical microscope system. Thus, this alternative measurement technique was employed. The sample was mounted on an electrically non-conducting x–y translation stage keeping one end of the sample free to allow for the laser induced actuation. This mounted sample was then illuminated by an external light source and placed under the objective lens of a SHODENSHA™ High Resolution 2-Megapixel USB Microscope in such a way that it directly faced the incoming laser beam. The associated software of the microscope was used to measure the microactuation data. The software recorded the actuation data at a scale of 1:10 i.e. the actual amplitudes of actuation of the samples were ten times the value obtained by the software which are reported in the subsequent chapters of this thesis. Other optical components required to control the PIMA effect were placed in the path of the incident laser beam and the whole experimental setup was then mounted on an optical breadboard as shown in Figure 2.16 [2.24]. Three different coloured partially polarized diode laser modules each having a nominal power output of 100mW were used to excite the FSMA ribbons. The wavelengths (λ) of the three lasers were 655 nm for the red, 532 nm for the green and 450 nm for the blue coloured laser respectively. The power output of the laser beams was controlled by using a continuously variable neutral density filter manufactured by Edmund Optics. The polarization of the output laser beams was controlled by a glass linear polarizer manufactured by Hoya which could be rotated a full 360°. A Stanford Research Systems Inc. made optical chopper with Model No. SR540 was used to study the response time of the PIMA effect of the samples [2.24].

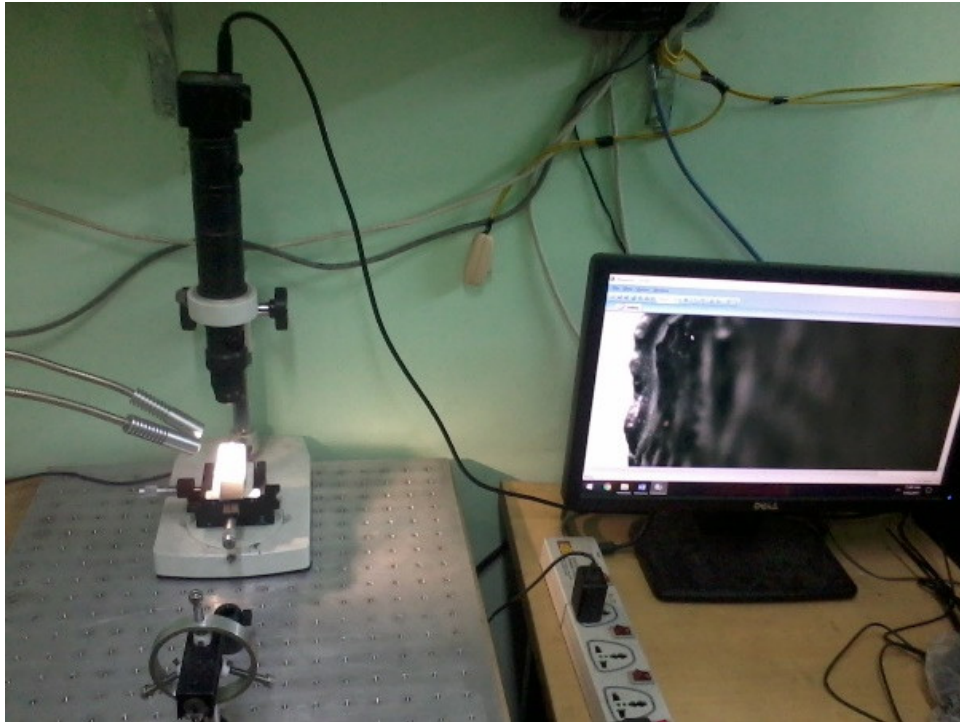


Figure 2.16 SHODENSHA USB Microscope setup [2.24]

2.7 Simulation techniques

2.7.1 Analysis of Variance (ANOVA)

An experiment is performed to observe and determine the causes of the changes occurring in the output response of a process with respect to the controlled changes made to the input signals [2.25]. In order to analyse the experimental data of the PIMA effect before actual implementation of the phenomenon in design and control of FSMA microactuator systems, basic Design of Experiments (DOE) analysis was performed on the PIMA data to find out the relations between response i.e. actuation of the sample with respect to various controlling factors. Thus, Analysis of Variance (ANOVA) studies was implemented on the PIMA experimental data to conclusively provide evidence in support of the relationship between the actuation of the sample and the various controlling factors. ANOVA is a statistical method to compare the fitting of two models [2.26]. While performing the ANOVA studies on the experimental data to prove the dependence of the PIMA property of the samples on the controlling factors, a

standard confidence level has to be selected which determine a standard significance level or alpha (α) value. This indicates the percentage risk of concluding that the response i.e. the microactuation of the sample is not dependent on the controlling factors i.e. the various parameters of the incident laser beam even when the response is dependent on the factors. If the obtained risk factor or 'P' value is less than the predetermined ' α ' value, it can be statistically proved that the obtained response is dependent on the controlling factors. There are certain prerequisite conditions that need to be validated before drawing conclusions from ANOVA analysis. The first condition that has to be validated is the normality assumption. It requires that the residuals be normally distributed. The second condition that has to be satisfied is that the residuals should be randomly distributed and have constant variance. The third condition that has to be satisfied to validate the ANOVA results is the independence condition i.e. the residuals should be independent of each other especially of time related effects. The ANOVA studies were conducted using standard commercial software.

2.7.2 Finite Element Analysis (FEA)

The perceived PIMA operated microactuators were first designed using the Finite element modelling (FEM) technique in standard commercial solid modelling software. The material of construction of the different parts of the microactuator were chosen accordingly in the software. As the FSMA materials are not available in the materials library of any FEM software, they were created in the software using the properties obtained earlier by mechanical characterizations performed on the alloys. This ensured that the physical and mechanical properties of the simulated model was same as that of the actual fabricated microactuator. Finite Element Analysis (FEA) of the developed model was then performed by simulation in the standard software. As the PIMA property is a newly discovered phenomenon, no FEA software is available which can simulate its effect on the designed FSMA microactuators. Thus, the FEA simulations were carried out using mechanical force on the designed models resulting in deflection and other physical and mechanical parameters. Based on the designs of the simulated models, the actual microactuators were then fabricated. Optical experiments were then performed on the fabricated microactuators following the procedures described

earlier. The deflection data obtained from the simulation was calibrated against the experimental PIMA data. Thus, the correlation between the force exerted by the focused laser beam on the FSMA microactuators can be inferred from the applied simulated force. In this way, the FEA studies help in the characterization of the PIMA effect and its potential applications.

CHAPTER 3: PHOTO INDUCED MICRO ACTUATION PROPERTY OF Co-Ni-AI FSMA

3.1 Introduction

In the year 2012 it was first observed that a Ferromagnetic Shape memory Alloy (FSMA) was showing a photo induced micro actuation (PIMA) effect when subjected to a focused laser beam [3.1]. Here, when a tiny spot of a focused laser beam, power about 20mW, was incident on the sample it immediately moved away, only to return to the original position as soon as the light was shut off. A lot of effort was given to fully understand the cause of this phenomenon. However, till now it is not understood what causes this effect. Nonetheless, this PIMA effect is a unique phenomenon and does not have any parallel with any hitherto known phenomenon. In this chapter, detailed experimental investigations were carried out to explore various characteristics of PIMA effect at room temperature. In order to understand and characterize this effect, a systematic study has been conducted. The first effort was to try to see if any other material would show this effect. Experiments were tried with pieces of paper, aluminium foil, thin sheets of iron, copper, various plastics etc. but it was never observed in any of them. It seems that somehow only some FSMA materials are endowed with this property.

Even with little understanding of the basic Physics behind this property, it is still possible to utilize this effect for practical use. For proper harnessing the use, the PIMA effect must be fully characterized. These are the main objectives of the work towards which, the present thesis was devoted to. FSMA materials have immense potential to be used as microactuators due to their ability to generate mechanical work under the influence of thermal or magnetic stimuli [3.2 – 3.6]. Other controlling mechanisms have also been studied and developed to achieve remote operation of the FSMA microactuators making the systems much more compact. One such mechanism was to supply the thermal cycling energy of the FSMA by light energy in the form of high powered laser beams as the heat source [3.7 – 3.10]. With the discovery of the PIMA effect a new method to effectively control the actuation mechanism of the microactuator systems can be proposed. In

the first ever report of the PIMA effect only a red coloured laser of wavelength (λ) 660 nm and power of 20 – 80 mW was studied [3.1]. In order to understand this effect in detail, investigations were carried out using three different coloured visible diode lasers viz. red, blue and green respectively. Systematic experiments were conducted with the help of various optical components in the presence of the three coloured lasers to study the microactuation effect. Thus, the effect of wavelength of light on the actuation phenomenon was studied. With the study of effect of colour on the microactuation effect an effective, new and unique controlling mechanism for the fabrication and operation of various microactuator systems can be proposed.

3.2 Compositional dependence of Photo Induced Micro Actuation effect

Ribbons of various compositions of Co-Ni-Al FSMAs were prepared by melt spinning bulk samples of the desired composition in an r. f. induction furnace. The sample preparation techniques are already given in detail in Sections 2.1.1 and 2.1.2 of this thesis. During the melt spinning process, the cooling rate was controlled to warrant the formation of both β and γ phases in the prepared alloys. This was done to introduce some ductility in the melt spun samples for use in practical applications. The different Co-Ni-Al ribbons were then cut keeping the dimensions of the samples same. Optical characterization of the different samples was then carried out as before [3.1]. The detailed methods are given in Section 2.6.1 of this thesis. These initial optical experiments were carried out on the different Co-Ni-Al compositions to find out the FSMA sample which showed the highest photo induced micro actuation (PIMA) effect. The samples that were prepared had compositions of $\text{Co}_{34}\text{Ni}_{35}\text{Al}_{31}$, $\text{Co}_{36}\text{Ni}_{36}\text{Al}_{28}$, $\text{Co}_{39}\text{Ni}_{34}\text{Al}_{27}$, $\text{Co}_{37}\text{Ni}_{34}\text{Al}_{29}$ in atomic weight percentage respectively. It was experimentally found out that a Co-Ni-Al sample having a composition of $\text{Co}_{34}\text{Ni}_{35}\text{Al}_{31}$ in atomic weight percentage showed the highest PIMA effect among all the selected Co-Ni-Al FSMA samples. Initial structural characterization of the $\text{Co}_{34}\text{Ni}_{35}\text{Al}_{31}$ sample by XRD analysis shown in Figure 3.1 confirms the presence of both β and γ phases in the prepared sample. As already told earlier, the β phase is responsible for the shape memory effect (SME) in the sample whereas the γ phase results in ductility of the prepared alloy. Therefore, the selected sample has suitable mechanical properties for use as

microactuators. Thus, this FSMA ribbon was chosen for carrying out the detailed studies to properly characterize the PIMA property shown by it. With the help of this detailed knowledge about the PIMA phenomenon, an effective, new and unique controlling mechanism for the fabrication and operation of various microactuator systems fabricated from the $\text{Co}_{34}\text{Ni}_{35}\text{Al}_{31}$ alloy have been proposed in Chapter 6 of the present thesis.

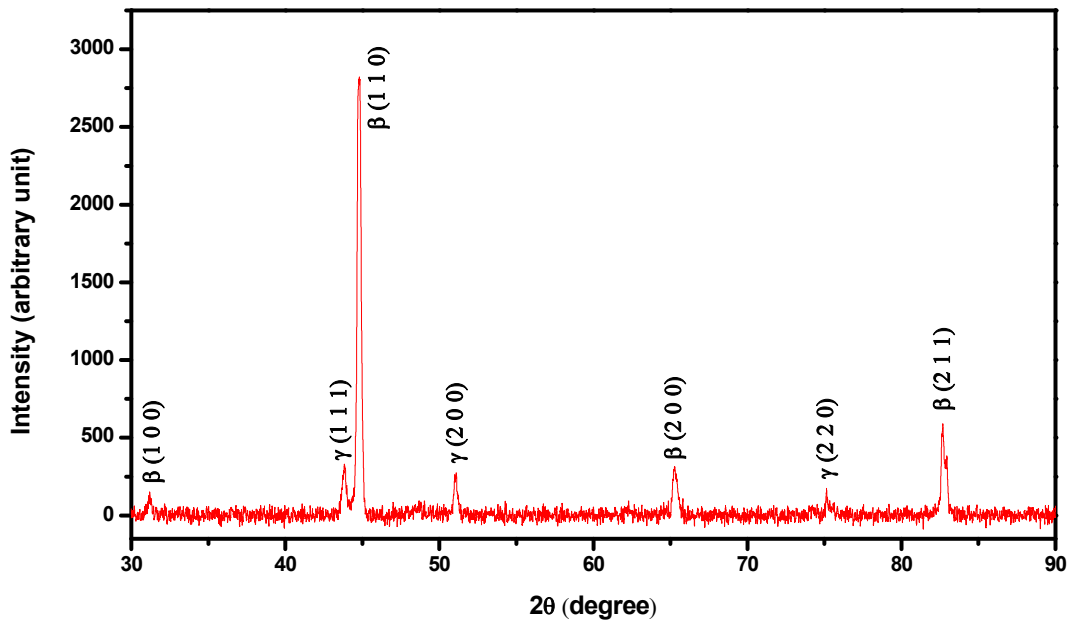


Figure 3.1 XRD analysis of $\text{Co}_{34}\text{Ni}_{35}\text{Al}_{31}$ ribbon sample

3.3 Colour dependence of Photo Induced Micro Actuation effect

The $\text{Co}_{34}\text{Ni}_{35}\text{Al}_{31}$ FSMA ribbon sample with thickness of 100 μm was cut to a dimension of 20 mm x 2.5 mm for conducting the optical experiments. One end of the sample was attached to an electrically non-conducting x-y translation stage while the other end was kept free to allow for the actuation. The sample was placed in such a way that it directly faced the incoming laser beam. An external light source was used to view the sample. The amplitude of actuation of the free end of the sample was measured using optical microscope system as described in Section 2.6.1 of this thesis. To observe the effect of colour of laser beam on the actuation phenomenon three different coloured diode lasers were used. The red laser had a wavelength (λ) of 655 nm with a nominal power of 100 mW. Similarly,

the blue laser had a λ of 450 nm and same 100 mW nominally. Finally, a green laser with λ of 532 nm and power of 100 mW was used to conduct the PIMA characterizations. It was found that all of them had no definite polarization in the output beams i.e. the as received diode laser modules were unpolarized. The first set of experiment that was done was to measure the actuation of the sample when the laser beam was directly focused onto the sample without using any optical component. The diode laser was rotated from 0° to 360° at an interval of 10° and the actuation of the sample was noted down using the software provided with the microscope. This experiment was repeated using all the three coloured lasers. During this experiment the power of all the lasers were reduced to and kept constant at 95 mW. This ensured that all incident powers were exactly the same.

The optical experiments showed that when the laser beam was focused on the sample, the sample deformed and moved away from the direction of the incident light ray. This deformation of the sample was very swift (in a few milliseconds) and was found for all the three coloured lasers used in the experiment. The ribbon sample held its new deformed position as long as the laser beam was kept on. As soon as the light source was cut off, the sample reverted to its original quiescent shape. This reversal in the shape of the sample was also found to be very quick. As it was reported earlier the PIMA effect of the FSMA sample was found to be fatigue resistant [3.1]. The PIMA effect of the selected FSMA ribbon in action against the blue, green and red lasers are shown in the Figure 3.2(a – c). Panel (i) of each of the three figures shows the sample at its rest position i.e. when it was not excited by any laser beam. The actuated or deformed sample in response to the incident laser beam is shown in panel (ii) of the three figures. The panel (iii) of the figures shows the sample when it returned to its initial resting position after the lasers were switched off. These figures were captured in real time using the optical microscope system and its associated software. The measurements taken by the provided software were at a scale of 1:10. Studies were then conducted to fully characterize this PIMA effect, so that this phenomenon can be controlled and successfully implemented in the fabrication and operation of suitable microactuator systems.

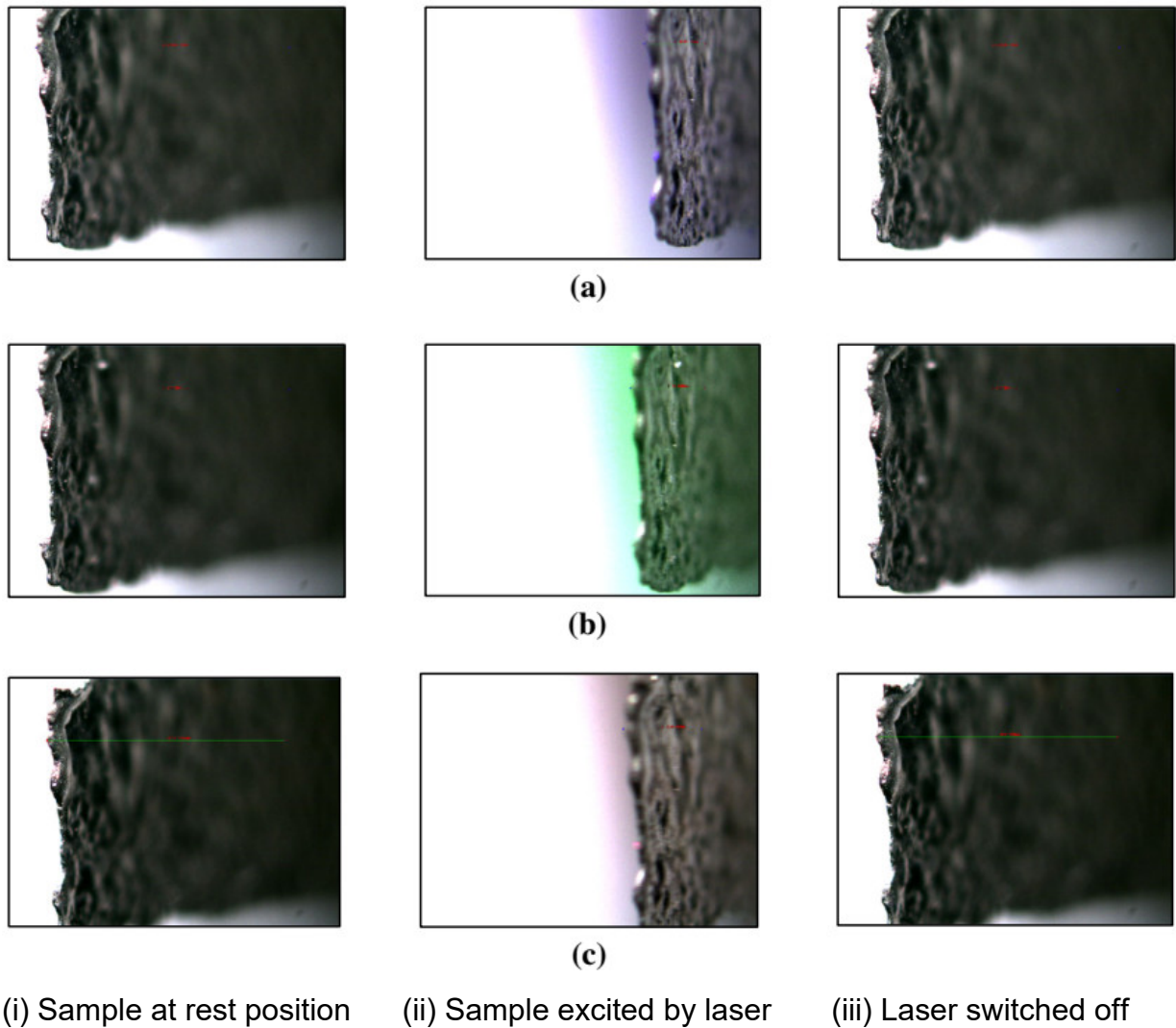


Figure 3.2 (a) PIMA effect of FSMA sample in presence of blue laser (b) green laser (c) red laser

The first study that was conducted to characterize the PIMA property of the FSMA sample was to measure the amplitude of actuation achieved by the sample when it was excited by the three different coloured laser beams. The amplitude of the actuation phenomenon found in the sample with respect to all the three as received diode lasers is graphically shown in Figure 3.3. Here the 0° was assumed randomly at the starting time and the laser was rotated at a fixed angle from it each time. The result shows that the actuation does not follow any predefined pattern and is not dependent on the angle of rotation of the unpolarized lasers. The variations are more than that are expected from random noise, so it indicates the partially polarized nature of the as received lasers, even if it is evident from the

data that colour of light does play an important role in the amplitude of actuation of the sample. The sample showed maximum actuation for the blue lasers whereas it showed minimum amplitude for the red coloured laser. Although the reason for the PIMA effect is not known, but somehow it seems that the photon energy ($h\nu$) [3.11, 3.12] was getting coupled to the actuation energy. This is very surprising, for there is no known analogy wherein this photonic energy ($h\nu$) can do a macroscopic work, generally this is manifested in quantum objects like photoelectric effect. PIMA effect may be the first macroscopic evidence for the effect in large objects. From analysing Figure 3.3, it can be said that the amplitude of actuation of the sample can be varied by simply using different coloured lasers as is evident from the marked wavelength dependence of actuation. However, it is quite evident that the amplitude of actuation of the sample cannot be fully controlled in this way. To effectively control the operation of any microactuator system, amplitude of actuation of the sample needs to be reliably controlled.

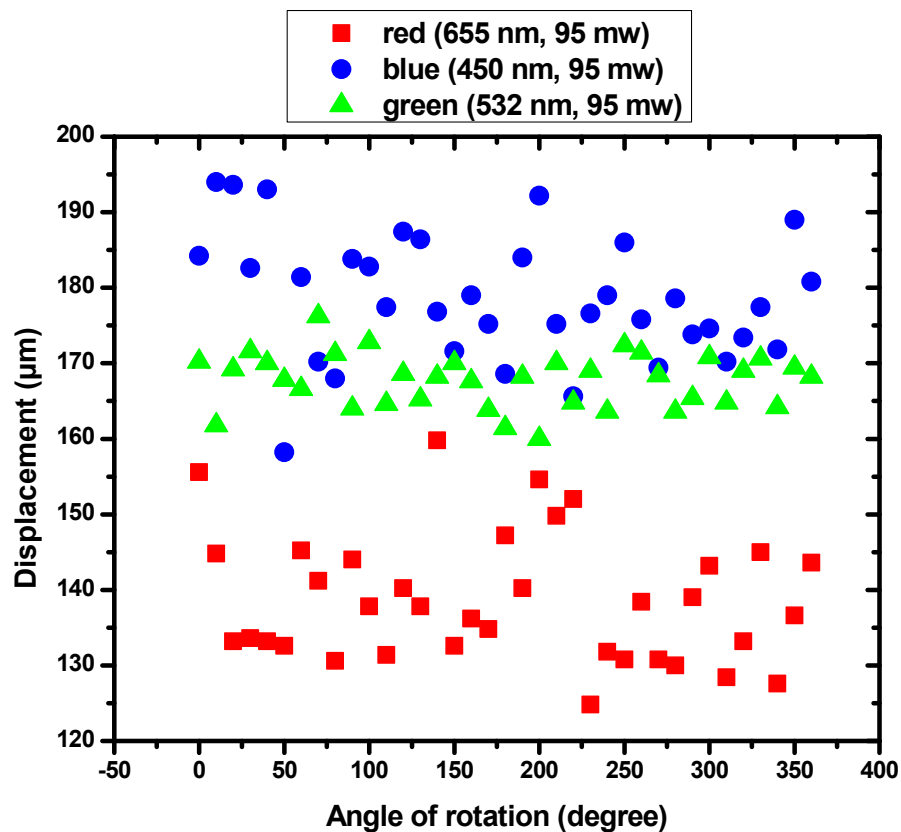


Figure 3.3 Microactuation of sample against unpolarized lasers

3.4 Control mechanisms of Photo Induced Micro Actuation effect

3.4.1 Laser power and wavelength dependent control mechanism

One of the important parameters of the different coloured diode lasers is the output power of the incident laser beam. The initial report on the PIMA effect had shown a linear dependence of the actuation of the FSMA ribbon sample on the power of the incident laser beam [3.1]. However, the report was based on the study of only a low power red coloured laser beam of wavelength 660 nm. The power dependence of the PIMA effect was measured in detail for all the three coloured laser beams viz. blue, green and red respectively. The laser diodes were fixed at the 0° position which was chosen randomly before studying the colour dependence of the PIMA effect. The laser power dependence of the micro actuation phenomenon was studied by placing a continuously variable neutral density filter in the path of the laser beam to vary the output power of the incident laser beam. The output power of the laser was varied from 5 mW upto its maximum value at an interval of 5 mW. The micro actuation data obtained are plotted in Figure 3.4. The analysis of the obtained data shows the linear relationship between power of all different coloured lasers and the micro actuation of the sample, up to the maximum laser power incident on the sample. The slopes of the linearly fitted blue, green and red lines of the Figure 3.4 are 1.97, 1.79 and 1.60 respectively, implying that the blue laser is far more effective (about 25%) in achieving PIMA effect. This observation is clearly consistent with the observation made in Figure 3.3 where the blue laser achieved more actuation than the green laser which in turn had more actuation of the alloy sample compared to the red coloured laser beam. Here also the effect of colour of laser plays an important role on the micro actuation phenomenon.

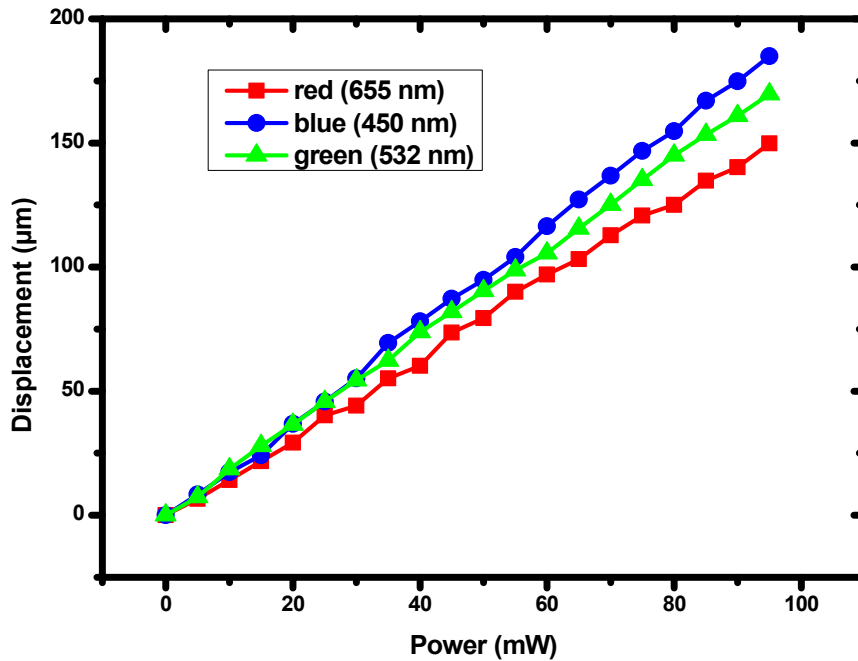


Figure 3.4 Laser power and colour dependence of PIMA effect

3.4.2 Laser polarization and wavelength dependent control mechanism

The laser power dependent control mechanism of the PIMA effect has been established in the previous section. In this regard it can be noted that the control mechanism of the PIMA effect will be much more effective if the polarization of the incident laser beams can also be controlled. To test the effect of polarization of the incident laser beam, studies were carried out using all the three coloured diode lasers. In order to investigate the effect of polarization of the laser beams, observations were carried out in the presence of a glass linear polarizer. During this experiment the linear polarizer was kept in the path of the incident laser beam and it was rotated from 0° to 360° at an interval of 10° . The angle of rotation of the polarizer was measured by the scale attached to it. The diode laser modules were kept fixed at a predetermined position. During these observations also, the output power of all the three lasers were kept at a constant 95 mW. The output power of the incident laser beams after passing through the linear polarizer was measured for all the polarization angles mentioned above. The output power was found to remain constant after passage through the polarizer in all polarization angles, although the power was reduced to approximately one third of the power rating of

the diode lasers. The data obtained are shown graphically in Figure 3.5. From the graph it can be seen that the maximum amplitude of the actuation of the sample have drastically reduced to one third when the linear polarizer was used as against the unpolarized laser beams. This is due to some inevitable absorption in the linear polarizer. From the figure it can be observed that much more controlled actuation of the FSMA sample can be achieved with the help of the linear polarizer. The effect of colour of the laser beam on the amplitude of actuation of the FSMA sample is also evident from the data obtained, with blue still giving more displacement than green which gave more than red. Most importantly, it can be seen that all the colours have exactly the same periodicity, and showed a dip at 90° and 270° , while the peaks were at 0° and 180° . This observation is as intriguing as the colour dependence of the PIMA effect. Thus, it can be inferred that the combination of laser colour and the polarization of the incident laser beam can also be implemented as a suitable control mechanism for the PIMA property of the FSMA ribbons to be used in the fabrication and operation of various perceived microactuator systems.

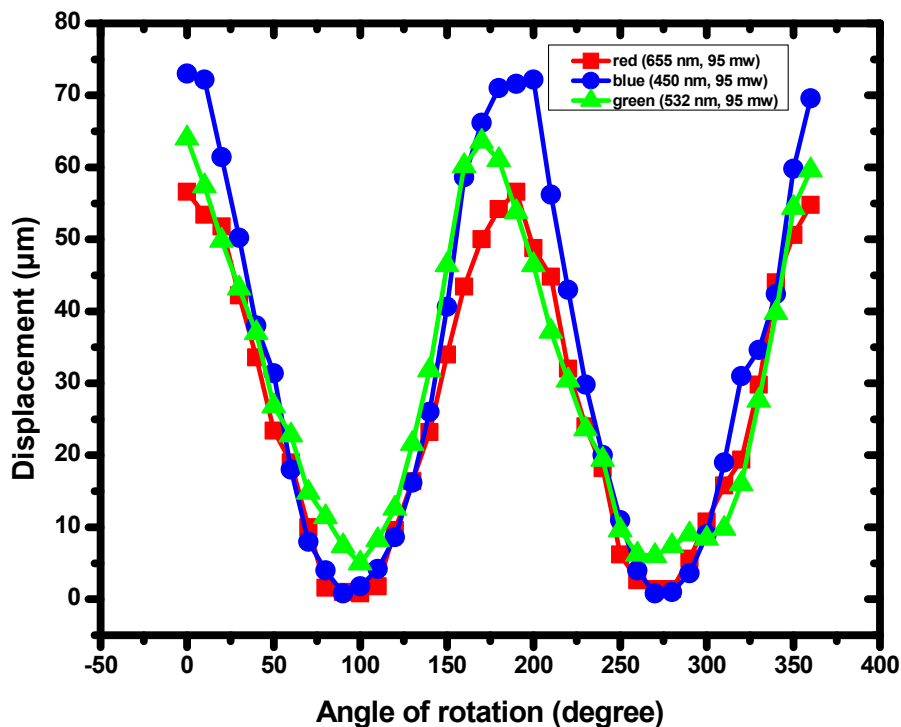


Figure 3.5 Laser polarization and colour dependence of PIMA effect

3.5 Response time of Photo Induced Micro Actuation effect

Optical experiments were conducted to study the response time of the deformation of the sample using an optical chopper for the three different coloured laser beams. The vibration amplitude of the ribbon sample at different chopping frequencies as well as the total deformation showed by the FSMA ribbon at different chopping frequencies in response to the colour of the laser beam were also measured. The effect of the optical chopper on the vibration amplitude of the sample when subjected to stimulation from the three differently coloured laser beams respectively is depicted graphically in Figure 3.6. It can be seen from the graph that the vibration amplitude of the sample along the direction of its actuation remained almost similar for all the three different coloured lasers. The vibration amplitude is solely dependent on the frequency of rotation of the optical chopper. At a frequency of 0 Hz or when there is no chopper present, the sample does not vibrate at all and remains in its deformed state as long as the laser is kept on. As the frequency of the optical chopper was kept on increasing, the vibration amplitude of the sample was seen to decrease until it completely stopped near 50 Hz and beyond. This vibration of the sample is a result of the constant on – off like operation of the optical chopper. There is a time required for the sample to physically respond fully to the incident beam as well as to revert back to its unexcited state, and if the on/off like operation of the optical chopper happens before that, the sample could not deform properly during that time.

The total actuation achieved by the FSMA sample with respect to its unexcited quiescent state is depicted graphically in Figure 3.7. As the frequency of the optical chopper was gradually increased the total deformation that the ribbon sample was able to achieve gradually decreased. Beyond a chopping frequency of 20Hz, the alloy had minimum excitation. Thus, from the Figures 3.6 and 3.7 it can be inferred that for a constant laser power, though the total amplitude of actuation achieved by the sample was related to the colour of laser used to excite it, the response time required by the sample to deform and come back to its original position is independent from the wavelength of the incident laser beam. Knowledge of this property of the sample will be useful when operating an actual FSMA microactuator system based on the PIMA effect.

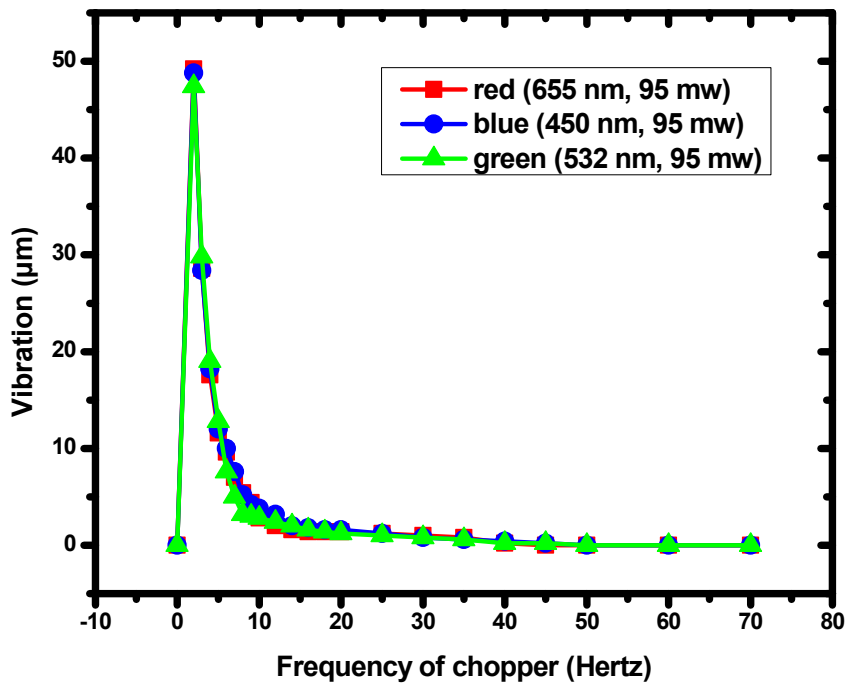


Figure 3.6 Vibration amplitude of the $\text{Co}_{34}\text{Ni}_{35}\text{Al}_{31}$ FSMA sample at different chopping frequencies

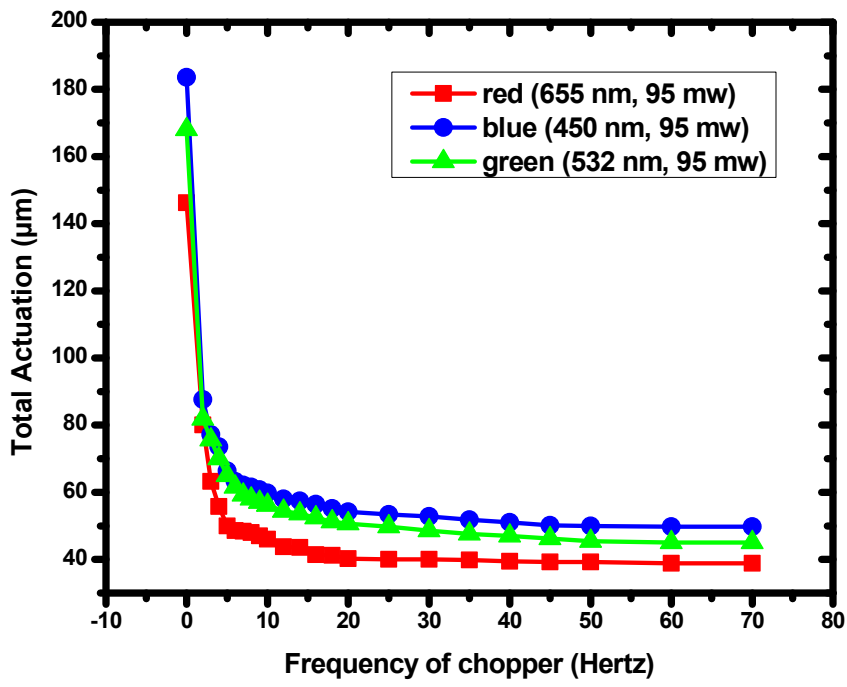


Figure 3.7 Total micro actuation of the $\text{Co}_{34}\text{Ni}_{35}\text{Al}_{31}$ FSMA sample at different chopping frequencies

3.6 Statistical analysis of experimental data

3.6.1 Introduction to Design of Experiments

From the experimental data shown in the above sections, it can be presumably inferred that the photo induced micro actuation (PIMA) property of the $\text{Co}_{34}\text{Ni}_{35}\text{Al}_{31}$ FSMA ribbon sample is dependent on various factors. To implement this property of the sample to actually fabricate and operate any perceived microactuator system, analysis of the results of the optical experiments is needed to be done in detail. Then only it can be concluded which controlling mechanism can be suitably used to operate any proposed microactuator system. Thus, basic “Design of Experiments” (DOE) analysis [3.13, 3.14] was performed on the optical experimental data to find out the relationships between response i.e. actuation of the ribbon sample with respect to various controlling factors. Thus, “Analysis of Variance” i.e. ANOVA studies was chosen to be implemented on the experimental data.

3.6.2 One way ANOVA studies on unpolarized laser data

In the optical experiments performed, the actuation shown by the FSMA ribbon sample due to the PIMA property of the sample was dependent on the various factors of the incident laser beams which were used to excite the sample. Firstly, one way ANOVA study was performed on the unpolarized laser data. This is due to the fact that the only difference between the three lasers used was their colours as all of them had the same output power and no other optical component was used to control the amplitude of actuation of the sample. So, the output response or the PIMA effect that was shown by the sample was only dependent on one controlling factor i.e. the colour of the laser used. While performing the one way ANOVA study, displacement or actuation of the sample was selected as the response against laser colour as the factor. The standard confidence level of 95% was selected which means the significance level or alpha (α) value was set to 0.05. This indicates that there is a 5% risk of concluding that response is not dependent on the factor even if it depends on it. The results obtained are shown in Table 3.1.

One-way ANOVA: Displacement versus Laser Colour					
Source	DF	SS	MS	F	P
Laser Colour	2	31462.3	15731.1	306.55	0.000
Error	108	5542.1	51.3		
Total	110	37004.4			
S = 7.164 R-Sq = 85.02% R-Sq(adj) = 84.75%					

Table 3.1 One way ANOVA analysis of unpolarized laser data

The 'P' value (0.000) obtained from the analysis is less than the predetermined ' α ' value (0.05). This proves that the laser colour has statistically significant effect on the level of actuation of the sample. But this data analysis does not determine which data falls under which group. To convincingly prove that the actuation obtained in the sample is significantly different for each laser colour used, Tukey Grouping Information Method was implemented on the data analysis [3.15]. The results obtained are shown in Table 3.2. From the analysis of the obtained data it can be concluded that the actuation obtained in the sample by using three different coloured lasers is significantly different. This signifies that on an average the different coloured laser beams though having the same output power produced different levels of actuation in the sample. This can also be proved by looking at the boxplot of the obtained data shown graphically in Figure 3.8. The effect of the controlling factor i.e. the laser colour in this case on the response i.e. displacement or actuation of the sample can be displayed by using the boxplot of the data. The graph shows that actuation of the sample due its PIMA property increases when the colour of the incident laser beam was changed from red to green to blue respectively.

Grouping Information Using Tukey Method			
Laser Colour	N	Mean (μm)	Grouping
Blue	37	178.584	A
Green	37	167.692	B
Red	37	138.692	C
Means that do not share a letter are significantly different.			
Tukey 95% Simultaneous Confidence Intervals			
All Pairwise Comparisons among Levels of Laser Colour			
Individual confidence level = 98.07%			

Table 3.2 Grouping analysis of unpolarized laser data using Tukey method

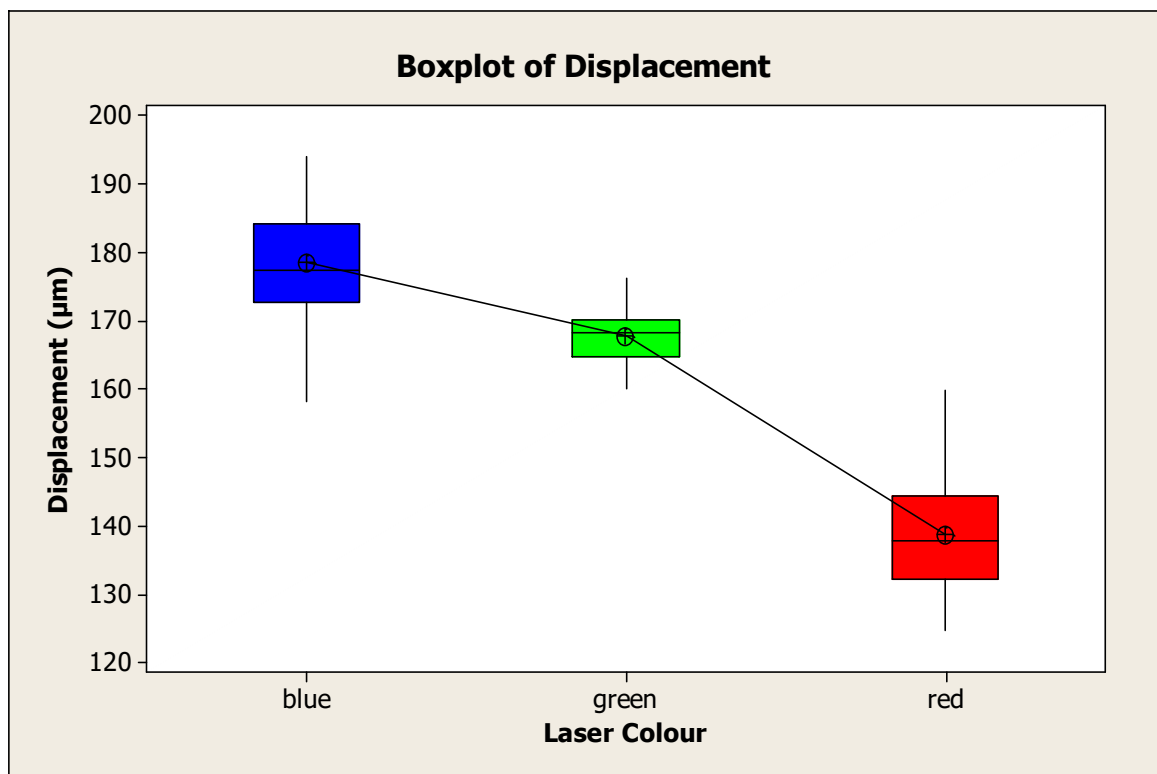


Figure 3.8 Boxplot of displacement for unpolarized laser data

ANOVA makes certain assumptions before analysing any data. If those assumptions can be validated it can definitely be proved that the conclusions that were drawn from the ANOVA results are true [3.13, 3.14]. ANOVA requires that the

residuals be normally distributed. The normplot of the residuals for the displacement of the sample is shown graphically in Figure 3.9. The straight line obtained from the plot signifies that the residuals are normally distributed. Thus, the normality assumption of the ANOVA analysis is validated for the unpolarized laser data. The second assumption that ANOVA makes is that the residuals are randomly distributed and have constant variance. The residuals vs fits plot shown in Figure 3.10 validates this assumption as it can be seen that there is no recognizable pattern in the graph with the points randomly falling on both sides of zero. The third assumption that ANOVA makes is independence i.e. the residuals are independent from one another. Here also the random nature of the graph shown in Figure 3.11 signifies that the residuals are independent of each other especially of time related effects. Thus, the order of data collection does not play any part in determining the response. Hence, it has been conclusively proved by statistical analysis of the experimental data that different levels of PIMA effect can be achieved by just varying the colour of the incident laser beam.

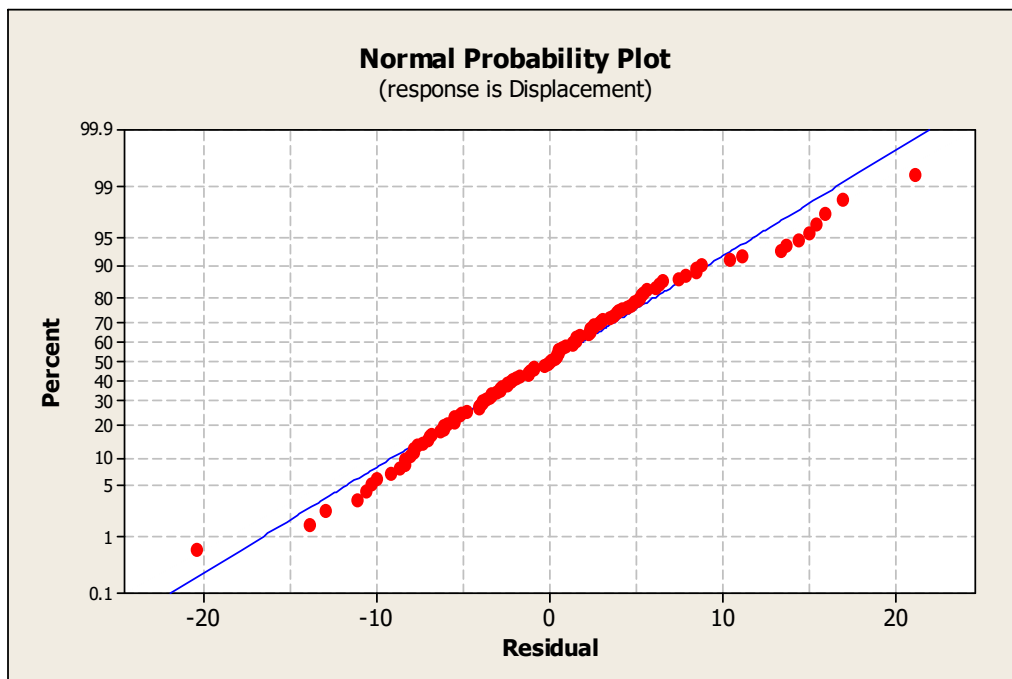


Figure 3.9 Normplot of Residuals for displacement for unpolarized laser data

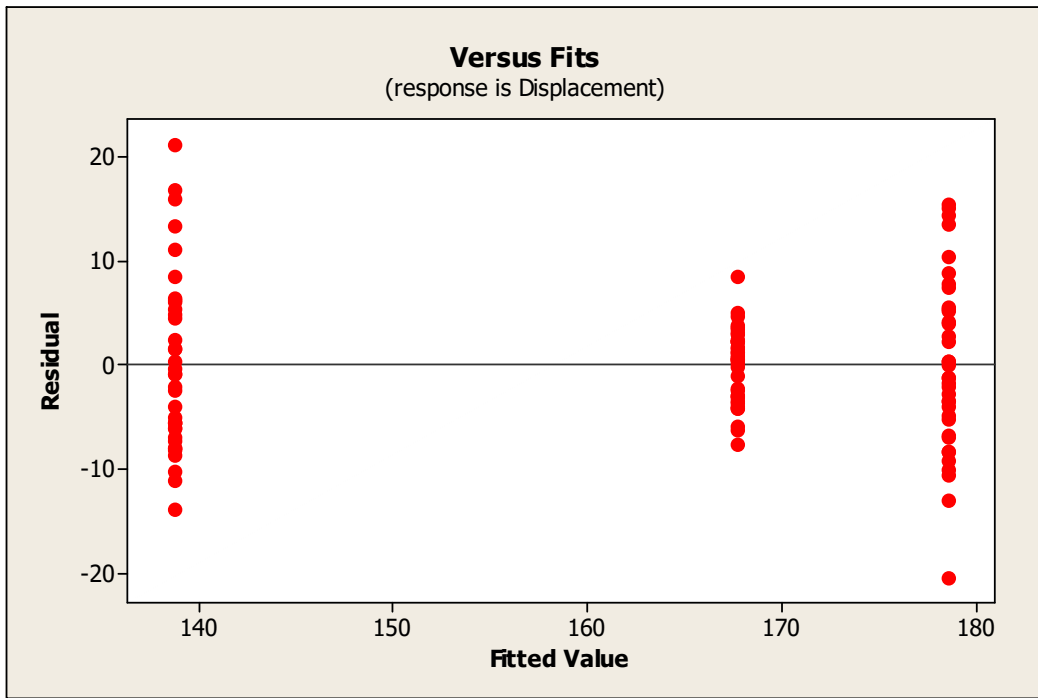


Figure 3.10 Residuals vs Fits for displacement for unpolarized laser data

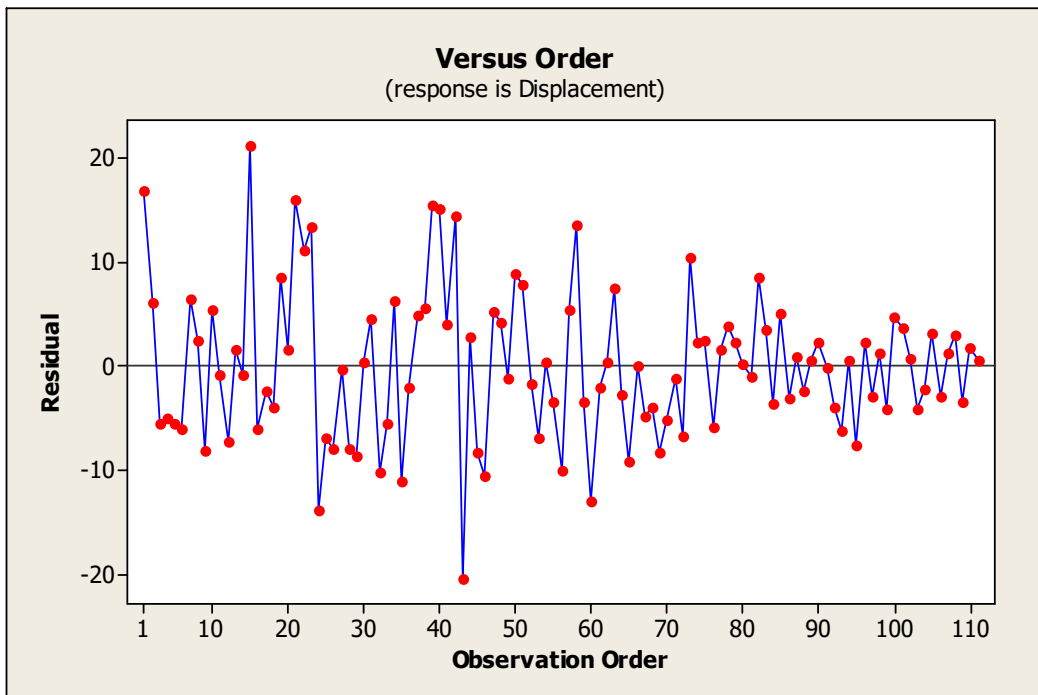


Figure 3.11 Residuals vs Order for displacement for unpolarized laser data

3.6.3 Two way ANOVA studies on laser power data

Once it has been conclusively proved by statistical analysis that the degree of the PIMA effect exhibited by the FSMA ribbon sample can be altered by just varying the colour of the incident laser beam, analysis of the effects of various optical components on the microactuation phenomenon can be done in order to provide evidence in support of the claim to achieve control over the amplitude of the PIMA effect. This will pave the way to propose an effective control mechanism for use in future microactuator systems. Two way ANOVA analysis have been used on the next experimental data sets as the PIMA effect found was in response to two controlling factors viz. the colour of the laser beam as well as the optical component used to control the effect. When applying the two way ANOVA study on the power dependence of the PIMA effect the colour of the laser beam and the output power of the laser were selected as the two factors which controls the response that is the actuation or displacement of the sample. The results obtained are shown in Table 3.3.

Two-way ANOVA: Displacement versus Colour, Power					
Source	DF	SS	MS	F	P
Colour	2	2822	1410.95	42.61	0.000
Power	19	159644	8402.33	253.74	0.000
Error	38	1258	33.11		
Total	59	163725			
S = 5.754 R-Sq = 99.23% R-Sq(adj) = 98.81%					

Table 3.3 Two way ANOVA analysis of laser power data

The result clearly shows that ‘P’ value is less than the ‘ α ’ value for both the controlling factors i.e. colour and power of laser respectively. Hence it can be inferred that the actuation achieved by the sample is dependent on both the controlling factors. The correlation between the actuation or displacement of the sample with the two controlling factors viz. colour and output power of the incident laser beam is shown graphically in Figure 3.12. Thus, by controlling these two

factors together, significant variations in the actuation amplitude of the sample can be achieved and hence it proves to be an effective control mechanism to be deployed in future microactuator systems.

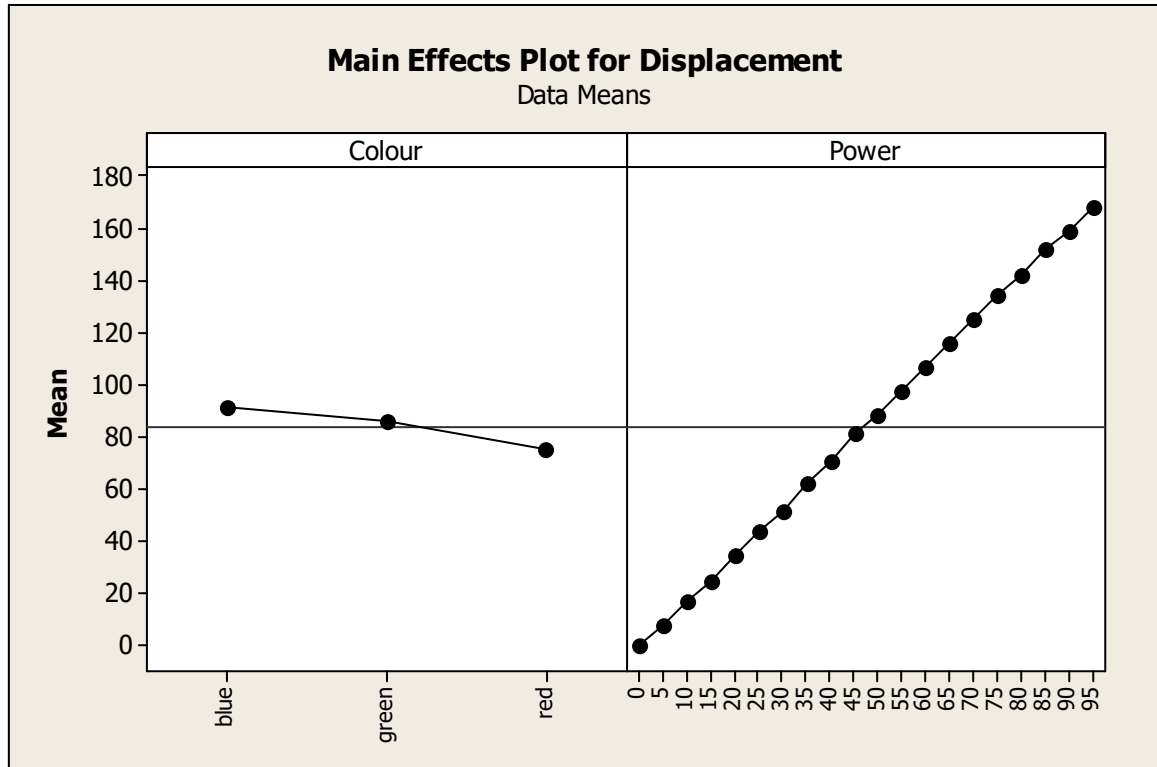


Figure 3.12 Main Effects plot for laser power data

The assumptions made by ANOVA were validated by following the earlier guidelines discussed in Section 3.6.2. The results of the normal distribution validation of the ANOVA study conducted on the laser power data are shown graphically in Figure 3.13. Similarly, the results of the random distribution validation and the independence validation of the ANOVA study on the laser power experimental data are depicted in Figure 3.14 and Figure 3.15 respectively.

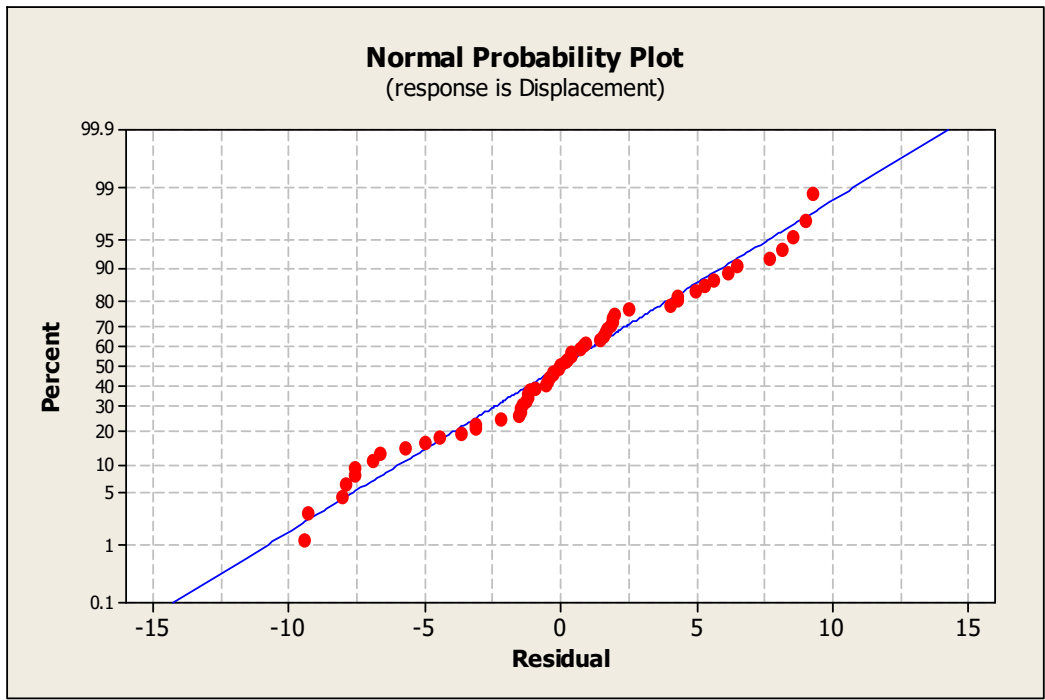


Figure 3.13 Normplot of Residuals for displacement for laser power data

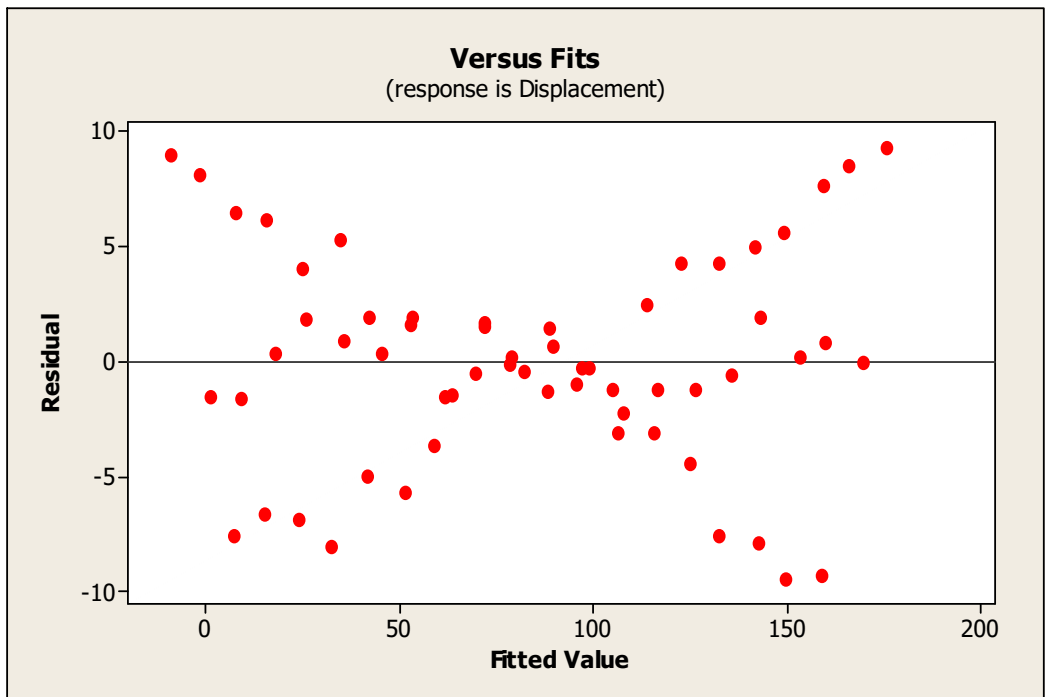


Figure 3.14 Residuals vs Fits for displacement for laser power data

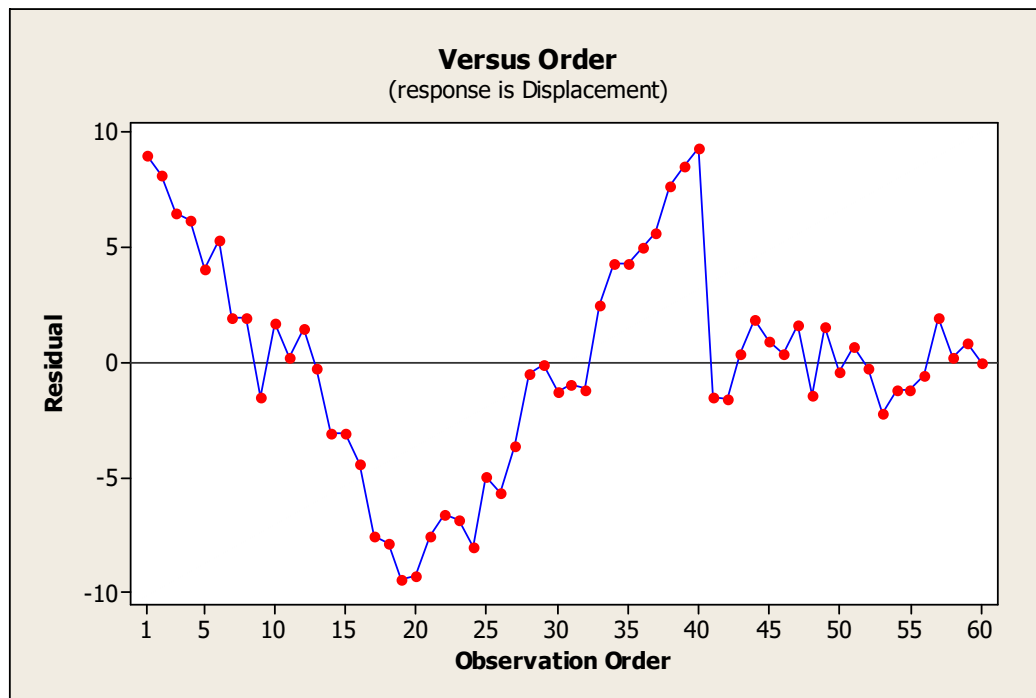


Figure 3.15 Residuals vs Order for displacement for laser power data

3.6.4 Two way ANOVA studies on laser polarization data

Another control mechanism that was proposed for operating any perceived microactuator system in the near future was by controlling the polarization of the incident laser beams. Hence, two way ANOVA study was applied to the linear polarizer data assuming the colour of the laser and the polarization angles as the two controlling factors while the actuation or displacement of the sample was considered as the response. The obtained results are depicted in Table 3.4. Here also, analysing the 'P' value of the ANOVA calculations it can be said without any doubt that the actuation phenomenon of the sample is very much dependent on both the controlling factors i.e. colour of laser as well as polarization angle of the incident beam. The relationship between the response i.e. actuation of the sample and the two controlling factors is shown graphically in Figure 3.16. Thus, another mechanism to effectively control and apply the PIMA effect to operate any suitable FSMA microactuator design has been successfully proposed.

Two-way ANOVA: Displacement versus Colour, Angle of rotation					
Source	DF	SS	MS	F	P
Colour	2	752.7	376.34	14.86	0.000
Angle of rotation	36	50927.5	1414.65	55.87	0.000
Error	72	1823.1	25.32		
Total	110	53503.3			

S = 5.032 R-Sq = 96.59% R-Sq(adj) = 94.79%

Table 3.4 Two way ANOVA analysis of laser polarization data

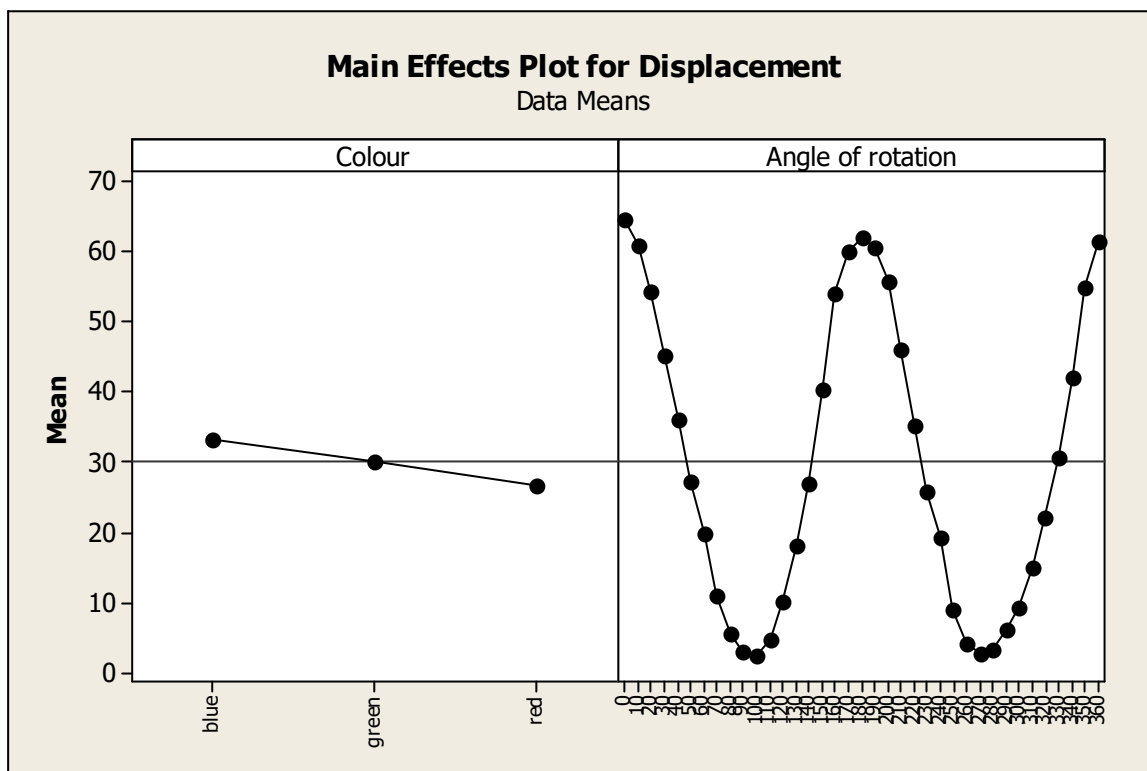


Figure 3.16 Main Effects plot for laser polarization data

The assumptions made by ANOVA were again validated and the results are shown in Figures 3.17, 3.18 and 3.19 respectively.

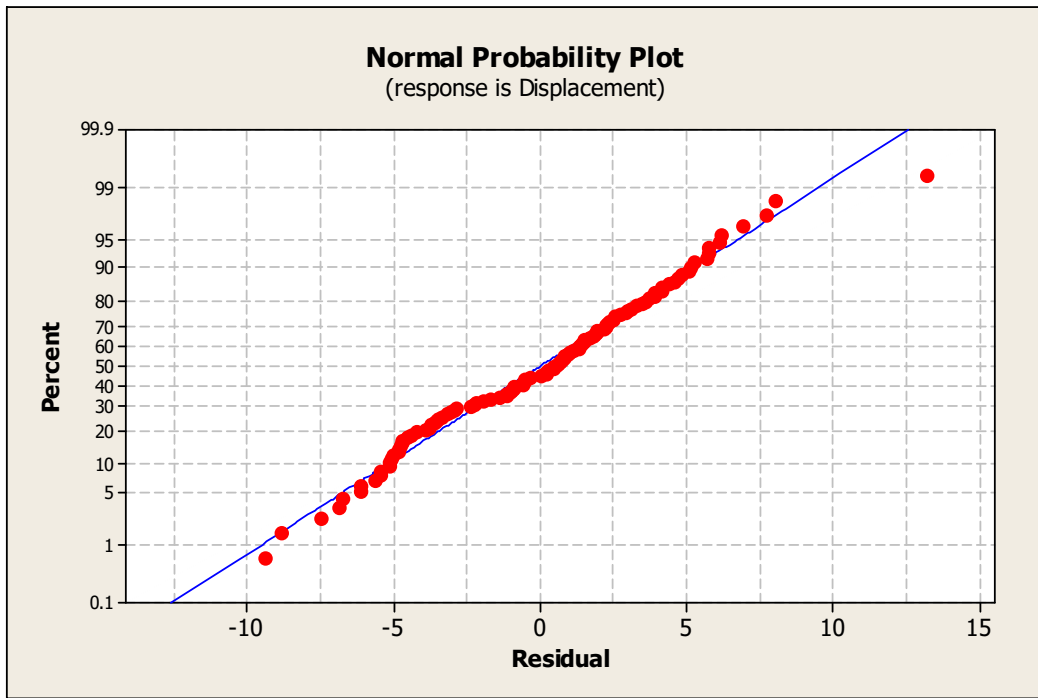


Figure 3.17 Normplot of Residuals for displacement for laser polarization data

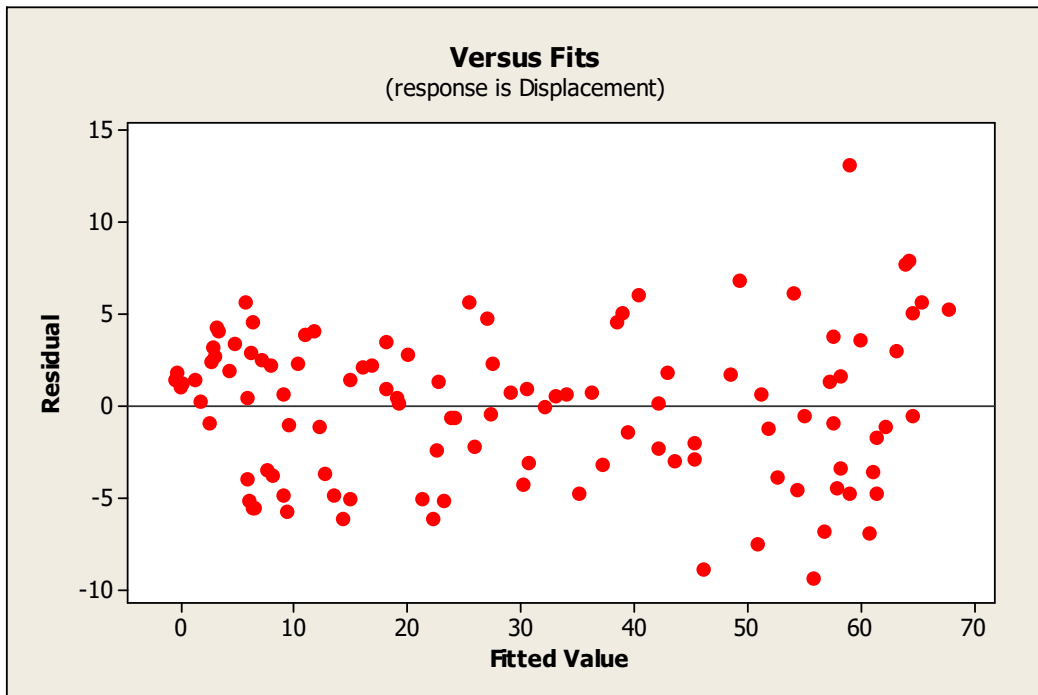


Figure 3.18 Residuals vs Fits for displacement for laser polarization data

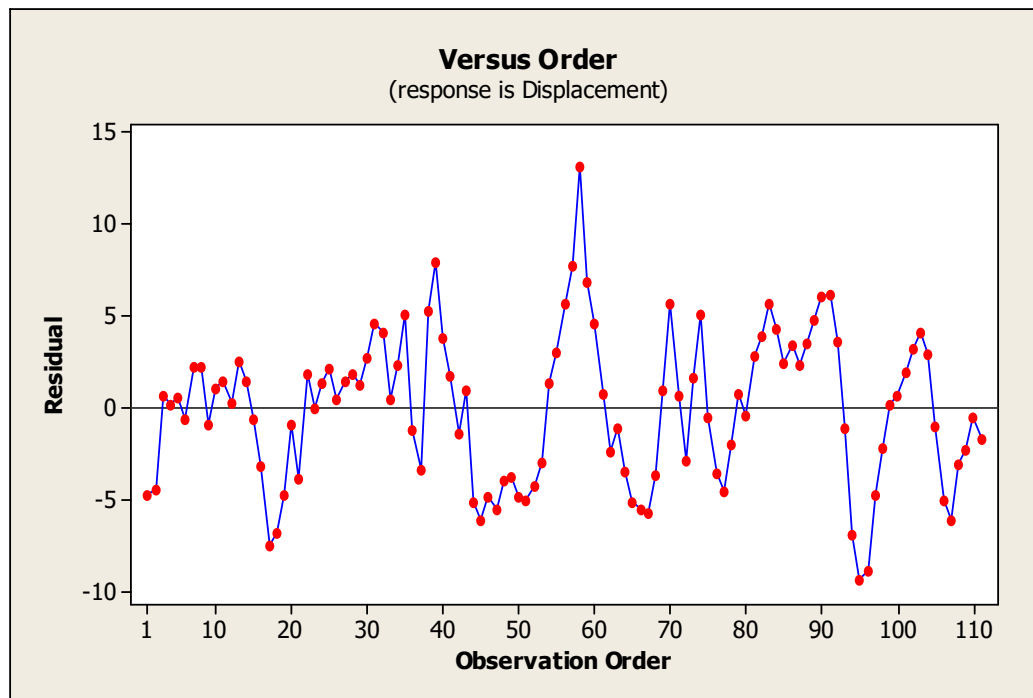


Figure 3.19 Residuals vs Order for displacement for laser polarization data

3.6.5 Two way ANOVA studies on sample response time data

Finally, the effect of the optical chopper on the actuation of the sample was analysed. Here, colour of the incident laser beam and frequency of the optical chopper were considered as the two controlling factors. In this analysis two different responses were taken into consideration viz. total actuation as well as the vibration amplitude of the FSMA ribbon. The results of the two way ANOVA analysis of the optical experimental data are shown in Tables 3.5 and 3.6 respectively. Looking at the total actuation data of the sample in presence of the optical chopper from Table 3.5, it can be inferred that both laser colour and frequency of chopper can be considered as an effective control mechanism for the PIMA effect as again the 'P' value is well within the significance level or ' α ' value. But on further analysis of the vibration data from Table 3.6, it can be seen that control of the actuation mechanism of the sample cannot be definitely achieved as the vibration patterns of the sample cannot be differentiated by controlling the colour of the laser beam. This is evident from the fact that here the obtained 'P' value is larger than the selected standard ' α ' value. Further it can be said that as the sample is vibrating in presence of the optical chopper it will not be suitable to

apply this control mechanism to any microactuator system. The actuator will not be able to perform to its maximum potential as it will be vibrating and it is very difficult to control this vibration. If any special purpose microactuator is designed where the actuator is supposed to vibrate then only this design option can be considered. Otherwise it is not feasible to consider this control mechanism for further study.

Two-way ANOVA: Displacement versus Colour, Frequency					
Source	DF	SS	MS	F	P
Colour	2	2460.0	1229.98	141.45	0.000
Frequency	22	42296.7	1922.58	221.10	0.000
Error	44	382.6	8.70		
Total	68	45139.2			
S = 2.949 R-Sq = 99.15% R-Sq(adj) = 98.69%					

Table 3.5 Two way ANOVA analysis of chopper total actuation data

Two-way ANOVA: Vibration versus Colour, Frequency					
Source	DF	SS	MS	F	P
Colour	2	2.01	1.004	2.83	0.070
Frequency	22	8755.00	397.955	1121.10	0.000
Error	44	15.62	0.355		
Total	68	8772.63			
S = 0.5958 R-Sq = 99.82% R-Sq(adj) = 99.72%					

Table 3.6 Two way ANOVA analysis of chopper vibration data

3.7 Structural characterization of Co₃₄Ni₃₅Al₃₁ FSMA

Since, it has already been reported in Chapter 1 of this thesis that somehow only FSMA materials are endowed with the photo induced micro actuation (PIMA) property, efforts were undertaken to find out the cause of this unique effect. As a result, studies were conducted to characterize the microstructure of the Co₃₄Ni₃₅Al₃₁ FSMA ribbon in order to find a correlation between the ferromagnetic

shape memory effect (FSME) and the PIMA effect of the $\text{Co}_{34}\text{Ni}_{35}\text{Al}_{31}$ ribbon sample [3.16]. Transmission Electron Microscopy (TEM) was used to characterize the microstructure of the melt spun FSMA ribbon samples.

A bright field TEM image of the ribbon sample is shown in Figure 3.20. The selected area diffraction patterns from the region marked as 'S' in Figure 3.20 are shown in Figure 3.21(a-b). These patterns can be indexed as $[01\bar{1}]$ and $[001]$ zone axis of ordered solid solution of the BCC grain with B2 type ordering. The fundamental reflection (h k l) planes are indicated in red and superlattice ones in yellow respectively. Moreover, the selected area diffraction patterns taken from the continuous matrix channel also confirms the $L1_2$ ordering of the cobalt rich matrix. The corresponding diffraction pattern taken along the $[100]$ zone axis of the FCC matrix is presented in Figure 3.22(a). To achieve strong diffraction contrast in the dark field image, the 2 beam imaging technique was adopted by taking direct beam (000) and (011) plane in the 2 beam imaging condition from the selected area diffraction pattern along the $[100]$ zone axis of the FCC matrix. A high magnification TEM dark field image of the continuous matrix as marked by the red box in Figure 3.20 formed by the (011) plane of $L1_2$ ordered super lattice spots in 2 beam condition, is also shown in Figure 3.22(b), revealing the presence of $L1_2$ ordered domains inside the matrix. Thus, microstructural studies confirm the existence of B2 ordered micron sized grains embedded in $L1_2$ ordered matrix channel. This B2 ordered phase is the key responsible and active phase for ferromagnetic shape memory response whereas the $L1_2$ ordered FCC matrix only imparts the ductility into the alloy.

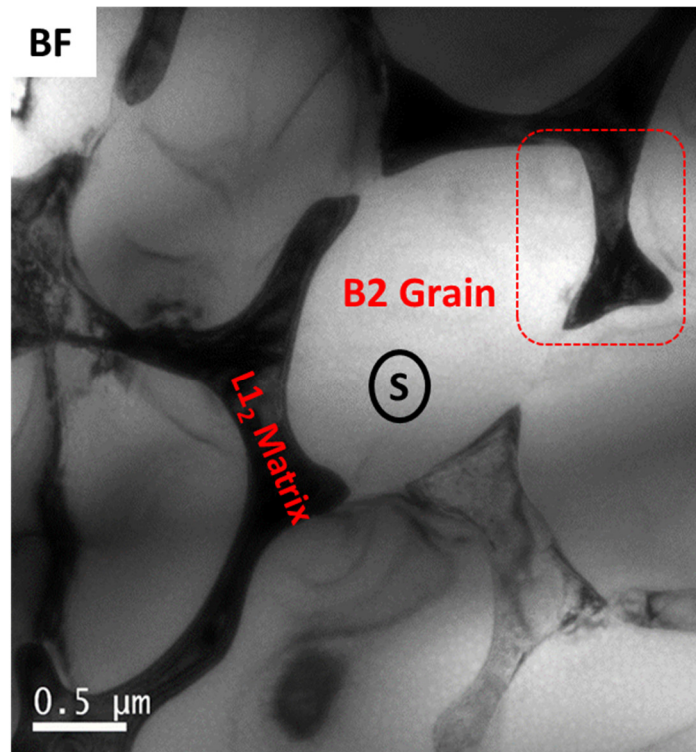


Figure 3.20 Bright field TEM image showing the existence of B2 ordered grain and L₁₂ ordered matrix channel in the $\text{Co}_{34}\text{Ni}_{35}\text{Al}_{31}$ sample

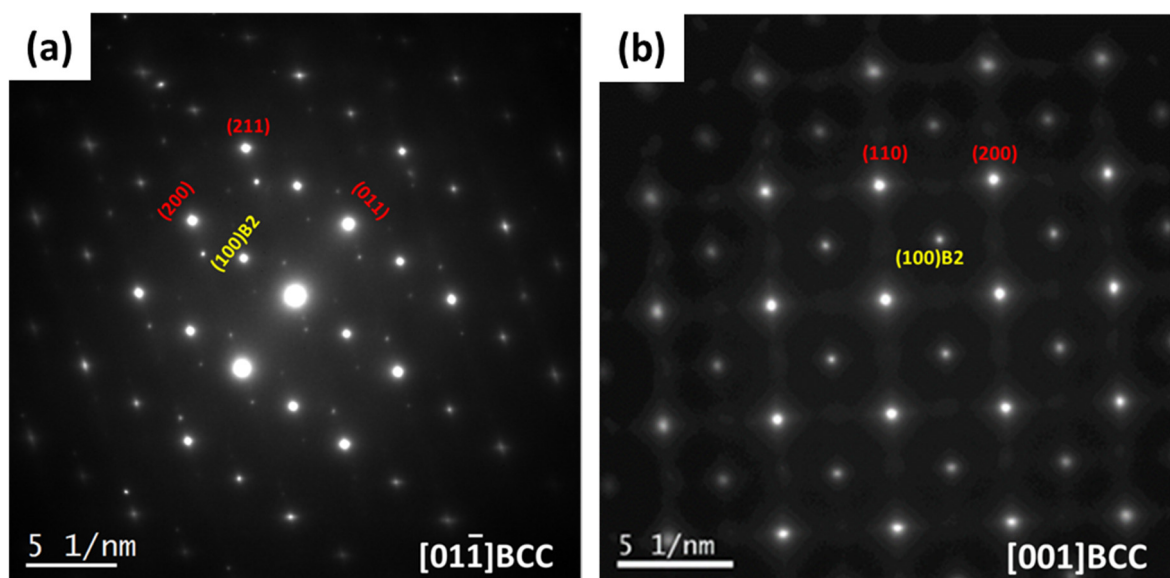


Figure 3.21 (a – b) Selected area diffraction patterns taken along the $[01\bar{1}]$ and $[001]$ zone axis of the BCC grain

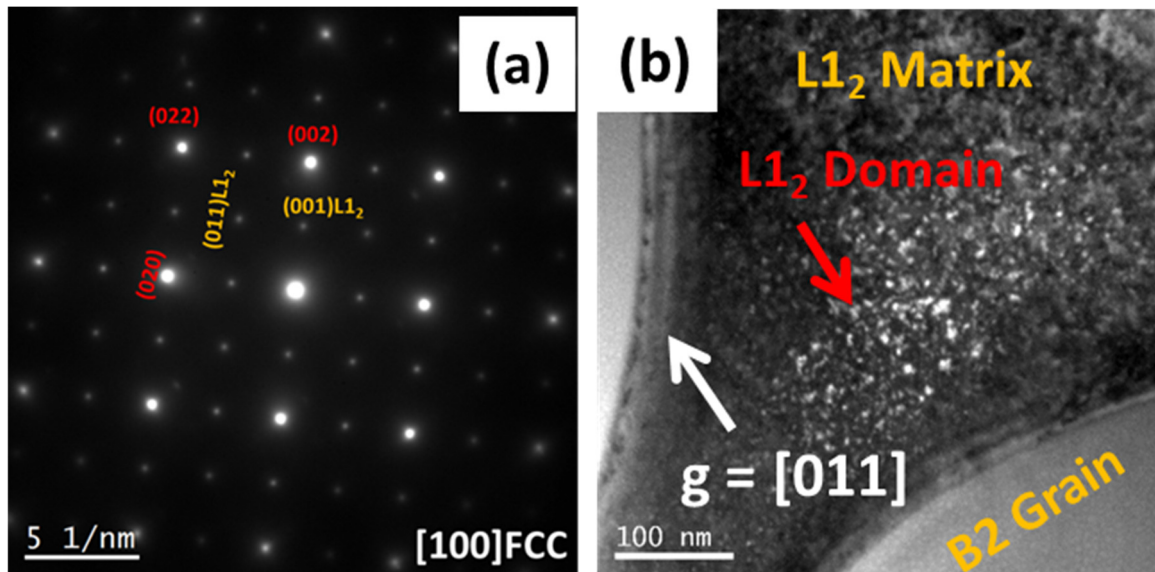


Figure 3.22 (a) Selected area diffraction pattern taken along the [100] zone axis of FCC matrix channel (b) Dark field image of the red dotted box marked area of Figure 3.20

Scanning transmission electron microscopy – high angle annular dark field (STEM – HAADF) image analysis provides the atomic number contrast of the constituent phases of the melt spun sample. The STEM – HAADF image of the $\text{Co}_{34}\text{Ni}_{35}\text{Al}_{31}$ ribbon sample is depicted in Figure 3.23. From the figure, the existence of sub micron sized grains with darker contrast embedded in the lighter contrast matrix channel can be seen. The obtained STEM – HAADF image shows that the darker contrast sub micron sized grain is the B2 grain or the β phase of the FSMA ribbon giving rise to the FSME. Similarly, the lighter contrast matrix channel is the L_{12} or the γ phase resulting in the ductility in the selected FSMA system. The scanning transmission electron microscopy – energy dispersive spectroscopy (STEM – EDS) spectrum image elemental mappings shown in Figure 3.24(a-c) demonstrate the spatial elemental distribution of the constituent elements of the alloy in the evolved microstructure. These mapping images qualitatively indicate that the grains embedded in the matrix and also within the channel and having dark appearance in the STEM – HAADF image of Figure 3.23 are rich in nickel and aluminium whereas the matrix phase, appearing brighter in the same image is rich in cobalt. Figure 3.24(a) indicates the existence of cobalt in lower concentration inside the grains whereas, Figures 3.24(b) and 3.24(c) also confirm the presence of

nickel and aluminium in the matrix relatively in lower concentrations as compared to that of cobalt in the matrix. A STEM – EDS line composition profile is also shown in Figure 3.25 and it depicts the distribution of the elements along the red dotted line 'AB' as labelled in Figure 3.24(a). The point composition analysis results obtained by TEM-EDS for both the darker grain and the lighter matrix channel are shown in Table 3.7. It can be clearly observed from the data that the mid band is rich in cobalt and two adjacent grains have comparable Co-Ni and constant aluminium composition. This knowledge about the microstructure of the $\text{Co}_{34}\text{Ni}_{35}\text{Al}_{31}$ alloy will be useful when the correlation between the evolution of microstructure of the ribbon sample and the PIMA effect are reported in detail in the next chapters [3.16].

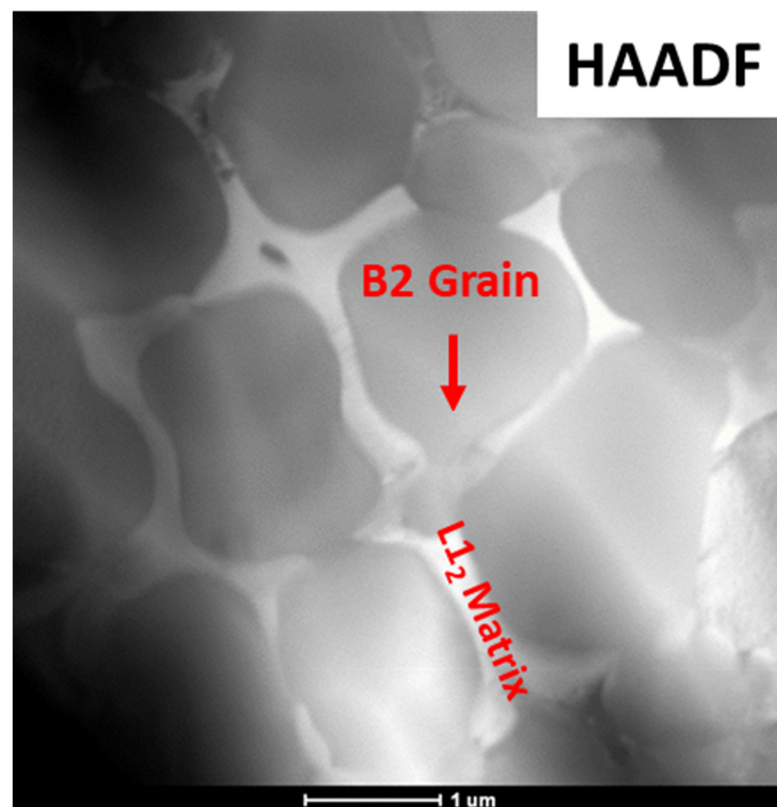


Figure 3.23 STEM – HAADF of $\text{Co}_{34}\text{Ni}_{35}\text{Al}_{31}$ FSMA

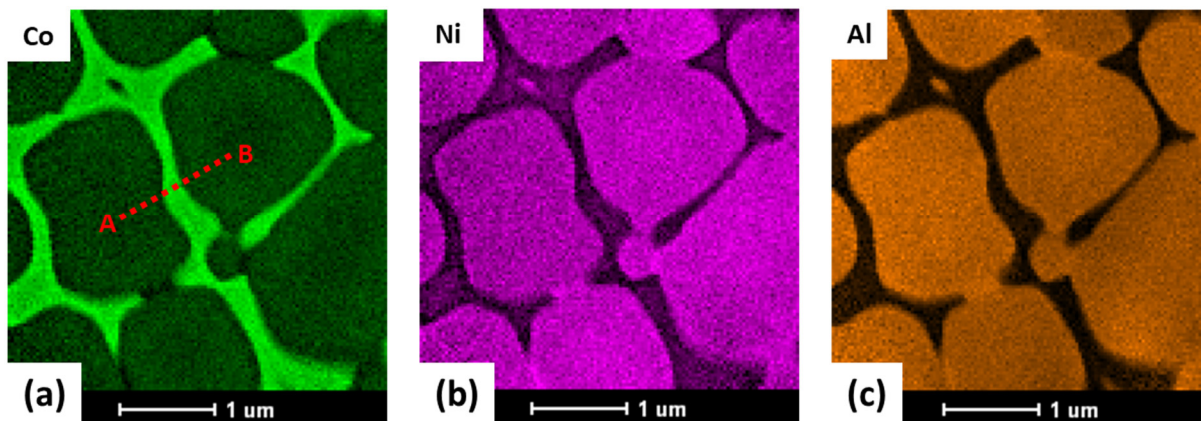


Figure 3.24 (a – c) Elemental mappings of the sample using STEM – EDS nano probe

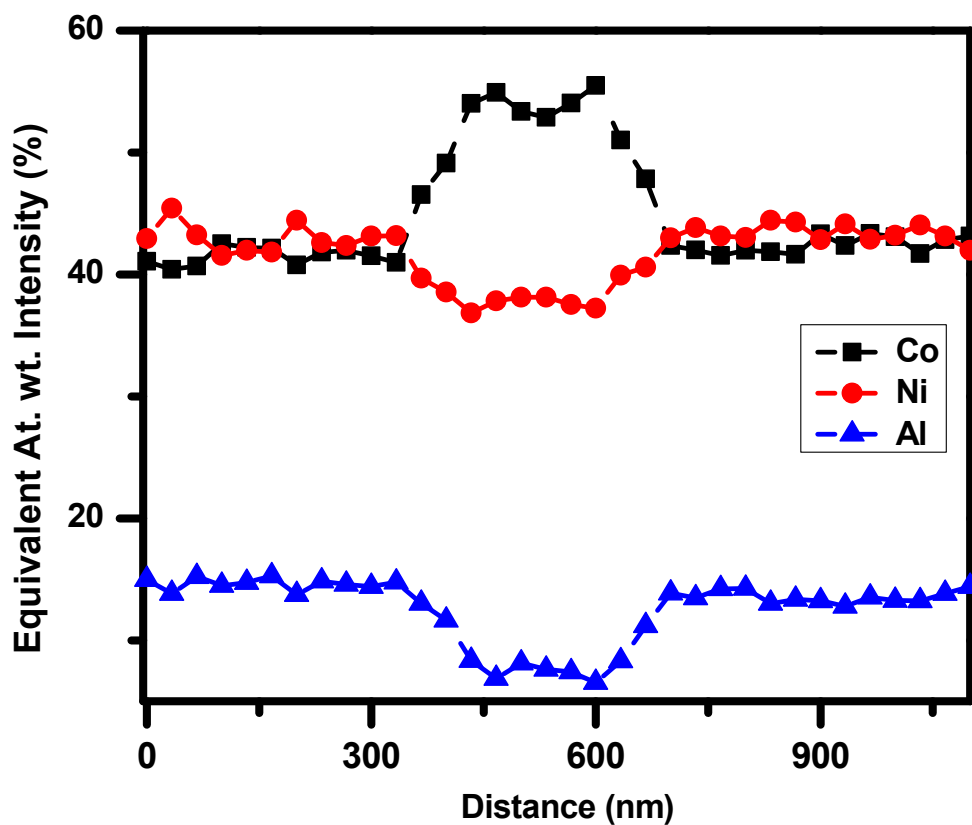


Figure 3.25 STEM – EDS line composition profile across the grain and matrix channel using STEM nano probe along red line ‘AB’ of Figure 3.24(a)

Elements	Overall measured alloy composition (atom %)	B2 ordered grain (atom %)	L1₂ ordered matrix channel (atom %)
Co	34.2 ± 0.1	35.0 ± 0.4	48.5 ± 0.1
Ni	35.3 ± 0.4	37.5 ± 0.2	37.4 ± 0.4
Al	30.5 ± 0.3	27.5 ± 0.3	14.1 ± 0.2

Table 3.7 Composition of the melt spun alloy and various microstructural features determined by TEM – EDS analysis

3.8 Conclusions

In conclusion it can be said that detailed studies have been made of the photo induced microactuation effect of an FSMA sample when excited by a focused laser beam. The effect of colour of the incident laser beam on the microactuation properties of the sample was studied. In these studies, it was found that laser colour plays an important role in the actuation properties of the sample. Efforts were made to control the amplitude of actuation of the sample by using various optical components. Thus, the relation of the actuation amplitude with various controlling factors like colour of the laser, output power of the laser and polarization of the laser beam was established. The response time of the actuation phenomenon for the different coloured lasers was also studied. From the studies that were conducted and also from the statistical analysis of the experimental data, two controlling mechanisms for the microactuation property of the sample can be proposed. One control mechanism which is dependent on the power and wavelength of the laser is linear in nature. Another one which is dependent on the angle of polarization and wavelength of the incident laser beam is periodic in nature. These control mechanisms can be implemented to successfully fabricate and operate suitably designed microactuator systems in the near future. Hence, a remotely controlled micro-mechanical system can be conceived by implementing this property of the FSMA samples. Though the cause of this unique phenomenon is still not clear, efforts are being made to find out the exact reasons for this behaviour of the alloy system. Structural, magnetic, thermal and mechanical

properties of the system are being systematically studied to explain the reasons behind this photo induced microactuation effect which will be discussed in detail in the next chapters of this thesis.

CHAPTER 4: THERMAL EFFECTS ON THE PROPERTIES OF PIMA OPERATION

4.1 Introduction

It has been shown in the previous chapter that the photo induced micro actuation (PIMA) property of the $\text{Co}_{34}\text{Ni}_{35}\text{Al}_{31}$ FSMA ribbons could be effectively regulated by controlling the amplitude of actuation of the alloy samples using various factors like colour, output power and polarization of the incident laser beams. These studies paved the way for successful implementation of a new class of laser controlled remotely operated microactuator systems in the near future. Before actual implementation of this unique phenomenon in fabricating suitable microactuator systems is done, investigations have been carried out to determine the workability of the selected Co-Ni-Al FSMA system in various environmental conditions where it is subjected to different levels of temperature and oxidation. When the photo induced microactuation (PIMA) property of a Co-Ni-Al FSMA was first reported, the effect of temperature on the actuation of the sample was also reported. But the experiment was conducted in a vacuum sealed environment to prevent the oxidation of the sample [4.1]. Thus, it is still unknown how the PIMA property of the alloy would be affected by the varying levels of temperature and oxidation in different working environments. Hence, investigations were carried out to determine the effect of temperature and oxidation on the PIMA property of the Co-Ni-Al sample for use in practical applications. A detailed structural analysis of the different microstructural features of the alloy system has been done and the possible mechanism of their evolution and correlation with PIMA effect along with the changes in the magnetic properties of the sample is discussed in this chapter. As a result, the systematic studies on the PIMA effect as well as the evolution of the structural and magnetic properties of the alloy system will help to adjudge the feasibility of implementing the PIMA effect for operation and control of suitable microactuator systems in varying environments in the near future.

4.2 Gradual degradation of photo induced micro actuation effect

4.2.1 Heat treatment procedure of Co-Ni-Al FSMA

The Co-Ni-Al FSMA sample used to carry out the optical experiments to study the effect of temperature and oxidation on the photo induced micro actuation (PIMA) property was the same $\text{Co}_{34}\text{Ni}_{35}\text{Al}_{31}$ ribbon as used before. Thus, the size and shape of the ribbon was kept the same as earlier experimental setup. This was done to ensure that any change arising in the PIMA property shown by the ribbon sample was only due to the effect of temperature and oxidation of the sample. In order to study the effect of increasing temperature on the PIMA property of the selected sample, the alloy ribbons were placed inside a box furnace as described in Section 2.1.3 without any vacuum sealing. The sample was heated to the desired temperature with a controlled heating rate of $10\text{ }^{\circ}\text{C}/\text{min}$ and kept at that temperature for 2 hrs. Afterwards, the sample was furnace cooled. After reverting to room temperature, this heat treated sample was used to perform the laser induced optical experiments for actuation studies as well as all other investigations. After performing the optical experiments, the same alloy ribbon was again placed inside the box furnace and heated treated to attain the next set of desired heating cycles. This heat treatment schedule and corresponding optical experiments were continued until the actuation of the annealed ribbon ceased to take place.

4.2.2 Gradual degradation of laser power dependent actuation

In order to systematically study the effect of temperature and oxidation on the micro actuation property of the Co-Ni-Al FSMA system, firstly the power dependence of the PIMA effect was observed. The sample was first heat treated at $50\text{ }^{\circ}\text{C}$ following the procedure mentioned above. Optical experiments were then carried out on this sample to study the changes in the power dependence of the PIMA property of this heat treated alloy. The amplitude of actuation of the $\text{Co}_{34}\text{Ni}_{35}\text{Al}_{31}$ alloy annealed at $50\text{ }^{\circ}\text{C}$ when subjected to different coloured focused laser beams as compared to the actuation amplitude achieved at room temperature is shown in Figure 4.1. From the figure it can be seen that the PIMA effect holds its linear nature as earlier. It is observed from this plot that even though the sample

was annealed at 50 °C for two hours, the colour dependence of the PIMA effect reported earlier is still present. It can be thus inferred that the control mechanism achieved earlier by selecting the laser power as well as colour of the incident laser beam is still applicable in operating any proposed microactuator system when the sample is heated and gets oxidized at 50 °C. It can also be seen from the figure that heat treatment at a temperature of 50 °C has decreased the amplitude of actuation of the Co-Ni-Al FSMA sample by approximately 30% as compared to the amplitude achieved at room temperature. As reported in Chapter 3, the slopes of the linear fitted curves of the data recorded at room temperature are 1.97, 1.79 and 1.60 for the blue, green and red lasers respectively. Similarly, the slopes of the linear fitted curves of the data obtained from heat treating the sample at 50 °C are 1.49, 1.34 and 1.18 for the blue, green and red lasers respectively.

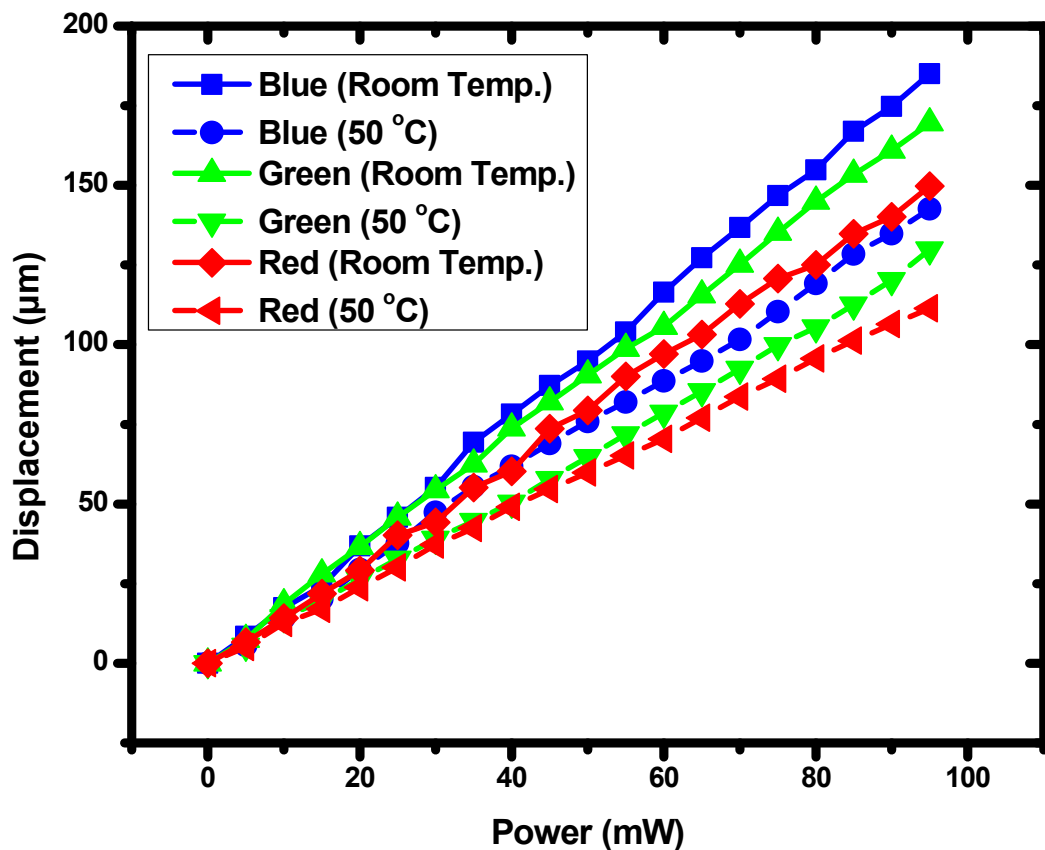


Figure 4.1 Power dependent PIMA effect at room temperature and 50 °C

After performing the optical experiments on the sample annealed at 50 °C, the same sample was heat treated at a temperature of 100 °C for two hours as before. The amplitude of laser induced actuation of the sample annealed at 100 °C as compared to the actuation amplitude achieved at room temperature is shown in Figure 4.2. From the figure it can be seen that the PIMA effect still holds its linear nature. But it can also be observed from this plot that even though the nature of the linear control of the PIMA effect is still intact, the colour dependence of the effect reported earlier has diminished significantly. The slopes of the linear fitted curves of the data obtained from heat treating the sample at 100 °C are 0.71, 0.69 and 0.63 for the blue, green and red lasers respectively. This implies that the sample shows almost the same amplitude of actuation for the blue and green lasers while the red laser still induces slightly less amplitude of PIMA effect. It is also found from the graph that exposing the sample to a temperature of 100 °C has dramatically decreased the amplitude of actuation of the Co-Ni-Al FSMA sample to approximately one third of the actuation amplitude achieved at room temperature. This data will help in determining the limitations of the working environment of any proposed laser operated microactuator system in the near future.

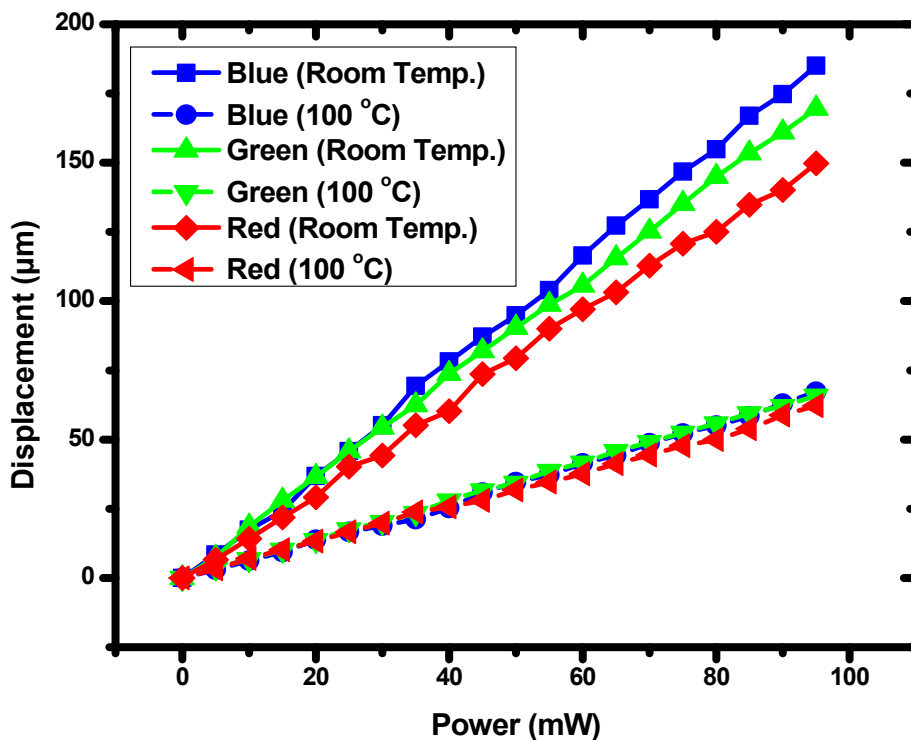


Figure 4.2 Power dependent PIMA effect at room temperature and 100 °C

The same optical experiment was repeated in a similar fashion with the sample now heat treated at 150 °C for a period of two hours. The microactuation amplitude data obtained from the experiment is very similar in nature to the data obtained at 100 °C as shown in Figure 4.3. This is evident from the slopes of the linear fitted curves of the data obtained from heat treating the sample at 150 °C, which are 0.71, 0.69 and 0.63 for the blue, green and red lasers respectively. It shows minimal change in the amplitude of actuation of the sample when the temperature was increased by a further 50 °C. Thus, it can be inferred that the PIMA property would almost hold its nature even when the sample gets heated and oxidized to 150 °C.

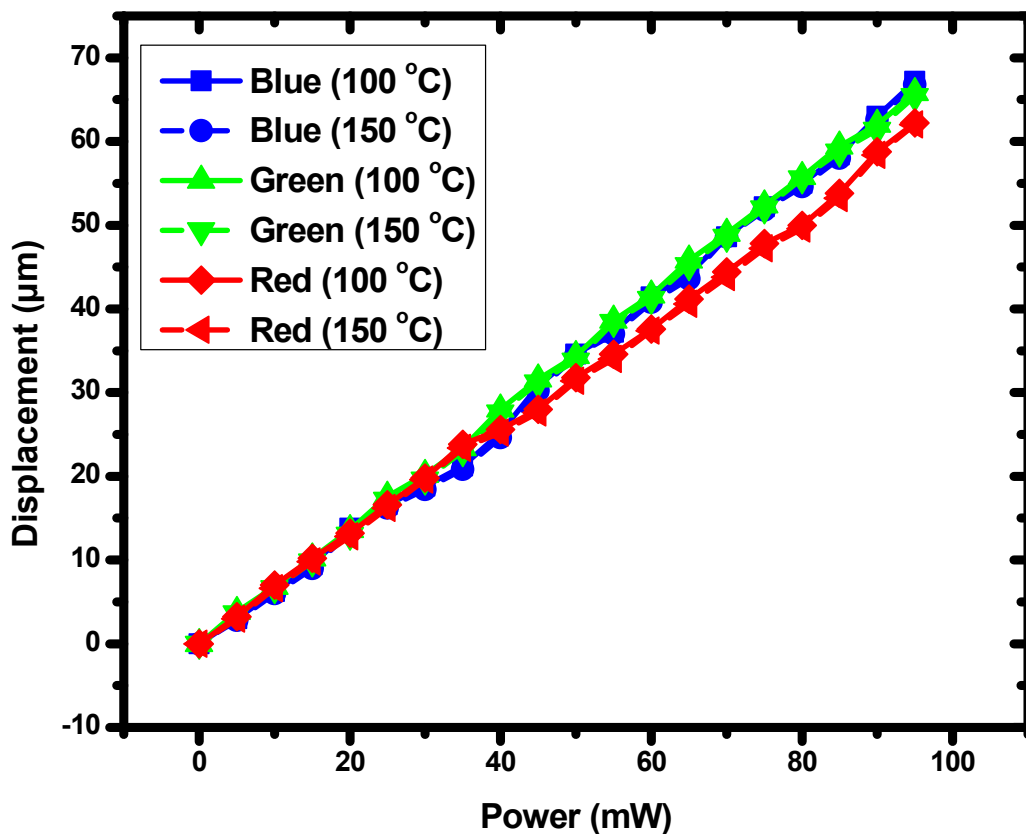


Figure 4.3 Power dependent PIMA effect at 100 °C and 150 °C

As it was found out that there was no major difference between the actuation amplitude of the sample annealed at 100 °C and 150 °C, the sample was then heat treated to a much higher temperature of 250 °C, under the same environmental conditions as before to perform the next set of optical experiments. The actuation data obtained is plotted in Figure 4.4. From this it is seen that, annealing at a temperature of 250 °C, the quality of the linear control over the amplitude of actuation of the sample has started to degrade, especially at lower laser powers. It can also be said that the colour dependence of the microactuation does not follow the earlier pattern anymore and has become more or less haphazard. So, the Co-Ni-Al system is not suitable to act as any microactuator when it gets oxidized at a temperature of 250 °C.

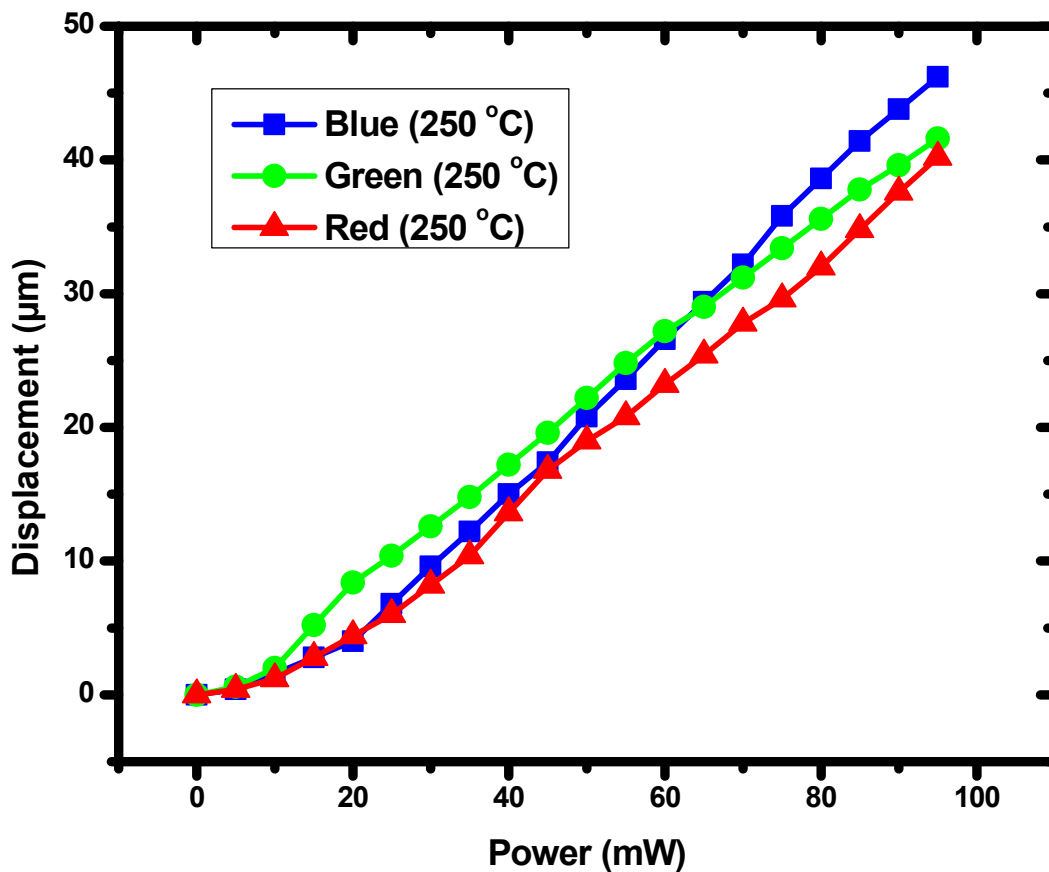


Figure 4.4 Power dependent PIMA effect at 250 °C

Next, further investigations were carried out to find out the temperature where the Co-Ni-Al FSMA system will not show any actuation at all. To do this, the sample was then annealed at a temperature of 300 °C for a duration two hours. The actuation data obtained is plotted below in Figure 4.5(a). It can be seen that even when the sample is heated upto a temperature of 300 °C, there was some residual PIMA property at higher laser powers of 25 mW and above. It is interesting to note here that the sample showed more PIMA effect for the green coloured laser at lower output powers. Next the sample was again heated at a temperature of 350 °C for a period of two hours. The data obtained is shown in Figure 4.5(b). Here also it can be seen that the sample still shows some negligible actuation for laser powers of 50 mW and above, however the effect of the blue laser is now less than that of the green laser. Linear fitting of the curves at higher laser powers give the slopes of the straight lines as 0.12 for the green, 0.11 for the blue and 0.09 for the red laser respectively.

The sample was then again placed inside the furnace and annealed at a temperature of 400 °C for a period of two hours. When the optical experiments were again performed on this sample, no actuation was observed for any laser colour. Thus, it can be inferred that the PIMA effect of the Co-Ni-Al FSMA system ceases to exist when the ribbon sample is heated upto this high temperature of 400 °C. As it was found out that the PIMA effect of the ribbon sample was completely lost at an annealing temperature of 400 °C, so that was the maximum temperature of heat treatment applied to the sample. The progressive fall in actuation or the gradual degradation of the colour dependent PIMA effect of the $\text{Co}_{34}\text{Ni}_{35}\text{Al}_{31}$ FSMA system as the extensive temperature was increased is shown summarily in Figure 4.6 at 95mW incident laser power. It shows that the blue laser that initially had maximum displacement lost its effectiveness as the temperature was increased, till it became less than that of green. The red laser was lowest efficient of all and that trend remained upto the total disappearance of the PIMA property shown by the alloy ribbon.

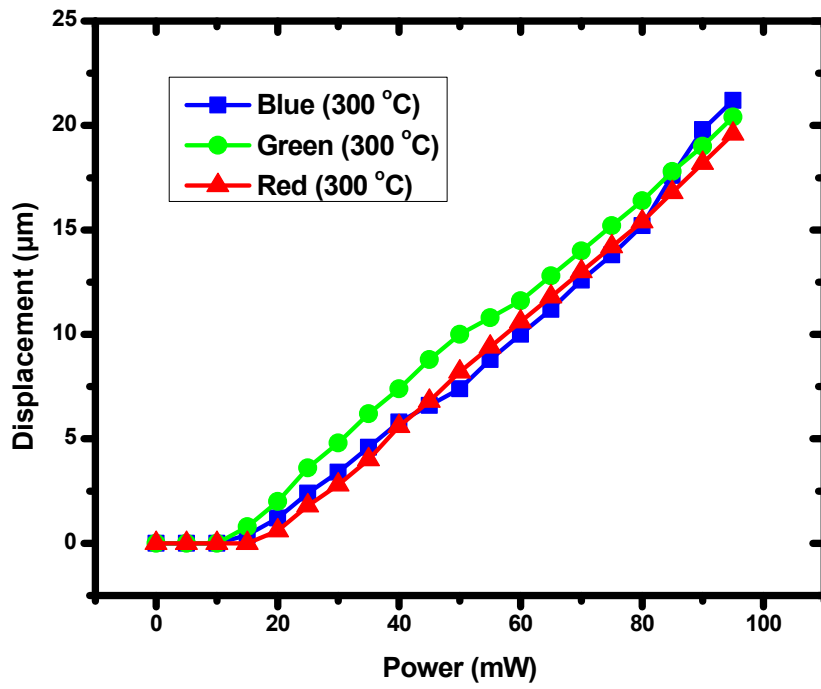


Figure 4.5 (a) Power dependent PIMA effect at 300 °C

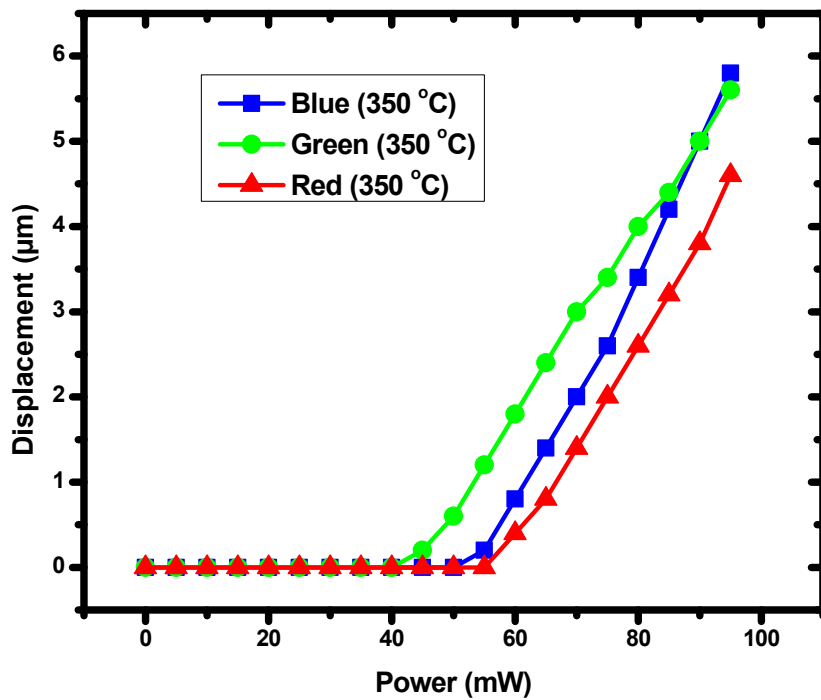


Figure 4.5 (b) Power dependent PIMA effect at 350 °C

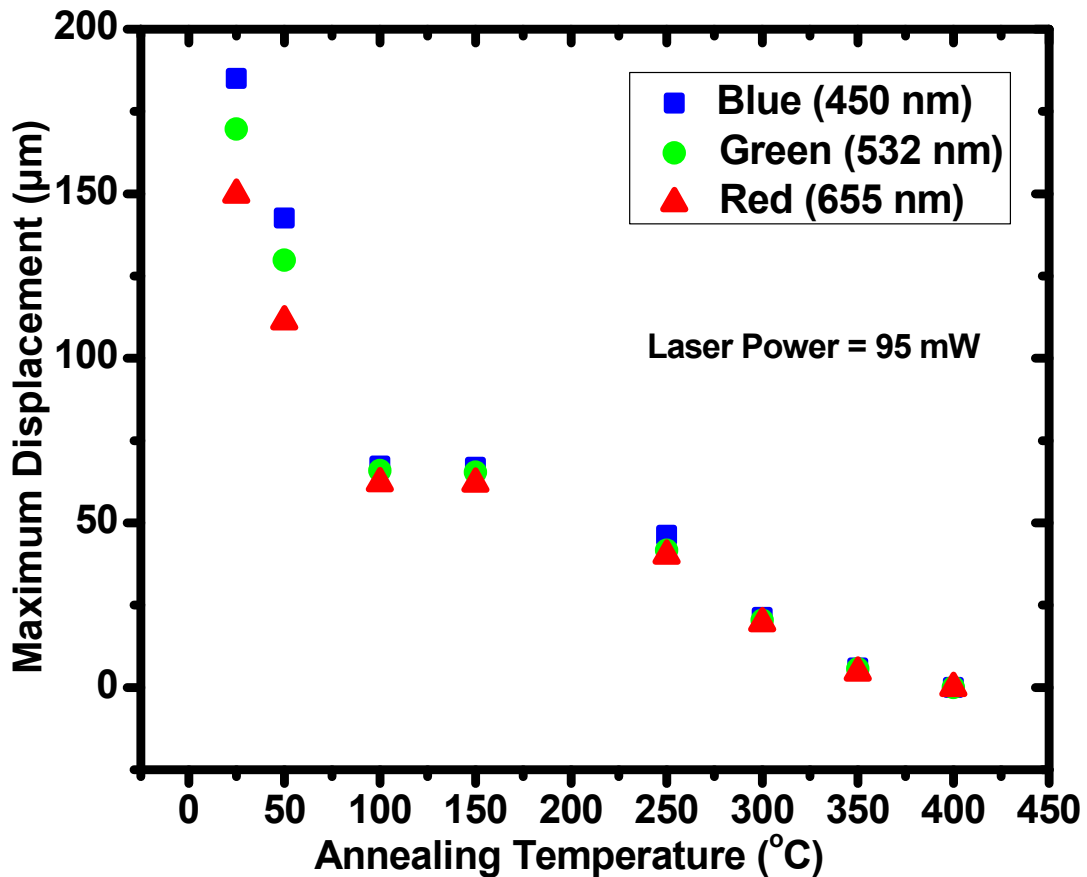


Figure 4.6 Colour dependent PIMA effect at various annealing temperatures

4.2.3 Gradual degradation of laser polarization dependent actuation

In the Chapter 3 of this thesis, the laser polarization dependence of the photo induced micro actuation (PIMA) effect was reported. Controlling the laser polarization was proposed as one of the controlling factors of operation of any perceived microactuator system. Thus, the effect of heat treatment on the polarization dependence of the PIMA effect was also studied. The necessary optical experiments were thus performed simultaneously with the power dependence study on the Co-Ni-Al FSMA ribbon sample annealed at the temperatures discussed in the previous section. The result of the optical experiments performed on the sample heat treated at 50 °C as compared with the polarization dependence data of the sample recorded earlier at room temperature is shown graphically in Figure 4.7. It can be observed from the figure that the PIMA effect still shows the polarization dependence of the ribbon sample when it was

annealed at a temperature of 50 °C for a duration of two hours. The presence of the effect of laser colour is also evident from the graph as reported earlier. The PIMA effect is also able to hold its same periodicity for all the three laser colours. There is only a nominal decrease in the total actuation achieved by the sample with the nature of periodic control over the actuation still intact. Thus, it can be inferred from the figure that the periodic nature of the PIMA property of the Co-Ni-Al FSMA ribbon system is also quite resistant to heat treatment and oxidation, when it is exposed to a temperature of only 50 °C.

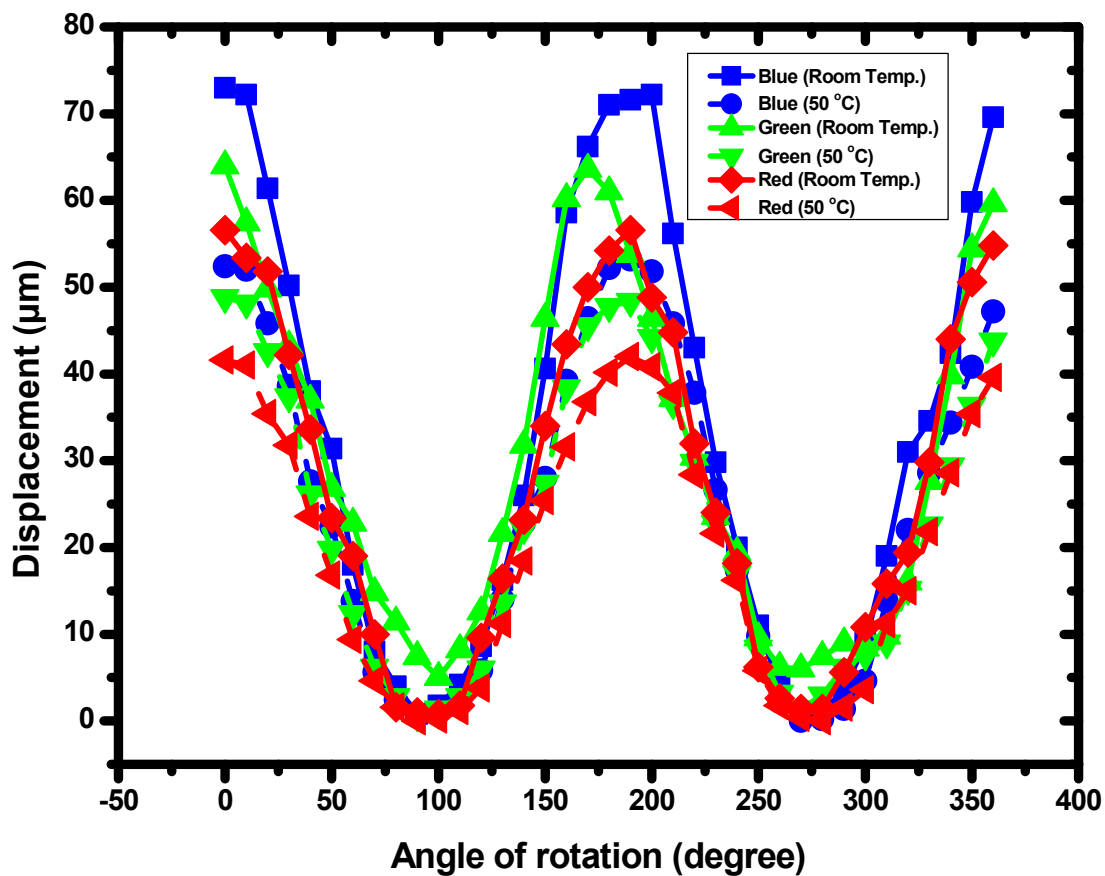


Figure 4.7 Polarization dependent PIMA effect at room temperature and 50 °C

Next, the polarization dependence of the PIMA effect was studied on the sample annealed at 100 °C. The comparison between the polarization dependence of the actuation data of the sample heat treated at 50 °C and 100 °C is plotted in Figure 4.8. From the figure it can be seen that the polarization dependence of the PIMA effect still holds its periodic nature. It can also be observed from this plot that even though the nature of the periodic control of the PIMA effect is still intact, the colour dependence of the effect reported earlier has diminished significantly. This observation is in accordance with the power dependence of the PIMA effect of the sample discussed in the previous section. The decrease in the overall amplitude of actuation of the sample is quite evident from the figure and this decrease again follows the trend reported earlier.

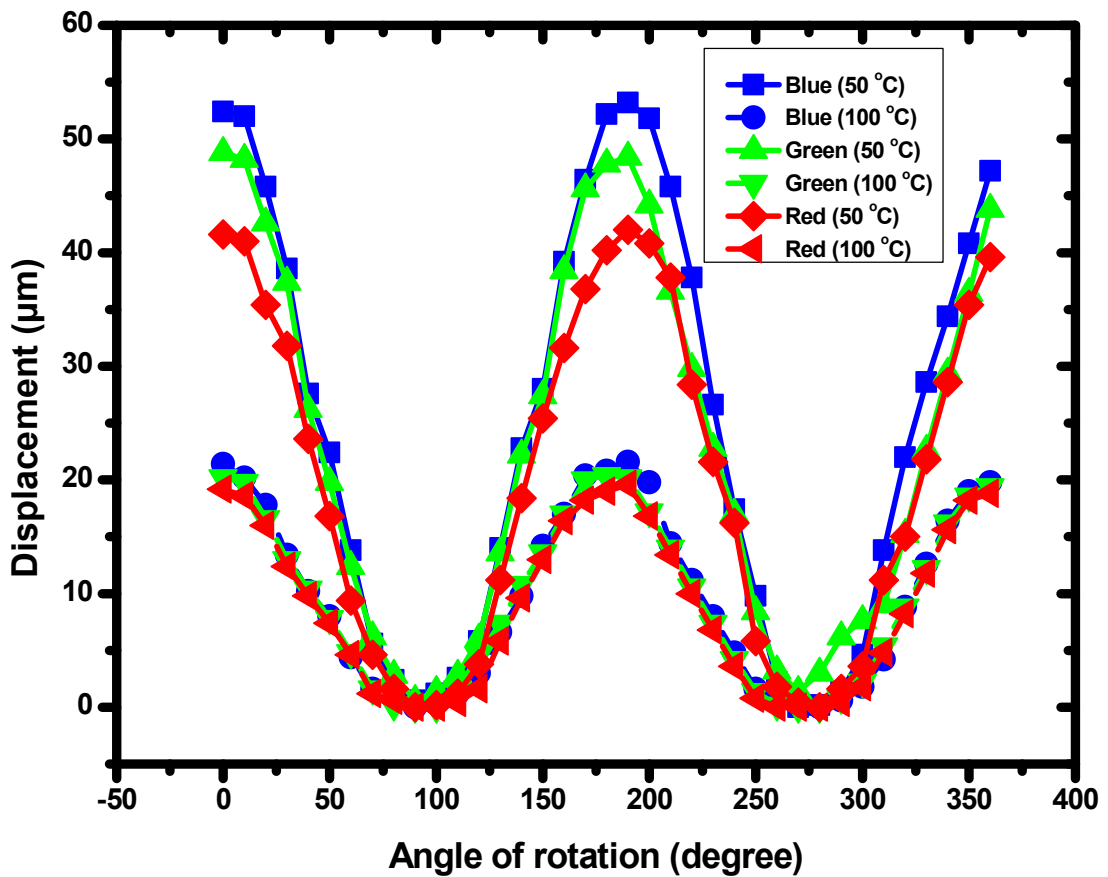


Figure 4.8 Polarization dependent PIMA effect at 50 °C and 100 °C

The polarization dependence study was then performed on the sample annealed at 150 °C. The comparative data plotted in Figure 4.9 shows that the nature of the periodic control over the microactuation of the sample is almost consistent with the data obtained for the sample heat treated at 100 °C. This is in accordance with the laser power dependent actuation data which means that there is almost a negligible change in the PIMA property shown by the Co-Ni-Al FSMA sample for the temperature range of 100 °C to 150 °C. This data will be useful in determining the limits of operation and control of any perceived microactuation system in the near future.

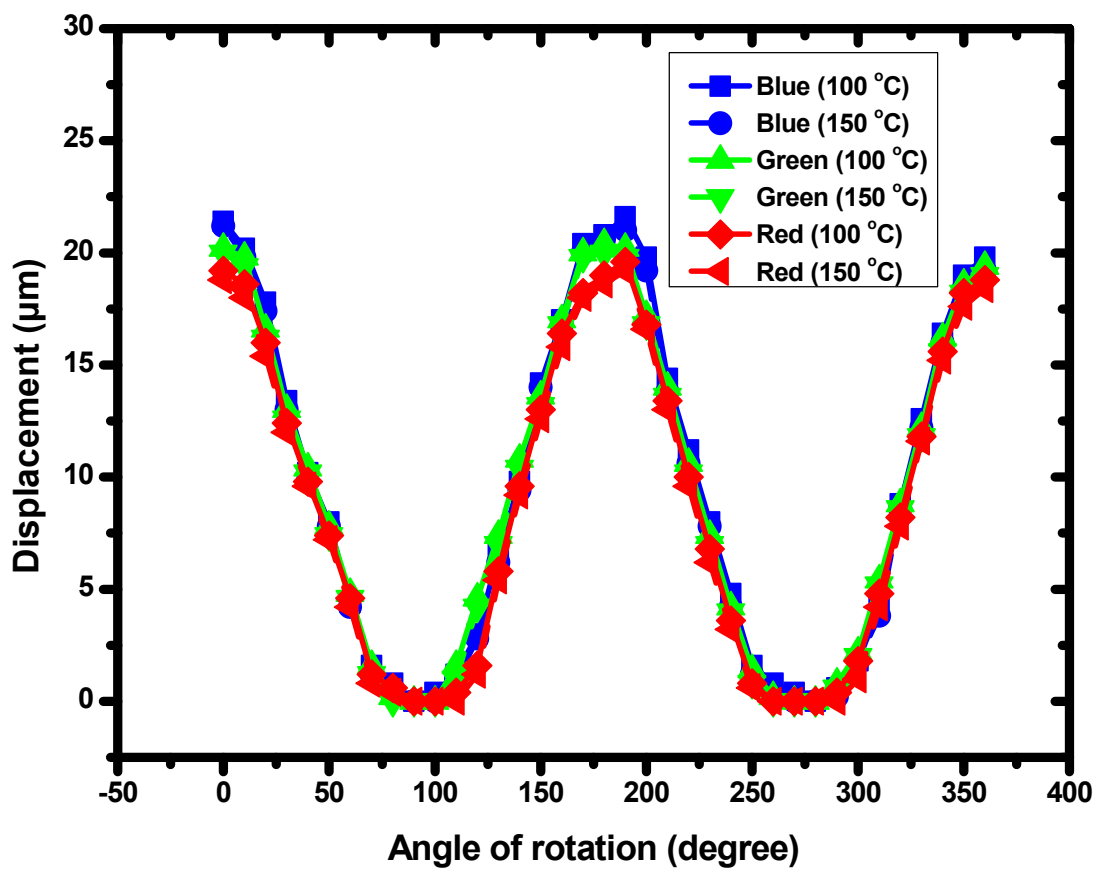


Figure 4.9 Polarization dependent PIMA effect at 100 °C and 150 °C

It has already been established in the previous section of this chapter that when the Co-Ni-Al FSMA ribbon sample is annealed at a temperature of 250 °C it is no longer suitable for use as any microactuator. None the less, the effect of polarization on the microactuation property of the sample was studied simultaneously. The data obtained is plotted in Figure 4.10. It can be seen from the

graph that when the sample is heat treated at a temperature of 250 °C, the periodic nature of the control over the microactuation is considerably diminished along with its colour dependence. It can be seen that the total amplitude of actuation in response to the polarized lasers has also decreased substantially to a level where it is no longer suitable to control any perceived microactuator system using this control mechanism. In the end, when the lasers polarized by the glass linear polarizer was incident on the sample annealed at 300 °C it showed no actuation. This was because of the linear polarizer removes components from all directions of the laser source except one, which reduces the output intensity of the polarized laser beams as reported earlier. This reduced intensity of the laser beam was insufficient to cause any microactuation in the sample which was subjected to heat treatment at a temperature of 300 °C.

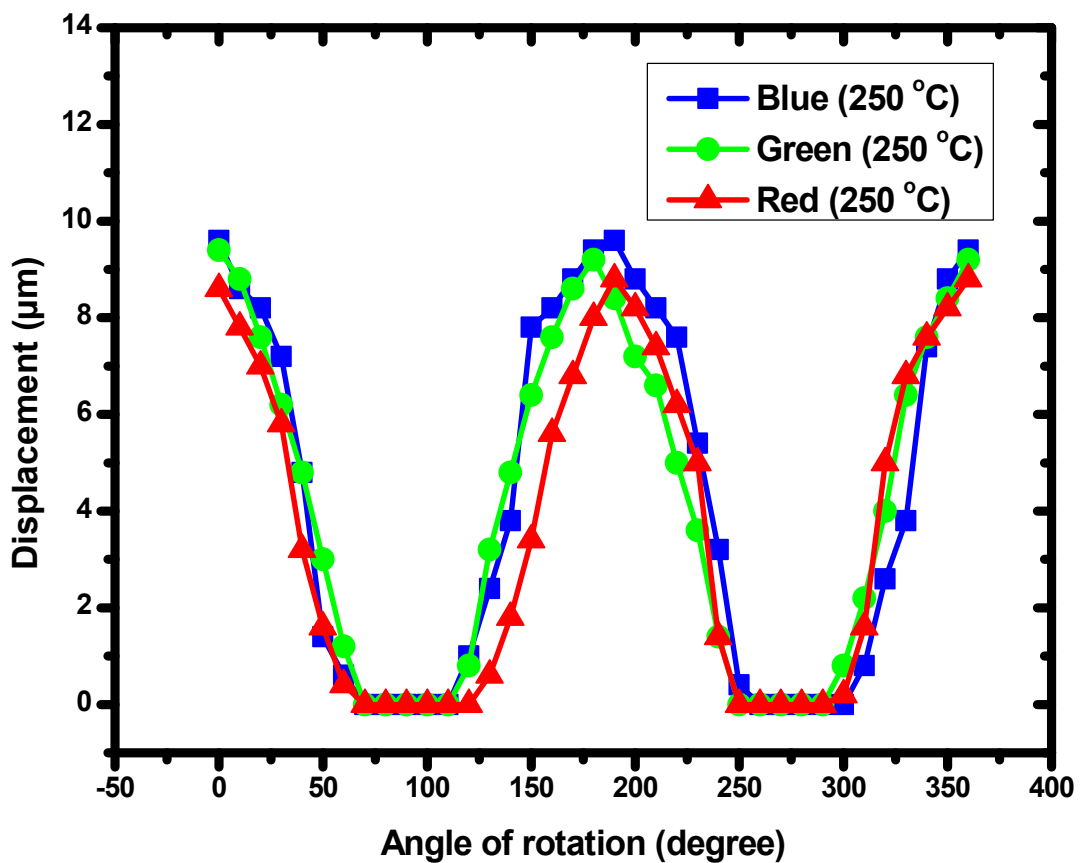


Figure 4.10 Polarization dependent PIMA effect at 250 °C

4.3 Microstructural evolution during heat treatment

Since, the FSMA samples showed no PIMA property when it was subjected to heat treatment at 400 °C, investigations were carried out to study the changes in the microstructure of the selected alloy and to correlate the obtained results with the observed gradual degradation of the PIMA property. Detailed TEM analysis of the ribbon sample annealed at 400 °C for a holding time of 2 hrs. were carried out and the results were compared with the TEM data of the melt spun ribbons already reported in the previous chapter. A standard cross-sectional specimen preparation technique was adopted in order to observe the surface as well as the sub-surface morphology of the heat treated samples.

A representative TEM bright field image inside the B2 ordered grain of the heat treated sample is shown in Figure 4.11(a). This figure indicates the appearance of nanometre sized precipitates having modulated kind of morphology inside the B2 ordered grain after the annealing at 400 °C for 2 hrs. A closer look into the red dotted box marked in the figure indicates that these nanosized particles have some fine black and white alternating lines in their morphology. A blown up version of the image presented in Figure 4.11(b) implies that the black and white alternating lines seen in the red dotted boxes are fine fault type morphology. This faulted type morphology can be related to the strain field contrast around these particles. The presence of this contrast suggests that these nanometre sized precipitates are associated with a coherency strain due to the lattice parameter mismatch with the particles and B2 matrix. This type of small misfit precipitate particles with strain field contrast around them that gave rise to these contrast features is known as Ashby – Brown contrast [4.2 – 4.5]. This type of diffraction contrast has been interpreted as an elastic distortion of the matrix around the coherent particles. High magnification bright field and dark field images of the same region shown in Figure 4.11(a) are presented in Figure 4.12(a) and Figure 4.12(b) respectively.

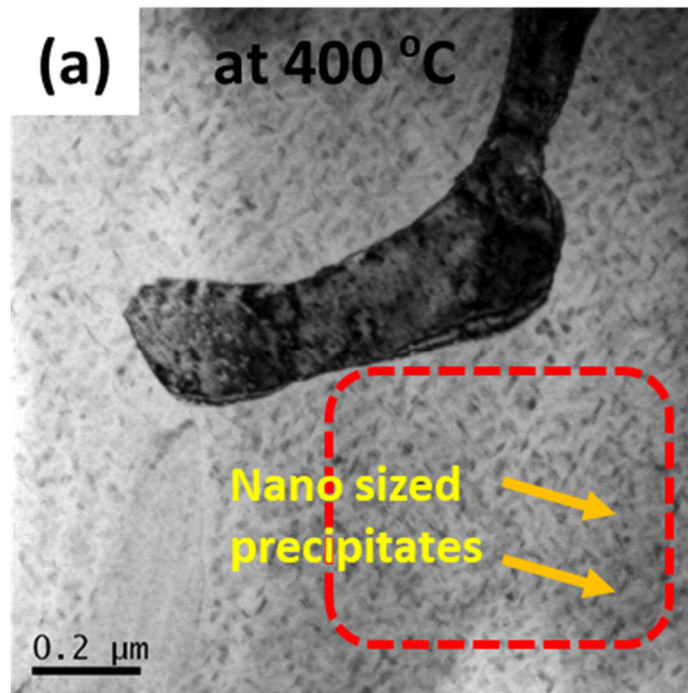


Figure 4.11 (a) Bright field TEM image of the heat treated Co-Ni-Al sample

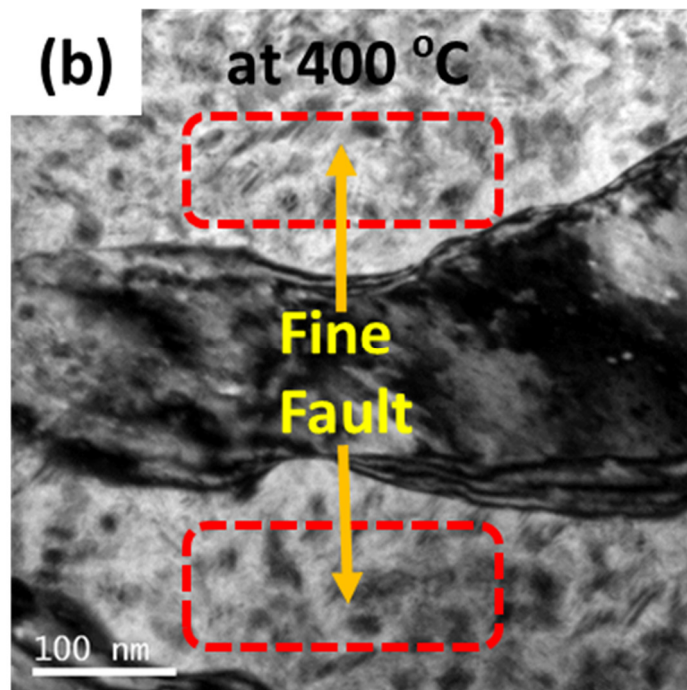


Figure 4.11 (b) Blow up version of Figure 4.11(a) showing fine fault morphology

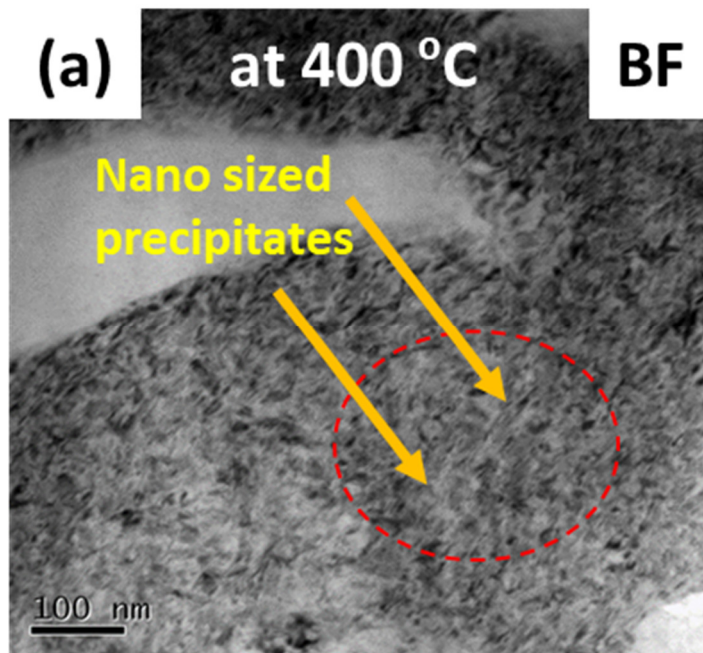


Figure 4.12 (a) High magnification bright field TEM image

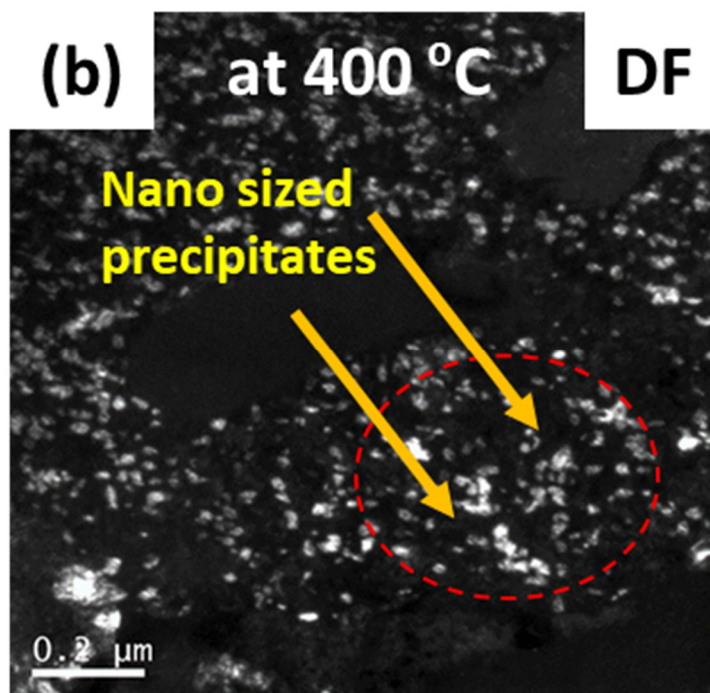


Figure 4.12 (b) Dark field TEM image

A selected area electron diffraction pattern shown in Figure 4.13(a), taken from within a B2 structured grain confirms the existence of extra spots of weak intensity, arranged in a pattern as shown by the white dotted line along with the B2 ordered super lattice (100) and fundamental (200) spot. The dark field TEM image already shown in Figure 4.12(b) was obtained by selecting one of the weak spots marked by the red circled area in the diffraction pattern shown in Figure 4.13(a). It also indicates the evolution of nanometre sized precipitates inside the B2 grain after the annealing of the alloy sample at 400 °C. Preliminary indexing of these weak spots hints at the evolution of cobalt rich precipitates phase inside the B2 grain of the FSMA sample after undergoing the heat treatment process. The selected area diffraction pattern taken from the cobalt rich L1₂ ordered matrix channel is shown in Figure 4.13(b). The diffraction pattern confirms that there are no structural changes observed in the matrix phase except for some diffused diffraction intensities with L1₂ reflections marked by the red arrows in the image after the annealing process of the sample. Thus, it can be concluded that the B2 ordered active phase for FSMA response was affected more after the heat treatment procedure in comparison to the L1₂ ordered matrix phase.

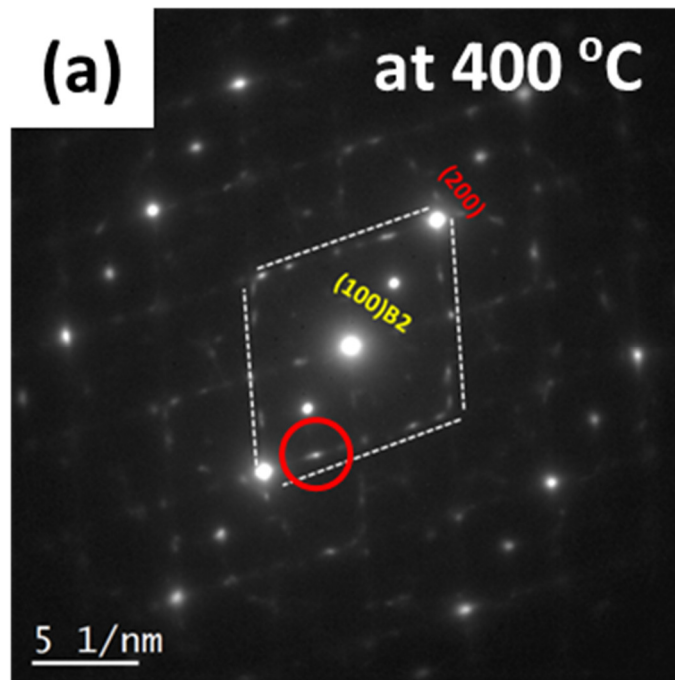


Figure 4.13 (a) Diffraction pattern taken inside B2 grain of annealed sample

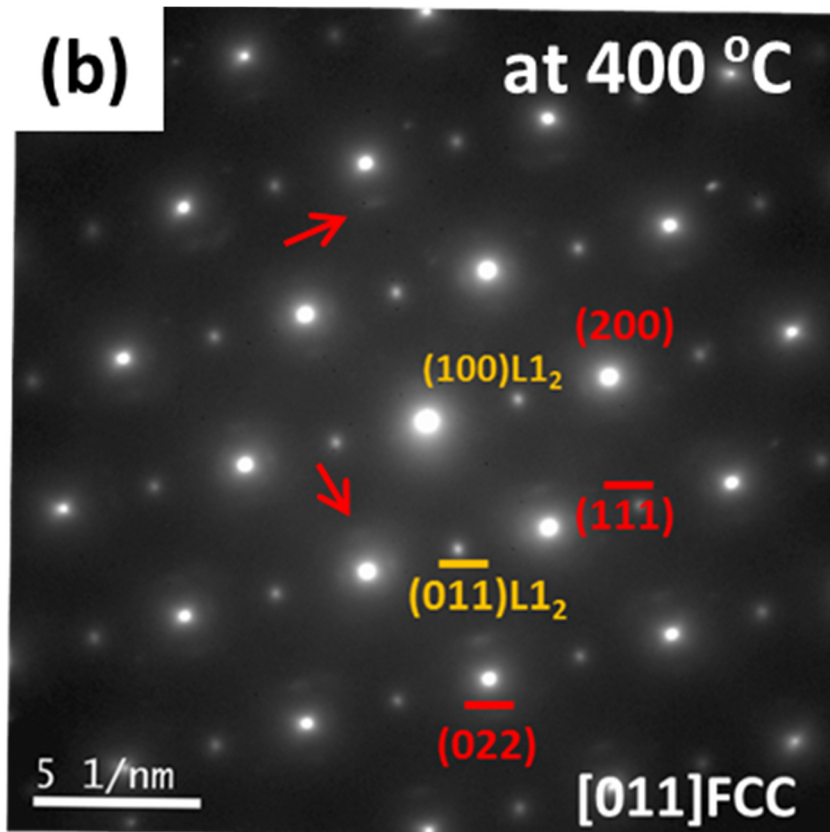


Figure 4.13 (b) Diffraction pattern taken along [011] zone axis of L₁₂ matrix

A STEM – HAADF image shown in Figure 4.14 is taken in the same region as depicted in Figure 4.11(a). The Figure 4.15(a-d) shows the elemental mappings of this region using a STEM – EDS nano probe. It shows that the nanosized precipitates, newly evolved during annealing of the alloy sample at 400 °C, are relatively rich in cobalt as marked by red arrows in Figure 4.15(a), with a trace concentration of oxygen inside the B2 ordered grain. This result along with the diffraction pattern analysis indicates changes in the composition of the B2 ordered phase affect the FSMA properties of the alloy sample [4.6 – 4.9]. A plausible cause to form a cobalt rich phase can be the higher stability of Ni-Al phase of the B2 grain over the Co-Al phase for a pseudo type (Co, Ni)-Al B2 ordered structure.

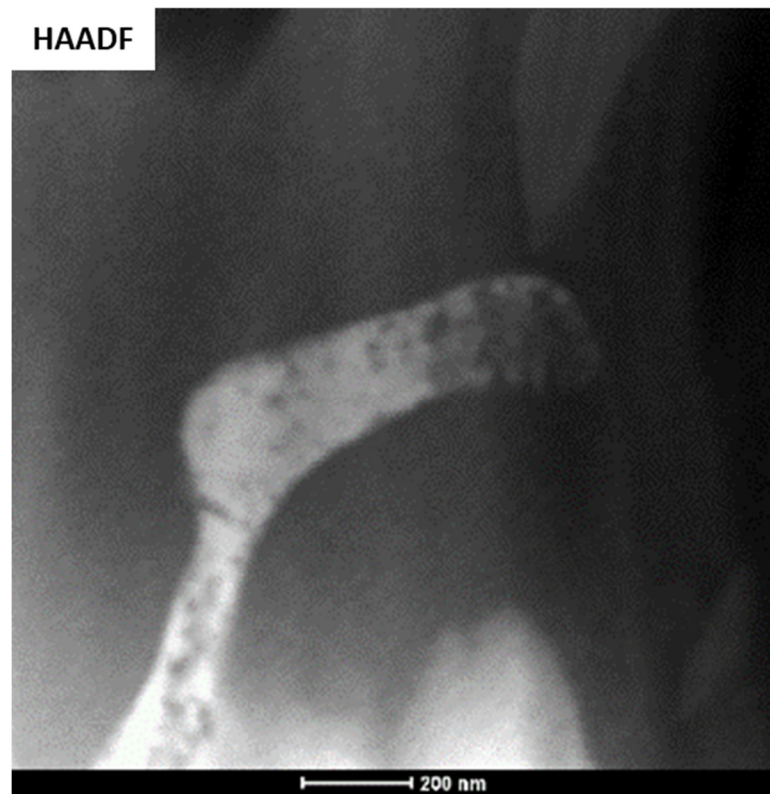


Figure 4.14 STEM-HAADF image of the same region shown in Figure 4.11(a)

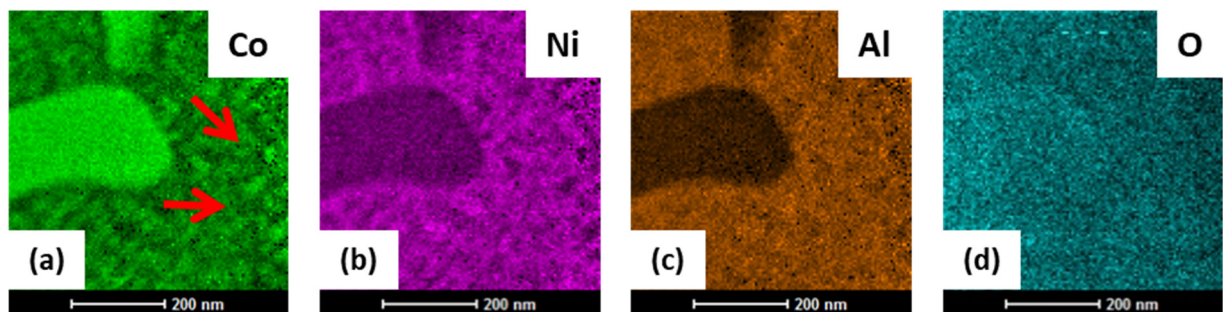


Figure 4.15 (a-d) Elemental mappings using STEM – EDS nano probe, showing the cobalt rich nano sized precipitates along with the existence of oxygen inside the B2 ordered grain, evolved during annealing of the Co-Ni-Al alloy at 400 °C

4.4 Oxidation studies

4.4.1 Oxidation kinetics study

The rate of formation of oxides in the melt spun FSMA ribbon samples was characterized by the weight gain of the alloys. The measurement of weight gain measures the amount of oxygen consumption, and is a prevalent and convenient method [4.10 – 4.14]. In order to obtain a set of kinetic data, several specimens of the selected alloy system having the same size and shape were taken and heat treated at 400 °C for different holding times according to the procedure followed earlier. Isothermal oxidation studies of the Co-Ni-Al FSMA system were conducted at different prolonged time scales in order to understand the kinetics of the sample at 400 °C. A standard cross sectional specimen preparation technique was adopted in order to observe the oxide surface and study the sub surface morphology of the oxidized samples.

X-ray diffraction (XRD) technique was employed to identify the different constituent phases in the as prepared as well as the oxidized alloy samples. The representative X-ray diffraction (XRD) patterns obtained from different holding time during annealing at 400 °C along with the as spun alloy sample are presented in Figure 4.16(a). Indexing of the reflections from different phases confirms the presence of both B2 ordered phase and FCC phase as shown in Figure 4.16(b) which is an expanded view of the diffraction intensities marked by the purple dotted box depicted in Figure 4.16(a). From the XRD pattern it can be seen that with increased temperature of annealing, the diffraction peaks for both B2 ordered and FCC phases exhibit increased amount of broadening. Such increased broadening of diffraction peaks may be rationalized with the earlier observed phenomenon of a strained crystal lattice caused by strain field associated with the coherent nano sized fine faulted cobalt rich precipitates [4.6].

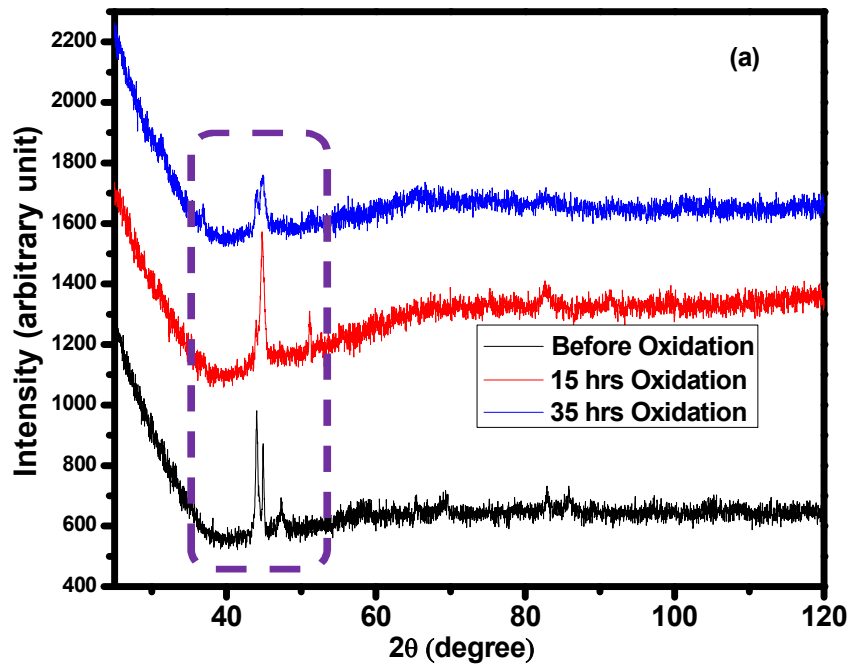


Figure 4.16 (a) XRD pattern of the as spun and oxidized Co-Ni-Al samples

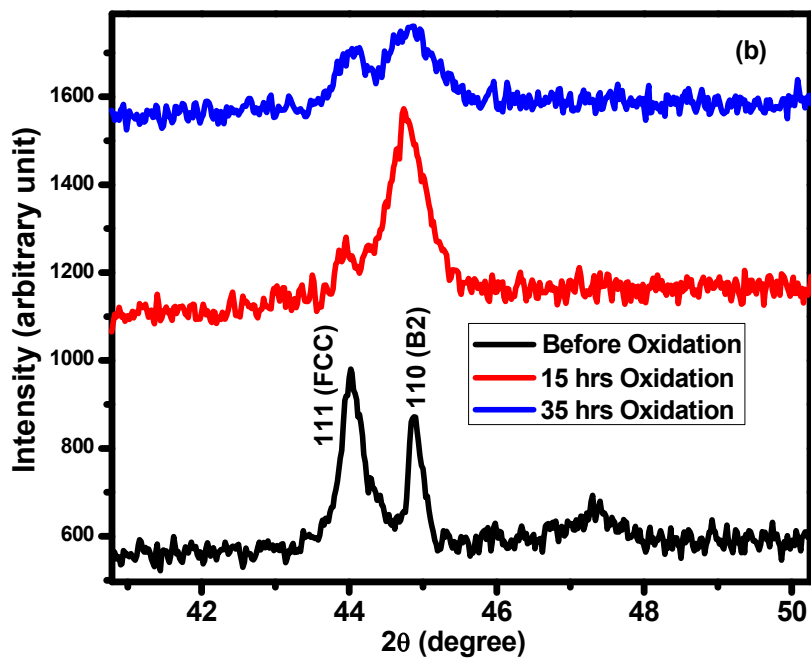


Figure 4.16 (b) Expanded view of the XRD pattern of the as spun and oxidized Co-Ni-Al samples

Figure 4.17 depicts the nature of isothermal oxidation kinetics in the sample. It shows a complex nature of the change in specific mass with oxidation time. It can be seen from the figure that initially the alloy showed a significant gain in weight after 15 hrs. of annealing and maximum increase or saturation in mass gain was observed upon heat treatment of the sample at 400 °C for 35 hrs. The curves can be fitted by a straight line, which represents rate constant 'k' where, $(\Delta m/A)^2 = k \cdot t$ [4.10]. Here, ' Δm ' is the mass change of the specimen, ' A ' is the surface area of the specimen, ' k ' is the oxidation rate constant and ' t ' is the oxidation time. The slope of a linear regression fitted line of $(\Delta m/A)^2$ versus ' t ' plot is shown in Figure 4.17, which indicates the complex nature of oxidation kinetics. The oxidation rate constant value is calculated as $2.9 \times 10^{-3} \text{ (mg}^2 \cdot \text{cm}^{-4} \cdot \text{h}^{-1}\text{)}$ for the selected alloy.

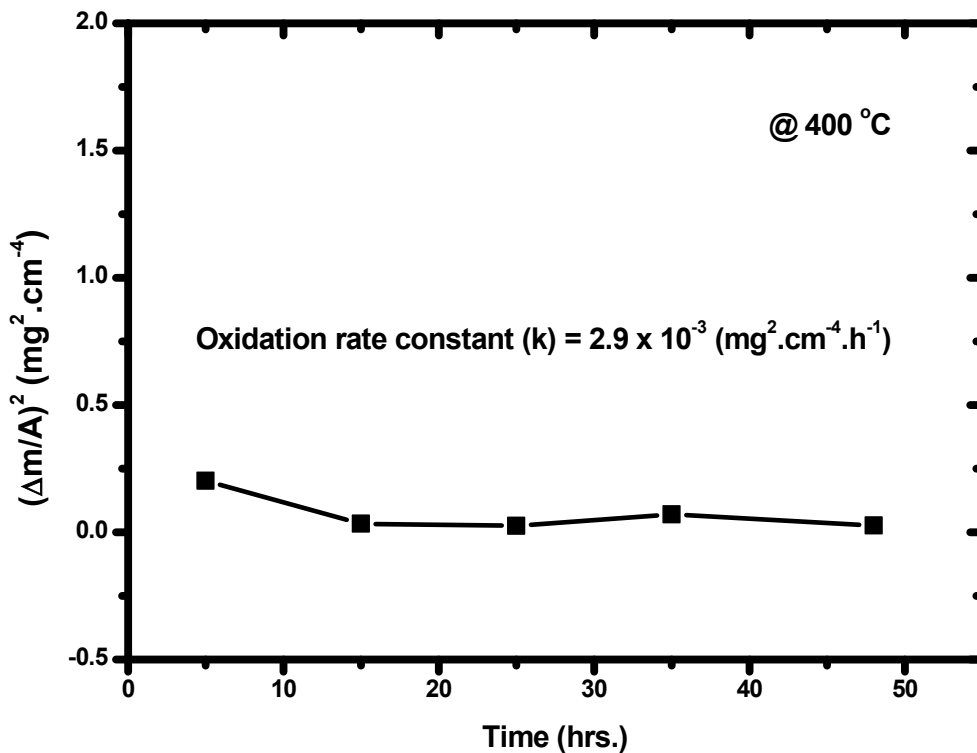


Figure 4.17 Square of mass gain versus oxidation time for the selected Co-Ni-Al FSMA at 400 °C

4.4.2 Microstructural features of oxidized $\text{Co}_{34}\text{Ni}_{35}\text{Al}_{31}$ FSMA

The detailed microstructural features of the oxidized alloys were further characterized using a transmission electron microscope (TEM). The cross section of the alloy sample, kept at 400 °C for 35 hours was examined to correlate the oxidation kinetics with the evolved microstructure. Figure 4.18(a) and Figure 4.18(b) demonstrates the TEM bright field and STEM – HAADF image of the cross section of the oxidized alloy sample on a similar scale as shown for the as spun sample in the previous chapter of this thesis. It displays the irregular shaped composite layer of surface oxides of several hundred nanometre thickness and modified microstructure of the alloy underneath.

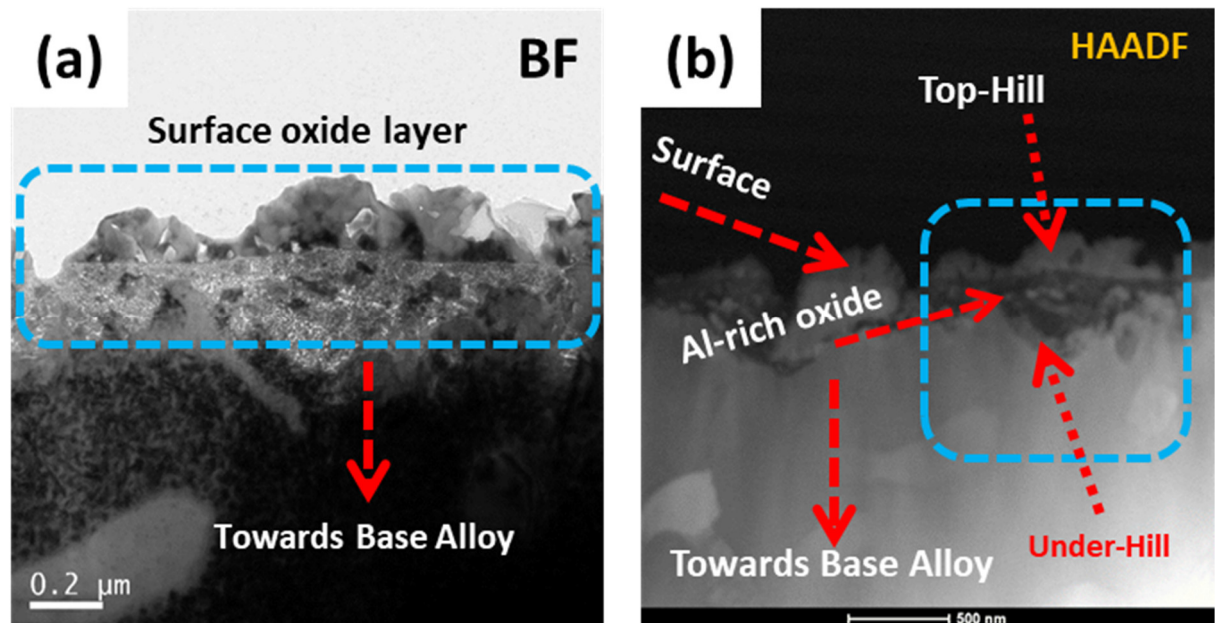


Figure 4.18 (a) TEM bright field image showing the formation of irregular and composite surface oxide layer along with the base alloy of the Co-Ni-Al sample oxidized at 400 °C for 35 hrs. (b) Corresponding HAADF image showing the atomic contrast of the composite oxide layer

The STEM – EDS elemental mapping of the oxidized alloy is also shown in Figure 4.19(a-d). It can be seen from Figure 4.19(a) that the surface oxidation caused cobalt to diffuse out of the metallic alloy to the top surface to form an uneven layer of Co-oxide named ‘top-hill’. Figure 4.19(c) also reveals an Al-oxide layer just underneath the Co-oxide layer called the ‘under-hill’. These ‘top-hill’ and ‘under-hill’ oxide layers can also be seen from the STEM – HAADF image in the previous figure. This loss of Co from the underneath alloy causes the grains of Ni-rich phases to evolve under the oxidised layer comprising of these Co and Al-oxides.

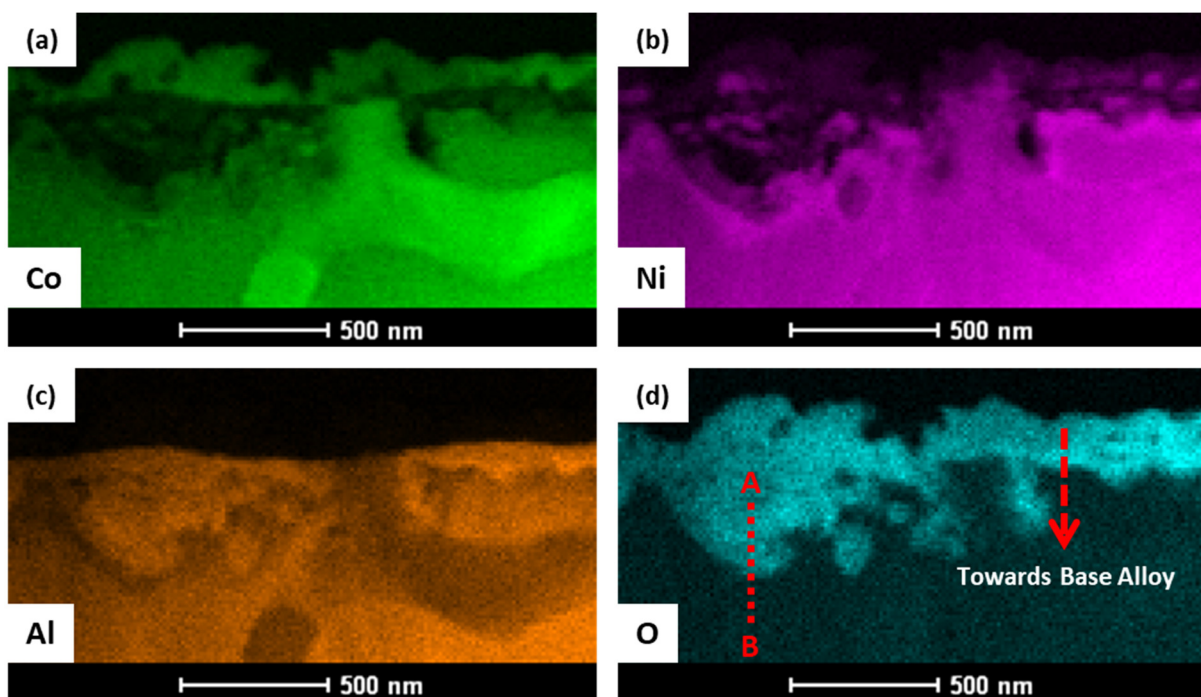


Figure 4.19 (a – d) Spatial elemental mappings using STEM – EDS nano probe, showing the distribution of Co, Ni, Al, O in the composite oxide surface layer

The difference between the selected area diffraction patterns from both the ‘top-hill’ and ‘under-hill’ oxide surface are also shown in Figure 4.20(a) and Figure 4.20(b) respectively. The composite oxide layer evidently comprises of two distinct layers viz. the Co-rich surface oxide and the Al-rich nano porous oxide, which grew over the base alloy just underneath Co-rich oxide layer. The STEM – EDS line composition profile taken along the straight dotted line ‘AB’ of Figure 4.19(d) is

shown in Figure 4.21 and it shows the distribution of the constituent elements from the 'top-hill' oxide surface layer to the bulk alloy. It also confirms the presence of oxygen, aluminium and cobalt at the top and oxygen concentration diminishing towards the bulk alloy. STEM – EDS quantitative point composition analyses from different places of the oxide surface layer and from the base alloy are tabulated in Table 4.1. It also confirms the presence of lesser amount of oxygen in bulk alloy and thus hints towards the hindrance of further diffusion of oxygen towards the bulk alloys.

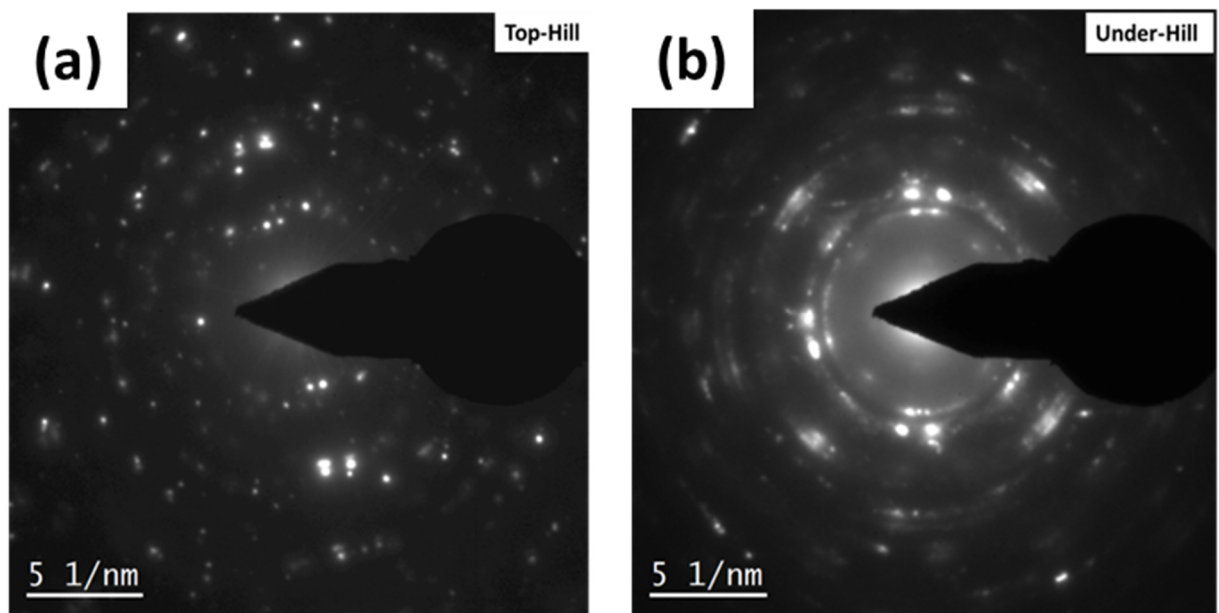


Figure 4.20 (a – b) Selected area diffraction pattern taken from top and under hill oxide layer showing the formation of different types of oxide layer

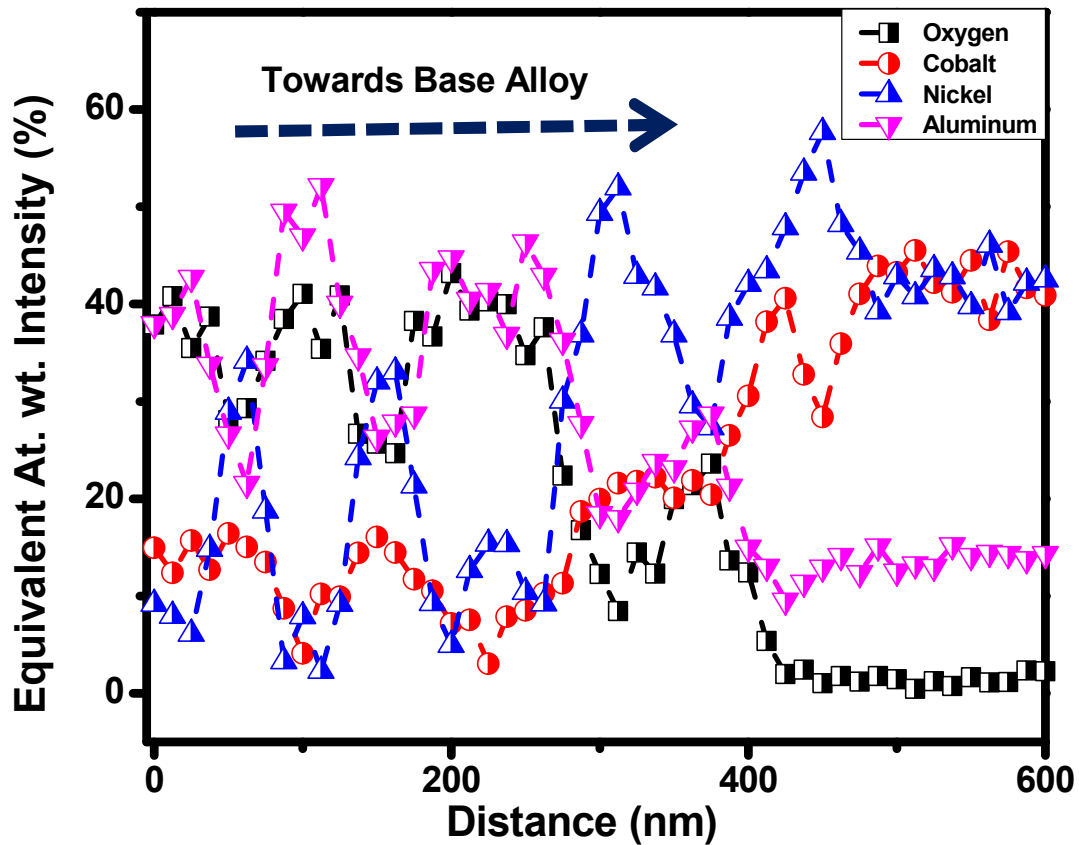


Figure 4.21 STEM – EDS line composition profile across the top hill layer and base alloy using a STEM nano probe along red line ‘AB’ of Figure 4.19(d)

Element	Top-Hill (atom %)	Under-Hill (atom %)	Base Alloy (atom %)
Co	32.0 ± 1.0	5.0 ± 0.3	32.3 ± 0.3
Ni	5.7 ± 0.5	9.7 ± 0.5	33.4 ± 0.6
Al	0.3 ± 0.02	28.0 ± 0.7	29.0 ± 1.0
O	62.0 ± 0.4	57.3 ± 1.0	5.3 ± 0.4

Table 4.1 Composition analysis of different composite oxide layers determined by STEM – EDS analysis for the Co-Ni-Al sample oxidized at 400 °C for 35 hrs.

Lower concentration of oxygen in the bulk alloy as confirmed from Table 4.1 and moderate rate constant of oxidation as shown in Figure 4.17 can be explained from the point of view that aluminium and cobalt rich oxide layers form a protective coating which restrict the further diffusion of oxygen over the prolonged time. It can also be noticed that under the oxidized layers, it is primarily still the B2 + L1₂ two phase microstructure. However, the B2 grains oxidized to a greater extent as compared to the L1₂ ordered phase to precipitate out plausibly the cobalt rich oxide nano sized precipitates within the B2 grains. These nano sized faulted type precipitates contribute extra weak spots in the diffraction pattern from B2 grains as shown in Figure 4.13(a). The L1₂ ordered matrix phase, being resistant to oxidation, possibly have dissolved oxygen, contributing to diffused intensities around the electron diffraction spots of the L1₂ reflections observed at 400 °C for a lesser holding time 2 hrs. as shown in Figure 4.13(b). This alloy is comparatively oxidation resistant with a moderate oxidation rate constant value in comparison to other Co and Ni based alloys [4.11, 4.15, 4.16]. This can be attributed to the formation of irregular shaped composite oxide surface and the presence of an aluminium rich oxide layer. Al rich oxides tend to show less spallation because of its better adhesion and work as a protective layer [4.16].

4.5 Magnetic characterization of oxidized sample

All the magnetization measurements of the Co-Ni-Al FSMA sample were performed using a Lake Shore model 7400 vibrating sample magnetometer and were done in a temperature range from 80 K to 400 K. As a result of heat treatment and oxidation of the sample at 400 °C for different holding times, the magnetic properties of the alloy are found to be remarkably affected as is evident from the Figure 4.22(a-c). The saturation magnetization (M_s) and coercivity (H_c) of the as spun as well as the oxidized samples at different holding times are tabulated below in Table 4.2. From the tabular data it is quite evident that the ferromagnetic behaviour of the ribbon sample drastically improved after the first heat treatment. The H_c was greatly enhanced by about 8 times and M_s similarly got improved by 1.5 times. Further heat treatment eventually suppressed the M_s , even if H_c monotonically kept on enhancing. This remarkable turn of events can be understood by looking at the microstructure evolution during prolonged annealing

discussed in the previous sections of this chapter. While the annealing temperature is too low for further grain growth or change in overall morphology, nonetheless, it had notable changes in the intergrain. Fine nanometre sized Co precipitates appeared inside the B2 grains and oxygen leaching of the grains. Magnetic property followed a similar trend. Initially, with the emergence of pure Co nanoparticles, ferromagnetic property improved, but later on due to the oxidation of Co and Ni atoms, it became ferritic, so only H_c could be enhanced [4.17].

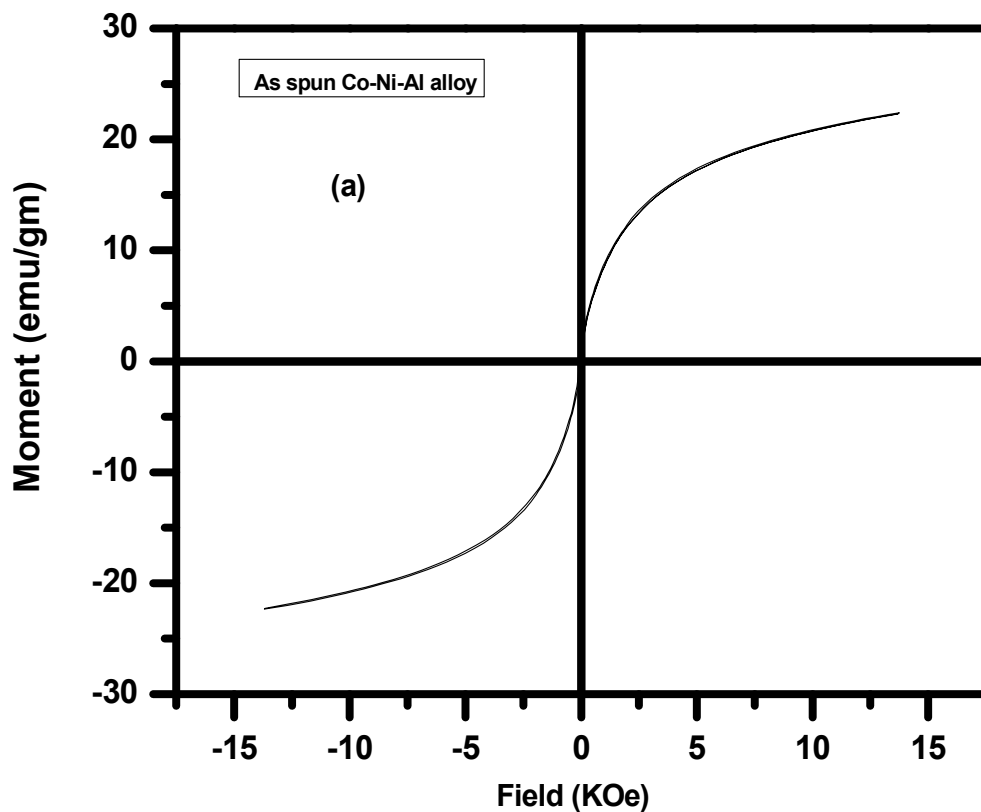


Figure 4.22 (a) Magnetization hysteresis (M – H) curve of as spun $Co_{34}Ni_{35}Al_{31}$

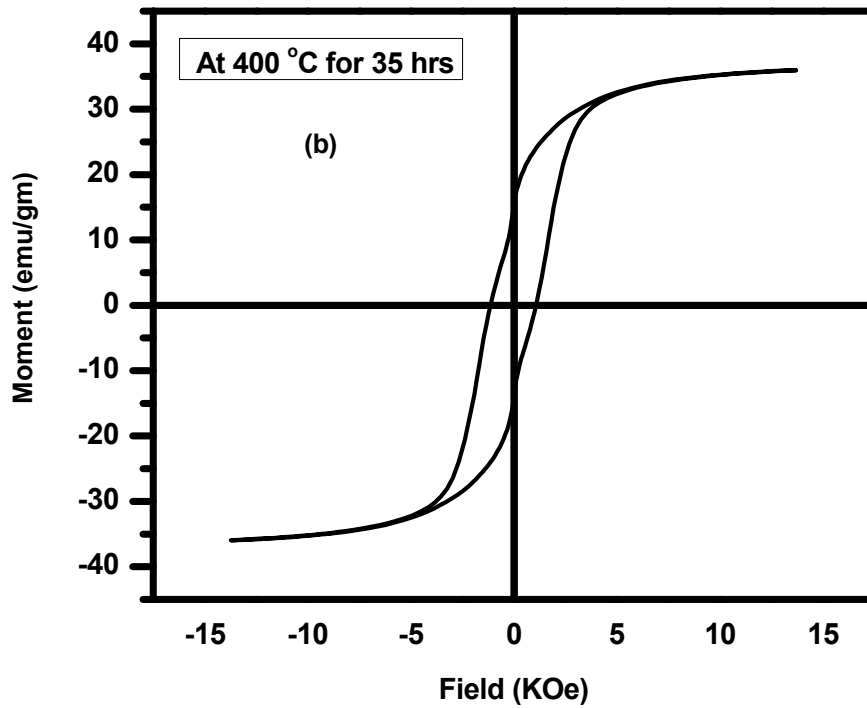


Figure 4.22 (b) (M – H) curve of the alloy oxidized at 400 °C for 35 hrs.

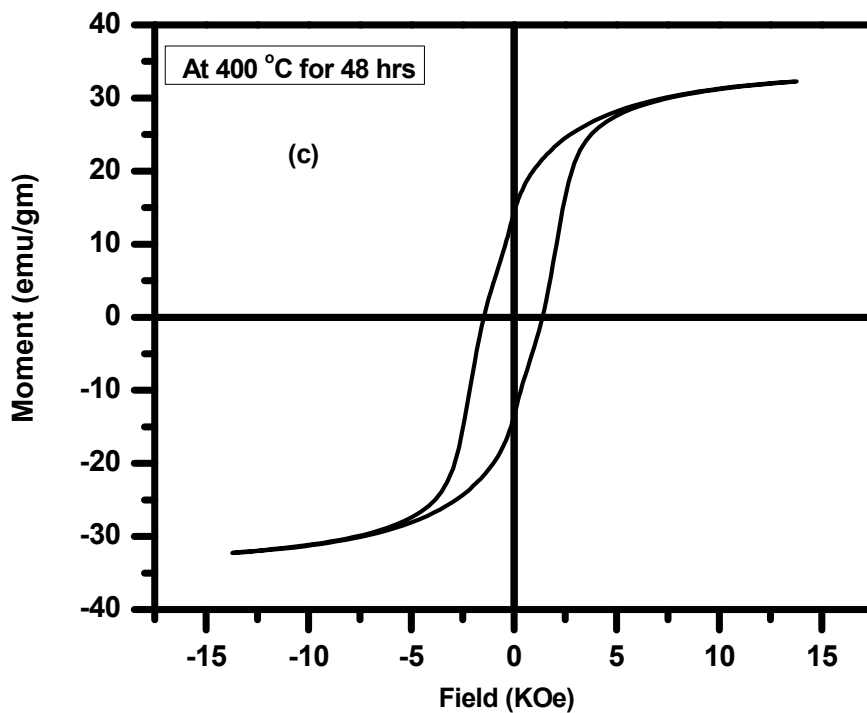


Figure 4.22 (c) (M – H) curve of the alloy oxidized at 400 °C for 48 hrs.

Sample	Saturation Magnetization (M_s) (emu/gm)	Coercivity (H_c) (Oe)
Co ₃₄ Ni ₃₅ Al ₃₁ as spun alloy	22	78
Co ₃₄ Ni ₃₅ Al ₃₁ alloy oxidized at 400 °C for 5 hrs.	35	456
Co ₃₄ Ni ₃₅ Al ₃₁ alloy oxidized at 400 °C for 35 hrs.	36	1141
Co ₃₄ Ni ₃₅ Al ₃₁ alloy oxidized at 400 °C for 48 hrs.	32	1468

Table 4.2 Magnetic properties of as spun and oxidized Co₃₄Ni₃₅Al₃₁ FSMA

This assertion about the presence of Co-oxide atoms can also be brought out in another way. The difference between the initial parts of M-H loops for the as spun sample shown in Figure 4.22(a) and another oxidized sample, like the one with the 35 hrs. heat treatment as depicted in Figure 4.22(b) may be plotted together along with their difference and is shown in Figure 4.23. The characteristic soft magnetic behaviour, small rise and droop after a quick saturation in a small field were also reported before for Co-Oxide nanoparticles [4.18]. These Co-oxide rich precipitates associated with strain fields provided the pinning centres, thus hindering the domain wall rotation and consequently opening up the hysteresis loop. The total effect is an increase in the hysteresis loop, even if with higher magnetic moments, and thus the ferromagnetic character of the sample is enhanced [4.17]. It has to be noted that it is not possible to draw the full M-H loop this way, because each of the two field values are not the same due to different instrument run and this error is magnified near zero values, but most importantly the H_c and remnant values being quite different for the two samples render the subtraction meaningless.

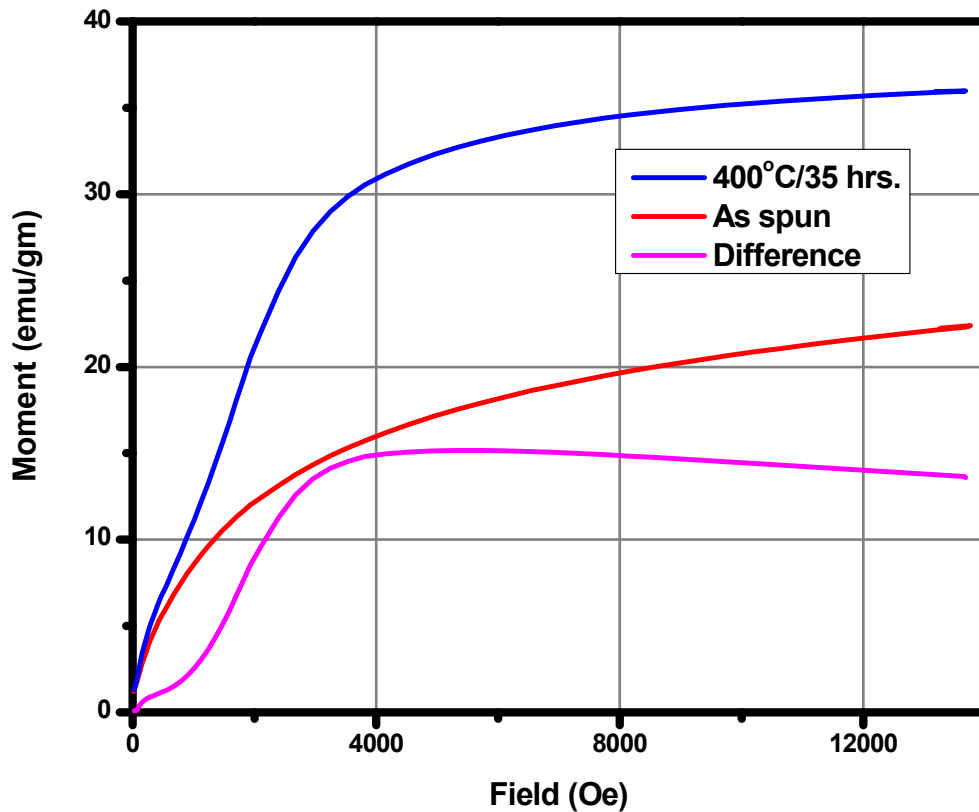


Figure 4.23 Initial rise of (M – H) for as spun and oxidized samples with their difference

4.6 Conclusions

In this chapter, the limiting functionality of photo induced micro actuation (PIMA) effect of this particular $\text{Co}_{34}\text{Ni}_{35}\text{Al}_{31}$ alloy at elevated temperatures and in ambient atmosphere was studied to establish the correlation between the microstructural changes and its direct effect on PIMA property. This will be useful information for further engineering design in future. The results show that with increasing annealing temperature, PIMA property monotonically degrades and stops at 400 °C. Earlier studies on this specific alloy system implicitly suggested that combination of ferromagnetically coupled shape memory property is the key possible reason behind the PIMA effect [4.1]. Only ferromagnetic alloy or pure shape memory alloy system does not show this unexplored PIMA property. Therefore, in this chapter, the focus was on the changes in these two important functioning properties during the heat treatment of the FSMA sample. The microstructural studies confirm the existence of B2 ordered micron sized grains

embedded in L1₂ ordered matrix channel, where the B2 ordered phase is the key responsible and active phase for ferromagnetic shape memory response whereas the L1₂ ordered FCC matrix only imparts the ductility into the alloy [4.19 – 4.22]. Detailed structural study shows the evolution of nanometre sized cobalt rich precipitates with fine faulted type morphology inside the B2 ordered grain along with traces of oxygen at 400 °C. The evolution of cobalt rich nano meter sized precipitates at 400 °C inside the B2 ordered grain certainly alters the B2 ordered phase and thus affect the functionality of the ferromagnetic shape memory effect. A plausible cause to form Co rich phase can be the stability of Ni-Al phase of the B2 grain over the Co-Al phase for a pseudo type (Co, Ni)-Al B2 ordered structure.

The opening up of the hysteresis loop, exhibiting enlarged coercivity of the FSMA alloy sample at 400 °C, enhancing the ferromagnetic characteristics of the sample was also reported in this chapter. This can be associated with oxidation or the pinning of magnetic domain due to the presence of coherently strained cobalt rich precipitates phase, evolved during heat treatment of the alloy sample. The magnetic studies of the as prepared and the oxidized samples also point to the fact that only better ferromagnetic nature by itself will not always enhance the PIMA effect shown by FSMAs. It is evident that the broadening of XRD peak at 400 °C can be attributed with strained matrix due the presences of this nano sized precipitates. Prolonged annealing of the sample at 400 °C in ambient atmosphere shows the diffusion of cobalt from the bulk alloy to the top surface of the newly formed irregular composite oxide layer. Due to this, the saturation magnetization increases along with the coercivity for the heat treated alloy. The diffraction studies also confirm that the B2 grain oxidized more compared to L1₂ ordered phase to precipitate out plausibly Co rich oxide nano sized precipitates within B2 grains.

Limited oxidation kinetics studies of the sample show that this alloy is comparatively oxidation resistant with a moderate oxidation rate constant value in comparison to other Co and Ni based alloys. This can be attributed to the formation of irregular shaped composite oxide surface and the presence of aluminium rich oxide layer. Al rich oxides tend to show less spallation because of its better adhesion and work as a protective layer. The gradual suppression of colour dependence of the PIMA effect is highly intriguing. From the blue coloured laser

beam having the highest amplitude of actuation in room temperature, it gradually weakened to having equal and then lower value than that of green, which had middle efficiency before. This is another riddle in the physical aspect of PIMA effect and is actually making the effect more diverse. This present chapter attempts to report the effect of temperature and oxidation on the photo induced micro actuation property shown by Co-Ni-Al FSMA. Systematic studies have been carried out to determine the feasibility of implementing the PIMA effect for operation and control of any perceived microactuator system in the near future where the system will be exposed to various levels of heat exposure in open air condition.

CHAPTER 5: INVESTIGATION OF COPPER DOPING ON PIMA EFFECT IN Co-Ni-Al ALLOYS

5.1 Introduction

The investigations carried out to determine the workability of the selected Co-Ni-Al FSMA system in various environmental conditions where it is subjected to different levels of heat and oxidation, have been reported in detail in the previous chapter of this thesis. These studies paved the way for successful implementation of a new class of laser controlled remotely operated microactuator systems in the near future. Co-Ni-Al was chosen as the preferred FSMA system for use in practical applications due to their better ductility and other mechanical properties as compared to conventionally studied FSMAs like Ni-Mn-Ga. While the base system was fine with PIMA effect, there is a need to find more efficient systems for PIMA property. Hence, further efforts were made to improve the ductility, elastic modulus and other mechanical properties of the $\text{Co}_{34}\text{Ni}_{35}\text{Al}_{31}$ sample hereby denoted as 'Sample A' in this chapter, while retaining an optimized level of the PIMA properties. Attempts have been made in the recent past to improve the mechanical properties as well as to optimize other operational properties of different FSMA systems by doping appropriate proportions of copper and other doping elements [5.1 – 5.4]. These efforts were successful in improving the mechanical properties while fine tuning other operational properties of the chosen FSMAs.

Appropriate proportions of copper were added as a partial substitution for cobalt and aluminium sites to the earlier composition. In the first copper doped Co-Ni-Al system that was prepared, 2% of cobalt by atomic weight percentage was replaced by copper resulting in an alloy composition of $\text{Co}_{32}\text{Cu}_2\text{Ni}_{35}\text{Al}_{31}$ hereby denoted as 'Sample B'. The next set of copper doped Co-Ni-Al alloy had an atomic weight percentage composition of $\text{Co}_{24}\text{Cu}_{10}\text{Ni}_{35}\text{Al}_{31}$ denoted as 'Sample C' from hereon. The third alloy was prepared to try to replace aluminium with copper by 10 atomic weight percentage resulting in the $\text{Co}_{34}\text{Ni}_{35}\text{Al}_{21}\text{Cu}_{10}$ sample henceforth symbolized as 'Sample D'. Investigations were then carried out to determine the

effect of different proportions of copper doping on the PIMA effect of the as-spun Co-Ni-Al alloy. Simultaneous studies were also carried out to determine the improvement in the desired mechanical properties of the newly developed copper doped Co-Ni-Al FSMAs. Comparing both the PIMA data as well as other physical properties of the undoped Co-Ni-Al and the different copper doped alloys, the effect of copper doping on the PIMA property of Co-Ni-Al alloys could be established. Transmission Electron Microscopy (TEM) and X-ray diffraction (XRD) studies were also used to characterize the underlying microstructure for the undoped Co-Ni-Al and the newly developed copper doped FSMA samples. Magnetic properties of the new alloy systems were also studied systematically to adjudge the feasibility of implementing the PIMA effect of the newly developed copper doped Co-Ni-Al alloys for operation and control of suitable microactuator systems.

5.2 Effect of copper doping on PIMA property

5.2.1 Effect of copper doping on laser power dependent actuation

In order to systematically compare the outcome of copper doping on the microactuation property of Sample A, firstly the power dependence of the PIMA effect was observed for the as prepared copper doped Co-Ni-Al ribbon samples. This was done to study the change in the amplitude and nature of microactuation achieved by the newly prepared copper doped ribbons as compared to the original microactuation data of the undoped sample recorded earlier [5.5]. The first system that was chosen for the laser induced optical experiments was the Sample B discussed earlier. The amplitudes of microactuation or displacements of Sample B ribbon when excited by the focused laser beams as compared to the undoped Sample A are plotted in Figure 5.1. From the graph it can be seen that the PIMA effect of the copper doped Sample B holds its linear nature as reported earlier when the sample is incident by the focused laser beams. It can also be observed from this plot that the colour dependence of the PIMA effect reported earlier is still present in the doped alloy system. Hence, it can be inferred that the fine-tuned control mechanism achieved earlier by selecting the laser power as well as colour of the incident laser beam is still applicable in operating any proposed microactuator system if this alloy system is used to fabricate the sensing and

actuating parts of the perceived microactuators. Analysis of the microactuation data of the Sample B indicates that the slopes for the blue, green and red lasers are 1.62, 1.47 and 1.28 respectively. These values are somewhat less than the data of the undoped sample as reported in Chapter 3. There is a loss of approximately 20% in the total amplitude of actuation achieved by this copper doped sample as compared to the undoped sample. Thus, it can be inferred from this investigation that the copper doped Sample B alloy system is quite suitable for fabrication and controlled operation of any perceived microactuator based on the PIMA property, even if at a lower level of actuation.

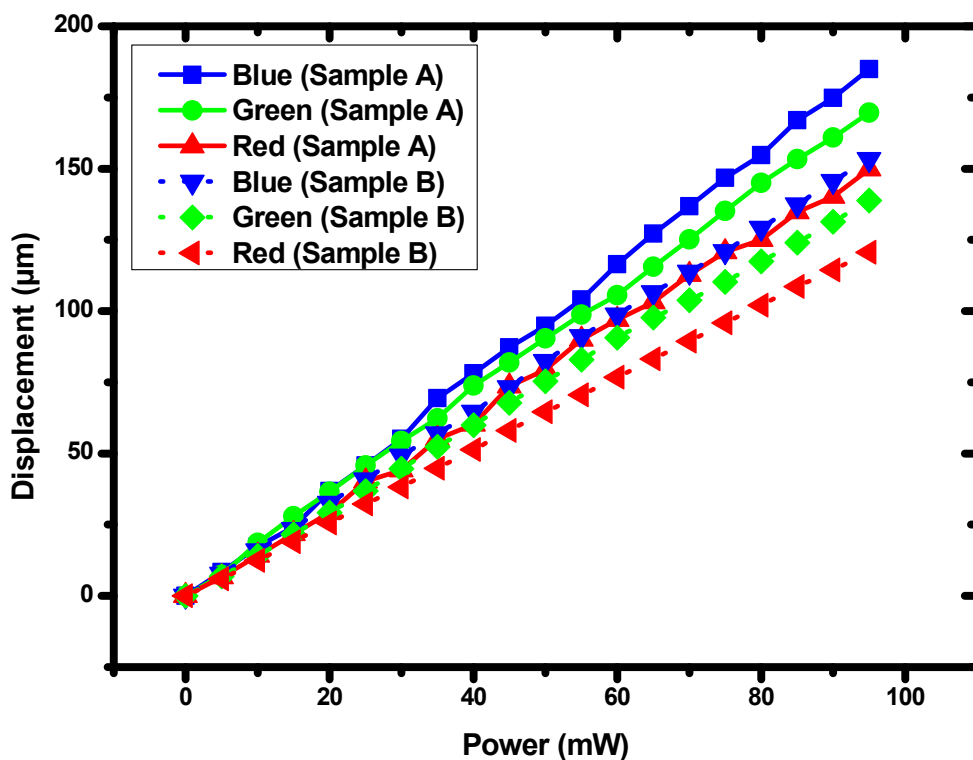


Figure 5.1 Comparison between laser power dependent PIMA effect of Sample A ($\text{Co}_{34}\text{Ni}_{35}\text{Al}_{31}$) and Sample B ($\text{Co}_{32}\text{Cu}_2\text{Ni}_{35}\text{Al}_{31}$)

After performing the laser power dependent optical experiments on Sample B, the same laser induced investigations were carried out on the next set of copper doped Co-Ni-Al FSMA system i.e. the Sample C. The amplitudes of microactuation achieved by the Sample C ribbon when excited by the focused laser beams as compared to the undoped Sample A is shown in Figure 5.2. From the figure it can be seen that the PIMA property of the as prepared Sample C still holds the linear

nature of the earlier FSMA samples, however, the colour dependence of the effect reported earlier has changed significantly. Though the blue coloured laser still achieves more microactuation than the green coloured laser which in turn attains more microactuation than the red coloured laser, the differences in the amplitudes for them have diminished considerably i.e. the microactuation accomplished is much closer to each other than before, as is evident from the slopes of the plots, 0.64 for blue, 0.57 for green and 0.47 for red respectively. It is noteworthy to infer from the data shown in the figure that the total amplitudes of microactuation of the ribbon Sample C have drastically reduced to less than one third of the microactuation achieved by the undoped sample. These observations will help in determining the limitations of using this system in the fabrication and operation of any perceived microactuators in the near future.

The next set of copper doped Co-Ni-Al FSMA system that was used to perform the optical experiments was the final alloy denoted as Sample D. When the laser power dependent optical experiments were done on this sample, no microactuation was observed in the ribbon even when it was excited by the focused laser beams at their maximum output power of 95 mW. Hence it can be concluded that this alloy composition or Sample D does not possess the PIMA property as shown by the other melt spun FSMA ribbons and thus is unsuitable for use in any PIMA operated microactuator application. The maximum amplitude of microactuation achieved by the copper doped Co-Ni-Al FSMA samples in comparison with the undoped Co-Ni-Al FSMA for all the three different coloured laser beams is shown schematically in Figure 5.3. The comparative data shows that the Sample B can act as a suitable replacement for the Sample A FSMA system if its ductility and other relevant mechanical properties are relatively improved.

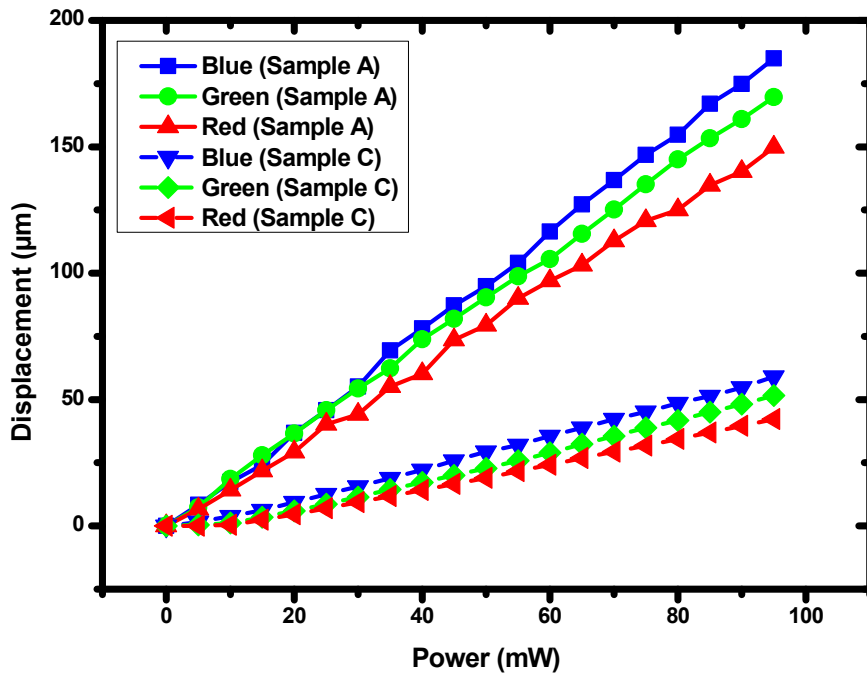


Figure 5.2 Comparison between laser power dependent PIMA effect of Sample A ($\text{Co}_{34}\text{Ni}_{35}\text{Al}_{31}$) and Sample C ($\text{Co}_{24}\text{Cu}_{10}\text{Ni}_{35}\text{Al}_{31}$)

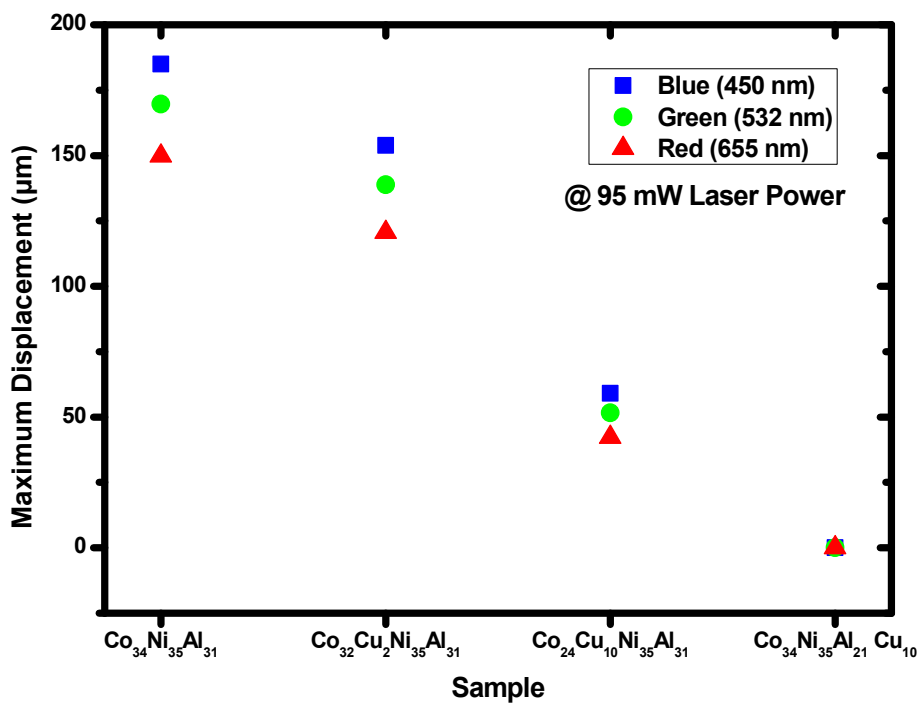


Figure 5.3 Comparison between maximum displacement of all the samples at room temperature

5.2.2 Effect of copper doping on laser polarization dependent actuation

Besides the laser power dependent control mechanism, another controlling factor of the PIMA effect was reported earlier which depended on the polarization of the output laser beams [5.5]. Hence the laser polarization dependent PIMA properties of the copper doped Co-Ni-Al FSMA samples were studied additionally for the three different coloured laser beams. The first copper doped sample that was chosen for the laser polarization dependent optical experiments was the Sample B system. The amplitude and nature of microactuation achieved by the Sample B ribbon when excited by the polarized laser beams as compared to the undoped FSMA is shown in Figure 5.4. It can be seen from the graph that the laser polarization dependent PIMA effect of the copper doped Sample B holds its periodic nature as reported earlier when the sample was irradiated by the focused laser beams. It is also evident from this plot that the colour dependence of the PIMA effect is still present along with the laser polarization dependent control mechanism. Thus, it can be inferred that the fine-tuned control mechanism achieved earlier by selecting the laser polarization as well as colour of the incident laser beam is still applicable for the Sample B. The comparative graph also shows a nominal decrease in the total actuation achieved by the copper doped sample. Hence, it can be again inferred from this investigation that the copper doped Sample B ribbon is quite suitable for fabrication and controlled operation of any perceived microactuator based on the PIMA property.

After performing the laser polarization dependent optical experiments on the Sample B, the same laser stimulated investigations were carried out on the next set of copper doped Co-Ni-Al FSMA system i.e. Sample C. The amplitude and nature of microactuation achieved by the Sample C when stimulated by the different coloured polarized laser beams as compared to the undoped Sample A is plotted in Figure 5.5. From the plot it can be observed that the laser polarization dependent PIMA property of the as prepared Sample C alloy still holds the periodic nature of the earlier FSMA samples. It is also evident from this plot that even though the periodic nature of the PIMA property is still intact for this second copper doped Co-Ni-Al FSMA, the colour dependence of the effect reported earlier has reduced slightly as compared to the undoped sample. This observation is in accord

with the laser power dependent data of the PIMA property shown by the sample in Figure 5.2. The decrease in the overall amplitude of actuation achieved by this sample is quite evident from the graph and this decrease again follows the trend plotted earlier in Figure 5.2. As it has already been established that the Sample D does not possess the PIMA property like the other melt spun FSMA ribbons, the laser polarization dependent investigations were not conducted on this sample.

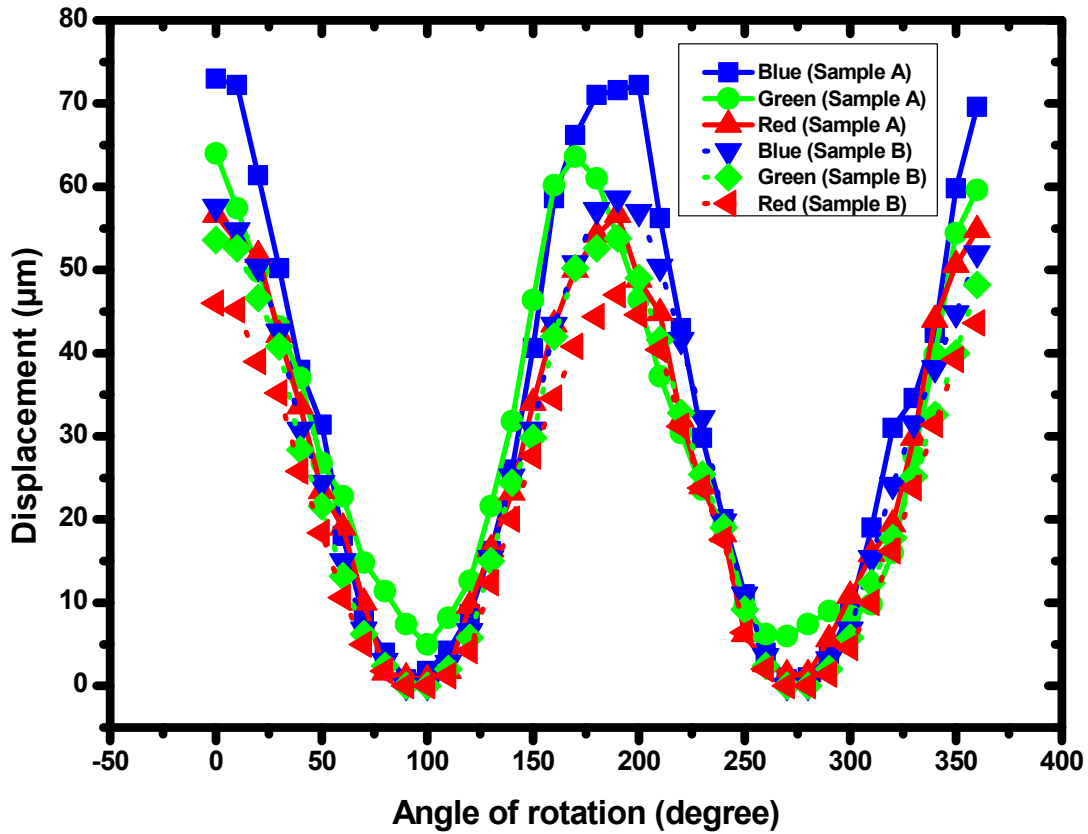


Figure 5.4 Comparison between laser polarization dependent PIMA effect of Sample A ($\text{Co}_{34}\text{Ni}_{35}\text{Al}_{31}$) and Sample B ($\text{Co}_{32}\text{Cu}_2\text{Ni}_{35}\text{Al}_{31}$)

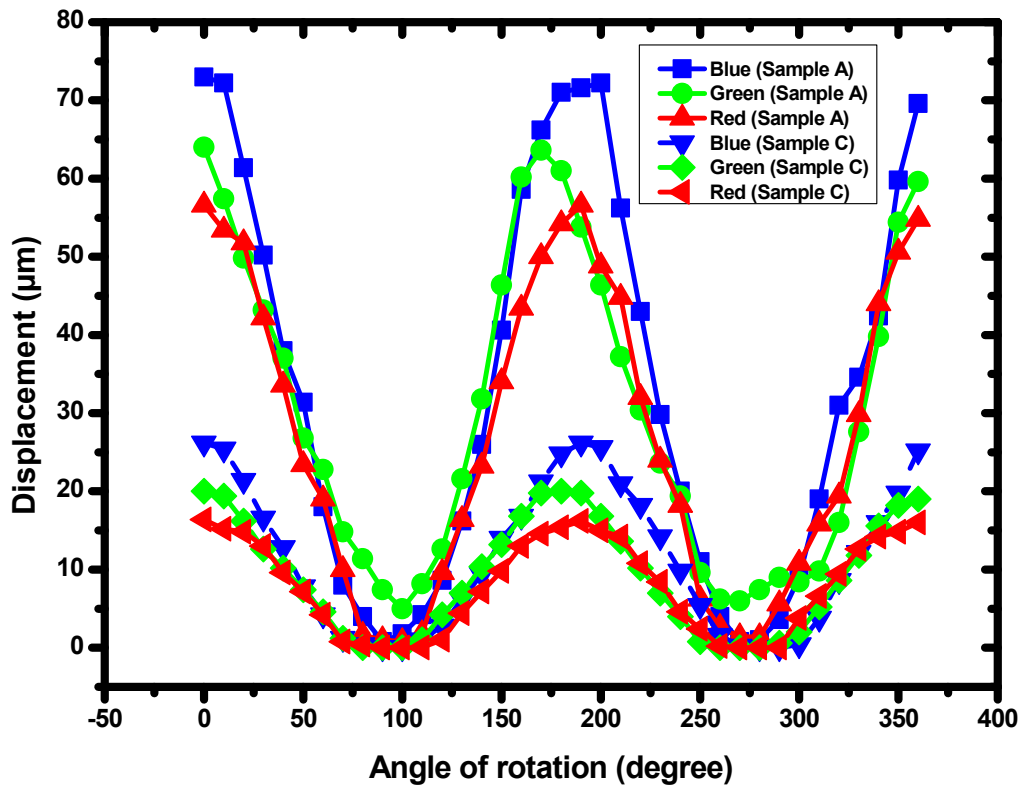


Figure 5.5 Comparison between laser polarization dependent PIMA effect of Sample A ($\text{Co}_{34}\text{Ni}_{35}\text{Al}_{31}$) and Sample C ($\text{Co}_{24}\text{Cu}_{10}\text{Ni}_{35}\text{Al}_{31}$)

5.3 Improvement in mechanical properties of copper doped Co-Ni-Al

It has already been stated earlier in Chapter 2 that the tensile testing of the alloy ribbons was performed using an INSTRON Model 3365 electromechanical universal testing system to study the yield strength and the ductility of the samples so that the usability of the selected FSMA's in practical applications can be determined. To optimize the strain rate, tests were performed with 10^{-3} s^{-1} and 10^{-4} s^{-1} strain rates initially. As the alloys did not show any strain rate sensitivity in this range, all the subsequent tests were performed with a strain rate equal to 10^{-3} s^{-1} . From Section 5.2 it can be observed that the Sample D does not react to the laser interaction at all, whereas the Sample C alloy demonstrates the limiting case of the PIMA property. Thus, the undoped Sample A i.e. $\text{Co}_{34}\text{Ni}_{35}\text{Al}_{31}$ and the copper doped Sample C i.e. $\text{Co}_{24}\text{Cu}_{10}\text{Ni}_{35}\text{Al}_{31}$ alloys were investigated for the comparison of mechanical properties. The thinness of the melt spun alloy ribbons as compared to the length and breadth of the ribbon samples will contribute to the size effects of

the mechanical properties of the samples and thus alter the mechanical behaviour of the melt spun ribbons from the standard ASTM samples used to determine the mechanical properties of bulk samples of the same composition [5.6, 5.7]. Hence, only a qualitative trend of the obtained data was evaluated to determine the mechanical performance of the undoped as well as the copper doped alloys. The samples were cut into a rectangular shape with its length and breadth ratio larger than 10:1. Hard epoxy was applied to both the ends of the rectangular samples for gripping with the wedge type gripper of the INSTRON system to avoid slipping during tensile testing.

The Engineering Stress vs. Engineering Strain plots of the Sample A and the Sample C obtained under tension at room temperature is shown in Figure 5.6. From analysing the results, it can be calculated that at room temperature, copper doped Sample C exhibits 0.2% yield stress around 51 ± 8 MPa with $53 \pm 1\%$ elongation to failure. Similarly, it can be calculated that the undoped Sample A attains 0.2% yield stress near 12 ± 5 MPa with $25 \pm 2\%$ elongation to failure. A significant improvement in the ductility and strength of the Sample C can be observed as compared to the Sample A. The serrated flow curve observed in case of the Sample A alloy may be ascribed to the presence of frozen free volume originated during melt spinning and normal observation for ribbon samples [5.6, 5.7]. From analysing the effects of copper doping on both the PIMA property as well as the mechanical properties of the FSMAs, significant improvement of the mechanical properties of the FSMAs can be observed at the expense of a systematic degradation of its PIMA property. As copper itself is a ductile element, the effect of copper doping in the cobalt sub lattice of the sample may have induced a softer phase in the microstructure of the sample which results in significant improvement in the ductility of the copper doped samples as compared to the undoped Co-Ni-Al sample. The microstructural evolution of the copper doped sample is discussed in details in the next section of this chapter. Based on these results, an optimized copper doped Co-Ni-Al FSMA system can be designed which will be suitable for various practical applications employing the PIMA effect.

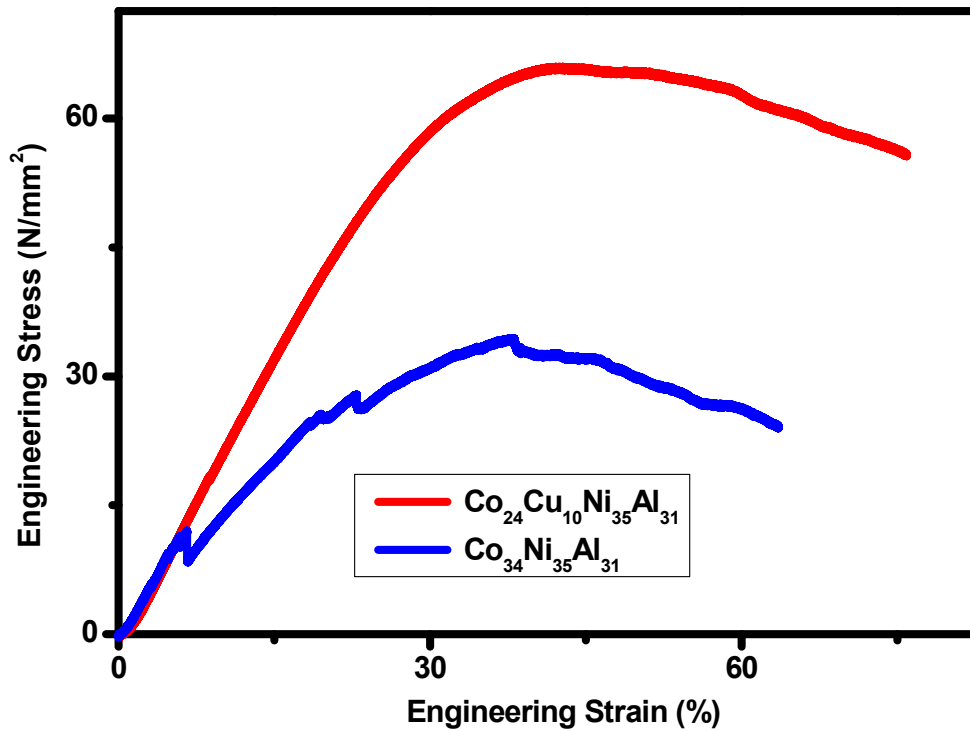


Figure 5.6 Engineering Stress vs Engineering Strain plot under tension at room temperature for Co₃₄Ni₃₅Al₃₁ and Co₂₄Cu₁₀Ni₃₅Al₃₁ alloys

5.4 Microstructural evolution of copper doped samples

The results of the thorough microstructural investigations reported in the earlier chapters of this thesis established the basic notion about the role of the Ni-Al type active B2 phase for the PIMA property shown by the FSMA sample. As reported earlier in Section 5.2, Sample D does not possess the PIMA property whereas Sample C demonstrates the limiting case of the PIMA effect. As a result, these two above mentioned samples were chosen for the microstructural investigations as two limiting case where the role of copper doping in PIMA and mechanical properties can be correlated with the microstructural information.

5.4.1 Microstructural evolution of $\text{Co}_{24}\text{Cu}_{10}\text{Ni}_{35}\text{Al}_{31}$

The bright field TEM image of the Sample C alloy sample is shown in Figure 5.7. This bright field image indicates the evolution of different kinds of morphology in the microstructure during phase transformation process. The selected area diffraction patterns taken along the [001] zone axis of the BCC phase marked as 'A' in Figure 5.7 confirms the BCC based B2 type ordering of the embedded grains as shown in Figure 5.8(a). Similarly, the selected area diffraction patterns taken along the [011] zone axis of the FCC type matrix channel marked as 'B' in Figure 5.7 confirms the FCC based $L1_2$ ordering of the matrix channel as shown in Figure 5.8(b). From Figure 5.7 it is also evident that in addition to the existence of B2 ordered grains, that were observed in the undoped Sample A, the B2 ordered grains of this copper doped alloy have different kinds of morphological features. The bright field TEM image of one of the B2 grains shown in Figure 5.9(a) reveals the compositional wave type modulated morphology. The diffraction pattern taken from this B2 region shown in the inset of Figure 5.9(a) hints at the existence of spinodal type compositional modulation features inside this particular B2 ordered grain [5.8]. The blown-up version of the blue dotted box of Figure 5.7 is shown in Figure 5.9(b). It reveals the presence of another type of microstructural attribute inside one of the adjacent B2 ordered grains. Localized morphology of the selected B2 grain shows the presence of martensitic plates. Splitting of the diffraction spots along with the fundamental spots of classical B2 ordered diffraction pattern indicates the occurrence of martensitic phase within this grain as shown in the inset of Figure 5.9(b). Slight variation of the fundamental spots from regular square type arrangement in the diffraction pattern along with diffused streaking between the diffraction spots along the [001] BCC zone axis establishes the structural modulation of the martensite plates as is evident from the inset of Figure 5.9(b) [5.9 – 5.13].

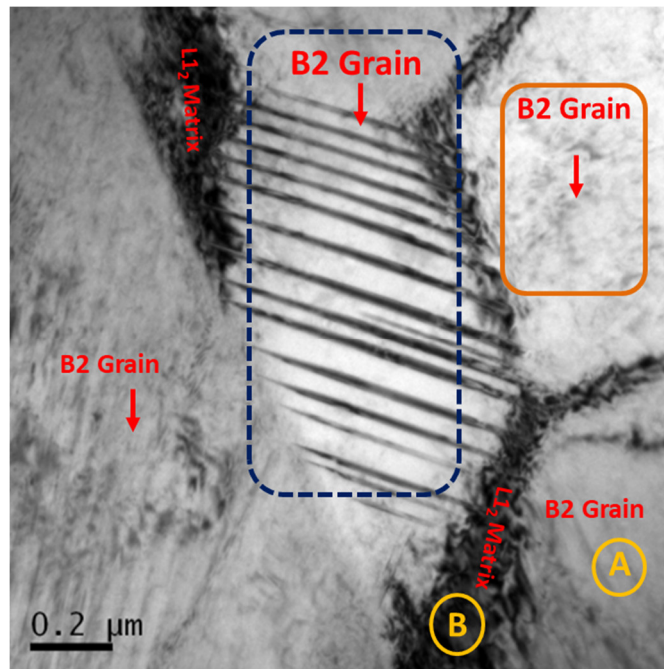


Figure 5.7 Bright field TEM image showing the existence of B2 ordered grain having two different kinds of phase transformational morphology and L1₂ ordered matrix channel in the as spun Co₂₄Cu₁₀Ni₃₅Al₃₁ alloy sample

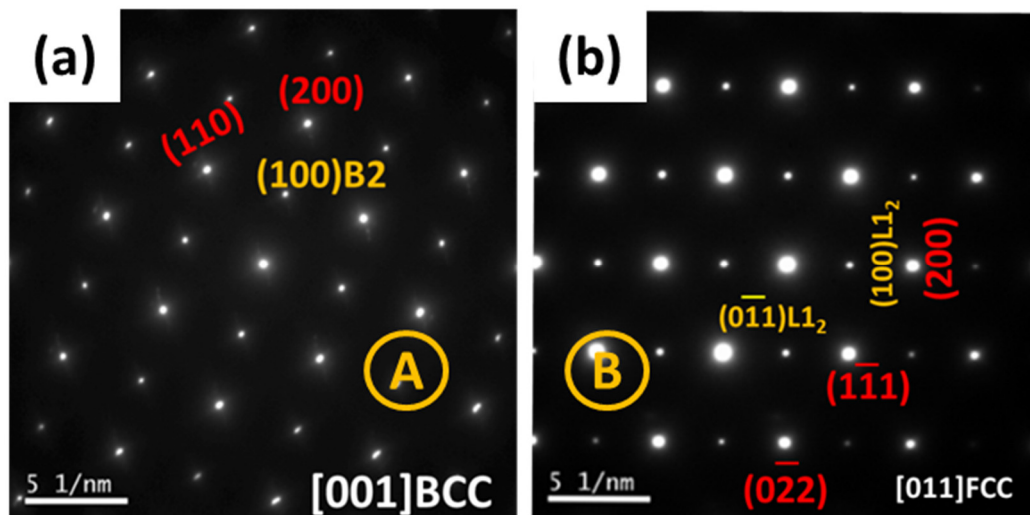


Figure 5.8 (a) Selected area diffraction pattern taken along [001] zone axis of the BCC grain marked as 'A' in Figure 5.7 (b) Selected area diffraction pattern taken along the [011] zone axis of FCC matrix channel marked as 'B' in Figure 5.7

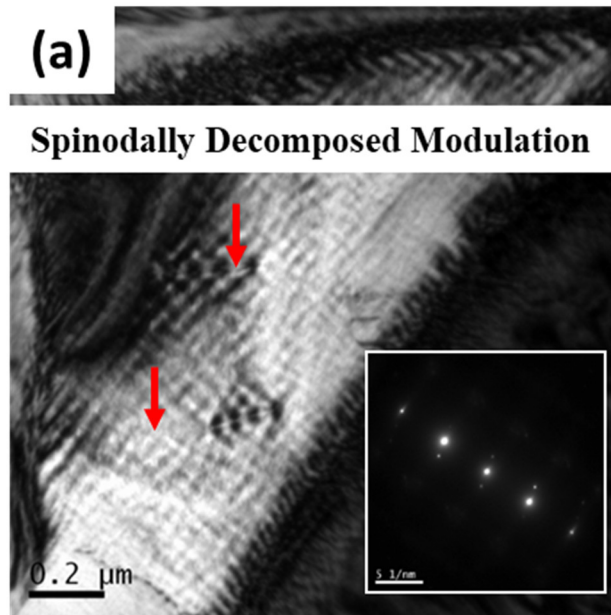


Figure 5.9 (a) Bright field image of orange box marked area of Figure 5.7 showing the compositionally modulated and spinodally decomposed morphology of the B2 ordered grain

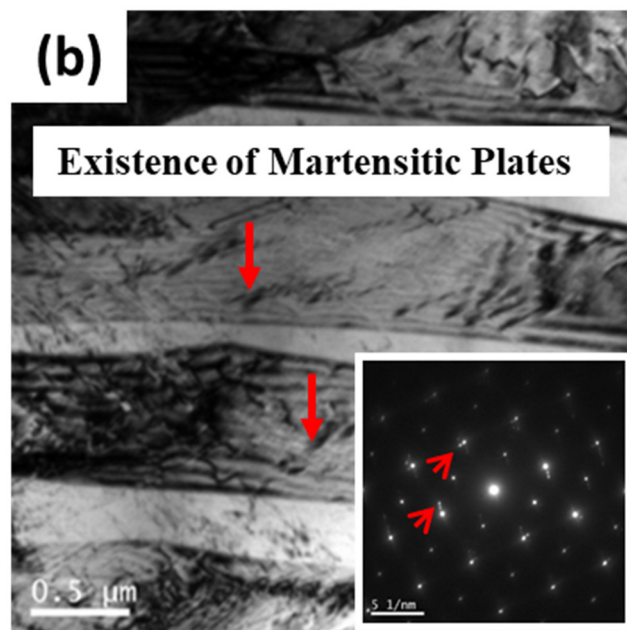


Figure 5.9 (b) Bright field image of blue dotted box marked area of Figure 5.7 showing the existence of martensitic plates inside the B2 ordered grain

The STEM – HAADF image shown in Figure 5.10 displays the atomic number contrast of the constituent phases of the as spun Sample C. The image reveals that the L1₂ ordered phase along the channels surrounding the B2 grains are composed of higher concentration of relatively heavy elements as compared to the B2 grains. The STEM – EDS mapping images shown in Figure 5.11(a – d) demonstrate the spatial elemental distribution of the constituent elements of the alloy in the evolved microstructure. The qualitative analysis of these mappings indicates that the dark contrast B2 ordered grains, embedded in the L1₂ matrix channel are rich in nickel and aluminium as reported in the earlier chapters of this thesis for the case of the undoped Sample A. It can also be observed qualitatively that the B2 ordered grains have partially lesser concentration of cobalt and copper inside them. Similarly, it can be concluded from the figures that the L1₂ ordered matrix channels are depleted in nickel and aluminium whereas it is rich in cobalt and copper. Interestingly, it can be noted that FCC copper has chosen the structurally comfortable FCC based L1₂ ordered matrix channels and it has a significant role in improvement of mechanical properties of this alloy as discussed earlier in Section 5.3 of this thesis. The STEM – EDS line composition profile presented in Figure 5.12 validates the similar distribution nature of the elements as seen in the spatial elemental mapping along the yellow dotted line marked as ‘AB’ in Figure 5.10.

It is evident from the obtained data that partial substitution of cobalt by copper changes the parent microstructure of the undoped Sample A. Composition alteration of FSMAs always plays a significant role in the modification of FSME properties and influences the transformation temperature of the alloys [5.11, 5.14 – 5.16]. The relatively unexplored PIMA property shown by FSMAs is qualitatively associated with the presence of active B2 ordered phase and structural and compositional degradation of B2 ordered phase always plays an important role on this PIMA property as discussed earlier in Chapter 4 of this thesis. The partial substitution of cobalt by copper does not disturb the concentration of main constituent Ni-Al phase for the B2 ordered phase as is evident from Figure 5.11(a – d). The affinity of copper towards the L1₂ ordered matrix phase thus does not hamper the structural integrity of the B2 ordered phase and hence does not affect the PIMA property drastically. The presence of martensitic plates inside the B2

ordered grain can be directly associated with the doping of copper due to the change in transformation temperature [5.11, 5.14 – 5.16]. Apparently, evolution of martensitic structure inside the B2 grain brought in accommodation strain in the lattice. This strain can lead to the stress assisted spinodally decomposed modulated structure in the adjacent B2 ordered grain to minimize the overall lattice strain [5.8]. Evidently, simultaneous presence of unaltered B2 ordered grains and the presence of martensitic plates and spinodal modulation inside some of the B2 ordered grains are the key factors for scaling down of the amplitude of PIMA effect in Sample C.

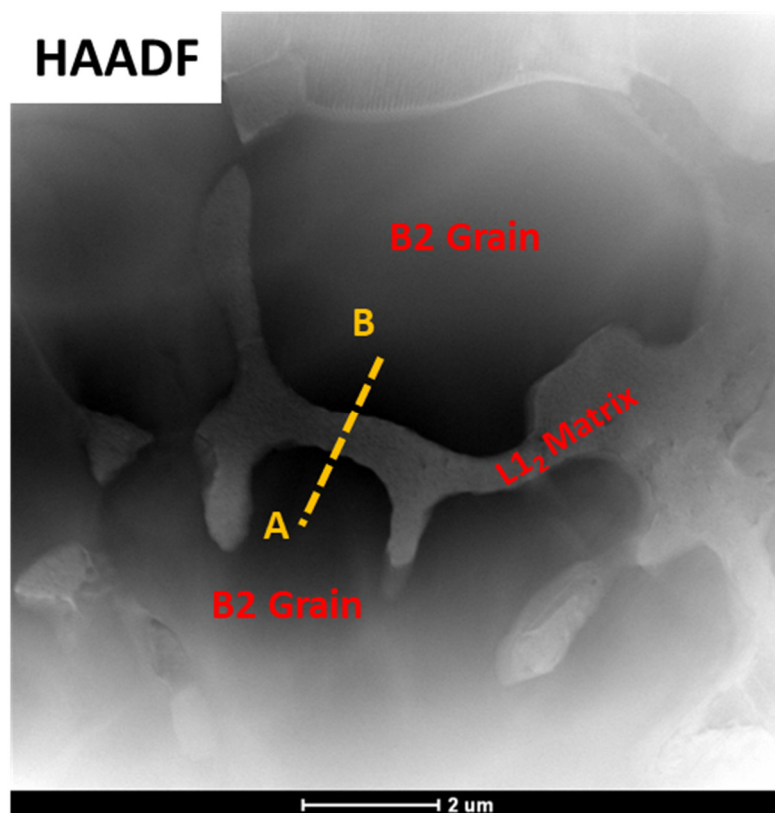


Figure 5.10 STEM – HAADF image of the STEM – EDS mapping region

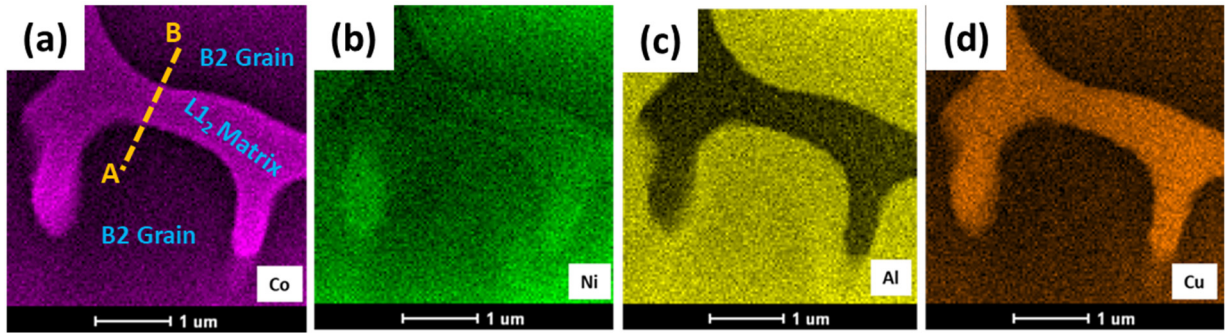


Figure 5.11 (a – d) Elemental mappings using STEM – EDS nano probe, showing B2 ordered grains are rich in nickel and aluminium whereas matrix channel is rich in cobalt and copper in $\text{Co}_{24}\text{Cu}_{10}\text{Ni}_{35}\text{Al}_{31}$ alloy

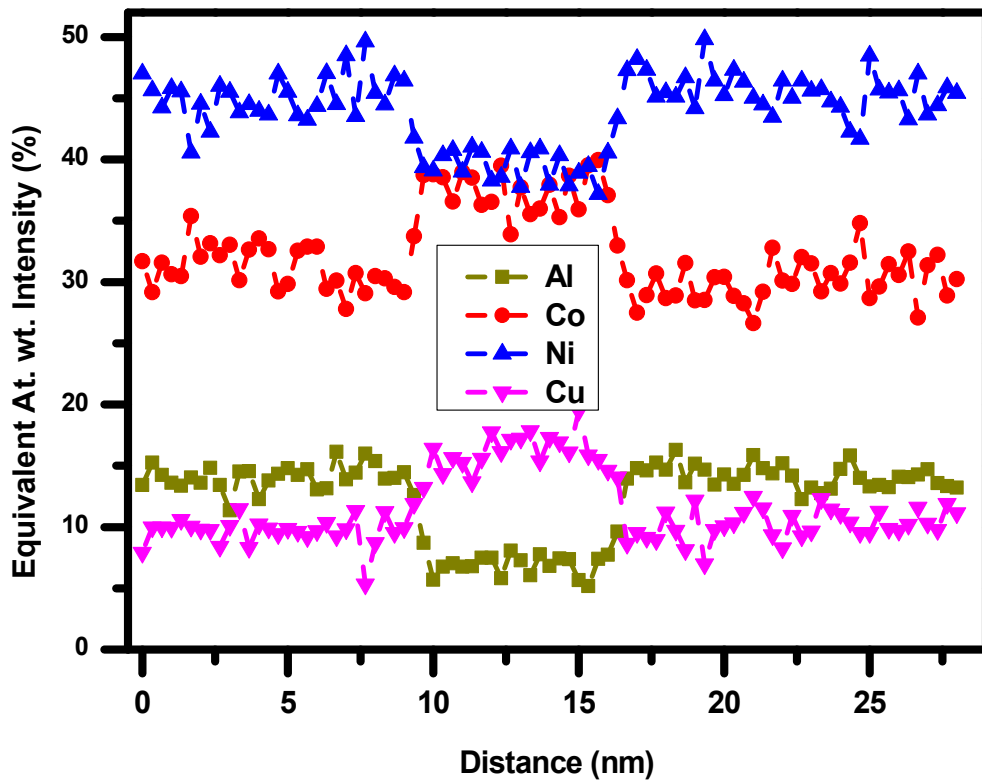


Figure 5.12 STEM – EDS line composition profile across the grain and matrix channel using an STEM nano probe along orange line ‘AB’ of Figure 5.10

5.4.2 Microstructural evolution of $\text{Co}_{34}\text{Ni}_{35}\text{Al}_{21}\text{Cu}_{10}$

The microstructural features of the Sample D alloy where aluminium is partially substituted by copper reveals a very interesting phenomenon. The TEM bright field image as shown in Figure 5.13 demonstrates the existence of similar kind of microstructure as before comprising grains showing lighter contrast embedded in the darker contrast matrix channel. A selected area diffraction pattern taken inside one of the grains of this alloy as shown in Figure 5.14(a) can be indexed as the [100] FCC zone axis of the grain and confirms the L_{12} ordering of the grain instead of B2 ordering as compared to the previous Sample A and Sample C. This result implies that, at the completely different type of microstructural evolution and the structural modification of the active B2 phase to L_{12} ordered phase due to the partial substitution of aluminium by copper. The blue dotted box marked in Figure 5.13 also reveals the presence of martensitic plates inside the darker contrast matrix channel connecting two adjacent L_{12} ordered grains. Absence of active B2 phase inside the grains which is responsible for FSME implies lesser total amount of this phase in the sample, thereby destroyed the PIMA effect. A selected area diffraction pattern taken from inside this matrix channel as shown in Figure 5.14(b), confirms the FCC structure of the matrix channel along the [011] zone axis. Absence of super lattice spots in this figure also confirms the FCC disordered solid solution nature of the matrix channel instead of the L_{12} ordering as was observed in the other alloys. Splitting of the diffraction spots also indicates at the typical martensitic transformation [5.9 – 5.13]. The corresponding dark field images of Figure 5.13, formed by taking two split (111) types of planes as shown in Figure 5.15(a-b) display the alternating martensitic plates inside the matrix channel. Therefore, the partial substitution of atoms at cobalt and at aluminium positions by copper produce two different microstructural features and thus profoundly influences the PIMA properties of the samples in a substantial manner.

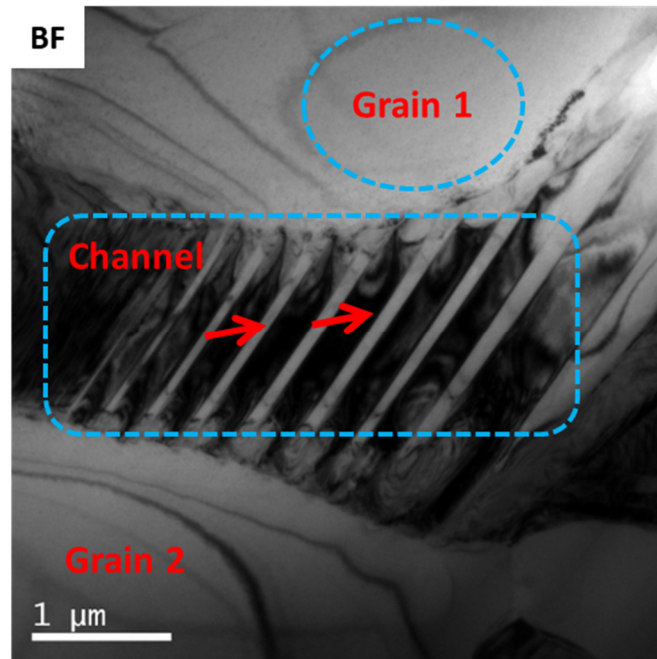


Figure 5.13 Bright field TEM image showing the existence of L1₂ ordered grain and martensitic plates inside the matrix channel of the Co₃₄Ni₃₅Al₂₁Cu₁₀ alloy

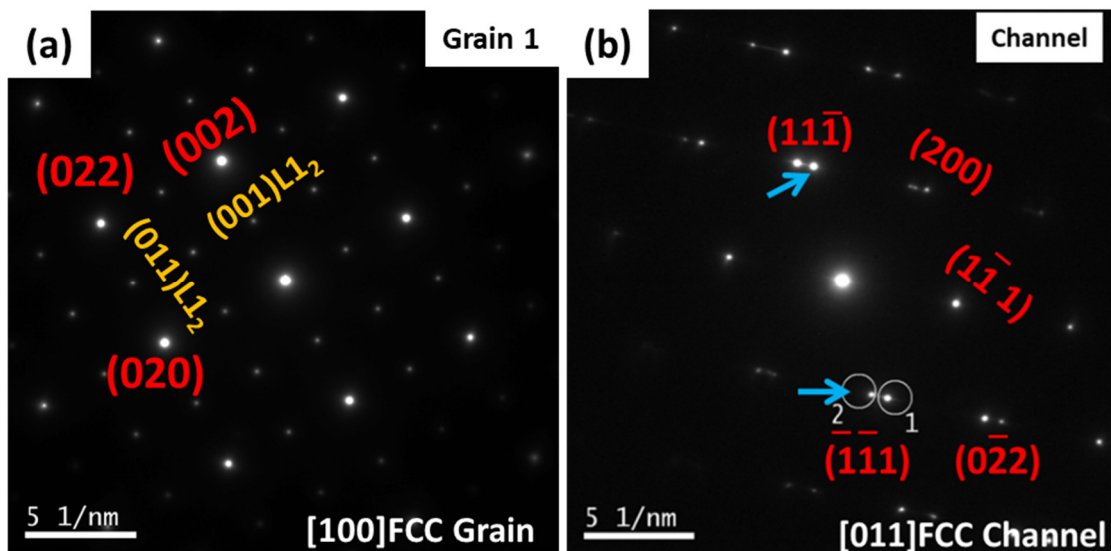


Figure 5.14 (a) Selected area diffraction pattern taken along the [100] zone axis of the grain confirming the L1₂ ordering (b) Selected area diffraction pattern taken along the [011] zone axis of the FCC matrix channel showing the splitting of (111), (022) and (200) types of planes

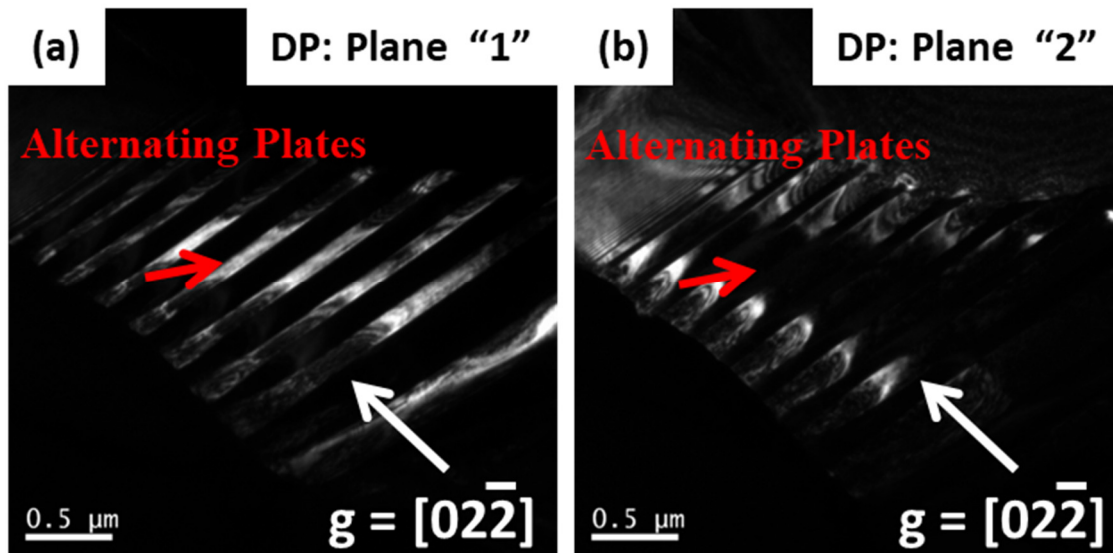


Figure 5.15 (a – b) Dark field image of the blue dotted box marked area of the matrix channel of Figure 5.13 formed by two split (111) type planes, showing the existence of alternating variants of the martensitic plates

A representative STEM – HAADF image of the same area as shown earlier in Figure 5.13 is depicted in Figure 5.16. The qualitative spatial elemental distribution maps obtained by STEM – EDS spectrum imaging technique for all the elements are shown in Figure 5.17(a-d) which demonstrate the nearly equal partitioning of all elements in the entire microstructure in Sample D. This equal and homogeneous distribution of all elements validates the solid solution nature of the microstructure as established in the diffraction studies. Hence, it can be inferred that the ratio of the key constituent elements for typical Ni-Al type B2 ordered phase has been disturbed due to partial substitution of aluminium by copper. Owing to lower availability of aluminium atoms, the system preferred Ni₃Al based structure over Ni-Al based structure. This also ended the PIMA property of this system.

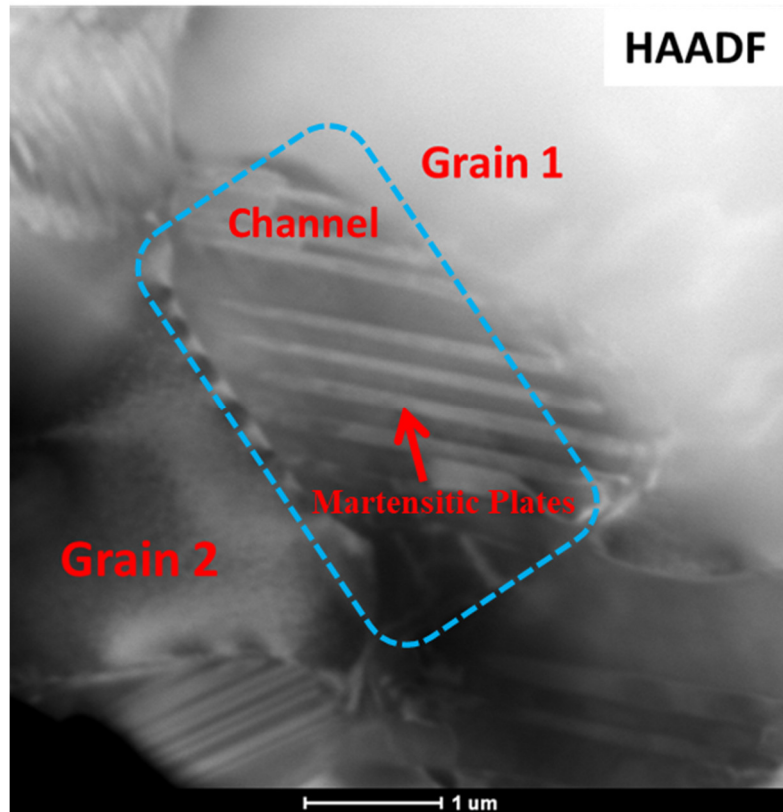


Figure 5.16 An STEM – HAADF image of the same region shown in Figure 5.13

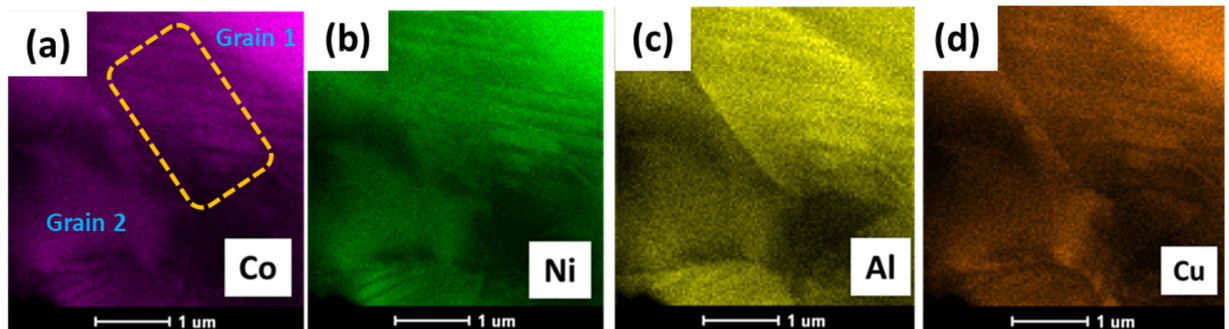


Figure 5.17 (a – d) Spatial elemental mappings using STEM – EDS nano probe, qualitatively showing the equal partitioning of cobalt, nickel, aluminium and copper in the entire microstructure of the $\text{Co}_{34}\text{Ni}_{35}\text{Al}_{21}\text{Cu}_{10}$ alloy

5.4.3 XRD analysis of the samples

X-ray diffraction (XRD) technique was employed to identify the different constituent phases of all the samples. The representative XRD patterns obtained for all the samples were analyzed by Rietveld refinement technique using FullProf software, shown in Figure 5.18 and tabulated in Table 5.1. Analysis of the data reveals the presence of Bragg peaks corresponding to both ' β ' and ' γ ' phases in all the four samples, and their relative amounts are also given in Table 5.1. It can be seen from the table that doping of copper at the cobalt site has improved the phase fraction of the ' β ' phase in Sample B and Sample C as compared to Sample A. However, in Sample D, doping of copper at the aluminium site has drastically reduced the phase fraction of the active ' β ' phase which is insufficient to induce the PIMA property in the sample. This data also confirms the observations made by TEM and presented in Section 5.4.2 of this chapter. The presence of reduced amount of B2 phase as well as their presence only in the grain boundaries rendered the Sample D practically incapable of showing any obvious PIMA effect. The unit cells are hardly modified due to the copper doping at either position, but the microstructural evolution takes different pathways.

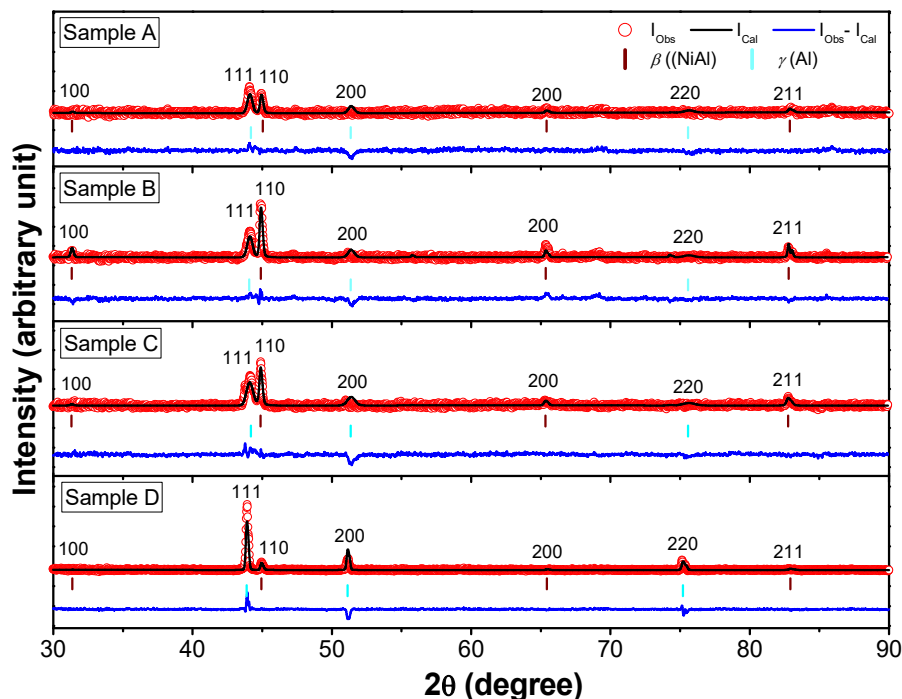


Figure 5.18 Rietveld refinement plots of XRD data of all the samples

Compositions	Crystal Structure	Phase Fraction (%)	Cell Parameters	Fitting Parameters
Sample A	Phase: β (NiAl) Space group: Pm-3m	82.1 ± 5.5	$a = b = c = 2.85$ (\AA) $V = 23.17$ (3) (\AA^3)	$\chi^2 = 2.64$ $R_p = 0.87$ $R_{wp} = 1.15$ $R_{exp} = 2.23$
	Phase: γ (Al) Space group: Fm3m	17.9 ± 1.0	$a = b = c = 3.56$ (\AA) $V = 44.95$ (6) (\AA^3)	
Sample B	Phase: β (NiAl) Space group: Pm-3m	85.8 ± 2.2	$a = b = c = 2.85 \text{ \AA}$ $V = 23.22$ (1) (\AA^3)	$\chi^2 = 2.23$ $R_p = 0.553$ $R_{wp} = 0.758$ $R_{exp} = 1.58$
	Phase: γ (Al) Space group: Fm3m	14.2 ± 0.5	$a = b = c = 3.55 \text{ \AA}$ $V = 44.96$ (2) (\AA^3)	
Sample C	Phase: β (NiAl) Space group: Pm-3m	88.4 ± 2.4	$a = b = c = 2.85 \text{ \AA}$ $V = 23.26$ (1) (\AA^3)	$\chi^2 = 4.43$ $R_p = 1.06$ $R_{wp} = 1.48$ $R_{exp} = 2.22$
	Phase: γ (Al) Space group: Fm3m	11.6 ± 0.3	$a = b = c = 3.56 \text{ \AA}$ $V = 44.98$ (3) (\AA^3)	
Sample D	Phase: β (NiAl) Space group: Pm-3m	34.5 ± 3.7	$a = b = c = 2.85 \text{ \AA}$ $V = 23.15$ (1) (\AA^3)	$\chi^2 = 1.81$ $R_p = 1.26$ $R_{wp} = 2.27$ $R_{exp} = 2.46$
	Phase: γ (Al) Space group: Fm3m	65.5 ± 2.6	$a = b = c = 3.57 \text{ \AA}$ $V = 45.51$ (\AA^3)	

Table 5.1 Rietveld refinement analysis of XRD data of all the samples

5.5 Magnetic characterization of all samples

Room temperature magnetic hysteresis of all four samples are plotted together in Figure 5.19 and it shows that all the samples are ferromagnetic. However, examining the comparative values presented in Table 5.2, a very interesting observation can be made. While Samples A to C show gradual decrease of magnetic moment, saturation magnetization and coercivity, as the copper amount is increased along with simultaneous decrease in cobalt content [5.17], there is an unexpected jump in magnetic moment in Sample D, even if the

total number of magnetic atoms i.e. cobalt and nickel remain the same in both systems i.e. Sample A and Sample D. The key to understanding this remarkable result is the following. The Co-Ni-Al system is composed of two phases, viz. 'β' and 'γ', which have B2 and L1₂ crystal structures, having T_C of 365 K for the 'β' phase and 1045 K for the 'γ' phase respectively [5.18]. Furthermore, as reported earlier in this thesis, only 'β' phase demonstrates the PIMA effect while 'γ' phase is oblivious to it. Therefore, tying the results from Table 5.1 and Table 5.2 together, it can be seen that, the huge increase in 'γ' phase is the cause for these magnetic behaviour. 'γ' phase, having a higher T_C has more magnetic moment at room temperature than 'β' phase with its lower T_C, so the increase in 'β' phase could only reduce magnetic moment of the total system. However, it is apparent that Martensitic transition is now shifted to a higher temperature than other samples. This probably hampered the PIMA effect by reducing the Austenitic phase at room temperature.

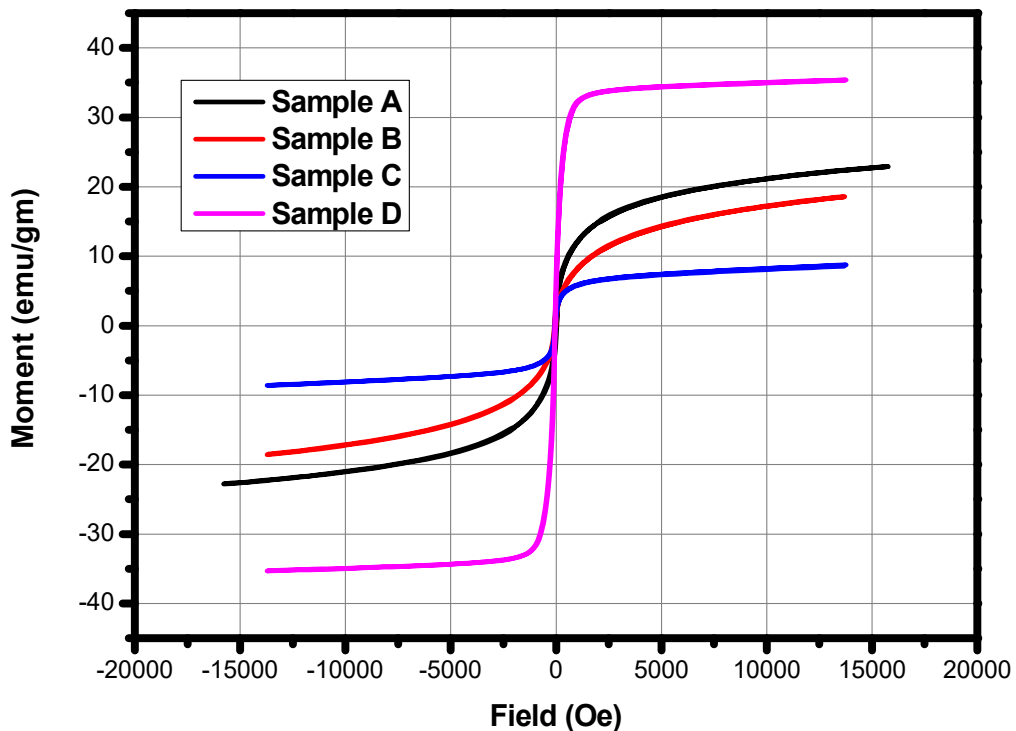


Figure 5.19 Comparison among M-H curves of Co₃₄Ni₃₅Al₃₁, Co₃₂Cu₂Ni₃₅Al₃₁, Co₂₄Cu₁₀Ni₃₅Al₃₁ and Co₃₄Ni₃₅Al₂₁Cu₁₀ samples

Sample	Saturation Magnetization (Ms) (emu/gm)	Coercivity (Hc) (Oe)	Magnetic Moment (μ_B) (Bohr Magnetron)
Co₃₄Ni₃₅Al₃₁	22	78	7.9
Co₃₂Cu₂Ni₃₅Al₃₁	19	76	6.4
Co₂₄Cu₁₀Ni₃₅Al₃₁	9	70	2.3
Co₃₄Ni₃₅Al₂₁Cu₁₀	35	65	12.6

Table 5.2 Magnetic properties of all the samples

5.6 Conclusions

Here was presented the effect of a non-magnetic atom doping in a Co-Ni-Al system in this chapter. Copper atoms were tried to be doped in place of cobalt and aluminium atomic positions to find the resulting effect on the physical properties, especially on the PIMA effect. It was demonstrated that the effect of substitution was on almost all physical properties, including PIMA effect, although the unit cell structure was retained in all the samples. The effect of substitution of cobalt was to enormously reduce the magnetic moment and PIMA properties, even if 'β' fraction slightly increased. On the other hand, it was observed that choice of partial substitution of cobalt by copper is a potential option for improving the mechanical properties of the Co-Ni-Al system at the expense of the PIMA effect. The overall conclusion that can be drawn is that, the PIMA effect depends directly on the amount of Austenite phase present in the system. Also, depending on need at hand, PIMA efficiency and physical strength can be chosen in each case.

CHAPTER 6: DEVELOPMENT OF FSMA MICROACTUATORS

6.1 Introduction

Conventional micro electro-mechanical systems (MEMS) and microactuators used in various engineering applications are bulky due to presence of complex electro-mechanical control mechanisms. These make the systems heavy. In order to overcome these problems, FSMA have been used as the sensing and actuating materials in various perceived MEMS and microactuators due to their ability to generate mechanical work by virtue of its shape recovery property under the influence of thermal or magnetic stimuli [6.1 – 6.6]. The discovery of the PIMA effect discussed in the earlier chapters of this thesis opened a new horizon in the fabrication and operation of suitable microactuator systems for carrying out various engineering applications [6.7]. It has since been definitely established in the previous chapters of this thesis that the selected Co-Ni-Al as well as the Co-Cu-Ni-Al FSMA systems are suitable for the fabrication and operation of various laser controlled microactuators based on the PIMA effect. Hence, attempts were made to actually implement this newly discovered PIMA phenomenon in actual practical applications.

In order to achieve the implementation of the PIMA property in actual engineering applications, suitable designs of microactuators and MEMS devices to perform specific tasks were perceived for the fabrication, operation and control of the selected devices utilizing the PIMA phenomenon. The perceived microactuators to perform the specific tasks were then fabricated using the FSMA samples as the sensing and actuating parts of the microactuators, and also other suitable materials to fabricate the other parts of the devices according to structural and functional requirements of the applications to be performed. The fabricated microactuators and MEMS devices were then operated by controlling the PIMA property of the sensing and actuating parts of the devices made from the selected FSMA samples. The actuation data of the microactuators employing different controlling mechanisms were recorded using the optical microscope systems described earlier in Chapter 2 of this thesis. Other suitable parameters of the

fabricated devices especially the force exerted by the focussed laser beams on the FSMA components of the concerned devices were calculated using software simulation of the perceived microactuators.

In order to achieve the simulation results, the designs of the fabricated FSMA microactuators were developed using standard solid modelling software. Once the solid modelling render of the microactuators was successful, the operation of the newly modelled microactuators were thoroughly characterized using standard Finite Element Analysis (FEA) software. The newly discovered PIMA property shown by FSMAs is such a unique and unexplained phenomenon, that at present there is no FEA software available in the world which can successfully replicate the PIMA operation. As a result, the actuation of the designed microactuators was achieved by the application of mechanical force in the standard FEA software used for the simulation studies. The Co-Ni-Al FSMAs developed to carry out the present studies are not standard materials. Hence, their mechanical properties are not listed in the material libraries of any FEA software in the world. So, the selected samples were added as new materials in the material library of the FEA software used. The mechanical properties of the sample obtained earlier and reported in Chapter 5 of this thesis were used to fulfil this purpose. On completion of successful FEA studies of the simulated microactuator models the actuation data obtained from the simulation was compared with the experimental actuation data of the actual fabricated microactuators operated by the focussed laser beams. By performing this calibration, the mechanical work done by the focussed laser beams on the FSMA samples based on the PIMA phenomenon could be successfully calculated. In this manner, the present study paved the way for actual fabrication and controlled operation of various suitably designed FSMA microactuators and MEMS devices based on the newly developed and unique PIMA property shown by FSMAs.

6.2 PIMA operated FSMA microgripper system

6.2.1 Design of the microgripper system

Various microactuator systems made of FSMA materials have been proposed and built over time. These systems have been deployed to carry out specific applications. One such application of microactuator systems is to grip small objects. Various designs of microgripper systems have been proposed in the past [6.6, 6.8 – 6.10]. The basic working principle of these microgripper systems is to grip and hold onto objects for as long as desired and then also to release the objects at the correct place and time. These microgripper systems can also be attached to robotic arms to carry out their work [6.11]. A very simple design of a microgripper is proposed in this section so as to implement the PIMA effect to control the gripper mechanism. The operation and controlled actuation mechanism of the fabricated microgripper model was systematically studied by three different coloured laser light sources as reported in the earlier chapters of this thesis. The design of the fabricated microgripper system is shown schematically in Figure 6.1. From the figure it can be seen that the prototype microgripper system consists of three parts. Part A of the microgripper is the main actuating part of the assembly. Here the actuating part was fabricated from a metglass $\text{Co}_{34}\text{Ni}_{35}\text{Al}_{31}$ ribbon prepared by melt spinning nominal composition of pure cobalt, nickel and aluminium in an r. f. induction furnace in pure argon atmosphere as discussed in Chapter 2 of this thesis. The reasons behind choosing this FSMA sample are also discussed in detail in the earlier chapters of this thesis. Part B is the right arm of the microgripper system as seen from the front in Figure 6.1. It can be fabricated from any lightweight and ductile material. In this present study, aluminium was chosen as the material of construction for this gripper arm. The left arm of the microgripper prototype is a mirror image of the right arm having the same dimensions and fabricated from the same material.

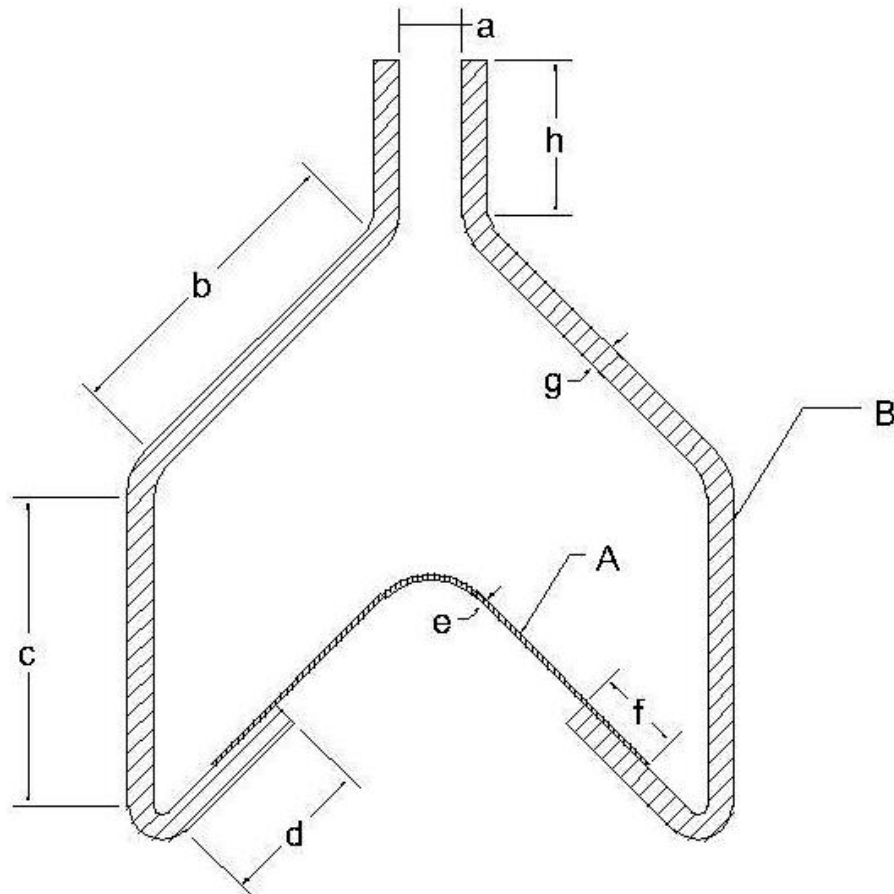


Figure 6.1 Design of the FSMA microgripper system

The approximate dimensions followed in the fabrication of the prototype microgripper are as follows. The main part of the microgripper system was the FSMA material which acted as both the sensor as well as the actuator part of the microgripper. This is denoted as Part 'A' in Figure 6.1. The thickness of the selected FSMA ribbon i.e. dimension 'e' was 100 μm . The width of the selected FSMA actuator was 2.5 mm. The length of each side of the FSMA actuator was approximately 5.5 mm. The two sides of the actuator were kept at an angle of approximately 90 degrees. The radius of curvature of the sample in the middle of the actuator is kept at approximately 1.5 mm. The width of each arm i.e. Part 'B' of the microgripper assembly was kept similar to the width of the FSMA actuator, here it was about 2.5 mm. The thickness of each arm was kept the same as each other. Here the arms had an approximate thickness of 0.6 mm. The portion 'd' of the aluminium arms of the microgripper system as shown in Figure 6.1 was approximately 3.5 mm in length, whereas portion 'c' of the gripper arms was

approximately 7.1 mm in length. The angle between the portions 'c' and 'd' of both the arms was kept at approximately 45 degrees. The outer radius of curvature between the portions 'c' and 'd' was approximately 0.8 mm and the inner radius of curvature between the two portions was 0.2 mm approximately. The dimension of portion 'b' of the two arms of the microgripper assembly was approximately 7.2 mm in length. Portion 'b' was curved inwards from portion 'c' at an approximate angle of 135 degrees. The inner radius of curvature of the bend between portions 'b' and 'c' was approximately 1 mm while the outer radius of curvature at the same bend was 1.6 mm approximately. Portion 'h' of the two microgripper arms was designed to act as the end effector of the assembly to grip any suitable objects. This portion was approximately 3.6 mm in length. The outer angle between portions 'b' and 'h' of each arm was kept at an approximate angle of 135 degrees. The inner radius of curvature at the junction between portions 'b' and 'h' was approximately 0.4 mm while the outer radius of curvature was approximately 1 mm. The two arms were attached to the FSMA actuator as shown in Figure 6.1. From the figure it can be seen that the FSMA actuator was attached to the portion 'd' of the two arms by using an adhesive. The FSMA actuator and the two aluminium arms were overlapped by a portion 'f' as shown in the figure. The length of the overlapping between the FSMA material and the arms i.e. the dimension 'f' was approximately 2 mm. The gap between the end effectors of the two arms was approximately 1.8 mm. The actual $\text{Co}_{34}\text{Ni}_{35}\text{Al}_{31}$ sample which acted as both the sensor and actuator of the fabricated microgripper assembly is shown in Figure 6.2(a). Similarly, one of the two identical aluminium arms which were attached to the FSMA is shown in Figure 6.2(b). The final fabricated microgripper prototype is shown in Figure 6.2(c). These parts were engineered according to the dimensions mentioned above.



Figure 6.2 (a) Actuating part of FSMA microgripper system

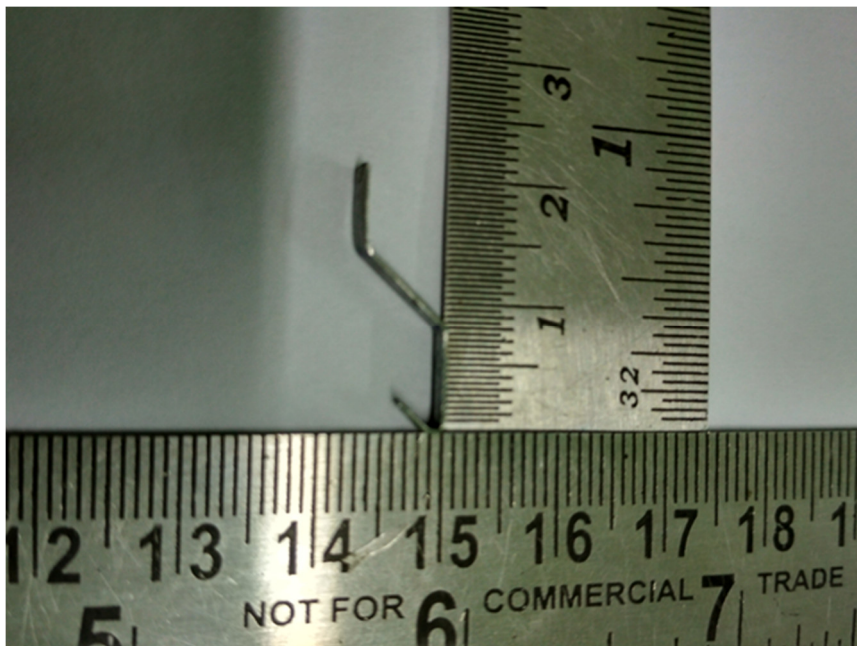


Figure 6.2 (b) Gripping arm of FSMA microgripper system

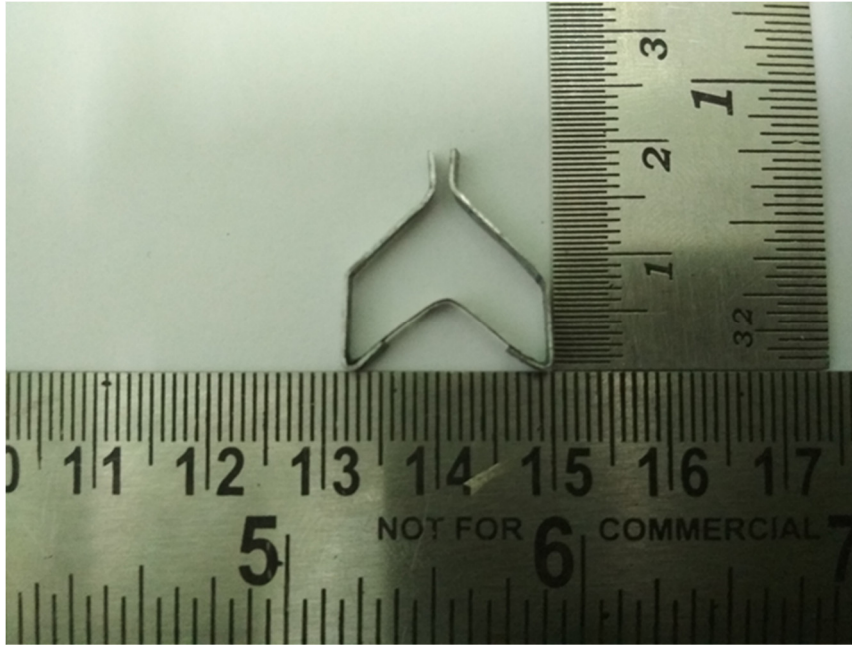


Figure 6.2 (c) Prototype FSMA microgripper system assembly

6.2.2 Working principle of the microgripper system

As described in the previous section, the prototype microgripper assembly is made up of three parts, viz. the FSMA actuator and the two aluminium arms. To operate this microgripper system, one side of the assembly was kept fixed by attaching it to a fixed support. The other arm of the microgripper assembly was kept free for actuation. This was the rest state or open state of the microgripper system when the FSMA sample was not excited by any laser beam. The microgripper assembly in this open state was positioned in the path of the incoming laser beam from the laser diode sources in such a way that the part A of the assembly i.e. the FSMA actuator directly faced the incident laser beam. The focussed laser beam was incident on the face of the radius of curvature in the middle of the FSMA actuator. When the laser beam was focussed onto the face of the actuator the FSMA material deformed and tried to become straight. Due to this deformation of the sample, the angle of the material which was set at an approximate value of 90 degree increased along with the radius of curvature of the FSMA actuator. This deformation was measured to take only 0.4 s to achieve its new position. As one of the arms of the microgripper assembly was kept in a fixed position, this deformed FSMA actuator exerted a force on the free arm of the

assembly which resulted in the end effector of the free arm to come closer to the end effector of the fixed arm of the microgripper system. This resulted in the closing operation of the fabricated microgripper system. The microgripper assembly remained in its closed state as long as the laser beam was incident on the FSMA actuator. As soon as the laser beam was switched off, the FSMA material reverted back to its original quiescent position, i.e. the open position. This opening and closing operation of the prototype microgripper system was found to be fatigue resistant. Hence, it can be inferred that the gripper mechanism will be able to close its grip and hold onto any object for as long as required and then it will also be able to release its grip on the object when it is deemed necessary. This is the simple operating principle followed for the operation and control of the proposed prototype microgripper system. The opening and closing mechanisms of the fabricated microgripper system was observed by the elaborate optical microscope system described in Chapter 2 of this thesis and is shown here in Figure 6.3.

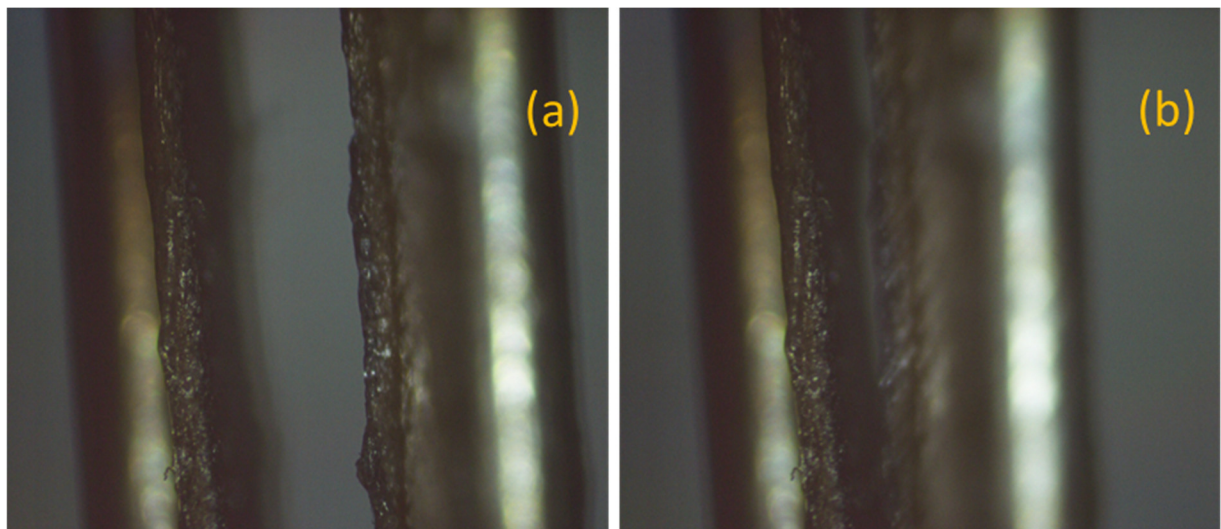


Figure 6.3 (a) Microgripper assembly in open position (b) Microgripper assembly in closed position when excited by focussed laser beam

6.2.3 Finite element analysis of simulated microgripper

As discussed briefly in Section 6.1 of this chapter, the mechanical properties of the Co-Ni-Al FSMA system derived earlier using the universal testing machine was used to add the new material in the materials library of the standard simulation

software. This material along with other standard materials available in the materials library were used to model the solid render of the different parts of the microgripper system following the specifications of the fabricated microgripper prototype. The simulated parts were then assembled in the software to complete the solid modelling of the microgripper system which is shown in Figure 6.4.

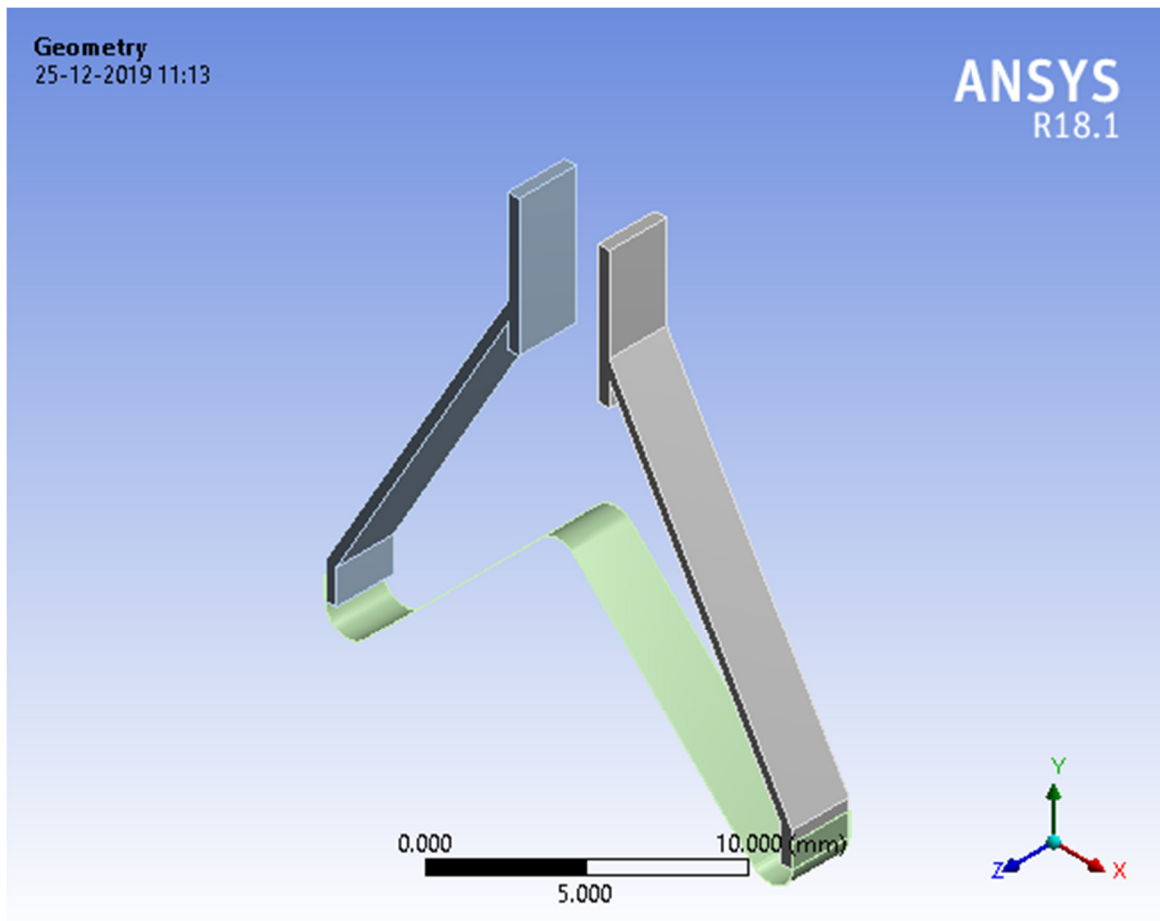


Figure 6.4 Solid modelling of microgripper assembly

FEA studies were then conducted on this solid model of the microgripper assembly to find out the force exerted by the three different coloured focused laser beams used to operate the fabricated microgripper system. In order to achieve this, static structural studies were conducted on the developed solid model. The mesh creations and other parameters required to carry out the static structural analysis of the developed microgripper model were kept in their default settings set by the selected FEA simulation software. The static structural analysis

of the microgripper model performed by the software is shown in Figure 6.5. The FEA studies were then conducted by simulating the actual actuation mechanism of the fabricated microgripper system operated by the focussed laser beams. Thus, one arm of the simulated model was selected as a fixed support, while the other microgripper arm was kept free for the actuation mechanism. In order to simulate the PIMA effect, a mechanical force was applied to the inner radius of curvature of the FSMA part of the model. Due to the application of this force, the free arm of the solid model of the microgripper actuated in the direction of the fixed arm of the assembly to mimic the closing mechanism of the microgripper assembly following the actuation mechanism showed by the actual fabricated microgripper. The amplitude of actuation of the free arm of the simulated microgripper system derived from the FEA software is shown in Figure 6.6. From the figure, it can be seen that the static arm which was selected as the fixed support did not show any actuation at all. This observation from the simulated results is in accord with the actual operating mechanism of the fabricated microgripper system. The actual amplitude of actuation of the fabricated microgripper with respect to the output power of the different coloured focussed laser beams was determined experimentally. In the selected FEA software, appropriate mechanical force was applied to the simulated model to achieve the amplitude of actuation of the microgripper model calibrated with the actual experimental data. By performing this calibration between the experimental and simulated amplitude of actuation, the relationship between the optical power output of the focussed laser beams and the applied mechanical force can be determined. Thus, the force applied by the different coloured focussed laser beams on the FSMA microactuator part can be calculated in this way which is plotted graphically in Figure 6.7.

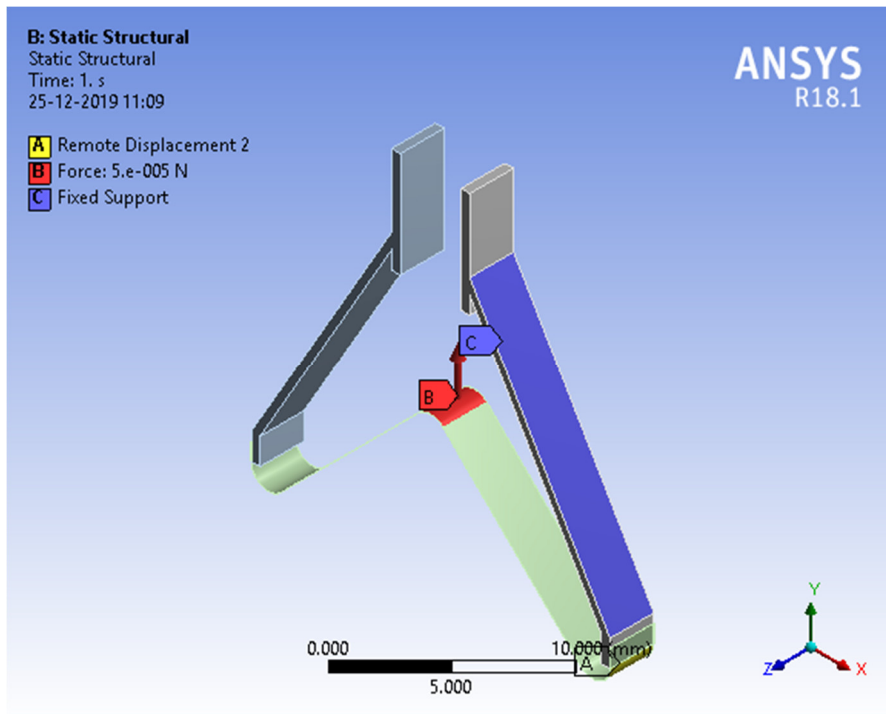


Figure 6.5 Static structural analysis of microgripper system

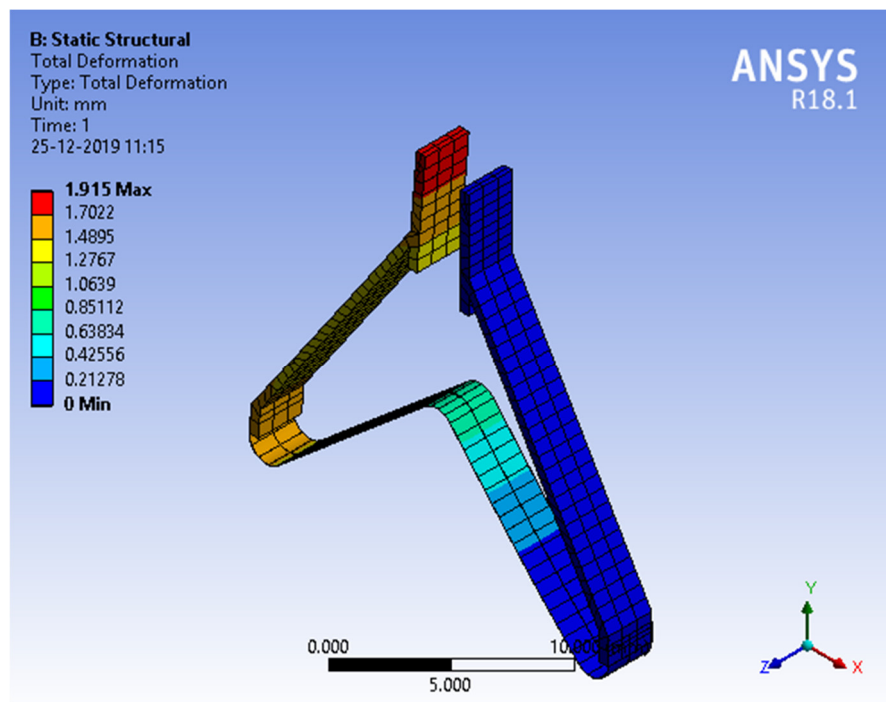


Figure 6.6 Actuation of microgripper on application of mechanical force

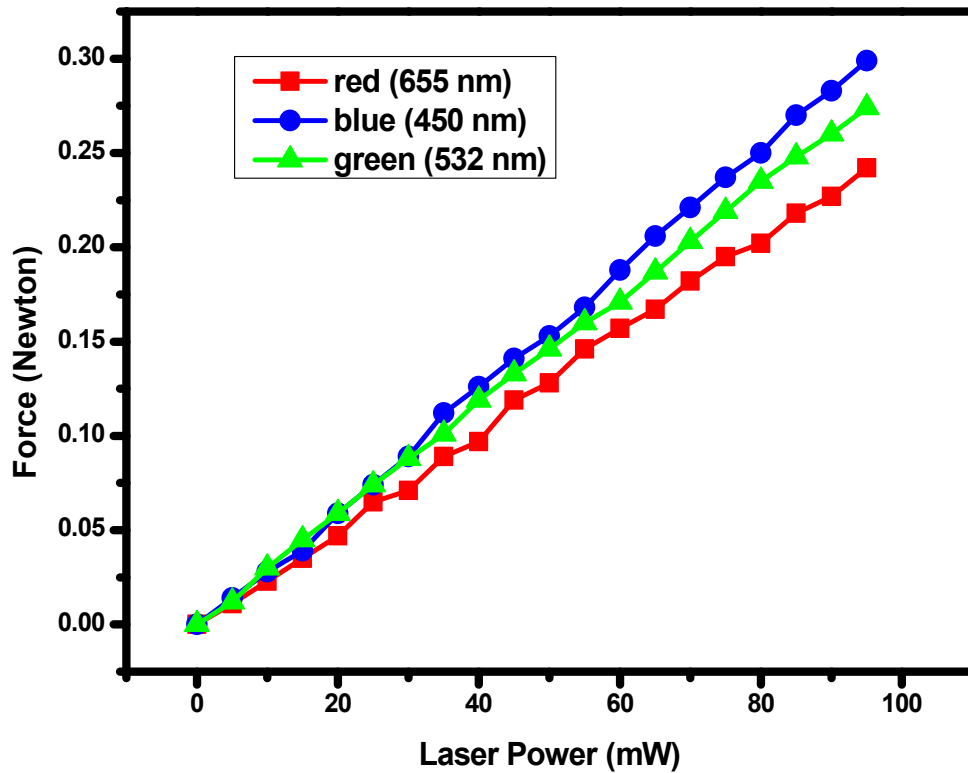


Figure 6.7 Force applied by focussed laser beams

Another important aspect of the fabricated microgripper system is the gripping force of the prototype assembly. In order to calculate the gripping force of the fabricated microgripper on a suitable object, FEA studies were again conducted on the simulated microgripper model with a suitable solid object placed in between the jaws of the two gripper arms. The size of the object to be held was chosen as 1.5 mm X 1.5 mm X 1.5 mm. This was because the gap between the jaws of the two gripper arms was kept at 1.8 mm in the fabricated microgripper prototype. As one of the arms of the microgripper was kept fixed in both the actual prototype as well as the simulated model, the object was kept in contact with the fixed arm of the simulated microgripper assembly. The object was also selected as a fixed support in the FEA software so that it does not fall off when the microgripper is in its open position. The simulated model of the microgripper assembly along with the object is shown in Figure 6.8. Static structural studies were again conducted on this simulated model to determine the gripping force of the microgripper system on the selected object. Like before, a mechanical force was applied to the inner radius of curvature of the FSMA part of the assembly to mimic the PIMA effect. Due to the

application of this force, the free arm of the solid model of the microgripper actuated in the direction of the object placed in between the free and static arms of the assembly to mimic the closing and gripping mechanism of the microgripper assembly. The other parameters required to conduct the static structural studies were kept at their default values as earlier. The static structural analysis of the gripping mechanism of the microgripper model performed by the FEA software is shown in Figure 6.9. The actuation achieved by the free arm of the simulated microgripper assembly is depicted in Figure 6.10. From the figure it can be seen that the free arm closes in on the object placed in between the two jaws and holds onto the object. As the same mechanical force was applied to the FSMA actuator part of the assembly as before, the free arm tries to actuate upto the full deformation it achieved when there was no object placed in between the two jaws. Due to the presence of the object in between, the free arm exerts a force on it which can be determined by the contact tool of the selected FEA software. The status of the contact region between the arms of the microgripper and the object due to the gripping mechanism is shown in Figure 6.11. In order to find out the gripping force of the perceived microgripper on a specifically sized object by application of the PIMA property of the FSMA, the same mechanical force was applied to the FSMA actuator corresponding to the optical power output of the incident laser beams as derived from the Figure 6.7. The corresponding gripping force of the microgripper arms on the selected object was derived from the contact tool of the FEA software used to simulate the gripping mechanism. Hence, the gripping forces generated by the different coloured focussed laser beams on the selected object were determined in this manner which is plotted graphically in Figure 6.12. The above mentioned simulation methods can be followed to calculate the force exerted by the focussed laser beams on the FSMA materials which exhibit the unique property known as PIMA effect as well as the resultant force of any suitably perceived microactuators for actual practical applications.

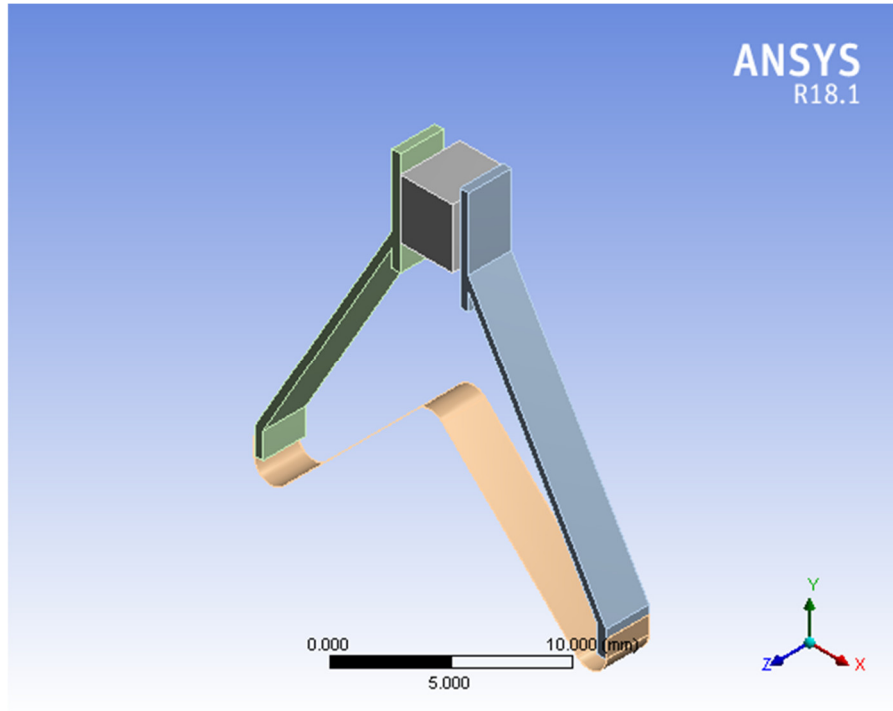


Figure 6.8 Solid modelling of microgripper assembly with object

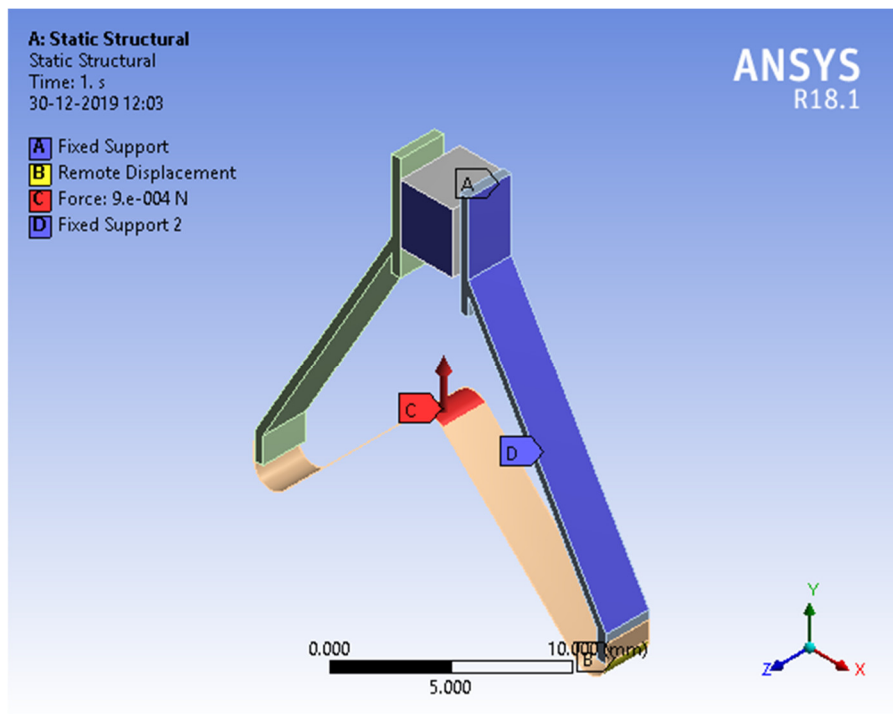


Figure 6.9 Static structural analysis of gripping mechanism

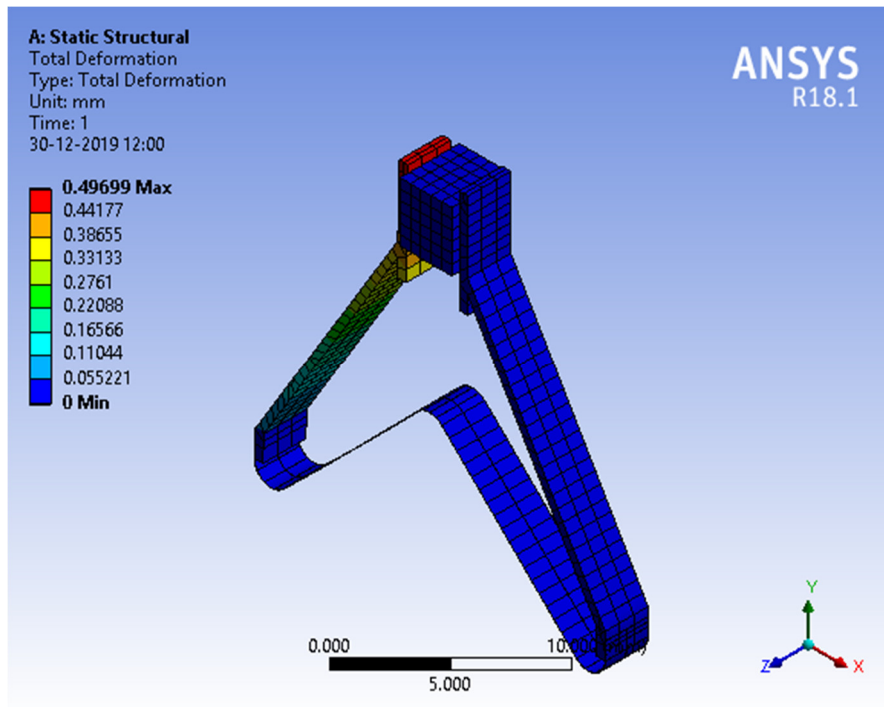


Figure 6.10 Gripping of object on application of mechanical force

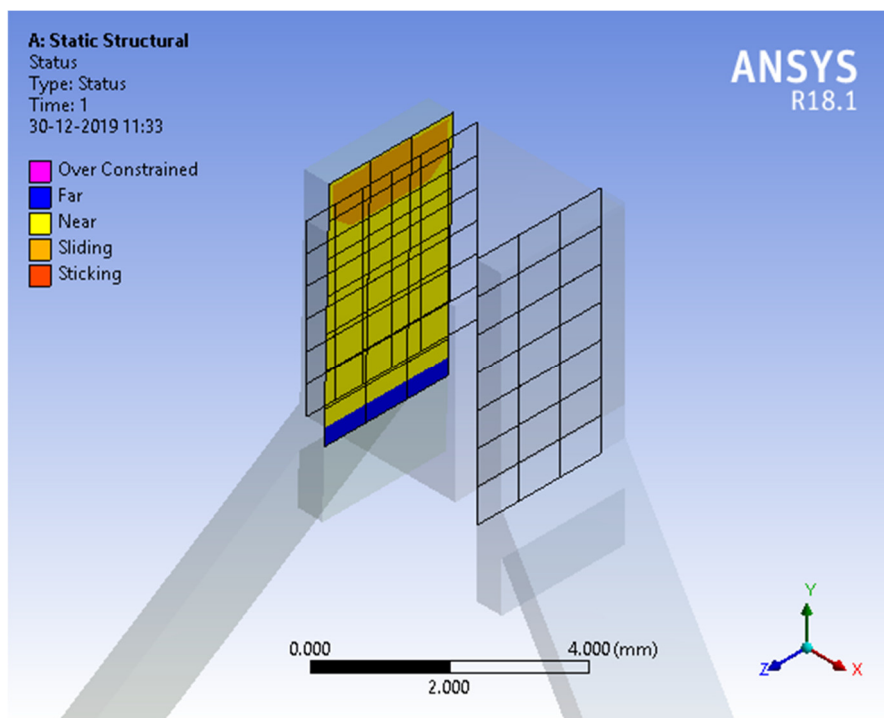


Figure 6.11 Static structural analysis of contact region

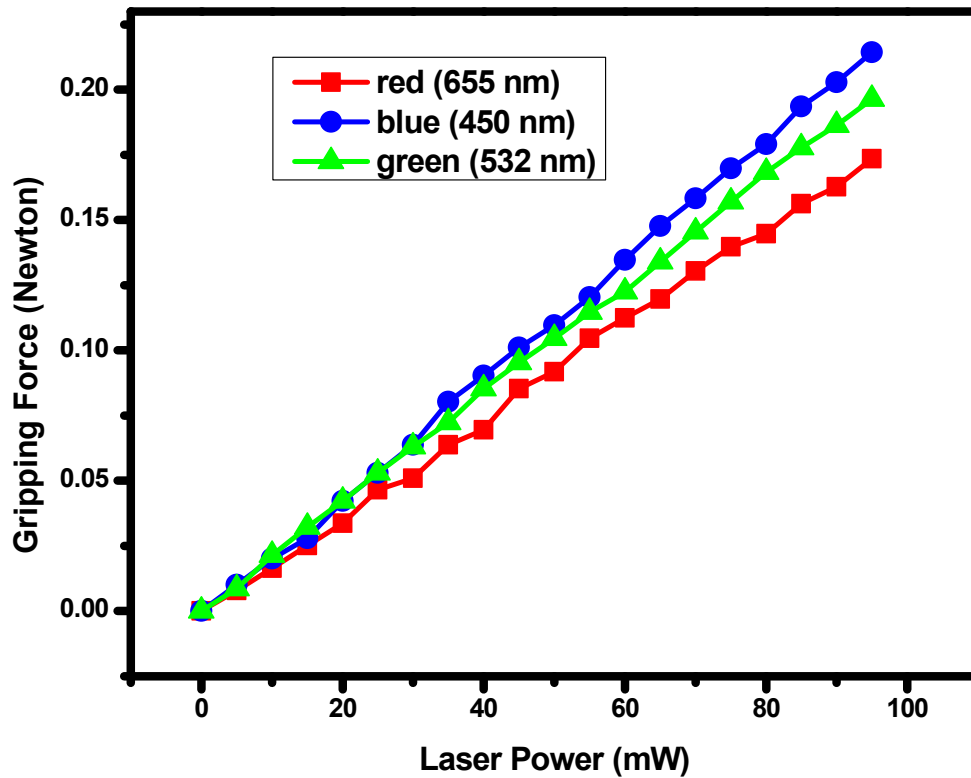


Figure 6.12 Gripping force generated by focussed laser beams

6.2.4 Assembly of FSMA microgripper on robotic arm

In order to operate the fabricated FSMA microgripper, it has to be attached to a suitable robotic arm [6.11]. To achieve this, a simple robotic arm having two degrees of freedom was designed and fabricated. The prototype microgripper system was attached to this robotic arm as its end effector. The main components used to fabricate the robotic arm were two stepper motors. These two stepper motors allowed the assembly to rotate along two degrees of freedom. Stepper motors were selected for the assembly to achieve controlled rotation of the motor shaft in both clockwise and anti-clockwise directions by programming control. The stepper motors were operated and controlled by programming on an Arduino Uno microcontroller. The microgripper attached to the end of the robotic arm could be controlled by focused laser beams through suitable optical fibre setup. This would make the system lightweight as well as achieve remote controlled operation of the FSMA microgripper as the laser source could be placed far from the actual prototype at the other end of the optical fibre setup with all the other optical

components necessary to control the power and polarization of the incident laser beam. But the optical fibre setup is beyond the scope of this thesis and can be tried in the near future. As such, the diode laser source was attached to the robotic arm in such a manner that the laser beam could be focused on the FSMA portion of the prototype microgripper to achieve its microactuation. The fabricated robotic arm along with the microgripper end effector and the attached diode laser module is shown in Figure 6.13.

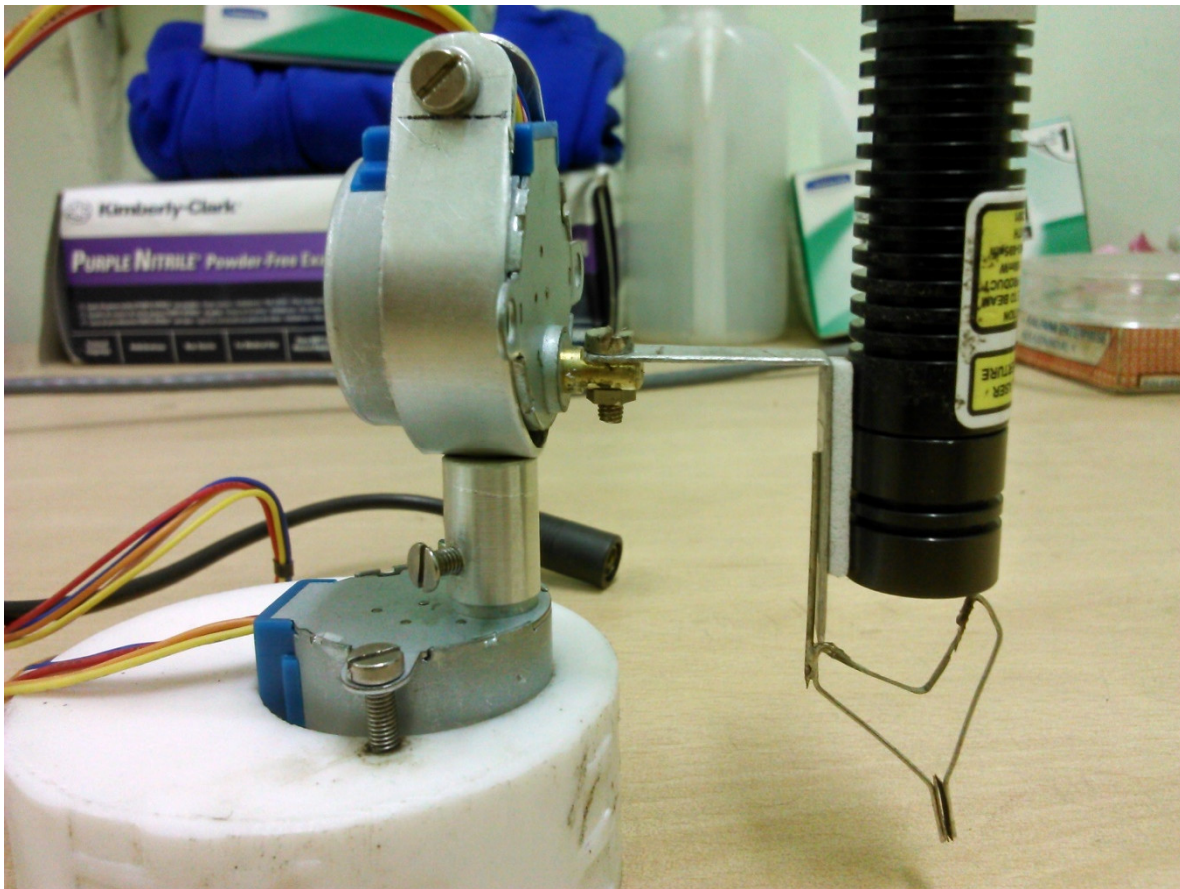


Figure 6.13 Robotic assembly with FSMA microgripper

6.3 PIMA operated FSMA relay system

6.3.1 Design of the relay system

As already discussed in Section 6.2.1 of this thesis, numerous FSMA microactuators have been perceived and fabricated in the past to perform some particular functions. One such application in the form of a FSMA microgripper system has already been deliberated in detail in Section 6.2 of this thesis. Another useful engineering application which can be included in the MEMS category is a relay system. Various relay systems have been designed and fabricated in the past according to specific requirements [6.12 – 6.14]. The function of these relays is to switch between two or more circuits. The basic working principle of these relays is a moving and electrically conducting actuator called its pole which switches between circuits on application of a magnetic field. These relay systems are bulky and heavy due to the presence of electromagnets and its associated electrical circuits. They also need a separate power supply of the electromagnets controlling the actuator for their operation. In order to overcome these disadvantages, efforts have been made in the past to fabricate relay systems using smart materials and operating them by employing the SME [6.15]. One of the most commonly used relay systems is a single pole double throw (SPDT) relay which is applied to switch between two circuits. A very simple design of a SPDT relay fitted with a FSMA pole to switch between two circuits is reported as an example so as to implement the PIMA effect to control another MEMS device. A model of a SPDT relay was developed and its working mechanism used for effectively switching between two electrical circuits, operated by this new method utilizing the PIMA effect was systematically studied.

The fabricated SPDT relay system consists of two parts namely Part A and Part B respectively. Part A of the fabricated relay is the main actuator or pole of the SPDT relay system. Part A is again subdivided into three components consisting of the FSMA microactuator and two electrically conducting contacts for completing the electrical circuit. The components of Part A of the relay is shown schematically in Figure 6.14. Here also, the FSMA actuating part was fabricated from the same $\text{Co}_{34}\text{Ni}_{35}\text{Al}_{31}$ metglass ribbon used earlier to fabricate the microgripper system

prepared by melt spinning nominal composition of pure cobalt, nickel and aluminium in an r. f. induction furnace in pure argon atmosphere. In Part A of the fabricated relay prototype, the electrical conductors other than the FSMA microactuator were made of aluminium. The dimensions of the different components of Part A of the prototype relay are also marked in Figure 6.14. The thickness of the selected FSMA ribbon was 100 μm . The width of the selected FSMA actuator was 2.5 mm. The length of each side of the FSMA actuator was kept at 5.5 mm. The two sides of the actuator were kept at an angle of 135 degrees. The radius of curvature of the FSMA in the middle of the actuator was kept at 1.5 mm. The width of each aluminium conductor piece of Part A of the relay assembly was kept similar to the width of the FSMA actuator i.e. 2.5 mm. The thickness of each conductor was kept the same as each other at 0.5 mm. Each of the two aluminium conductors of Part A of the relay system was 10 mm in length. The two aluminium conductors were soldered to the two ends of the FSMA microactuator to complete Part A of the relay system which acted as the moving electrical contact or the pole of the relay switching mechanism. Part A of the prototype relay system was connected with each other by soldering so as to enable the whole part to act as a single electrically conducting pole of the relay system.

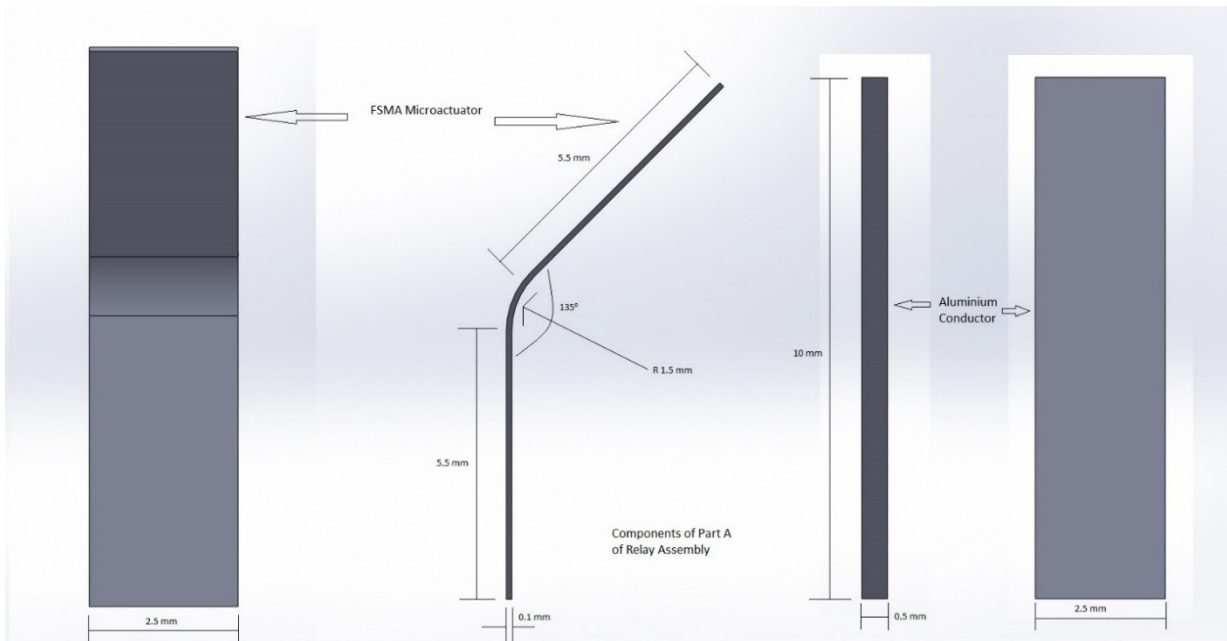


Figure 6.14 Components of Part A of the SPDT relay system

Part B comprises of the fixed electrical contact points of the fabricated relay system. The components of Part B of the fabricated SPDT relay system along with its dimensions are shown schematically in Figure 6.15. Part B of the assembly also comprises of three components. Out of these three components two are identical electrical conductors which were fabricated from aluminium. The third component of Part B of the relay system is an insulating material to electrically isolate the two fixed electrical conductors of Part B of the system. In this case Teflon was used as the insulating material. The two identical aluminium conductors of Part B of the fabricated relay were kept at a length of 20 mm each. Their width was kept at 2.5 mm in accordance with Part A of the relay assembly. Their thickness was kept at 0.5 mm. The insulating Teflon piece was fabricated with an approximate dimension of 5 mm X 2.5 mm X 2 mm. The two conductors were fixed on the two sides of this Teflon insulator in such a way so that the gap between the two conductors was 2 mm which was the thickness of the Teflon piece. In this way the two conductors of Part B were in a position parallel to each other with a gap of 2 mm in between them.

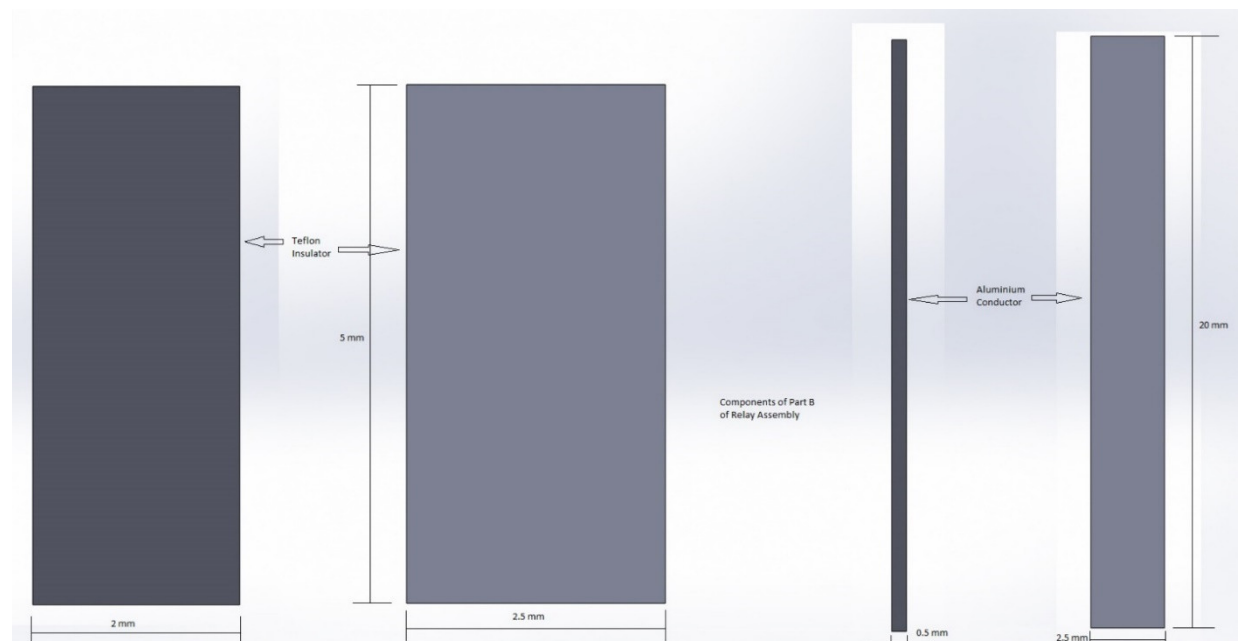


Figure 6.15 Components of Part B of the SPDT relay system

The Part A and Part B of the relay prototype were assembled in such a way that one end of the conductor of Part A was always in contact with the inner side of one of the two conductors of Part B. This contact was the normally closed contact

position of the relay. The conductor of Part A and the conductor of Part B which were not in contact with each other at rest position was the normally open contact of the fabricated relay system. The schematic diagram of the assembled SPDT relay system prototype is shown in Figure 6.16. This assembly was then sealed to prevent the SPDT relay system from ingress of contaminants and moisture. Three electrically conducting leads made of aluminium were externally attached to the sealed assembly of the relay device. One of the leads was soldered with one end of the Part A of the assembly. The other two leads were connected to the two conductors of the Part B of the assembly. This completed the fabrication process of the entire perceived optically operated relay device. In this sealed device a transparent aperture was present in front of the radius of curvature in the middle of the FSMA microactuator. This transparent aperture allowed the focused laser beams to be incident on the radius of curvature of the FSMA to control the microactuation of the relay actuator.

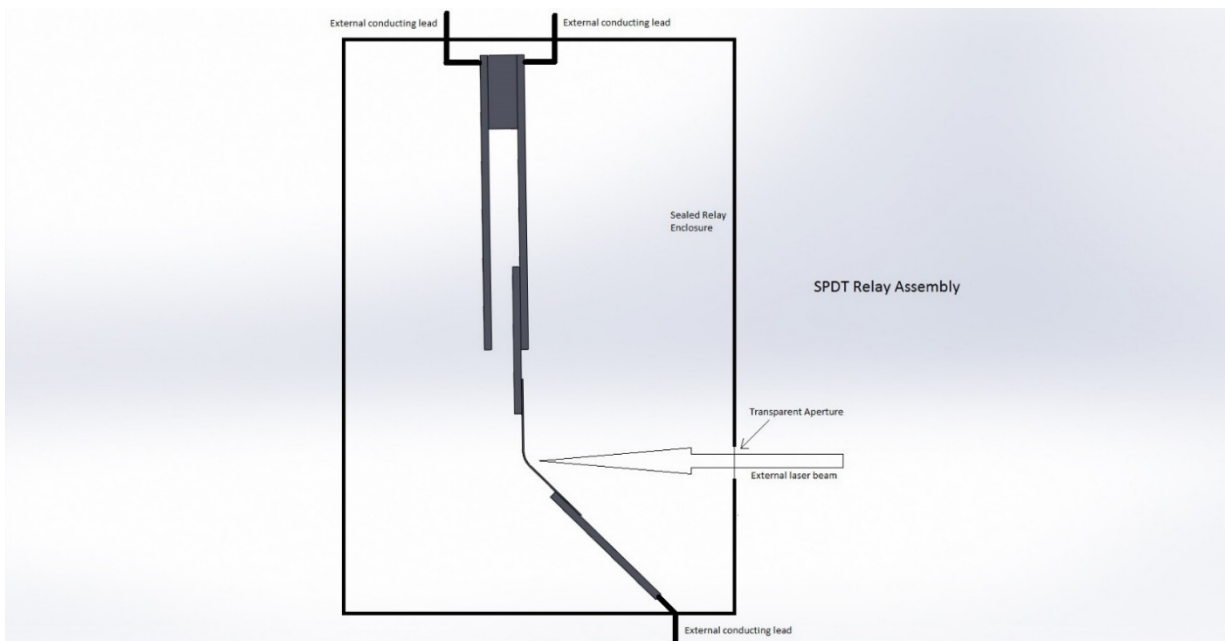


Figure 6.16 Schematic diagram of the SPDT relay assembly

6.3.2 Working principle of the relay system

The fabricated relay device can be used in both AC as well DC circuits. It is suitable for switching between two different circuits, each requiring a fixed power

supply. A simple electrical circuit was designed to test the working principle of the fabricated SPDT relay prototype. The electrical components used to make the circuit are as follows. A variable DC power supply as well as a variable AC power supply displaying the applied voltage were used separately as the power source for the designed circuit. A switch was added to turn on or turn off the entire circuit. Two variable resistors or rheostats were used as the two loads. Two moving iron type ammeters and two moving coil type ammeters were used with the AC and the DC power supply respectively to measure the current flowing through the two circuits. Connecting wires were used to complete the circuit along with the prototype relay on a bread board. The schematic circuit diagram is shown in Figure 6.17. One end of the power supply was connected to one end of the electrical switch. The other terminal of the switch was electrically connected to the external conducting lead of the relay assembly which was connected to one end of the conductor of Part A of the relay prototype. The two conductors of the Part B of the relay were connected to the two electrical loads. The other end of the load was connected back to the other terminal of the power supply to complete the circuit. An appropriate ammeter depending on the type of power supply used was connected in series with each of the two loads to measure the current flowing through the two circuits.

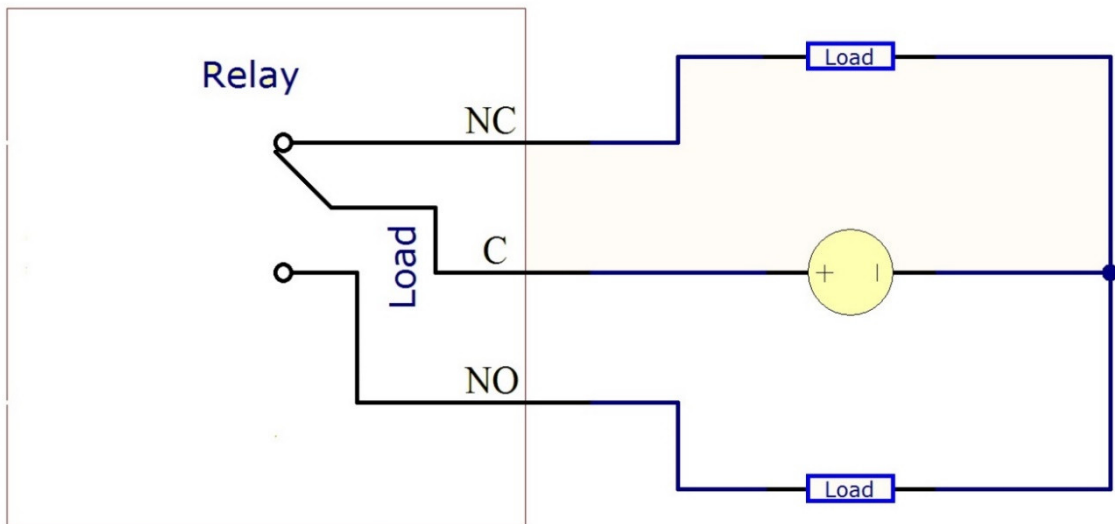


Figure 6.17 Schematic circuit diagram of the working mechanism of the SPDT relay system

In order to achieve remote controlled switching mechanism between the two circuits using the fabricated FSMA relay based on the PIMA phenomenon, the laser module was placed in such a way that the output laser beam from the laser diode source was incident on the face of the radius of curvature of the FSMA microactuator of Part A of the relay through the aperture of the assembly. The focused laser beam hits the face of the radius of curvature in the middle of the FSMA actuator from the front. As discussed in the earlier chapters of this thesis, any suitably coloured visible laser beam viz. red, blue, green or others could be used to actuate the prototype relay system. It was found that the colour of the laser beam played an important role in the amplitude of actuation of the pole of the fabricated relay system. When the laser beam was focussed onto the face of the actuator, the FSMA material deformed and tried to become straight. Due to this deformation the angle of the material which was set at an approximate value of 135 degree increased along with the radius of curvature of the FSMA actuator. This deformation was found to take only a few milliseconds to achieve its new position. As a result, the normally closed circuit of the relay system broke, resulting in the switching off of the first load. The conductor of Part A of the relay then came in contact with the normally open conductor of Part B of the assembly resulting in switching on of the second circuit. As long as the laser beam was incident on the FSMA actuator, Part A of the relay system remained in its deformed position, keeping the second circuit switched on. As soon as the laser beam was cut off, the FSMA material reverted back to its original quiescent position which resulted in the switching off of the second circuit and switching on of the first circuit. This relay mechanism was found to be fatigue resistant. This proves that the optically controlled FSMA relay system will be able to switch between two circuits effectively and keep each circuit active separately for as long as required without the requirement of other bulky control mechanisms e.g. the electromagnet for actuation of the pole of the relay. This is the operating principle of the proposed prototype SPDT relay system. The actual fabricated relay prototype without the protective casing is shown in Figure 6.18. LEDs were connected in series with the two circuits to indicate the current flow through the selected circuits.

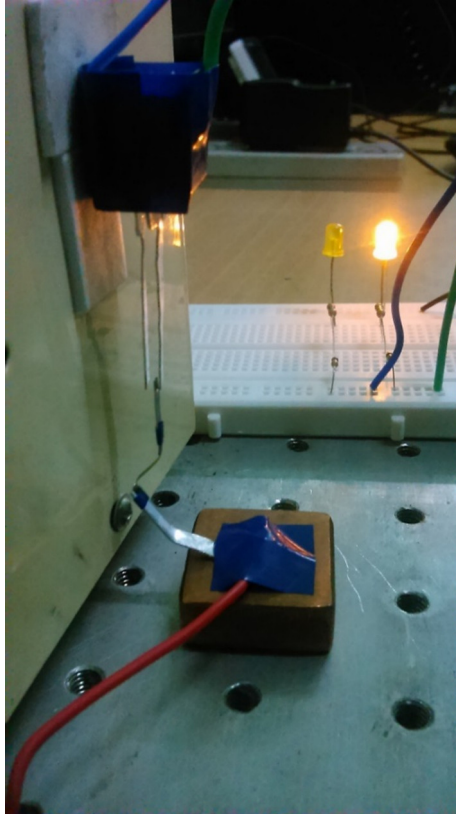


Figure 6.18 Prototype FSMA SPDT relay system

6.3.3 Electrical specifications of prototype relay system

The general electrical specifications of the fabricated relay prototype are described as follows.

i) Pole Specifications: Single Pole (SP), as the fabricated relay prototype has a single actuator with an electrical contact at the end.

ii) Throw Specifications: Double Throw (DT), as the fabricated relay prototype has three electrical conductors in total. In the first relay position the moving conductor is in contact with one of the fixed conductors but not with the second fixed contact. In the other relay position the moving conductor is in contact with the second fixed conductor but not with the first fixed conductor.

iii) Number of contacts: There are two contacts in the fabricated relay prototype. One of them is a normally closed (NC) contact where the relay contact pair is closed when it is not energized. Another contact is normally open (NO) where the relay contact pair is open when the relay is not energized.

iv) Maximum AC current of NC contact: The maximum AC current allowed to pass through the NC contact of the fabricated relay prototype is 2.18 Amp.

v) Maximum AC switching voltage of NC contact: The maximum AC switching voltage of the NC contact of the fabricated relay prototype is 114.6 Volt.

vi) Maximum DC current of NC contact: The maximum DC current allowed to pass through the NC contact of the fabricated relay prototype is 2.14 Amp.

vii) Maximum DC switching voltage of NC contact: The maximum DC switching voltage of the NC contact of the fabricated relay prototype is 12.4 Volt.

viii) Maximum AC current of NO contact: The maximum AC current allowed to pass through the NO contact of the fabricated relay prototype is 2.18 Amp.

ix) Maximum AC switching voltage of NO contact: The maximum AC switching voltage of the NO contact of the fabricated relay prototype is 114.6 Volt.

x) Maximum DC current of NO contact: The maximum DC current allowed to pass through the NO contact of the fabricated relay prototype is 2.14 Amp.

xi) Maximum DC switching voltage of NO contact: The maximum DC switching voltage of the NO contact of the fabricated relay prototype is 12.4 Volt.

xii) AC coil voltage: Not applicable, as the fabricated relay prototype is operated optically, it does not have any actuation coil to energize the pole.

xiii) DC coil voltage: Not applicable, as the fabricated relay prototype is operated optically, it does not have any actuation coil to energize the pole.

xiv) Coil resistance: Not applicable, as the fabricated relay prototype is operated optically, it does not have any actuation coil to energize the pole.

xv) Make time: The make time of the fabricated relay prototype is 0.4 sec, i.e. the actuator takes 0.4 sec to actuate from the NC contact to the NO contact.

xvi) Break time: The break time of the fabricated relay prototype is 0.6 sec, i.e. the actuator takes 0.6 sec to actuate back from the NO contact to the NC contact.

6.4 Conclusions

In conclusion, it can be said that a simple prototype microgripper system has been designed and fabricated as an example of a FSMA microactuator and a simple prototype single pole double throw (SPDT) relay system has been designed and fabricated as an example of a FSMA MEMS device. Both the fabricated microgripper system and the fabricated SPDT relay system can be operated by only a low power laser beam employing the hitherto unknown and unique PIMA effect shown by FSMAs. While the cause of this PIMA effect is still not known, efforts were made to harness the power of this effect in MEMS, robotics and bioengineering applications. The biggest advantage of this new mechanism is that it works on its own, entirely under the control of laser light guidance. Conventional gripper systems used in robotic arms are bulky due to presence of complex control mechanisms. Proposed microgripper system can be used as an end effector in suitable robotic arms. Main advantage of using this laser actuated gripper system is reduction in weight as there is no motor to operate the gripper as well as absence of batteries and other electrical accessories to power the motor. Similarly, conventional relay systems used in various electro-mechanical applications are bulky due to presence of complex electrical and magnetic control mechanisms. Proposed relay system can be used to effectively switch between suitable electrical circuits. Main advantage of using this laser actuated relay system is reduction in weight as there is no electromagnet to operate the relay as well as absence of other electrical accessories to power the electromagnet. Both the gripper and the relay can be remotely controlled by light only, using optical fibres to transmit and focus the laser beam on the gripper to control the actuation mechanism. This mechanism eliminates the need for sensors and transducers, thus there will be no radio interference of any sort, making the system discreet. This proposed system is also suitable for operation in various radioactive as well as bio hazardous environments due to the uniqueness of the system. These are the first systems attempted in the world where the PIMA effect was employed in any kind of MEMS application.

CHAPTER 7: CONCLUSIONS AND FUTURE OUTLOOK

7.1 Conclusions

In summary it can be said that the present thesis deals with the newly discovered and novel observation where FSMAs demonstrated Photo Induced Micro Actuation (PIMA) effect when they were excited by low powered focused laser beams. Since its origin is not understood as yet, the PIMA effect was studied systematically in order to characterize its nature. The discovery of the PIMA effect opened up a new avenue to utilize this property of FSMAs in actual engineering applications where control on the actuation mechanism of suitably designed microactuator systems can be achieved. For proper harnessing of this property, the PIMA effect was further characterized which is presented in detail in the present thesis. Effective control mechanisms for the amplitude of actuation of the PIMA property shown by FSMAs were proposed with various controlling factors like colour of the laser, output optical power of the laser and polarization of the laser beam. The response time of the actuation phenomenon of the FSMA sample for the different coloured lasers was also studied. Analysis of Variance (ANOVA) study was then chosen to be implemented on the experimental data to conclusively provide evidence in support of the relationship between the actuation of the sample and the various controlling factors. Efforts were then conducted to find out the exact reasons for this behaviour of the alloy system which are reported in detail in this present thesis. Structural characterization of the Co-Ni-Al sample was done using Transmission Electron Microscopy (TEM) to correlate between the ferromagnetic shape memory effect (FSME) and the photo induced micro actuation (PIMA) effect shown by the samples.

Once it was conclusively proved that the PIMA effect could be successfully implemented in the fabrication and controlled operation of a new class of laser controlled remotely operated microactuator systems, studies were conducted to determine the workability of the samples in various environmental conditions where temperature plays an important role and it is subjected to different levels of oxidation. The limiting functionality of PIMA effect at elevated temperatures and in

ambient atmosphere was studied to establish the correlation between the microstructural changes and its direct effect on PIMA property which is presented in details in this thesis. These investigations provided useful information for further engineering design in the near future. The results show that with increasing annealing temperature, the PIMA property monotonically degrades and stops at 400 °C. Detailed microstructural studies of the as prepared and the heat treated samples confirm the existence of B2 ordered micron sized grains embedded in L1₂ ordered matrix channel, where the B2 ordered phase is the key responsible and active phase for ferromagnetic shape memory response whereas the L1₂ ordered FCC matrix only imparts the ductility into the alloy. Further structural studies reported in this thesis indicate at the evolution of nanometre sized cobalt rich precipitates with fine faulted type morphology inside the B2 ordered grain along with traces of oxygen at 400 °C. Limited oxidation kinetics studies of the sample studied in this thesis also show that this alloy is comparatively oxidation resistant with a moderate oxidation rate constant value in comparison to other Co and Ni based alloys.

As already discussed in this thesis, one of the most important factors behind choosing Co-Ni-Al as the preferred FSMA system for practical applications is their better mechanical properties as compared to more widely studied FSMA systems like Ni-Mn-Ga. Efforts were made to further improve the ductility and other mechanical properties of the selected Co-Ni-Al FSMA system which is reported in this thesis. Simultaneous studies were thus conducted to determine the effect of different proportions of copper doping on the PIMA effect of the Co-Ni-Al alloy and also to determine the improvement in the desired mechanical properties of the newly developed copper doped Co-Ni-Al FSMA systems. Hence, comparing both the PIMA data as well as the mechanical properties of the undoped and the different copper doped alloys, optimal FSMA systems were investigated which can be suitably used for various microactuator applications in the near future. It was found out that partial substitution of cobalt and aluminium by copper develops two different classes of alloys with different microstructural features and properties. While substitution of cobalt by increased amount of copper resulted in gradual degradation of PIMA phenomenon in the resultant samples, addition of copper at the expense of aluminium resulted in complete disappearance of the PIMA

property of the resultant alloy. XRD and magnetic properties of the copper doped samples also were studied to adjudge the feasibility of implementing the PIMA effect of the newly developed copper doped Co-Ni-Al alloys for operation and control of suitable microactuator systems. These studies paved the way for the formulation of a new design scheme for optimization of FSMA alloy system where the desired properties can be balanced for proper and customized engineering applications.

Finally, this thesis presents the actual implementation of the PIMA property shown by FSMAs for carrying out real time engineering applications. Two important engineering prototypes were developed for the successful implementation of the PIMA effect in controlled operation of microactuators and MEMS devices. One of the applications was a FSMA microgripper while the other application was a FSMA SPDT relay system. Before actual fabrication and operation of the devices were done by implementing the PIMA property shown by the alloys, simulation studies were done in suitable software to successfully simulate the actual microactuation process. The simulations performed to conduct finite element analysis of the perceived microactuator devices are also presented in detail in this thesis. On completion of successful finite element analysis of the simulated microactuator models, efforts were made to actually fabricate the modelled microactuator designs using the Co-Ni-Al samples. The fabricated microactuators were then operated and controlled by employing the unique PIMA effect. Both the fabricated microgripper system and the fabricated SPDT relay system can be operated by only a remote low power laser beam, demonstrating that this property can be utilized in suitable MEMS, robotics and bioengineering applications. The biggest advantage of this new mechanism is that it works on its own, entirely under the control of laser light guidance. This reduces the overall weight of the microactuator device due the absence of power source as well as complex electrical and mechanical accessories including separate sensors and transducers to power and operate the devices. As there will be no radio frequency interference in this mechanism, the systems will be discreet. This thesis presents the first systems attempted in the world where the PIMA effect was employed in any kind of MEMS application.

7.2 Future outlook

Though the correlation between the PIMA property shown by FSMAs with FSME as well as other structural and magnetic properties of FSMAs have been reported in detail in this present thesis, the actual physical cause of the PIMA effect is still unknown. The main area of interest that can be pursued in future work is to investigate and find out the actual physical cause behind the occurrence of the PIMA effect. FSMA systems other than Co-Ni-Al systems presented in this thesis can also be investigated in the future for the study of PIMA effect. Those studies will be directed towards finding out FSMA systems which show better PIMA response than the currently studied Co-Ni-Al systems. FSMAs with better mechanical properties which are able to retain the PIMA properties over varied environmental conditions than Co-Ni-Al can also be designed in the future for implementation in real time practical applications. More suitable remotely operated optomechanical microactuators and MEMS devices can be perceived and fabricated in the near future to solve real time engineering problems.

REFERENCES

- [1.1] M. Schwartz (ed): "Encyclopedia of Smart Materials", Volume 1 and Volume 2, John Wiley and Sons (2002).
- [1.2] M. Shahinpoor, H. J. Schneider (eds): "Intelligent Materials", RSC Publishing (2008).
- [1.3] W. Cao, H. H. Cudney, R. Waser: "Smart materials and structures", Proc. Natl. Acad. Sci. USA, 96 (1999) 8330.
- [1.4] M. Schwartz (ed): "Smart Materials", CRC Press (2009).
- [1.5] D. C. Lagoudas (ed): "Shape Memory Alloys Modeling and Engineering Applications" Springer (2008).
- [1.6] K. Otsuka, C. M. Wayman (eds): "Shape Memory Materials", Cambridge University Press (1998).
- [1.7] R. C. O'Handley: "Model for strain and magnetization in magnetic shape-memory alloys", J. Appl. Phys., 83 (1998) 3263.
- [1.8] R. D. James, M. Wuttig: "Magnetostriction of martensite", Philos. Mag. A, 77 (1998) 1273.
- [1.9] K. Ullakko, J. K. Huang, C. Kantner, R. C. O'Handley: "Large magnetic-field-induced strains in Ni₂MnGa single crystals", Appl. Phys. Lett., 69 (1996) 1966.
- [1.10] H. E. Karaca, I. Karaman, B. Basaran, Y. I. Chumlyakov, H. J. Maier: "Magnetic field and stress induced martensite reorientation in NiMnGa ferromagnetic shape memory alloy single crystals", Acta Mater., 54 (2006) 233.
- [1.11] H. E. Karaca, I. Karaman, B. Basaran, D. C. Lagoudas, Y. I. Chumlyakov, H. J. Maier: "On the stress-assisted magnetic-field-induced phase transformation in Ni₂MnGa ferromagnetic shape memory alloys", Acta Mater., 55 (2007) 4253.
- [1.12] H. D. Chopra, C. Ji, V. V. Kokorin: "Magnetic-field-induced twin boundary motion in magnetic shape-memory alloys", Phys. Rev. B, 61 (2000) R14913.
- [1.13] M. R. Sullivan, H. D. Chopra: "Temperature- and field-dependent evolution of micromagnetic structure in ferromagnetic shape-memory alloys", Phys. Rev. B, 70 (2004) 094427.
- [1.14] A. A. Cherechukin, I. E. Dikshtein, D. I. Ermakov, A. V. Glebov, V. V. Koledov, D. A. Kosolapov, V. G. Shavrov, A. A. Tulaikova, E. P. Krasnoperov, T.

- Takagi: "Shape memory effect due to magnetic field-induced thermoelastic martensitic transformation in polycrystalline Ni–Mn–Fe–Ga alloy", *Phys. Lett. A*, 291 (2001) 175.
- [1.15] S. J. Murray: "Magneto-mechanical properties and applications of Ni-Mn-Ga ferromagnetic shape memory alloy", Ph.D thesis, Massachusetts Institute of Technology, (2000).
- [1.16] H. E. Karaca, I. Karaman, B. Basaran, Y. Ren, Y. I. Chumlyakov, H. J. Maier: "Magnetic Field-Induced Phase Transformation in NiMnCoIn Magnetic Shape Memory Alloys—A New Actuation Mechanism with Large Work Output", *Adv. Funct. Mater.*, 19 (2009) 983.
- [1.17] T. Kakeshita, T. Takeuchi, T. Fukuda, T. Saburi, R. Oshima, S. Muto, K. Kishio: "Magnetic Field-Induced Martensitic Transformation and Giant Magnetostriction in Fe-Ni-Co-Ti and Ordered Fe₃Pt Shape Memory Alloys", *Mater. Trans. JIM*, 41 (2000) 882.
- [1.18] X. J. Hao, H. Ohtsuka: "Phase Transformation in Fe-Based Alloys in High Magnetic Fields", *Mater. Sci Forum*, 475-479 (2005) 301.
- [1.19] T. Kakeshita, K. Shimizu, S. Funada, M. Date: "Composition dependence of magnetic field-induced martensitic transformations in Fe-Ni alloys", *Acta Metal.*, 33 (1985) 1381.
- [1.20] K. Shimizu, T. Kakeshita: "Effect of Magnetic Fields on Martensitic Transformations in Ferrous Alloys and Steels", *ISIJ Int.*, 29 (1989) 97.
- [1.21] A. A. Cherechukin, I. E. Dikshtein, D. I. Ermakov, A. V. Glebov, V. V. Koledov, D. A. Kosolapov, V. G. Shavrov, A. A. Tulaikova, E. P. Krasnoperov, T. Takagi: "Shape memory effect due to magnetic field-induced thermoelastic martensitic transformation in polycrystalline Ni-Mn-Fe-Ga alloy", *Phys. Lett. A*, 291 (2001) 175.
- [1.22] F. Albertini, L. Pareti, A. Paoluzi, L. Morellon, P. A. Algarabel, M. R. Ibarra, L. Righi: "Composition and temperature dependence of the magnetocrystalline anisotropy in Ni_{2+x}Mn_{1+y}Ga_{1+z} (x+y+z=0) Heusler alloys", *Appl. Phys. Lett.*, 81 (2002) 4032.
- [1.23] R. Kainuma, Y. Imano, W. Ito, Y. Sutou, H. Morito, S. Okamoto, O. Kitakami, K. Oikawa, A. Fujita, T. Kanomata, K. Ishida: "Magnetic-field-induced shape recovery by reverse phase transformation", *Nature*, 439 (2006) 957.

- [1.24] J. Bryzek: "Impact of MEMS technology on society", *Sens. Actuators A*, 56 (1996) 1.
- [1.25] J. W. Judy: "Microelectromechanical systems (MEMS): fabrication, design and applications", *Smart Mater. Struct.*, 10 (2001) 1115.
- [1.26] A. Sozinov, N. Lanska, A. Soroka, W. Zou: "12% magnetic field-induced strain in Ni-Mn-Ga-based non-modulated martensite", *Appl. Phys. Lett.*, 102 (2013) 021902.
- [1.27] A. Sozinov, A. A. Likhachev, K. Ullakko: "Magnetic and magneto-mechanical properties of Ni-Mn-Ga alloys with easy axis and easy plane of magnetization", *Proceeding of SPIE*, 4333 (2001) 189.
- [1.28] C. P. Henry, P. G. Tello, D. Bono, J. Hong, R. Wagner, J. Dai, S. M. Allen, R. C. O'Handley: "Frequency response of single-crystal Ni-Mn-Ga FSMAs", *Proceeding of SPIE*, (2003) 207.
- [1.29] M. Marioni, D. Bono, A. B. Banful, M. Del Rosario, E. Rodriguez, B. W. Peterson, S. M. Allen, R. C. O'Handley: "Pulsed field actuation of Ni-Mn-Ga ferromagnetic shape memory alloy single crystal", *J. Phys. IV*, 112 (2003) 1001.
- [1.30] R. Techapiesanchaenokij, J. Kostamo, S. M. Allen, R. C. O'Handley: "Frequency response of acoustic-assisted Ni-Mn-Ga ferromagnetic-shape-memory-alloy actuator", *J Appl. Phys.*, 105 (2009) 093923.
- [1.31] M. Kohl, Y. Srinivasa Reddy, F. Khelifaoui, B. Krevet¹, A. Backen, S. Fähler, T. Eichhorn, G. Jakob, A. Mecklenburg: "Recent Progress in FSMA Microactuator Developments", *Mater. Sci. Forum*, 635 (2010) 145.
- [1.32] M. Kohl, B. Krevet, M. Ohtsuka, D. Brugger, Y. Liu: "Ferromagnetic Shape Memory Microactuators", *Mater. Trans. JIM*, 47 (2006) 639.
- [1.33] M. Kohl, M. Gueltig, V. Pinneker, R. Yin, F. Wendler, B. Krevet: "Magnetic Shape Memory Microactuators", *Micromachines*, 5 (2014) 1135.
- [1.34] Y. Jia, Q. Xu: "MEMS Microgripper Actuators and Sensors: The State-of-the-Art Survey", *Recent Pat. Mech. Eng.*, 6 (2013) 132.
- [1.35] A. F. Alogla, F. Amalou, C. Balmer, P. Scanlan, W. Shu, R. L. Reuben: "Micro-tweezers: Design, fabrication, simulation and testing of a pneumatically actuated micro-gripper for micromanipulation and microtactile sensing", *Sens. Actuators A*, 236 (2015) 394.
- [1.36] M. Kohl, Y. Liu, B. Krevet, S. Durr, M. Ohtsuka: "SMA microactuators for microvalve applications", *J. Phys. IV*, 115 (2004) 333.

- [1.37] K. Bhattacharya, R. D. James: "The material is the machine", *Science*, 307 (2005) 53.
- [1.38] J. Tellinen, I. Suorsa, A. Jääskeläinen, I. Aaltio, K. Ullakko: "Basic properties of magnetic shape memory actuators", *Proceeding of 8th international conference on Actuator*, (2002) 566.
- [1.39] V. V. Kokorin, V. A. Chernenko, E. Cesari, J. Pons, C. Segui: "Pre-martensitic state in Ni - Mn - Ga alloys", *J. Phys. Condens. Matter*, 8 (1996) 6457.
- [1.40] J. Marcos, L. Manosa, A. Planes, F. Casanova, X. Batlle, A. Labarta: "Multiscale origin of the magnetocaloric effect in Ni-Mn-Ga shape-memory alloys", *Phys. Rev. B*, 68 (2003) 094401.
- [1.41] P. J. Webster, K. R. A. Ziebeck, S. L. Town, M. S. Peak: "Magnetic order and phase transformation in Ni₂MnGa", *Philos. Mag. B*, 49 (1984) 295.
- [1.42] V. V. Martynov, V. V. Kokorin: "The crystal structure of thermally and stress-induced martensites in Ni₂MnGa single crystals", *J. Phys. III*, 2 (1992) 739.
- [1.43] J. Pons, E. Cesari, C. Segui, F. Masdeu, R. Santamarta: "Ferromagnetic shape memory alloys: Alternatives to Ni-Mn-Ga", *Mater. Sci. Eng. A*, 481-482 (2008) 57.
- [1.44] V. A. Chernenko: "Compositional instability of β -phase in Ni-Mn-Ga alloys", *Scr. Mater.*, 40 (1999) 523.
- [1.45] S. Muto, R. Oshima, F. E. Fujita: "Relation of magnetic domain structure to FCT martensite variants in Fe-Pd alloys", *Scr. Metall.*, 21 (1987) 465.
- [1.46] T. Kakeshita, T. Takeuchi, T. Fukuda, T. Saburi, R. Oshima, S. Muto, K. Kishio: "Magnetic Field-Induced Martensitic Transformation and Giant Magnetostriction in Fe-Ni-Co-Ti and Ordered Fe₃Pt Shape Memory Alloys", *Mater. Trans. JIM*, 41 (2000) 882.
- [1.47] R. Kainuma, M. Ise, C. C. Jia, H. Ohtani, H. Ishida: "Phase equilibria and microstructural control in the Ni-Co-Al system", *Intermetallics*, 4 (1996) S151.
- [1.48] K. Oikawa, T. Ota, F. Gejima, T. Ohmori, R. Kainuma, K. Ishida: "Phase Equilibria and Phase Transformations in New B2-type Ferromagnetic Shape Memory Alloys of Co-Ni-Ga and Co-Ni-Al Systems", *Mater. Trans. JIM*, 42 (2001) 2472.

- [1.49] Y. Tanaka, T. Ohmori, K. Oikawa, R. Kainuma, K. Ishida: "Ferromagnetic Co-Ni-Al Shape Memory Alloys with $\beta+\gamma$ Two-Phase Structure", *Mater. Trans. JIM*, 45 (2004) 427.
- [1.50] K. Oikawa, L. Wulff, T. Iijima, F. Gejima, T. Ohmori, A. Fujita, K. Fukamichi, R. Kainuma, K. Ishida: "Promising ferromagnetic Ni-Co-Al shape memory alloy system", *Appl. Phys. Lett.*, 79 (2001) 3290.
- [1.51] A. Fujita, H. Morito, T. Kudo, K. Fukamichi, R. Kainuma, K. Ishida, K. Oikawa: "Magnetocrystalline Anisotropy in a Single-Variant Co-Ni-Al Ferromagnetic Shape Memory Alloy", *Mater. Trans. JIM*, 44 (2003) 2180.
- [1.52] H. Morito, A. Fujita, K. Fukamichi, R. Kainuma, K. Ishida, K. Oikawa: "Magnetocrystalline anisotropy in single-crystal Co-Ni-Al ferromagnetic shape-memory alloy", *Appl. Phys. Lett.*, 81 (2002) 1657.
- [1.53] J. Liu, H. Zheng, Y. Huang, M. Xia, J. Li: "Microstructure and magnetic field induced strain of directionally solidified ferromagnetic shape memory CoNiAl alloys", *Scr. Mater.*, 53 (2005) 29.
- [1.54] H. E. Karaca, I. Karaman, D. C. Lagoudas, H. J. Maier, Y. I. Chumlyakov: "Recoverable stress-induced martensitic transformation in a ferromagnetic CoNiAl alloy", *Scr. Mater.*, 49 (2003) 831.
- [1.55] H. E. Karaca, I. Karaman, Y. I. Chumlyakov, D. C. Lagoudas, X. Zhang: "Compressive response of a single crystalline CoNiAl shape memory alloy", *Scr. Mater.*, 51 (2004) 261.
- [1.56] C. Efstathiou, H. Sehitoglu, A. J. Wagoner Johnson, R. F. Hamilton, H. J. Maier, Y. Chumlyakov: "Large reduction in critical stress in Co-Ni-Al upon repeated transformation", *Scr. Mater.*, 51 (2004) 979.
- [1.57] R. F. Hamilton, H. Sehitoglu, C. Efstathiou, H. J. Maier, Y. Chumlyakov, X. Y. Zhang: "Transformation of Co-Ni-Al single crystals in tension", *Scr. Mater.*, 53 (2005) 131.
- [1.58] R. F. Hamilton, H. Sehitoglu, C. Efstathiou, H. J. Maier, Y. Chumlyakov: "Pseudoelasticity in Co-Ni-Al single and polycrystals", *Acta Mater.*, 54 (2006) 587.
- [1.59] F. Heusler: "Über magnetische manganlegierungen", *Verh. Dtsch. Phys. Ges.*, 12 (1903) 219.
- [1.60] T. M. Tritt (ed): "Recent Trends in Thermoelectric Materials Research I", *Semiconductors and Semimetals (Academic, New York)*, 70 (2001) 37.

- [1.61] F. Casper, T. Graf, S. Chadov, B. Balke, C. Felser: "Half-Heusler compounds: novel materials for energy and spintronic applications", *Semicond. Sci. Technol.*, 27 (2012) 063001.
- [1.62] C. Felser, A. Hirohata (eds): "Heusler Alloys Properties, Growth, Applications", Springer (2016).
- [1.63] E. Sasioglu: "First-principles study of the exchange interactions and Curie temperature in Heusler alloys", Ph. D. Thesis, Martin Luther University of Halle-Wittenberg, (2006).
- [1.64] G. K. Knopf: "Optically driven shape memory alloy microactuators", *Proc. of SPIE*, 5263 (2004) 22.
- [1.65] S. Baglio, S. Castorina, L. Fortuna, N. Savalli: "Modeling and design of novel photo-thermo-mechanical microactuators", *Sens. Actuators A*, 101 (2002) 185.
- [1.66] Y. Q. Fu, J. K. Luo, W. M. Huang, A. J. Flewitt, W. I. Milne: "Thin film shape memory alloys for optical sensing applications", *J. Phys.: Conf. Ser.*, 76 (2007) 012032.
- [1.67] S. S. Zaidi, F. Lamarque, J. Favergeon, O. Carton, C. Prella, M. Lejeune, A. Zeinert: "Wavelength dependent remote power supply for shape memory alloy", *J. Intell. Mater. Syst. Struct.*, 21 (2010) 175.
- [1.68] Z. Hu, B. Rajini Kanth, R. Tamang, B. Varghese, C. H. Sow, P. K. Mukhopadhyay: "Visible microactuation of a ferromagnetic shape memory alloy by focused laser beam", *Smart Mater. Struct.*, 21 (2012) 032003.
- [1.69] http://bose.res.in/~pkm/FSMA_Light_Actuation.
- [2.1] T. Ghosh: "Experimental and theoretical studies of magnetic alloys", Ph. D. Thesis, University of Calcutta, (2017).
- [2.2] Z. Hu, B. Rajini Kanth, R. Tamang, B. Varghese, C. H. Sow, P. K. Mukhopadhyay: "Visible microactuation of a ferromagnetic shape memory alloy by focused laser beam", *Smart Mater. Struct.*, 21 (2012) 032003.
- [2.3] A. Mühlbauer: "History of Induction Heating and Melting", Vulkan-Verlag (2008).
- [2.4] J. Goldstein, D. E. Newbury, P. Echlin, D. C. Joy, A. D. Romig Jr, C. E. Lyman, C. Fiori, E. Lifshin: "Scanning electron microscopy and x-ray microanalysis: a text for biologists, materials scientists, and geologists", 2nd Edition, Springer (1992).
- [2.5] <http://newweb.bose.res.in/facilities/TechnicalCell/EDAX.jsp>.

- [2.6] B. D. Cullity, S. R. Stock: "Elements of X-Ray Diffractions", Addison-Wesley Pub. Co. (1978).
- [2.7] B. E. Warren: "X-ray diffraction", Courier Corporation (1969).
- [2.8] https://en.wikipedia.org/wiki/X-ray_crystallography.
- [2.9] <http://newweb.bose.res.in/facilities/TechnicalCell/MiniXRD.jsp>.
- [2.10] D. B. Williams, C. B. Carter: "Transmission Electron Microscopy: A Textbook for Materials Science", Springer (1996).
- [2.11] L. Reimer: "Transmission Electron Microscopy: Physics of Image Formation and Microanalysis", Springer-Verlag (1984).
- [2.12] J. C. H. Spence: "High-Resolution Electron Microscopy", 4th Edition, Oxford University Press (2013).
- [2.13] A. V. Crewe, J. P. Wall, J. P. Langmore: "Visibility of Single Atoms", Science, 168 (1970) 1138.
- [2.14] S. T. Pennycook, P. D. Nellist: "Scanning Transmission Electron Microscopy: Imaging and Analysis", Springer (2011).
- [2.15] Z. L. Wang: "New Development in Transmission Electron Microscopy for Nanotechnology", Adv. Mater, 15 (2003) 1497.
- [2.16] E. Carlino, V. Grillo: "Atomic-Resolution Quantitative Composition Analysis using Scanning Transmission Electron Microscopy Z-Contrast Experiments", Phys. Rev. B, 71 (2005) 235303.
- [2.17] http://www.cgcri.res.in/images/facility_ana_micro.pdf.
- [2.18] S. Foner: "Versatile and Sensitive Vibrating-Sample Magnetometer", Rev. Sci. Instrum, 30 (1959) 548.
- [2.19] B. D. Cullity, C. D. Graham: "Introduction to Magnetic Materials", 2nd Edition, Wiley-IEEE Press (2008).
- [2.20] https://en.wikipedia.org/wiki/Vibrating-sample_magnetometer.
- [2.21] <http://newweb.bose.res.in/facilities/TechnicalCell/VSM.jsp>.
- [2.22] P. Müllner, Z. Clark, L. Kenoyer, W. B. Knowlton, G. Kostorz: "Nanomechanics and magnetic structure of orthorhombic Ni-Mn-Ga martensite", Mater. Sci. Eng. A, 481-482 (2008) 66.
- [2.23] "Nikon Eclipse Ti-U inverted microscope" user manual.
- [2.24] A. Bagchi, S. Sarkar, P. K. Mukhopadhyay: "Investigations on colour dependent photo induced microactuation effect of FSMA and proposing suitable mechanisms to control the effect", Indian J Phys, 92 (2018) 883.

- [2.25] D. C. Montgomery: "Design and Analysis of Experiments", 9th edition, Wiley (2017).
- [2.26] G. W. Oehlert: "A First Course in Design and Analysis of Experiments", W. H. Freeman & Co. Ltd (2000).
- [3.1] Z. Hu, B. Rajini Kanth, R. Tamang, B. Varghese, C. H. Sow, P. K. Mukhopadhyay: "Visible microactuation of a ferromagnetic shape memory alloy by focused laser beam", *Smart Mater. Struct.*, 21 (2012) 032003.
- [3.2] J. Abadie, N. Chaillet, C. Lexcellent: "An integrated shape memory alloy micro-actuator controlled by thermoelectric effect", *Sens. Actuators A*, 99 (2002) 297.
- [3.3] M. Kohl, B. Krevet, M. Ohtsuka, D. Brugger, Y. Liu: "Ferromagnetic Shape Memory Microactuators", *Mater. Trans. JIM*, 47 (2006) 639.
- [3.4] M. E. Piccini, B. C. Towe: "A shape memory alloy microvalve with flow sensing", *Sens. Actuators A*, 128 (2006) 344.
- [3.5] C. M. Pemble, B. C. Towe: "A miniature shape memory alloy pinch valve", *Sens. Actuators A*, 77 (1999) 145.
- [3.6] A.F. Alogla, F. Amalou, C. Balmer, P. Scanlan, W. Shu, R.L. Reuben: "Micro-tweezers: Design, fabrication, simulation and testing of a pneumatically actuated micro-gripper for micromanipulation and microtactile sensing", *Sens. Actuators A*, 236 (2015) 394.
- [3.7] G. K. Knopf: "Optically driven shape memory alloy microactuators", *Proc. of SPIE*, 5263 (2004) 22.
- [3.8] S. Baglio, S. Castorina, L. Fortuna, N. Savalli: "Modeling and design of novel photo-thermo-mechanical microactuators", *Sens. Actuators A*, 101 (2002) 185.
- [3.9] Y. Q. Fu, J. K. Luo, W. M. Huang, A. J. Flewitt, W. I. Milne: "Thin film shape memory alloys for optical sensing applications", *J. Phys.: Conf. Ser.*, 76 (2007) 012032.
- [3.10] S. S. Zaidi, F. Lamarque, J. Favergeon, O. Carton, C. Prella, M. Lejeune, A. Zeinert: "Wavelength dependent remote power supply for shape memory alloy", *J. Intell. Mater. Syst. Struct.*, 21 (2010) 175.
- [3.11] https://en.wikipedia.org/wiki/Photon_energy.
- [3.12] https://en.wikipedia.org/wiki/Planck%E2%80%93Einstein_relation.
- [3.13] G. W. Oehlert: "A First Course in Design and Analysis of Experiments", W. H. Freeman & Co. Ltd (2000).

- [3.14] D. C. Montgomery: "Design and Analysis of Experiments", 9th edition, Wiley (2017).
- [3.15] J. W. Tukey: "The Philosophy of Multiple Comparisons", *Statist. Sci.*, 6 (1) (1991) 100.
- [3.16] Abhishek Bagchi, Suman Sarkar, Sandip Bysakh, Susenjit Sarkar, P. K. Mukhopadhyay: "Possible mechanisms for degradation of Photo Induced Micro Actuation effect in a Ferromagnetic Shape Memory Alloy at high temperatures", *J. Appl. Phys.*, 125 (2019) 144505.
- [4.1] Z. Hu, B. Rajini Kanth, R. Tamang, B. Varghese, C. H. Sow, P. K. Mukhopadhyay: "Visible microactuation of a ferromagnetic shape memory alloy by focused laser beam", *Smart Mater. Struct.*, 21 (2012) 032003.
- [4.2] M. F. Ashby, L. M. Brown: "Diffraction contrast from spherically symmetrical coherency strains", *Philos. Mag.*, 8 (1963) 1083.
- [4.3] K. G. McIntyre, L. M. Brown: "Anomalous images in electron microscopy", *J. Phys. Colloques*, 27 (1966) C3-178.
- [4.4] S. Matsumura, M. Toyohara, Y. Tomokiyo: "Strain contrast of coherent precipitates in bright-field images under zone axis incidence", *Philos. Mag. A*, 62:6 (1990) 653.
- [4.5] S. Sarkar, C. Srivastava, K. Chattopadhyay: "Development of a new class of high strength copper alloy using immiscibility route in Cu-Fe-Si system: Evolution of hierarchical multi-scale microstructure", *Mater. Sci. Eng. A*, 723 (2018) 38.
- [4.6] Z. Liu, S. Yu, H. Yang, G. Wu, Y. Liu: "Phase separation and magnetic properties of Co–Ni–Al ferromagnetic shape memory alloys", *Intermetallics*, 16 (2008) 447.
- [4.7] W. Maziarz, J. Dutkiewicz, R. Santamarta, E. Cesari: "Microstructure changes in two phase $\beta + \gamma$ Co-Ni-Al ferromagnetic shape memory alloys in relation to Al/Co ratio", *Eur. Phys. J. Spec. Top.*, 158 (2008) 137.
- [4.8] J. B. Lu, D. Schryvers: "Microstructure and phase composition characterization in a $\text{Co}_{38}\text{Ni}_{33}\text{Al}_{29}$ ferromagnetic shape memory alloy", *Mater. Charact.*, 118 (2016) 9.
- [4.9] J. Ju, F. Xue, L. Sun: "Structure and performance changes of Ni-Co-Al shape memory alloys in relation to Co/Al atomic ratio", *J. Iron Steel Res. Int.*, 22 (2015) 652.

- [4.10] L. Liu, S. Wu, Y. Chen, S. Lu: "Oxidation behavior of RE-modified nickel-based superalloy between 950 °C and 1150 °C in air", *Trans. Nonferrous Met. Soc. China*, 26 (2016) 1163.
- [4.11] J. L. Smialek, D. L. Humphrey, R. D. Noebe: "Comparative Oxidation Kinetics of a NiPtTi High Temperature Shape Memory Alloy", *Oxid. Met.*, 74 (2010) 125.
- [4.12] K. Kawagishi, A. Sato, T. Kobayashi, H. Harada: "Oxidation Properties for 2nd – 5th Generation Ni – Base Single – Crystal Superalloys at 1023, 1173 and 1373 K", *J. Japan Inst. Metals*, 71 (2007) 313.
- [4.13] A. S. Suzuki, K. Kawagishi, T. Yokokawa, H. Harada, T. Kobayashi: "A New Oxide Morphology Map: Initial Oxidation Behavior of Ni-Base Single-Crystal Superalloys", *Metall. Mat. Trans. A*, 43 (2012) 155.
- [4.14] S. Pedrazzini, D. J. Child, G. West, S. S. Doak, M. C. Hardy, M. P. Moody, P. A. J. Bagot: "Oxidation behaviour of a next generation polycrystalline Mn containing Ni-based superalloy", *Scr. Mater.*, 113 (2016) 51.
- [4.15] A. S. Suzuki, K. Kawagishi, T. Yokokawa, T. Kobayashi, H. Harada: "Prediction of Initial Oxidation Behavior of Ni-Base Single Crystal Superalloys: A New Oxidation Map and Regression Analysis", *Superalloys*, (2012) 321.
- [4.16] J. Ejenstam, M. Halvarsson, J. Weidow, B. Jönsson, P. Szakalos: "Oxidation studies of Fe₁₀CrAl–RE alloys exposed to Pb at 550 °C for 10,000 h", *J. Nucl. Mater.*, 443 (2013) 161.
- [4.17] Abhishek Bagchi, Suman Sarkar, Sandip Bysakh, Susenjit Sarkar, P. K. Mukhopadhyay: "Possible mechanisms for degradation of Photo Induced Micro Actuation effect in a Ferromagnetic Shape Memory Alloy at high temperatures", *J. Appl. Phys.*, 125 (2019) 144505.
- [4.18] A. Mathur, T. Maity, S. Wadhwa, B. Ghosh, S. Sarma, S. C. Ray, B. Kaviraj, S. S. Roy, S. Roy: "Magnetic properties of microwave-plasma (thermal) chemical vapour deposited Co-filled (Fe-filled) multiwall carbon nanotubes: comparative study for magnetic device applications", *Mater. Res. Express*, 5 (2018) 076101.
- [4.19] G. J. Arputhavalli, S. Agilan, R. Johnson: "Microstructure and Phase Transformation Behaviour of Co–Ni–Al Alloy by Spark Plasma Sintering", *Recent Trends in Materials Science and Applications* (Ed. J. Ebenezer), 189 (2017) 391.

- [4.20] H. Y. Wang, Z. H. Liu, Y. G. Wang, X. F. Duan, G. H. Wu: "Microstructure of martensitic phase in the $\text{Co}_{39}\text{Ni}_{33}\text{Al}_{28}$ shape memory alloys revealed by transmission electron microscopy", *J Alloys Compd.*, 400 (2005) 145.
- [4.21] X. F. Dai, H. Y. Wang, G. D. Liu, Y. G. Wang, X. F. Duan, J. L. Chen, G. H. Wu: "Effect of heat treatment on the properties of $\text{Co}_{50}\text{Ni}_{20}\text{Ga}_{30}$ ferromagnetic shape memory alloy ribbons", *J. Phys. D: Appl. Phys.*, 39 (2006) 2886.
- [4.22] H. Y. Wang, K. Wang, Z. H. Liu, Y. G. Wang, G. H. Wu, X. F. Duan: "TEM Characterization of Twinning in $\text{Co}_{39}\text{Ni}_{33}\text{Al}_{28}$ Alloy", *Mater. Trans.*, 48 (2007) 2139.
- [5.1] L. Pan-Pan, W. Jing-Min, J. Cheng-Bao: "Martensitic transformation in Cu-doped NiMnGa magnetic shape memory alloys", *Chin. Phys. B*, 20 (2011) 028104.
- [5.2] J. Ju, H. Liu, L. Shuai, Z. Liu, Y. Kang, C. Yan, H. Li: "Martensite Transformation and Mechanical Properties of Polycrystalline Co-Ni-Al Alloys with Gd Doping", 8 (2018) 848.
- [5.3] C. Tan, Z. Tai, K. Zhang, X. Tian, W. Cai: "Simultaneous enhancement of magnetic and mechanical properties in Ni-Mn-Sn alloy by Fe doping", *Sci. Rep.*, 7 (2017) 43387.
- [5.4] K. Zhang, C. Tan, E. J. Guo, Z. C. Feng, J. C. Zhu, Y. X. Tong, W. Cai: "Simultaneous tuning of martensitic transformation behavior, magnetic and mechanical properties in Ni-Mn-Sn magnetic alloy by Cu doping", *J. Mater. Chem. C*, 6 (2018) 5228.
- [5.5] A. Bagchi, S. Sarkar, P. K. Mukhopadhyay: "Investigations on colour dependent photo induced microactuation effect of FSMA and proposing suitable mechanisms to control the effect", *Indian J. Phys.*, 92 (2018) 883.
- [5.6] D. Wu, W. C. Crone, J. Perepezko: "Mechanical Behavior of Nanostructured Melt Spun NiTi Shape Memory Alloy", *Society for Experimental Mechanics, 2002 SEM Annual Conference Proceedings*, (2002).
- [5.7] B. Jiang, J. Wang, L. Xu, C. Qian, T. Liu, J. Dai, X. Hou: "Tunable Mechanical Properties of Ti-Zr-Ni-Cr-V Amorphous Ribbons via Different Melt Spinning Speeds during Rapid Solidification Process", *Materials*, 11 (2018) 947.
- [5.8] B. J. Park, H. J. Chang, D. H. Kim, W. T. Kim, K. Chattopadhyay, T. A. Abinandanan, S. Bhattacharyya: "Phase Separating Bulk Metallic Glass: A Hierarchical Composite", *PRL*, 96 (2006) 245503.

- [5.9] H. Y. Wang, Z. H. Liu, Y. G. Wang, X. F. Duan, G. H. Wu: "Microstructure of martensitic phase in the Co₃₉Ni₃₃Al₂₈ shape memory alloys revealed by transmission electron microscopy", *J. Alloy Compd.*, 400 (2005) 145.
- [5.10] N. Zarubova, J. Gemperlova, A. Gemperle, Z. Dlabacek, P. Sittner, V. Novak: "In situ TEM observation of stress-induced martensitic transformations and twinning processes in CuAlNi single crystals", *Acta Mater.*, 58 (2010) 5109.
- [5.11] W. Maziarz, J. Dutkiewicz, R. Santamarta, E. Cesari: "Microstructure changes in two phase $\beta + \gamma$ Co-Ni-Al ferromagnetic shape memory alloys in relation to Al/Co ratio", *Eur. Phys. J. Special Topics*, 158 (2008) 137.
- [5.12] S. Sarkar, C. Srivastava, K. Chattopadhyay: "Development of a new class of high strength copper alloy using immiscibility route in Cu-Fe-Si system: Evolution of hierarchical multi-scale microstructure", *Mater. Sci. Eng. A*, 723 (2018) 38.
- [5.13] H. Y. Wang, K. Wang, Z. H. Liu, Y. G. Wang, G. H. Wu, X. F. Duan: "TEM Characterization of Twinning in Co₃₉Ni₃₃Al₂₈ Alloy", *Materials Transactions*, 48(8) (2007) 2139.
- [5.14] J. Ju, L. Yang, S. Hao, Q. Mao, S. Lou, H. Liu: "Microstructure, Martensite Transition and Mechanical Properties Investigations of Polycrystalline Co-Ni-Al Alloys with Er Doping", *J. Mater. Eng. Perform.*, 26 (2017) 1062.
- [5.15] J. Ju, F. Xue, L. Sun: "Structure and Performance Changes of Ni-Co-Al Shape Memory Alloys in Relation to Co/Al Atomic Ratio", *J Iron Steel Res Int* 22 (2015) 652.
- [5.16] Y. Tanaka, T. Ohmori, K. Oikawa, R. Kainuma, K. Ishida: "Ferromagnetic Co-Ni-Al Shape Memory Alloys with $\beta+\gamma$ Two-Phase Structure", *Mater. Trans. JIM*, 45 (2004) 427.
- [5.17] M. Khan, I. Dubenko, S. Stadler, N. Ali: "The structural and magnetic properties of Ni₂Mn_{1-x}MxGa (M=Co, Cu)", *J. Appl. Phys.*, 97 (2005) 10M304.
- [5.18] Abhishek Bagchi, Suman Sarkar, Sandip Bysakh, Susenjit Sarkar, P. K. Mukhopadhyay: "Studies on the effect of temperature on the Photo-Induced Microactuation effect of a Co-based FSMA system", *Shap. Mem. Superelasticity*, <https://doi.org/10.1007/s40830-020-00270-6>.
- [6.1] C. M. Pemble, B. C. Towe: "Miniature shape memory alloy pinch valve", *Sens. Actuator A Phys.*, 77 (1999) 145.

- [6.2] J. Abadie, N. Chaillet, C. Lexcellent: "An integrated shape memory alloy micro-actuator controlled by thermoelectric effect", *Sens. Actuator A Phys.*, 99 (2002) 297.
- [6.3] M. Kohl, B. Krevet, M. Ohtsuka, D. Brugger, Y. Liu: "Ferromagnetic Shape Memory Microactuators", *Mater. Trans. JIM*, 47 (2006) 639.
- [6.4] M. E. Piccini, B. C. Towe: "A shape memory alloy microvalve with flow sensing", *Sens. Actuator A Phys.*, 128 (2006) 344.
- [6.5] A. Nespoli, S. Besseghini, S. Pittaccio, E. Villa, S. Viscuso: "The high potential of shape memory alloys in developing miniature mechanical devices: A review on shape memory alloy mini-actuators", *Sens. Actuator A Phys.*, 158 (2010) 149.
- [6.6] A. F. Alogla, F. Amalou, C. Balmer, P. Scanlan, W. Shu, R. L. Reuben: "Micro-tweezers: Design, fabrication, simulation and testing of a pneumatically actuated micro-gripper for micromanipulation and microtactile sensing", *Sens. Actuator A Phys.*, 236 (2015) 394.
- [6.7] A. Bagchi, S. Sarkar, P. K. Mukhopadhyay: "Investigations on colour dependent photo induced microactuation effect of FSMA and proposing suitable mechanisms to control the effect", *Indian J. Phys.*, 92 (2018) 883.
- [6.8] Y. Jia, Q. Xu: "MEMS Microgripper Actuators and Sensors: The State-of-the-Art Survey", *Recent Pat. Mech. Engg.*, 6 (2013) 132.
- [6.9] P. Vargas-Chable, M. Tecpoyotl-Torres, R. Cabello-Ruiz, J. A. Rodriguez-Ramirez, R. Vargas-Bernal: "Modified U-shaped Microactuator with Compliant Mechanism Applied to a Microgripper", *Actuators*, 8 (2019) 28.
- [6.10] A. Thangavel, R. Rengaswamy, P. Sukumar: "Design and material analysis for prototyping of four arm mechanical microgripper with self-locking and anti-slipping capability", *Microsyst. Technol.*, 25 (2019) 851.
- [6.11] N. Dechev, W. L. Cleghorn, J. K. Mills: "Microassembly of 3-D MEMS Structures Utilizing a MEMS Microgripper with a Robotic Manipulator", *IEEE International Conference on Robotics and Automation*, 3 (2003) 3193.
- [6.12] J. Fujiki, N. Xu, L. Hutin, I-R. Chen, C. Qian, T. J. K. Liu: "Microelectromechanical relay and logic circuit design for zero crowbar current", *IEEE Trans. Electron Devices*, 61 (2014) 3296.
- [6.13] M. Spencer, F. Chen, C. Wang, R. Nathanael, H. Fariborzi, A. Gupta, H. Kam, V. Pott, J. Jeon, T. J. K. Liu, D. Marković, E. Alon, V. Stojanović:

- ““Demonstration of integrated micro-electro-mechanical relay circuits for VLSI applications”, IEEE J. Solid-State Circuits, 46 (2011) 308.
- [6.14] H. Fariborzi, F. Chen, R. Nathanael, J. Jeon, T. J. K. Liu, V. Stojanović: ““Design and demonstration of micro-electro-mechanical relay multipliers”, Proceedings of the IEEE Asian Solid-State Circuits Conference, (2011) 117.
- [6.15] S. Dilibal, H. Sahin, E. Dursun, E. D. Engeberg: “Nickel–titanium shape memory alloy-actuated thermal overload relay system design”, Electr. Eng., 99 (2017) 923.

Investigations on colour dependent photo induced microactuation effect of FSMA and proposing suitable mechanisms to control the effect

A Bagchi^{1,2}, S Sarkar² and P K Mukhopadhyay^{1*}

¹LCMP, S. N. Bose National Centre for Basic Sciences, Kolkata 700106, India

²Department of Mechanical Engineering, Jadavpur University, Kolkata 700032, India

Received: 02 June 2017 / Accepted: 01 December 2017 / Published online: 15 February 2018

Abstract: Three different coloured focused laser beams were used to study the photo induced microactuation effect found in some ferromagnetic shape memory alloys. Besides trying to uncover the basic causes of this unique and as yet unexplained effect, these studies are to help find other conditions to further characterize the effect for practical use. In this study some mechanisms have been proposed to control the amplitude of actuation of the sample. Control of the actuation of the FSMA sample both linearly with the help of a continuously variable neutral density filter as well periodically with the help of a linear polarizer was achieved. Statistical analysis of the experimental data was also done by applying ANOVA studies on the data to conclusively provide evidence in support of the relationship between the actuation of the sample and the various controlling factors. This study is expected to pave the way to implement this property of the sample in fabricating and operating useful micro-mechanical systems in the near future.

Keywords: Ferromagnetic shape memory alloys; Laser; Polarization; Microactuation; Analysis of variance

PACS Nos.: 42.55.Px; 42.62.Cf; 68.35.bd; 78.20.Ek

1. Introduction

In the year 2012 it was first reported that a Ferromagnetic Shape memory Alloy (FSMA) sample was showing photo induced micro actuation (PIMA) effect when subjected to a focused red laser beam [1]. When a tiny spot of a focused laser beam (of power about 20 mW) was incident on the sample it immediately moved away, only to return to the original position as soon as the light was switched off. A lot of effort has been given to fully understand the cause of this phenomenon. But till now the cause of this effect is not understood. This PIMA effect is unique and does not have any parallel with any hitherto known phenomenon. In order to understand this effect, a systematic study is now undertaken. The first effort was to try to see if any other material would show this effect. Experiments were tried with pieces of paper, aluminium foil, thin sheets of iron, copper, various plastics etc. but it was never observed in

any of them. It seems that somehow only some FSMA materials are endowed with this property.

However, even with little understanding of the basic Physics behind this, it is still possible to utilize this effect for practical use. For proper harnessing the effect for use, the PIMA effect must be fully characterized. Towards this, the present study was devoted. FSMA materials have immense potential to be used as microactuators due to their ability to generate mechanical work under the influence of thermal or magnetic stimuli [2–7]. With the discovery of the PIMA effect a new method to extend the control on the actuation mechanism of the microactuator systems can be proposed. In the first report of the PIMA effect only a red coloured laser of wavelength 660 nm and power of 20–80 mW was studied [1]. In order to understand this effect in detail, systematic investigations were carried out using three different coloured diode lasers viz. red, blue and green. In this communication the findings on one such alloy system are reported. With this study on the microactuation effect an effective, new and unique controlling mechanism for the fabrication and operation of various microactuator systems is proposed.

*Corresponding author, E-mail: pkm@bose.res.in

Possible mechanisms for degradation of photo induced micro actuation effect in a ferromagnetic shape memory alloy at high temperatures

Cite as: J. Appl. Phys. 125, 144505 (2019); doi: 10.1063/1.5088076

Submitted: 8 January 2019 · Accepted: 15 March 2019 ·

Published Online: 11 April 2019



View Online



Export Citation



CrossMark

Abhishek Bagchi,^{1,2}  Suman Sarkar,³ Sandip Bysakh,⁴ Susenjit Sarkar,² and P. K. Mukhopadhyay^{1,3,a)}

AFFILIATIONS

¹LCMP, S. N. Bose National Centre for Basic Sciences, Kolkata 700106, India

²Department of Mechanical Engineering, Jadavpur University, Kolkata 700032, India

³TRC, S. N. Bose National Centre for Basic Sciences, Kolkata 700106, India

⁴CSIR-Central Glass and Ceramic Research Institute, Kolkata 700032, India

^{a)} Author to whom correspondence should be addressed: pkm@bose.res.in

ABSTRACT

Ferromagnetic shape memory alloys (FSMAs) have been in active research nowadays for their unique properties of responses to both temperature changes and external magnetic fields. Recently, one such material, a CoNiAl based system, showed a photoinduced microactuation (PIMA) effect in which an incident spot of a tiny laser beam could induce actuation in these systems. This is unparalleled in ordinary materials, and its real cause is yet to be found. However, we tried to still use it in real world engineering applications, and for that, the limitations on its usability should be found. With this idea, we studied here in detail the effect of continuous degradation of the PIMA effect on a ribbon sample through TEM, as it was exposed to higher temperatures from room temperature. While the as-spun alloy had microstructured B2 ordered (Ni, Co)-Al micrometer sized grains embedded in a continuous L1₂ ordered cobalt-rich matrix channel, at 400 °C where the PIMA effect was fully destroyed, Co-rich nanosized precipitates were found to have formed inside the B2 grains, the actual FSMA component in the sample, and these are also found to have been oxidized. Concurrent oxidation studies showed the formation of an irregular shaped composite oxide layer with a thickness of about several hundred nanometers at the top surface. These are possibly the reasons behind the hindrance in the actuating motion. This was corroborated by magnetic studies also.

Published under license by AIP Publishing. <https://doi.org/10.1063/1.5088076>

I. INTRODUCTION

Worldwide, the search, both experimentally and theoretically, is for designing new materials that have exotic properties as compared to conventional materials. One such new class of materials has now evolved that are called smart materials; these materials have a more predictable and repeatable response to external stimuli like temperature and light and physical force like shear. These are nowadays being used for special purposes where ordinary materials could not be used. Among these is a special class of materials called ferromagnetic shape memory alloys (FSMAs).¹⁻³ They share common traits with a wider class of materials called shape memory alloys (SMAs), in that they have temperature driven reversible Austenite–Martensite (A–M) transformations, superelasticity, and also the strongest known magnetic coupling to the lattice strain,

giving rise to shape changes and even A–M transformations. They actually respond faster than thermal driven changes like in SMAs. With these interesting properties, there are attempts to harness them to various special cases.

While main work goes on with the traditional FSMAs like Ni–Mn–Ga based Full Heusler alloys due to their excellent response properties, these materials suffer from high brittleness, leading to difficulty in practical uses.⁴⁻⁶ Recently, Co–Ni–Al systems have become popular for their better mechanical properties. This system also demonstrated a photoinduced microactuation (PIMA) effect while interacting with a laser, in which a tiny spot of the laser beam can induce a mechanical actuation (movement) in these materials. This is a unique property that we failed to reproduce in any other system and is almost an imitation of living systems.



Studies on the Effect of Temperature on the Photo-Induced Microactuation Effect of a Co-based FSMA System

Abhishek Bagchi^{1,2} · Suman Sarkar^{3,4} · Sandip Bysakh⁵ · Susenjit Sarkar² · P. K. Mukhopadhyay^{1,4}

© ASM International 2020

Abstract In this work, we have studied the effect of open air annealing on photo-induced microactuation (PIMA) property of a Co–Ni–Al melt-spun FSMA ribbon sample. This is one of the alloy systems that demonstrate the special type of PIMA effect while interacting with laser. This property has opened up the scope of various laser-controlled micromechanical engineering applications. Due to this importance, a detailed study has been made to explore the applicability of this alloy in different environmental conditions, where temperature plays an important role. The correlation between microstructure and the photo-induced microactuation (PIMA) properties has also been addressed here. The variation in actuation of the alloy with different heat-treated conditions has been studied in details.

Transmission electron microscopy (TEM) was used to characterize the evolved microstructure for both the as-spun and the heat-treated alloy samples. The correlation between the evolution of the structural effects and resulting degradation of the PIMA property changes was also followed systematically to understand the correlation.

Keywords Ferromagnetic shape memory alloys · Laser · Microactuation · Heat treatment · Microstructure · TEM

Introduction

The photo-induced microactuation (PIMA) properties shown by a thin sample of Co–Ni–Al FSMA system was first reported in 2012 [1]. To understand this extraordinary effect, various experiments were conducted to see the effects of color, output power and polarization of the incident laser beams [2]. Apart from understanding the fundamental reason behind this effect, these studies are useful for successful implementation of a new class of laser-controlled remotely operated microactuator systems in the near future. Here, we carried out such a study on a sample which was subjected to different levels of heat treatment. Previously, the effect of temperature on the actuation of the sample was reported, but it was conducted in a vacuum sealed environment to prevent the oxidation of the sample. So the effect of rise in temperature in open air was still unknown and the present study was undertaken to tackle this issue. In addition to that, the microstructural properties of the system were also studied systematically to explore the cause of degradation of PIMA effect that occurred due to the heat treatment at different annealing temperatures in open environment.

This article is an invited submission to Shape Memory and Superelasticity selected from presentations at the International Conference on Ferromagnetic Shape Memory Alloys (ICFSMA) held June 2–7, 2019 in Prague, Czech Republic, and has been expanded from the original presentation.

✉ Suman Sarkar
sumrcvt@gmail.com; suman.sarkar@iitjammu.ac.in

✉ P. K. Mukhopadhyay
pkm@bose.res.in

¹ LCMP, S. N. Bose National Centre for Basic Sciences, Kolkata 700106, India

² Department of Mechanical Engineering, Jadavpur University, Kolkata 700032, India

³ Department of Materials Engineering, Indian Institute of Technology Jammu, Jammu 181221, India

⁴ TRC, S. N. Bose National Centre for Basic Sciences, Kolkata 700106, India

⁵ CSIR-Central Glass and Ceramic Research Institute, Kolkata 700032, India

Investigations on PhotoInduced Microactuation of FSMA

Abhishek Bagchi¹, B. Rajini Kanth² and P.K.Mukhopadhyay¹

¹ LCMP, S. N. Bose National Centre for Basic Sciences, JD Block, Salt Lake 700 098, India

² LSMS, T. K. R. College Engineering and Technology, Hyderabad 500097, India

e-mail: pkm@bose.res.in

Key words: FSMA, laser, photoinduced, microactuation

1 Introduction

In 2012 it was announced [1] that a FSMA material was showing photoinduced microactuation effect [PIMA]. This is a unique phenomenon and does not have any parallel with any other known phenomenon. Here, when a tiny spot of a laser beam, power about 20mW, was incident on the sample, it immediately moved away, only to return to the original position as soon as the light was shut off. A lot of effort was given to understand the effect, however, it failed. It is still not clear what causes this effect.

In order to understand this effect, a systematic study is now undertaken. The first effort was to try to see if any other material would show this effect. We tried with pieces of paper, aluminium foil, thin sheets of iron, copper, various plastics etc. but it was never found. It seems that somehow only FSMA materials are endowed with this property.

We then planned to find the effect of colour of light on the actuation. We used 3 different coloured lasers – red, green and blue and measured the effect. In this communication we report on the findings on one such alloy system.

2 Experimental procedures

Thin metallic ribbons of a CoNiAl system was made by rapid quenching of nominal composition alloy melted in an r.f. induction furnace and extracting on a water cooled copper wheel rotating at 1000rpm. A suitable piece was taken from the ribbons, and small pieces were cut from it for various measurements. The samples were about 2.4mm wide and 100µm thick.

Standard XRD, SEM, EDAX and M-T measurements were done to characterize the system. The PIMA effects were studied by separately shining lasers from three diodes, coloured red, green and blue. The system was placed on an optical breadboard, with the sample below the objective of a microscope. The light beam was interrupted with a shutter and the displacements were measured with the software provided with the microscope.

3 Results and discussions

3.1 Structural characterization

EDAX results showed that there was a nominal variation in composition, the average value taken was Co₃₄Ni₃₅Al₃₁. SEM showed that the system was finely structured. XRD analysis confirmed the glassy nature of

the system and the presence of two phases (β and γ) in the system.

3.2 Magnetic characterization

VSM data (100Oe) from 300K to 1073K and back is presented in figure 1. It can be seen that there are two types of magnetic transitions, one near 370K and another near 1070K. Return measurements showed that the low temperature phase was not recovered now. This is consistent with what was found for similar systems before [2]. Overall, it showed that the as prepared system would be ferromagnetic due to the β phase at around room temperature.

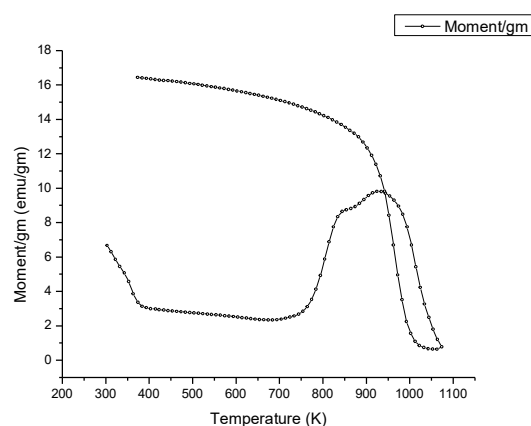


Figure 1. Magnetization of the sample showing irreversibility in phase transformation

3.3 Photo induced effect

A small piece with length about 2 cm was cut randomly from the bulk ribbon samples. One end of the ribbon was secured to a wooden frame with the help of adhesive tape, keeping the other end free. The middle of the ribbon was bent manually to form a hinged structure, like an elbow joint. The wooden frame with the sample attached to it was placed under the microscope. Next different coloured lasers were used to perform the experiments. Firstly, the sample was excited by a blue coloured laser with a wavelength of 450 nm and power output of 95 mw. The laser beam was focused on the hinged portion of the CoNiAl ribbon. Multiple readings were taken by rotating the laser source from 0° to 180° with an interval of 10° between each reading. The microactuation effect of the sample was measured using the software provided with

Photo Induced Control Mechanism of a proposed FSMA Microgripper System

Abhishek Bagchi^{1,2}, Susenjit Sarkar² and P. K. Mukhopadhyay¹

Affiliation:

¹ LCMP, S. N. Bose National Centre for Basic Sciences, Kolkata - 700106, India

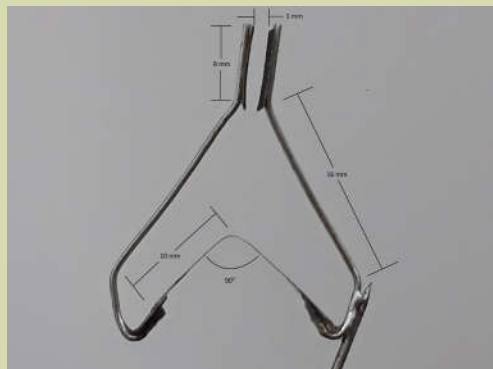
² Department of Mechanical Engineering, Jadavpur University, Kolkata - 700032, India

E-mail:

abhishekbagchi@bose.res.in,
susenjit_s@rediffmail.com,
pkm@bose.res.in

Abstract

In the year 2012 it was first observed that a Ferromagnetic Shape memory Alloy (FSMA) was showing a Photo Induced Micro Actuation (PIMA) effect when subjected to a focused laser beam [1]. Here, when a tiny spot of a focused laser beam, power about 20mW, was incident on the sample, it immediately moved away, only to return to the original position as soon as the light was shut off. This PIMA effect is a unique phenomenon and does not have any parallel with any other known phenomena. FSMA materials have immense potential to be used as microactuators due to their ability to generate mechanical work under the influence of thermal or magnetic stimuli. With the discovery of the PIMA effect, a new method to characterize and effectively control the actuation mechanism of the microactuator systems can be proposed. As an example of one such microactuator system a prototype of a very simple microgripper system made of FSMA is proposed in this study. A model was developed and its characteristics under different light sources were systematically studied. One most important parameter was the colour of the incident light. Here we used three different coloured lasers and the actuation phenomenon was studied [2]. An effective, new and unique controlling mechanism for the production and operation of various microactuator systems has been proposed here.



References:

1. Hu Z, Kanth B R, Tamang R, Varghese B, Sow C-H and Mukhopadhyay P K, Smart Mater. Struct, Vol. 21 (2012), 032003.
2. A Bagchi, S Sarkar and P. K. Mukhopadhyay, Indian J. Phys (2017), In Press.

Effect of temperature on the photo induced microactuation property of FSMA

Abhishek Bagchi^{1,2}, Suman Sarkar¹, Susenjit Sarkar² and P. K. Mukhopadhyay^{1,*}

¹LCMP, S. N. Bose National Centre for Basic Sciences, Kolkata-700106, India

²Department of Mechanical Engineering, Jadavpur University, Kolkata-700032, India

Email: pkm@bose.res.in

Abstract

Microstructures of Co-Ni-Al FSMA metglass ribbon systems show localized microactuation property when they are excited by a focused laser beam [1]. This photo induced microactuation (PIMA) effect in FSMA is found to be rapid and fatigue resistant over millions of oscillations. The PIMA effect is dependent on various factors like laser power, laser polarization as well as colour of the laser, apart from dependence on materials [2]. The effect of temperature on the PIMA property shown by the selected Co-Ni-Al FSMA system is reported here. For measuring the temperature dependence of the property, the ribbon sample was first placed in a vacuum sealed quartz tube in such a way that there was enough space for the sample to actuate when stimulated by a focused laser beam. The device was then placed on a heater with an attached thermometer to measure the temperature of the sample. The sample was then gradually heated upto 400 °C and simultaneously a focused laser beam was made incident on the ribbon. The amplitude of microactuation was measured by an optical microscope. It was observed that the Co-Ni-Al FSMA ribbon showed significant microactuation upto a temperature of 120 °C after which the sample did not show any microactuation for the same laser power used. The same experiment was repeated in the cooling cycle also which showed that even when the temperature of the sample was decreased below 120 °C, it did not regain its PIMA property.

REFERENCES:

[1] Z Hu, B Rajini Kanth, R Tamang, B Varghese, C H Sow and P K Mukhopadhyay *Smart Mater. Struct.* **21** 032003 (2012).

[2] A. Bagchi, S. Sarkar, & P.K.Mukhopadhyay *Indian J Phys* **92**: 883 (2018).

temperature is carried out. Scanning Electron Microscopy (SEM) analysis of milled powders was carried out to understand the powder morphology. Initial powders show granular morphology with size ~10-25 μm after 10hours of milling average size reduces to <8 μm . Investigation of Micro structural evolution on Sintering 10h milled powders at temperature 1050 $^{\circ}\text{C}$ to 1300 $^{\circ}\text{C}$ using Analytic Transmission Electron Microscopy and Microchemical analysis using Energy Dispersive X-Ray Spectroscopy is ongoing, results of which will be presented in the conference.

Keywords: Oxide Dispersion Strengthened Steel, Zirconia, High Energy Planetary Ball Milling, Spark Plasma Sintering

MICROSTRUCTURAL EVOLUTION AND FERROMAGNETIC SHAPE MEMORY RESPONSE IN RAPIDLY SOLIDIFIED Co-Ni-Al ALLOYS

Abhishek Bagchi^{1,3}, Suman Sarkar¹, Sandip Bysakh², Susenjit Sarkar³ and P. K. Mukhopadhyay¹

¹LCMP, S. N. Bose National Centre for Basic Sciences, Kolkata-700106, India

² CSIR-Central Glass and Ceramic Research Institute, Kolkata-700032

³Department of Mechanical Engineering, Jadavpur University, Kolkata-700032, India

pkm@bose.res.in sbysakh@cgcri.res.in

Ferromagnetic Shape Memory alloys (FSMA) are among the important and potential materials for the application as sensors and actuators due to their smart behavior and faster response than the traditional shape memory alloys (SMAs). Recently, Co-Ni-Al systems have emerged as one of the attractive FSMA system for their lucrative mechanical property in comparison to the other conventional FSMA systems like Ni-Mn-Ga. We are currently working on ferromagnetic shape memory response and mechanical properties under various environmental effects on this Co-Ni-Al alloy system. Attempts are also being made to establish the correlation between the microstructure and the various FSMA properties of this rapidly solidified melt spun alloy samples. In this work, we have studied the shape-memory properties and effect of annealing and oxidation of melt-spun ribbon alloy samples of half-Heusler composition. X-ray diffractometry (XRD) and analytical Transmission Electron Microscopy (TEM) characterization of the as-spun alloy microstructure show the existence of B2 ordered Ni-(Al, Co) micron size grains, embedded in a continuous L₁₂ ordered cobalt rich matrix. Initially, it has been confirmed that these B2 ordered AB type phases are the key responsible constituents for the ferromagnetic shape memory response. We have also carried out a detailed study on the temperature dependent FSMA properties and the oxidation kinetics of these alloys sample. The results of cross-section TEM characterization of oxidized melt-spun ribbons show the formation of irregular shaped complex oxide layer of several hundred nanometers thickness. The oxide layer is comprised of two distinct layers viz., the Co-rich surface oxide and the Al-rich nano-porous oxide grown over the base alloy just underneath Co-rich oxide layer. This composite oxide layer also helps in minimizing the diffusion rate of oxidation. The effect of temperature and the oxidation on the constituent microstructural phases in